Modelling the Impact of Cell Seeding Strategies on Cell Survival and Vascularisation in Engineered Tissue

Rachel Hannah Coy

A thesis submitted to

UCL

for the degree of

Doctor of Philosophy

Centre for Mathematics & Physics in the Life Sciences

& Experimental Biology (CoMPLEX)

and

Department of Mechanical Engineering

University College London

February 2020

I, Rachel Hannah Coy, confirm that the work presented in this thesis is my own. Where information has been derived from other sources, I confirm that this has been indicated in the work.

Signature: Date: 11th February 2020

Abstract

Currently, the design of tissue engineered constructs for peripheral nerve repair is informed predominantly by experiments. However, translation to the clinical setting is slow, and engineered tissues have not surpassed the outcomes achieved by nerve grafts. Therapeutic cell survival and vascularisation are important for the assimilation of engineered tissue, and vascularisation provides vital directional cues for regenerating nerves. In this thesis, mathematical modelling informed by experimental data is used to investigate the impact of different therapeutic cell seeding strategies on cell survival and vascularisation in engineered tissue nerve repair constructs.

A mathematical model of interactions between cells, oxygen and vascular endothelial growth factor (VEGF), consisting of three partial differential equations, is developed and parameterised against *in vitro* data. Key cell type-specific parameter values are derived, and the model is then used to simulate cell-solute interactions in a nerve repair construct over the first five days post-implantation *in vivo*.

Simulations using uniform seeding cell densities of 88 and 13×10^6 cells/ml result in the highest mean viable cell densities across the construct after 1 and 5 days respectively. However, simulations using seeding densities in the range of $200 - 300 \times 10^6$ cells/ml result in steeper VEGF gradients and higher total VEGF concentrations across the construct, which could be beneficial for vascularisation.

Simulations incorporating a porous construct sheath result in higher viable cell density predictions, but also lower total VEGF concentrations,

than those run using an impermeable sheath.

Subsequently, the cell-solute model is combined with a discrete model of angiogenesis that simulates vascular growth in response to gradients of VEGF. Simulation results suggest that different cell seeding strategies could influence the density, rate and morphology of vascularisation.

The predictions generated in this work demonstrate how mathematical modelling as part of a wider multidisciplinary approach can provide direction for future experimental work.

Impact Statement

Engineered tissue design for peripheral nerve repair involves consideration of a multitude of factors, including therapeutic cell types, materials, spatial configurations and provision of mechanical and chemical cues. Testing all of the possible designs experimentally is both time consuming and expensive, and the results of different experiments are often not directly comparable due to differences in experimental methods. Mathematical modelling, combined with targeted experimental work, has the potential to speed up and direct the design of engineered tissue.

This work is one of the first to use mathematical techniques to explore the impact of cell seeding strategies on cell survival and vascularisation in engineered tissue for peripheral nerve repair, as part of a multidisciplinary approach including experiments that were specifically designed to facilitate model parameterisation.

The results have demonstrated the potential of specific cell seeding strategies to improve therapeutic cell survival in engineered tissues and impact the rate and density of vascularisation. The quantitative predictions made by the model can be directly validated via *in vivo* experiments, and the qualitative hypotheses generated as part of this work have highlighted new avenues for exploration in the future.

The work contained in this thesis will be carried forward and extended by other PhD students and postdoctoral researchers as part of the ongoing research carried out by the recently established UCL Centre for Nerve Engineering, with emphasis on the continuation of the multidisciplinary

method set out here. In particular, the predictions and suggestions made in this thesis will contribute directly to plans for the experimental program. Further in the future, the mathematical model could be used by tissue engineers in the wider research community to help improve the design of various engineered tissue constructs.

A selection of the work contained in this thesis has been presented at conferences in the UK, Europe and Japan, including the TERMIS World Congress, as well as at the Houses of Parliament as part of the STEM for Britain poster exhibition. A review on the application of mathematical methods to tissue engineering has been published, and the parameterised cell-solute model is scheduled for publication in a separate paper. Other parts of the work are under preparation for publication.

Acknowledgements

I would like to thank my supervisors, Professor Rebecca Shipley and Dr James Phillips, for all of their encouragement, guidance and hard work. Aside from their scientific expertise, I feel lucky to have had supervisors who truly care about their students.

My PhD project would not have been possible without some of my fellow PhD students and collaborators. Particular thanks must go to Georgina and Céline, for persevering with the *in vitro* experiments, and to Paul Kingham and members of the Phillips lab (Adam, Caitriona and Kulraj) who also carried out or helped with experimental work along the way. I've also felt privileged to be part of Becky's ever-expanding, diverse and knowledgeable research group- a lovely collection of people.

Thanks are also due to the CoMPLEX staff and associated researchers, and the other CoMPLEX students, for making my experience as part of the programme so enjoyable. I am also grateful to the British Heart Foundation for funding my PhD.

To my partner Robyn: thank you for your love, support and patience over the past four years. This experience would have been far more difficult and much less fun without you.

Finally, thank you to my family for their unconditional love and support. Lois, I'm lucky to have a sister I consider to be a best friend; I'm looking forward to visiting Bristol more often. Mum and Dad: you have always encouraged my love for learning. I will never be able to thank you enough for everything you have done for me. I love you.

Contents

List of Figures

List of Tables

Publications

Peer-reviewed articles

R. Coy, G. Al-Badri, C. Kayal, C. O'Rourke, P. J. Kingham, J. B. Phillips & R. J. Shipley (2020). "Combining *in silico* and *in vitro* models to inform seeding strategies in tissue engineering." Journal of the Royal Society Interface DOI: 10.1098/rsif.2019.0801

R.H. Coy, O.E. Evans, J. B. Phillips & R. J. Shipley (2016). "An integrated theoretical-experimental approach to accelerate translational tissue engineering." Tissue Engineering and Regenerative Medicine DOI: 10.1002/term.2346

Conference talks

R. Coy, G. Al-Badri, P. Kingham, J. Phillips & R. J. Shipley (2018) "Modelling cell survival and VEGF gradients in engineered tissue using a joint theoretical-experimental approach." Tissue Engineering and Regenerative Medicine International Society World Congress, Kyoto, Japan.

R. Coy, G. Kennedy, C. Kayal, C. O'Rourke, P. Kingham, J. Phillips & R. J. Shipley (2018) "A parameterised cell-solute model to aid peripheral nerve construct design." 15th International Symposium on Computer Methods in Biomechanics and Biomedical Engineering, Instituto Superior Technico, Lisbon, Portugal.

R. Coy, R. J. Shipley & J. Phillips (2017) "A mathematical model to inform the design of peripheral nerve repair constructs." 6th Vienna Symposium

on Surgery of Peripheral Nerves, Millesi Center Vienna.

R. Coy, G. Kennedy, C. Kayal, C. O'Rourke, P. Kingham, J. Phillips & R. J. Shipley (2016). "A mathematical model informed by in vitro experiments to advance engineered nerve repair construct design." Tissue and Cell Engineering Society Annual Meeting, University College London. European Cells and Materials Vol. 32. Suppl. 4 (pp. 36).

R. Coy, G. Kennedy, C. Kayal, C. O'Rourke, P. Kingham, J. Phillips & R. J. Shipley (2016). "A joint theoretical-experimental approach to investigate the effects of low oxygen environments upon therapeutic cell viability and VEGF production." European Chapter Meeting of the Tissue Engineering and Regenerative Medicine International Society, Uppsala, Sweden. European Cells and Materials Vol. 31. Suppl. 1 (pp. 174).

Conference posters

R. Coy, G. Al-Badri, C. O'Rourke, C. Kayal, P. Kingham, J. Phillips & R. Shipley (2018). "A mathematical model to investigate the impact of seeded cell densities and distributions upon VEGF gradients and cell survival in engineered tissue." Tissue and Cell Engineering Society Annual Meeting, Keele University.

R. Coy, G. Kennedy, C. O'Rourke, P. Kingham, J. Phillips & R. Shipley (2018). "A combined mathematical-experimental approach to nerve repair." STEM for BRITAIN, Portcullis House, Westminster, London.

R. Coy, J. Phillips, R. J. Shipley (2017) "A combined theoretical and experimental strategy to inform the choice of cell density in engineered tissue constructs to maximise therapeutic cell survival." European Chapter Meeting of the Tissue Engineering and Regenerative Medicine International Society, Davos, Switzerland.

R. Coy, J. Phillips, R. J. Shipley (2015). "A mathematical model with the capacity to direct and accelerate the design of cellular peripheral nerve

repair conduits." Tissue and Cell Engineering Society Annual Meeting, University of Southampton. European Cells and Materials Vol. 29. Suppl. 3 (pp. 42).

Glossary

SC Schwann cell. 32

ECM Extracellular matrix. 32

PNI Peripheral nerve injury. 33

NRC Nerve repair construct. 36

EngNT Engineered neural tissue. 37

dADSC Differentiated adipose-derived stem cell. 37

VEGF Vascular endothelial growth factor. 44

EC Endothelial cell. 61

HUVEC Human umbilical vein endothelial cell. 62

HIF-1 Hypoxia-inducible factor 1. 65

FGF Fibroblast growth factor. 66

MMP Matrix metalloproteinases. 66

TEC Tip endothelial cell. 66

SEC Stalk endothelial cell. 66

PDGF Platelet derived growth factor. 68

HSPG Heparan sulphate proteoglycan. 68

GAG Glycosaminoglycan. 80

PLGA Poly(lactic-co-glycolic acid). 82

ADSC Adipose-derived stem cell. 128

PCL Poly(caprolactone). 129

BDF Backward differentiation formula. 175

Dll4 Delta-like ligand 4. 261

Nomenclature

Constants

α	Basal VEGF secretion rate. 120
β	Cell proliferation rate constant. 119
Δt	Angiogenesis model time step length. 269
Δx	Angiogenesis model lattice spacing. 269
δ	Cell death rate constant. 119
ϵ	Porosity. 206
$\mathrm{R_{max}}$	Maximum TEC migration speed in absence of VEGF gradient. 288
$\mathrm{R_{min}}$	Minimum TEC migration speed in absence of VEGF gradient. 288
τ	Diffusive tortuosity. 217
τ_s	Sprout tortuosity. 300
θ_{TEC}	TEC angle. 300
ζ	Non-uniform cell distribution multiplier. 251
b_{max}	Maximum probability of TEC tip branching. 280
B_s	Bunsen solubility coefficient. 295

c_0 Initial oxygen concentration in collagen NRC. 228

c_a Ambient oxygen concentration in incubator. 132

c_{tissue} Oxygen concentration in tissue. 121

c_b Oxygen concentration in blood. 295

c_h Hypoxic oxygen threshold for VEGF secretion. 120

$c_{1/2}$ Oxygen concentration at which oxygen consumption is half-maximal. 120

D_{eff} Effective diffusivity in the porous domain. 217

d_v VEGF degradation rate constant. 120

D_{c_g} Diffusion coefficient of oxygen in collagen gel. 120

D_{c_m} Diffusion coefficient of oxygen in media. 170

D_{v_g} Diffusion coefficient of VEGF in collagen gel. 120

D_{v_m} Diffusion coefficient of VEGF in media. 171

k_α VEGF secretion gradient parameter. 167

k_w Vessel wall permeability. 295

L NRC length. 119

M Oxygen metabolism constant. 120

n_0 Initial cell density (post-stabilisation). 131

n_{max} Maximum viable cell density. 119

n_{tot_0} Initial total number of cells seeded within a NRC. 251

n_{tot} Total number of viable cells within a NRC. 251

R_1 Radius of cylindrical collagen NRC. 225

R_2 Radius of combined cylindrical NRC and sheath geometry. 225

r_{ex} TEC sprouting exclusion radius. 278

r_{ana} Anastomosis distance. 291

r_a VEGF averaging radius for nodes on the circular faces of the NRC geometry. 276

r_f Filopodia sensing radius. 272

r_s Radius of spheres used to represent vessels in COMSOL. 295

r_v Vessel radius. 295

s_{max} Maximum sprout formation probability. 278

T NRC sheath thickness. 214

T_{branch} Threshold age for branching. 281

t_v Vessel wall thickness. 295

v_{tissue} VEGF concentration in tissue. 227

V_m VEGF secretion multiplier. 164

Functions

P_{branch} Branching probability function. 280

P_{dir} TEC migration direction probability function. 286

P_p TEC migration direction probability function directional persistence component. 286

P_{sprout} Sprouting probability function. 277

P_v TEC migration direction probability function chemotactic component. 286

R_0 TEC migration speed in absence of VEGF gradient. 288

R_g TEC migration speed multiplier in presence of VEGF gradient. 290

R_s TEC migration speed function. 288

D_{c_s} Effective diffusion coefficient of oxygen in a porous sheath. 227

D_{v_s} Effective diffusion coefficient of VEGF in a porous sheath. 227

K Porosity coefficient. 164

Variables

$\bar{n}$ Simulated mean cell density over the NRC geometry. 231

$\bar{n}_{\mathrm{g}}$ Simulated mean viable cell density over the gel. 178

$\bar{v}$ Simulated mean VEGF concentration over the NRC geometry. 231

$\bar{v}_{\mathrm{g}}$ Simulated mean VEGF concentration over the gel. 192

$\bar{v}_{\mathrm{m}}$ Simulated mean VEGF concentration over the media. 178

Δv VEGF gradient. 273

$\mathbf{d}_t$ Unit vector direction of migration of a TEC at time t. 286

c Oxygen concentration. 119

c_s Oxygen concentration in pore/fluid fraction of NRC sheath. 228

n Viable cell density. 119

n_{exp} Experimental mean viable cell density over the gel. 178

n_{SD} Standard deviation of the simulated cell densities over the NRC geometry. 231

r Radial coordinate of NRC geometry. 225

S_i Neighbourhood set of lattice nodes, defined by the sensing radius, for the i^{th} TEC. 273

t Time. 119

v VEGF concentration. 119

v_{exp} Experimental mean VEGF concentration over the media. 178

v_{SD} Standard deviation of the simulated VEGF concentrations over the NRC geometry. 231

v_s VEGF concentration in pore/fluid fraction of NRC sheath. 228

Chapter 1

Introduction

This thesis presents a multidisciplinary approach to nerve tissue engineering, comprising of the development of a mathematical model of important cell-solute interactions and vascular growth within engineered tissue, informed by *in vitro* data collected from specifically designed experiments. The aim is to investigate the potential impact of different initial cell distributions and densities within engineered tissue on the survival of the seeded cell populations and revascularisation, specifically in the context of nerve repair. More broadly, this thesis also explores and demonstrates the potential of a closely integrated multidisciplinary approach to tissue engineering. Thus the chosen experimental-theoretical method forms an integral part of the research.

In this chapter, general introductions to the peripheral nervous system and current approaches to peripheral nerve repair are provided (Sections 1.1 and 1.2), followed by an introduction to therapeutic cell seeding strategies for engineered tissue (Section 1.3), which motivates the study of the impact of different seeded cell densities and distributions upon outcomes. Subsequently, an overview of the merits and challenges of a joint theoretical and experimental approach to tissue engineering is provided (Section 1.4). Finally, the motivations and objectives of the project are outlined, and the structure of the thesis is presented (Sections 1.5 and 1.6).

1.1 The peripheral nervous system

The peripheral nervous system is a complex network of nerve bundles which facilitates the transfer of information between the central nervous system and the tissues and organs of the body, via impulses (action potentials) transmitted by sensory, motor and autonomic neurons. A single peripheral nerve (Figure 1.1) is composed of many neurons and their corresponding axon fibres. Many, but not all, of these axons are covered in a myelin sheath provided by Schwann cells (SCs), which improves the conduction of action potentials. SCs are the principal glial cells of the peripheral nervous system, and are instrumental in the process of peripheral nerve repair (Section 2.1.1). Bundles of axons are contained within the endoneurium of structures called fascicles, along with their supporting SCs and additional extracellular matrix (ECM). Each fascicle is surrounded by a perineurium, an additional supporting layer. Finally, the whole nerve, containing one or more fascicles, is covered by a final layer of dense connective tissue called the epineurium.

Vasculature is present throughout the body of the nerve and in the surrounding tissue in the form of an interconnected and tortuous network [210, 423]. The tortuosity of the blood vessels allows the delivery of vital nutrients to remain unhindered by twisting or movement of the nerve. Major vessels lie both on the outer surface of the nerve and within the epineurium, with microvasculature running throughout the perineurium and endoneurium. Local blood flow is therefore higher in the epineurium than the interior of the nerve [423]. The branching macro-structural forms of the vascular network and peripheral nerves are similar and appear closely related even at first glance (Figure 1.2). Although there are many differences between the two networks upon closer inspection, it is well established that the development, function and repair (Section 2.1.2) of the peripheral nervous system are closely tied to that of the vascular system [296].

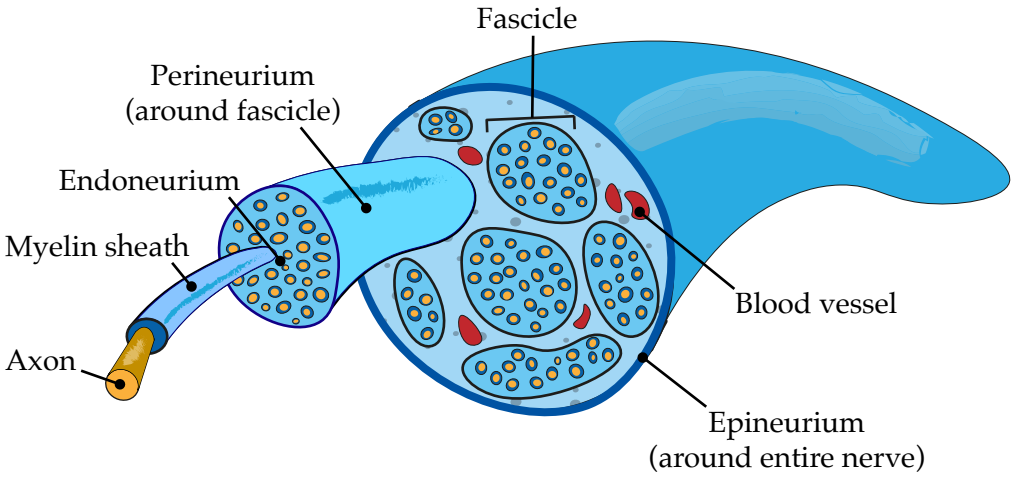

Figure 1.1: Cross section of a peripheral nerve. Axons range in diameter from 0.2 µm up to 20 µm.

1.2 Peripheral nerve injury and current strategies for repair

Damage to, or complete severance of, a peripheral nerve, categorised generally as peripheral nerve injury (PNI), has been estimated to occur in around 1.5 to 3% of trauma patients [38, 275] with young people disproportionately affected [194, 247, 263, 378]. Motor vehicle accidents are the most common cause of PNI [194]. Other causes include sports injuries, gun-shot and stabbing incidents and general military activity [329], falls, and diabetes [105]. Although not life threatening, PNI can have serious repercussions for those affected.

PNI can lead to permanent loss of function and refractory neuropathic pain along with a host of comorbidities [274], resulting in a marked reduction in quality of life for many patients [81]. Patients who do experience neuropathic pain are more likely to have other pain-related conditions such as fibromyalgia and oesteoarthritis [39]. Neuropathic pain and loss of function can have an impact upon every aspect of a patient's life, from their role in society to their relationships at home, according to the level of disability that they may experience. This often leads to distress, anxiety and depres-

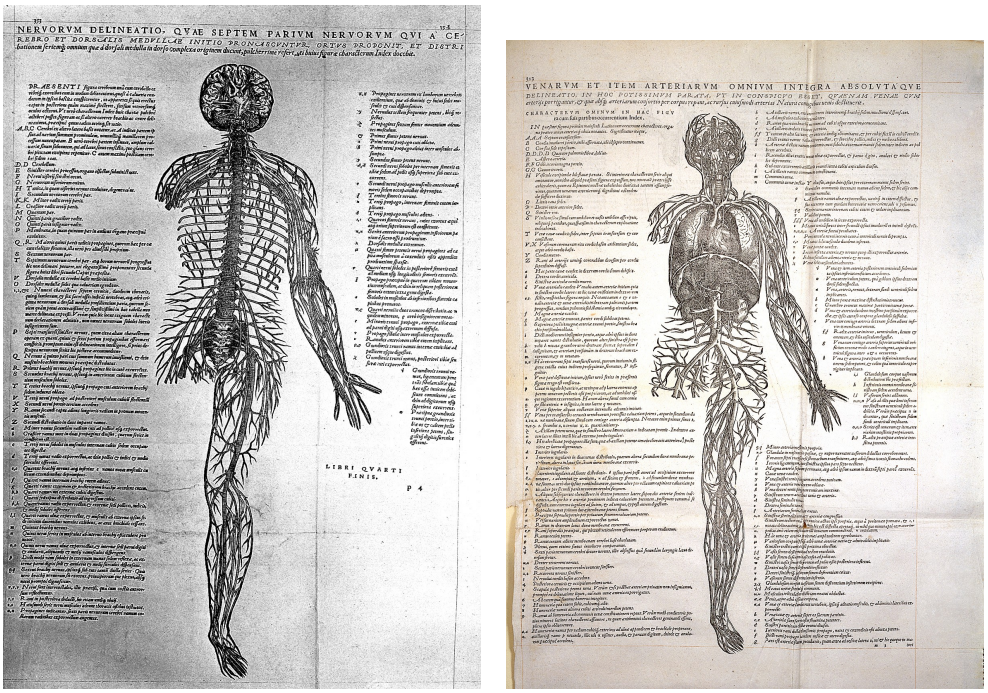

Figure 1.2: Depictions of the nervous system (left) and the arterial and venous system (right) from Andreas Vesalius' *De Humani Corporis Fabrica*, 1543. Although these early anatomical drawings are imperfect, they serve to demonstrate the similarity of the branch-like structure of these two networks. *'Final nerve-figure, by Vesalius.' by Vesalius, Andreas (left) and 'A. Vesalius, De humani corporis fabrica' (right). Credit: Wellcome Collection. CC BY 4.0*

sion [102, 146, 274]. Neuropathic pain can greatly affect a patient's ability to obtain quality sleep, further exacerbating any mental and physical issues [274].

Due to the ongoing treatment of pain and other symptoms in PNI patients, the healthcare cost of incurring such an injury is considerable. In one study, the cost of treating neuropathic pain, including PNI alongside other causes, was calculated from a US health insurance claims database for the year 2000 [39]. It was estimated to cost an average of $17,355 per patient per year, in comparison to $5,715 for age and gender matched controls without painful neuropathic disorders. A study based in Sweden calculated that a combined total of lost production costs and health care fees of approximately €51,238 is incurred for each employed person who experiences an injury to their one of the major nerves in the forearm, the

median nerve [334]. The median sick leave for the participants in the study was 210 days, but some individual patients's leave lasted over three times this length. Thus PNI presents a significant economic challenge to both patients and society in general, motivating the ongoing search for viable clinical treatments that will reduce the cost of therapy as well as the physical symptoms.

The current gold standard for repair of nerve gaps of length greater than 1 to 2 cm is the autologous nerve graft or autograft. This method of treatment involves the transplantation of nerve sections from elsewhere in a patient's body into the injury-induced nerve gap, thereby bypassing the issue of immunogenicity. Supporting therapeutic cells such as SCs, which release neurotrophic factors that aid regeneration, are transferred along with the body of the nerve. Autologous nerve grafts remain the most successful method of therapeutic intervention for PNI.

However, there are multiple issues with this approach to nerve repair. The success rate of autologous nerve grafts is far from ideal, with studies reporting that only around 50% of autograft patients manage to regain a good level of function [181, 210, 390, 412]. As a consequence of the surgery, additional nerve and tissue damage at the donor nerve site can lead to more pain, infection and loss of function. The need to harvest a donor nerve also lengthens the time spent in surgery, thereby incurring additional costs. Furthermore, the number of eligible nerve donor sites that can be harvested is limited, and it is often difficult to locate and harvest a sufficient quantity of donor nerve.

Allografts, tissues transferred from one member of a species to another genetically non-identical member of the same species, are an alternative nerve repair solution. This method does not require patients to suffer from donor nerve site comorbidity, and it would be possible to stockpile allografts for future use. However, cellular allografts do necessitate the use of immunosuppression, making them less than ideal candidates for

widespread use [358].

Bioengineered peripheral nerve repair constructs (NRCs) have the potential to become the most affordable, versatile and successful method of nerve repair. NRCs are segments of engineered tissue designed to aid peripheral nervous system regeneration (Figure 1.3). Once surgically implanted into a nerve gap, NRCs encourage neurite growth through the provision of structural and chemotactic guidance. NRCs are predominantly cylindrical in form to mimic the structure of the regenerating nerve. Due to the biological complexity of the process of neuronal regeneration NRC design requires the consideration of many different factors [265, 301]. A large number of combinations of materials, seeded cells and spatial arrangements have been trialled both *in vivo* and *in vitro*, with varying degrees of success [98, 270]. Base scaffold materials range from synthetic polymers to biopolymers such as type I collagen and fibrin. Additional structural components such as aligned rods or channels and porous surfaces have been added in attempts to increase cell guidance [91].

The theoretical investigation carried out in this thesis focuses on NRC designs constructed using a base material called engineered neural tissue, or EngNT [132]. Manufactured in the Phillips lab, EngNT is composed of cell-seeded type I collagen that has been tethered to induce cellular contraction of the gel and alignment of the cells along the longitudinal axis, and then stabilised via the removal of interstitial fluid in a process called plastic compression [54, 310]. Sheets of EngNT can then be rolled into cylindrical structures, inserted into a protective sheath, and implanted into a peripheral nerve gap *in vivo* to aid regeneration.

EngNT has been created using several different cell types, including differentiated adipose-derived stem cells (dADSCs) [133], differentiated human dental pulp stem cells [340] and differentiated CTX0E03 human neural stem cells [291]. The aligned nature of this cellular material provides an additional directional cue to regenerating neurons and, in contrast

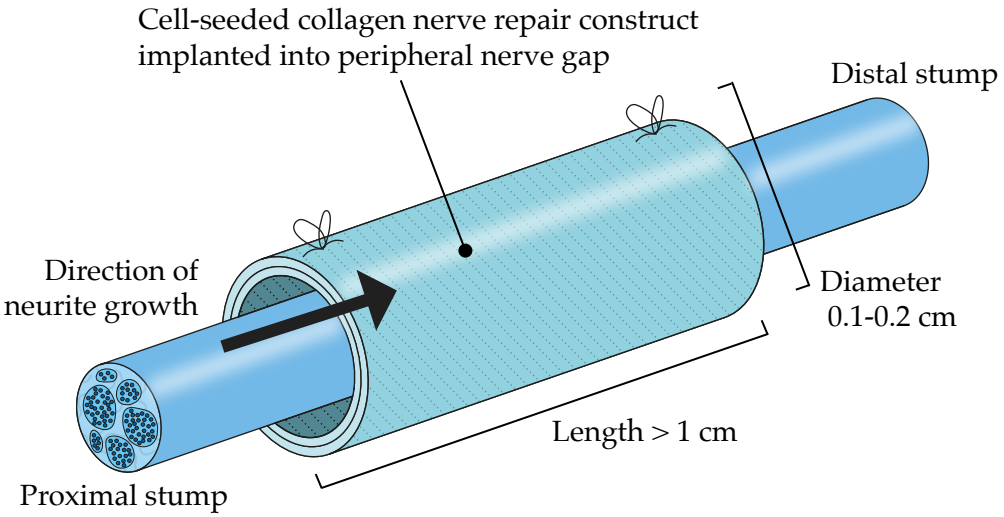

Figure 1.3: Simplified illustration of an NRC designed to guide and promote the regeneration of peripheral nerves. During surgery an NRC is sutured between the proximal and distal nerve stumps. The body of an NRC can be constructed using a range of different materials and additional components, such as rods and seeded cells.

to the use of unstable hydrogels, the process of manufacture of EngNT allows greater control over the arrangement of the therapeutic cells.

The use of EngNT removes several challenges typically encountered during the design and manufacture of engineered tissue scaffolds for peripheral nerve repair [132]. The therapeutic cells are initially distributed into the gel and therefore there is no separate cell seeding step or any need to engineer matrix surfaces that promote cell adhesion. The mechanical properties of EngNT are similar to that of native tissue, and thus it also avoids the complications that arise when cells are seeded on stiff matrix surfaces that provide significant and complex mechanical cues [311]. Importantly, EngNT could also feasibly be manufactured on a large scale according to clinical need because the processes of cellular alignment and plastic compression are suitable for automation.

Although studies involving EngNT-based NRCs and many other different NRC designs have offered some promising results, the efficacy of a NRC is yet to surpass that of an autograft and translation to the clinical setting is limited, signalling that further improvement is still required

[113, 140, 228, 270].

1.3 Cell seeding strategies: current approaches and potential for improvement

Therapeutic cells are a critical component of current NRC designs. They are used extensively across the entire field of tissue engineering and regenerative medicine [22, 44, 90, 119, 286, 348] and cell seeded engineered tissues have demonstrated improved outcomes when compared to acellular controls [175, 193, 422]. Seeded stem cells and in particular Schwann cell-like cells are commonly used in the context of peripheral nerve repair [91], and are especially important for long gap neuronal repair. These cell populations secrete important growth factors that aid both neuronal repair and revascularisation [30, 410], and can also provide mechanical support via the production of ECM proteins [55, 83] and directional cues [132]. The use of seeded SCs or SC-like cells has produced promising results both *in vivo* and *in vitro* [110, 141, 234].

In recent years, research into therapeutic cell seeding for NRCs and in tissue engineering in general has focused predominantly upon the choice of cell type. Different cell types have different strengths and weaknesses and can produce very different results *in vivo* and *in vitro*. Regardless of the cell type used, the survival of the seeded cell population is an important consideration in cellular tissue engineering. Note that in this thesis, the term "cell survival" will be used to refer to the persistence of a cellular population over time, as opposed to as a reference to the survival of specific individual cells.

There is some doubt about the need for longer term cell survival (on the order of weeks to months), due to examples of improved functional results using cell therapy with little evidence of enduring cell survival [298, 321]. However, shorter term cell survival is generally acknowledged as important for the efficacy of NRCs and other cellular engineered tissues.

Furthermore, the death of seeded cells post implantation has the potential to become a significant waste of resources and source of expense once NRCs finally achieve widespread translation to the clinical setting.

Seeded cell death is caused by hostile aspects of the *in vivo* repair environment, including hypoxia brought about by loss of blood vessels during injury, oxidative stress, and the host immune response [152, 373]. The transcription factor Hypoxia-Inducible Factor-1α (HIF-1α) mediates the hypoxia response of cells, which is activated when oxygen availability does not meet cellular metabolic demand. Under hypoxic conditions, the degradation of HIF-1α is inhibited, which permits HIF-1α to undergo nuclear translocation and thereby activate Hypoxia Response Element (HRE) genes. HRE genes are involved in metabolic adaptation, including the production of angiogenic factors, such as VEGF, and pro-survival factors, such as antioxidants [198]. However, HIF-1α can also induce apoptosis [62].

Additionally, the effect of hypoxia on reactive oxygen species (ROS) and ROS scavenger secretion can impact cell survival. ROS are highly reactive molecules that are produced during the metabolism of oxygen; the ROS family work as messengers but can also cause oxidative damage to cells. Conversely, ROS scavengers are compounds that react with ROS to counteract their negative effects. Due to anaerobic respiration, ROS production and acidosis increases in hypoxic conditions [67]. Excess levels of ROS can in turn lead to severe damage to cell structures and consequently cell death [330].

A lack of sufficient supporting extra cellular material could also negatively impact the survival of populations of cells by inducing anoikis, which is cell death induced by the loss of cell-matrix interactions [52, 60, 123].

Survival rates of seeded cells post implantation in nerve injury scenarios vary according to the cell type and time interval, with measurements ranging between 0.5 and 1% after 4 months for neural stem cells injected into a rat nerve gap [148], and from 25 to 38% after 2 months for skin-

derived stem cells transplanted within both collagen and polymer-based NRCs [243], as reviewed by Walsh and Midha [400]. Here the % values are proportions of the number of cells originally injected or implanted. In general, most existing measurements of cell survival are taken at relatively late time points (beyond 6 weeks post-implantation). However, loss of therapeutic SCs has been found to occur predominantly during the first 3 weeks post implantation [152, 302], although the exact time scale and degree of cell death differs according to the scenario.

In a different paper, Walsh et al. demonstrated that the nerve environment into which the cells are seeded could have a significant impact upon their survival rates by recording the survival rates of 300,000 skin-derived precursor cells delivered after transplantation into intact nerve, and injured nerve immediately after injury (acutely denervated nerve) and 8 weeks after injury (chronically denervated nerve) [401]. The measured survival rates varied significantly with the scenario type and time point, from a high of 10.48% in the acutely denervated scenario after 2 weeks, to a low of 2.68% in the uninjured scenario after 8 weeks. However, the cells in this study were injected, and therefore did not benefit from the support of a scaffold. Interestingly cell survival rates were lowest in the uninjured scenario.

A few studies provide evidence of the importance of cell survival for the efficacy of tissue engineered constructs, although the fact that the majority of researchers do not record survival rates makes comparison difficult. Itosaka et al. compared different methods of delivering bone marrow stromal cells into rat spinal cord injury sites, and found that the cells seeded in a fibrin matrix achieved both better survival rates and better neurological function than the cells that were injected into the gap without a supporting scaffold [163]. It is important to note that this result does not necessary imply that larger cell survival rates produce better functional outcomes due to the potential impact of the supporting matrix. However, the cell seeded

fibrin matrix also produced better functional outcomes than the fibrin matrix alone, so it seems likely that increased cell survival facilitated by the matrix at least played a role in the improvement of the functional outcomes.

Similarly, Patel et al. found that blood vessel and axonal density correlated strongly with seeded SC numbers in rat spinal cord implants [300], and Parr et al. also found a significant positive correlation between functional scores and neural stem/progenitor cell survival in rat spinal cord injury [298].

Overall, studies on tissue engineering for peripheral nerve repair often do not track the implanted cells or do so using imperfect techniques [400], and therefore data describing cell survival specifically in the peripheral nerve repair scenario is scarce. However, awareness of the need for at least some minimal survival time has lead to the development of various techniques to increase or enhance cell survival. Specific choices of scaffold material have been shown to improve cell survival [60, 85]. Delivery of growth factors to support the cells, as well as encourage repair, has also been implemented [295] and the short half life of these proteins has lead to the development of slow-release delivery methods to increase their efficacy [235, 297]. The immunosuppressive cyclosporine is also routinely used in allogeneic cell transplantation studies, including in the peripheral nerve repair setting [340], to enhance cell survival.

Although many of the previously mentioned techniques for increasing cell survival have achieved improved results, so far there has been little research on the impact of the quantity and distribution of the seeded therapeutic cells upon cell survival. Cell density can also affect the proliferation and death rates of the cells. First of all, cells seeded in engineered tissue *in vivo* have access to only limited nutrient and oxygen supplies, especially in the initial period after implantation; areas of tissue with higher cell densities will consume nutrients faster, leading to low levels of nutrients in these regions and increasing the risk of cell death. Oxygen in particular is con-

sumed quickly by dense populations of cells, but has only a short diffusion distance, which can lead to necrotic regions in the centre of engineered tissues.

Additionally, interactions between cells within a population can affect rates of proliferation and death. Contact inhibition of proliferation, the slowing of cell proliferation due to contact between the surfaces of adjacent cells, is a well-documented *in vitro* phenomenon [248, 364]. *In vivo*, this curbing of cellular proliferation has been speculated to act as a mechanism for ensuring effective organisation of tissue. Juxtacrine signalling and growth factor production can also help to increase cell survival.

Some existing studies appear to assume that using more therapeutic cells is better, but this is not necessarily the case: although increasing the initial number of seeded cells in engineered tissue could result in more cells surviving, on the other hand very high densities could increase competition for resources, resulting in the opposite effect.

Thus careful thought is required to identify seeding cell strategies that allow for necessary levels of cell survival: certainly some cells need to survive for a period of time, but seeding a construct with an excessive number of cells in the hope that enough will survive to achieve the desired effect is an inefficient and wasteful solution. This thesis will investigate the hypothesis that there is potentially an optimal seeding cell density at which enough cells survive for the tissue to remain useful, whilst limiting the number of cells that die, thus reducing the waste of excessive cell seeding.

As reviewed by Walsh and Midha [400], the total number of therapeutic cells used for peripheral nerve repair varies considerably from as low as 4000 [16] to as high as 20×10^6 [160, 400]. The initial therapeutic cell density used tends to vary widely in the approximate range of 1×10^6 to 200×10^6 cells/ml. It is also worth noting for comparison that the average density of SCs in normal nerve is around 20×10^6 cells/ml [264, 333]. However, due to variance in the injury types, cell types and therapeutic approaches used

it is difficult to directly compare the results of these studies.

Published research does not always specify the number or density of cells used, and only a few studies have specifically investigated the impact of the initial density at which cells are seeded upon outcomes. One such study by Mosahebi et al. trialled polyhydroxy butyrate NRCs using four different initial densities of seeded SCs: 20, 40, 80 and 160×10^6 cells/ml [264]. The measured axonal regeneration distance after 3 weeks post-implantation for the 20×10^6 cells/ml NRCs was not statistically significantly greater than that of the acellular controls, but doubling the density to 40×10^6 cells/ml also approximately doubled the axonal regeneration distance, and this increased again when a density of 80×10^6 cells/ml was used. Interestingly, relative to this 160×10^6 cells/ml resulted in a small decrease in the regeneration distance, implying that the optimal seeding cell density for this scenario lies somewhere between 80 and 160×10^6 cells/ml. This provides evidence that there is a threshold after which increasing cell density delivers poorer results, perhaps due to an increase in cell death as a result of competition for nutrients.

Guénard et al. found that higher seeding densities of 80 and 120×10^6 cells/ml SCs in channel constructs increased the mean number of myelinated axons across a rat peripheral nerve gap of 8 mm, compared to 40×10^6 cells/ml and the acellular control [141]. Overall 120×10^6 cells/ml was the density that resulted in the best regeneration. However, in this study the luminal volume of the nerve constructs was also increased at the same time as the seeding density, meaning the isolated effect of the seeding density alone is less clear.

Rutkowski et al. seeded therapeutic Schwann cells at densities of 10^4, 10^5, 10^6 and 10^7 cells/ml in NRCs and placed a dorsal root ganglion at the open end of each construct as a source of neurons [337]. They reported that only constructs with seeding densities greater than 10^7 cells/ml resulted in significantly greater axon lengths than those without Schwann cells. Al-

though this study tested a wide range of densities, the highest cell density was still less than the densities reported as delivering the best results in the works by Guénard et al. and Mosahebi et al., and so it potentially did not explore the upper limits of seeding cell density efficacy. Furthermore, none of these studies assessed cell survival rates at the time point of the outcome measurements, but previously referenced studies have shown that increased cell survival, and therefore increased density of viable cells, has a positive impact on outcomes. Therefore it seems probable that the improvement in outcome gained from increases in initial cell density stems from the fact that progressively higher seeding densities lead to denser cell populations over time, up to the point where competition and overcrowding becomes an issue.

Overall, the existing studies on the impact of cell density upon efficacy for peripheral nerve repair are limited but do suggest that there may be an optimal seeded cell density for improved repair, and research in tissue engineering in general indicates that this will probably vary according to the injury type, cell type and the repair approach taken. Certain tissue engineered scaffold and therapeutic cell type combinations may be more conducive to cell survival and thus require fewer seeded cells to achieve a desired level of regeneration.

Although inconclusive due to lack of data, existing studies appear to suggest that increased cell survival is beneficial for tissue regeneration post-implantation. Working on this assumption, it would be useful to be able to pinpoint the cell seeding density, for a particular NRC scaffold and cell type combination, that will provide the highest number of viable cells in the short term post-implantation. This is one specific aim of this thesis.

Another potentially important, but thus far generally overlooked, consideration is the spatial distribution of cells across NRCs. Cells are currently seeded uniformly across most types of engineered tissue. However, little research has been conducted to investigate whether alternative, non-

uniform distributions of seeded cells could help to improve cell survival, potentially by seeding fewer cells in less hospitable regions of tissue.

Non-uniform distributions could also encourage vascularisation via the production of steeper vascular endothelial growth factor (VEGF) gradients across the engineered tissue. VEGF is an important angiogenic factor which promotes vascular permeability and basement membrane degradation during the initial stages of angiogenesis [33]. Additionally, concentrations and gradients of VEGF influence the rate and direction of endothelial cell migration [31, 282, 413]. The role of VEGF in angiogenesis is described in more detail in Sections 2.1.3 and in Chapter 5. Areas of tissue with higher densities of cells would be expected to generate larger quantities of VEGF and other important growth factors. The growth of vasculature is in turn closely linked to the issue of cell survival via the provision of oxygen to the hypoxic repair environment and, in the context of peripheral nerve repair, endothelial cell migration in response to VEGF aids neuronal regrowth. The important relationship between neuronal repair and vascularisation is explored in detail in Section 2.1.2 and the emphasis upon VEGF motivated in Section 2.1.3.

In summary, exploration of the potential impact of different seeded cell densities and distributions upon outcomes in tissue engineering is so far incomplete, although research published so far has suggested the existence of optimal cell densities. This thesis will explore how the seeded cell densities and distributions in NRCs could be altered to enhance cell survival and the production of VEGF gradients, and thereby improve outcomes including the degree and rate of vascular growth.

1.4 Motivation for a multidisciplinary approach

Mathematical modelling is capable of accelerating and refining design choices in tissue engineering but so far has not been exploited to its full potential [86]. This is despite acknowledgement that mathematics and com-

putational modelling has the potential to be a key tool for tissue engineers from as early as 1993 [19, 206], around the time when the field was first beginning to grow rapidly [41]. This thesis aims to improve the cell seeding strategy of tissue engineered NRCs through the use of a mathematical model, but also to demonstrate and explore how mathematical modelling can be properly implemented alongside experimental work in tissue engineering as part of an effective and efficient multidisciplinary workflow.

Current research in soft tissue engineering, encompassing nerve and skin engineering, is still predominantly experimental. Decisions regarding factors such as the materials used to manufacture NRCs, and the spatial arrangement of cells and other components used to promote axon growth, have been made based upon the results of existing experimental publications. These publications are both numerous and diverse, featuring many combinations of different nerve construct designs, experimental models and assessment methodologies [14, 270]. Although this provides a wealth of information to draw upon, this diversity also means that it is often difficult to compare outcomes reported in different papers. The sheer number of possible designs means that choosing which one to test from the wide range of choices is not an easy task, and so far translation to the clinical setting has been slow.

Prior to clinical introduction, designs must be tested using *in vivo* animal models. However, the 'Three Rs' of experimental science dictate that the replacement, reduction or refinement of animal use should be an aim for scientists. *In vitro* models go some way towards reducing the number of animal experiments required to refine NRC designs by helping to identify substandard designs before they reach the *in vivo* testing stage [135], but it is worth noting that the *in vitro* models used are not always good representations of the *in vivo* scenario. The introduction of mathematical modelling as an additional step prior to or alongside the use of *in vitro* models would help to reduce the waste of both animal and general laboratory resources.

A parameterised, data-validated model would have the ability to identify poor nerve construct designs before their implementation in the *in vivo* setting, thereby aiding scientists in their compliance with the 'Three Rs', as well as saving money that would otherwise be wasted experimentally testing clinically inviable designs.

Essentially, modelling can help provide focus to experimental work, narrowing the breadth of potential options that experimental scientists face in this field. In contrast to experiments, once a mathematical model has been created, simulations to test different designs are comparatively quick and very cheap to run. Furthermore, mathematical models can be used to generate hypotheses, as well as test them. Sweeping over parameter values has the potential to throw up unexpected and exciting results that can inspire future experimental research.

Further in the future, mathematical models could even help to bridge the species-specific gap between animal and human studies. Rat models feature in a majority of *in vivo* peripheral nerve repair studies, but frequently the results do not translate smoothly to human clinical application [14, 183]. It could be possible to create a mathematical model of peripheral nerve regeneration incorporating features and parameters relating specifically to human biology, which might help us to understand the differences between the rat model and the human more thoroughly.

So far, the majority of modelling in the field of tissue engineering has been implemented to study bone regeneration and tissue cultivation. These studies, along with examples of modelling from other related areas of biology, can be used to demonstrate the possible efficacy and potential pitfalls of a joint theoretical-experimental approach to tissue engineering. An extensive review of mathematical modelling in biology and tissue engineering relevant to the work in this thesis is presented in Section 2.2.3; a small selection of papers are referred to in the following paragraphs to illustrate important benefits and issues associated with using mathematical

modelling in combination with experimental data to study biological or engineered tissues.

One example of the use of mathematical modelling in tissue engineering is provided by Sanz-Herrera et al., who developed a multi-scale mathematical model to simulate the *in vivo* regeneration of bone tissue within a scaffold implant [341]. The study aimed to inform the design of bone scaffolds via the prediction of their behaviour *in vivo* and their interactions with the regenerating bone tissue. Both the micro-scale bone regeneration within the scaffold and the organ-level bone remodelling were captured through the use of mechanics in combination with a finite element voxel method. A micro-CT generated geometry of an actual scaffold was used within the simulations. Parameter values such as scaffold stiffness were varied to assess their impact upon model outputs including scaffold resorption and percentage bone regeneration. The results of this investigation suggested that, within the parameter ranges investigated, the rate of bone regeneration within the scaffold increases with increased scaffold stiffness and mean pore size. Seeding the scaffold with cells prior to implantation also improved the simulated rate of regeneration. These results demonstrate the ability of mathematical modelling to pin point which design variables, represented by corresponding model parameters, are most likely to affect experimental and clinical results, and to suggest promising values for such variables.

However, this study also draws attention to the need for proper model validation, which is a crucially important aspect of mathematical modelling in the field of tissue engineering and in biology in general. Sanz-Herrera et al. were unsatisfied with their attempts to validate their model against experimental data. They pointed out that many of the input parameter values needed for the model were difficult to find in the literature, making it hard to compare their final results against experimental data. They found that data from previous experimental studies in rabbits fell in the general range

of their model results, but acknowledged that the experimental set ups differed from their corresponding *in silico* configuration, preventing accurate validation. In the study conclusion, they advocated a multidisciplinary approach to this problem, combining the work of experimental scientists with modellers to enable proper model validation. This is the approach adopted in this thesis.

The importance of consistency between experimental and theoretical work also became apparent when Hossain et al. developed a computational model of 3D chondrocyte cell growth within a porous scaffold, placed within a bi-directional flow perfusion bioreactor, which incorporated the influence of cell growth over time upon local fluid flow [156]. The study compared the predicted cell growth rate with experimental work, and found that the two were approximately in agreement. However, the initial conditions used for the experimental work did not correspond directly to the model, preventing definitive validation of the theoretical framework. This further motivates the use of specifically designed experimental work to validate as well as parameterise mathematical models, if possible, in order to prevent such issues from reducing accuracy and confidence in the validation process.

Occasionally it is possible to achieve model validation using existing data collected for a different purpose, but this requires some careful thought about whether the existing experimental metrics can be matched to model outputs. De Pillis et al. presented a model that described interactions between immune cells and tumour cells, and succeeded in validating their analytical framework against both mouse and human experimental data sets provided by previous research [94]. Interactions between immune cells and tumour cells were described by a set of coupled differential equations, including functions representing growth and death rates. Some parameter values were gleaned from previous papers, whilst others were derived using optimisation methods with the experimental data. Finally,

patient data values for percent $CD8^+$ T cell induced tumour lysis was used to validate the model. The results of the model suggested that increasing the activity of the $CD8^+$ T cell specifically could be necessary for tumour regression, providing an interesting hypothesis that could direct and inspire further research.

Based upon existing studies, it is clear that a carefully planned methodology is required to make the most of the capabilities of mathematical modelling in combination with experimental data. Data from specifically designed experiments, in combination with relevant existing values found in the literature, can be used to increase the accuracy of the parameterisation process. If possible, further experiments should also be carried out to validate model predictions. The use of existing data for validation is less reliable due to almost certain discrepancies between the previously conducted experimental set-up and the model framework. Validation experiments need not be carried out for the sole purpose of confirming the predictive powers of the model. In the proposed joint theoretical-experimental workflow (Figure 1.4), experiments that would have taken place regardless of the existence of a theoretical model can be adjusted according to the model predictions, perhaps involving a reduction in the number of designs that are to be tested or a greater focus on designs predicted by mathematical simulations to perform well. The results of these experiments can act both as model validation and as experimental evidence in their own right.

In summary, mathematical modelling could act as a useful complementary tool for tissue engineers that would allow experimental scientists to extract more value from existing data, reduce animal experimentation and cost, and streamline their workflow. Data from experiments can be used to iteratively improve mathematical models, as well as published and analysed in its own right. This integrated method of working will require close interaction between experimental and theoretical scientists.

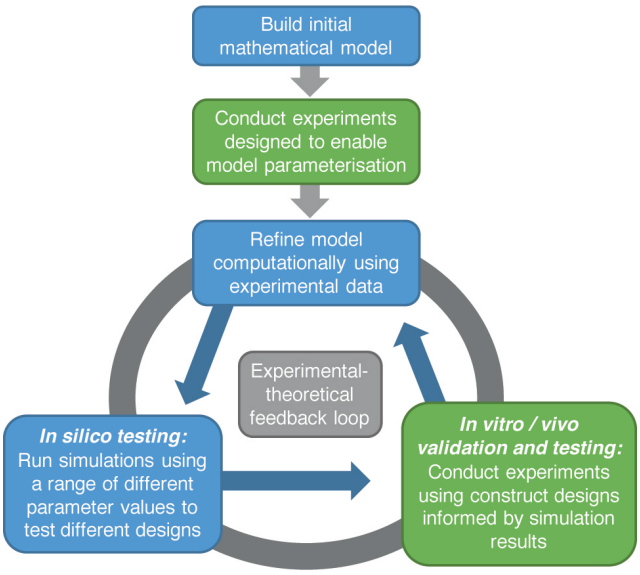

Figure 1.4: Diagram demonstrating the proposed theoretical-experimental workflow followed by this project, reproduced from Coy et al. [86]. The initial mathematical model, informed by existing publications and knowledge, is iteratively improved using experimental data.

In this thesis, a combined experimental-mathematical approach is applied to the problem of cell seeding in tissue engineered NRCs. This involves the design of *in vitro* experiments incorporating cells and materials that are currently used to make NRCs in the Phillips lab, in order to collect relevant data for parameterisation of the mathematical framework. Thus far, such a multidisciplinary approach has not been used to investigate how different seeded cell densities and distributions could impact both cell survival and vascularisation within engineered tissue.

1.5 Thesis aims and objectives

Two specific objectives and one broader objective will be investigated in this thesis:

- **The impact of therapeutic cell seeding densities and distributions upon cell survival in engineered tissue** The number or density of cells seeded in engineered tissues such as NRCs has an impact on cell survival over time, but research into this has so far been scarce. The

first aim of this thesis is to investigate whether specific seeded cell densities and distributions could enhance cell survival, and thus reduce the waste of seeded cells whilst potentially improving functional outcomes, using a parameterised mathematical model of cell-solute interactions within an NRC.

- **The impact of cell seeding densities and distributions upon gradients of VEGF and vascularisation in engineered tissue** Vascularisation is vital for the success of engineered tissues, and the growth of blood vessels plays a particularly large role in peripheral nerve repair by guiding neuronal growth across the injury gap, as described in Section 2.1.2. The second aim of this thesis is to investigate whether specific seeded cell densities and distributions within an NRC could induce VEGF gradients, and thereby improve vascular growth into the engineered tissue, by using the parameterised cell-solute model in combination with a model of directional vascular growth in response to VEGF gradients. Although vascular growth models already exist as reviewed in Section 2.2, the discrete form of model used in this thesis has not been applied to the peripheral nerve repair scenario before.

- **A multidisciplinary method for tissue engineering** Mathematical modelling in tissue engineering has so far made some use of experimental data, but to achieve the full potential of modelling increased integration with experimental work is required. This work investigates this concept by proposing and testing an iterative joint mathematical-theoretical approach that involves the use of experimental data specifically collected for model parameterisation, and close collaboration with experimental tissue engineers (Figure 1.4). The third aim of this thesis is to assess this method and identify how to improve multidisciplinary efforts in tissue engineering to allow more successful collaborative work in the future.

1.6 Thesis structure

The literature review, Chapter 2, first of all provides an overview of peripheral nerve repair, focusing particularly on the close relationship between vascularisation and neuronal regeneration, and then identifies the key biological processes and factors that require consideration for the mathematical model. A review of existing relevant mathematical models of cell solute interactions and vascular growth follows, including justification for the mathematical approaches chosen for this research and outlining the differences between the work in this thesis and previous mathematical and computational models.

The flow of the work contained in Chapters 3, 4 and 5 is outlined in Figure 1.5. First, Chapter 3 describes the development of the model of cell-solute interactions in engineered tissue. This includes the description of *in vitro* experiments and analysis of the collected data. These experiments were carried out by collaborators: G. Kennedy (UCL Department of Mathematics), C. Kayal (UCL Department of Mechanical Engineering), C. O'Rourke (Biomaterials and Tissue, UCL Eastman Dental Institute) and P. Kingham (Department of Integrative Medical Biology, Umeå University, Sweden). Chapter 3 also includes a description of the process of fitting the mathematical model to this data.

In Chapter 4, the impact of different cell seeding strategies and NRC sheath designs upon cell survival and the generation of VEGF gradients is investigated using a range of model simulations.

Chapter 5 presents the development of a model of vascular growth in engineered tissue in response to gradients of VEGF. This model is then integrated with the cell-solute model and used to simulate the initial stages of vascularisation within an NRC, for a select number of therapeutic cell seeding strategies and NRC sheath designs.

Finally, Chapter 6 draws together the results of this thesis and offers some ideas for future work.

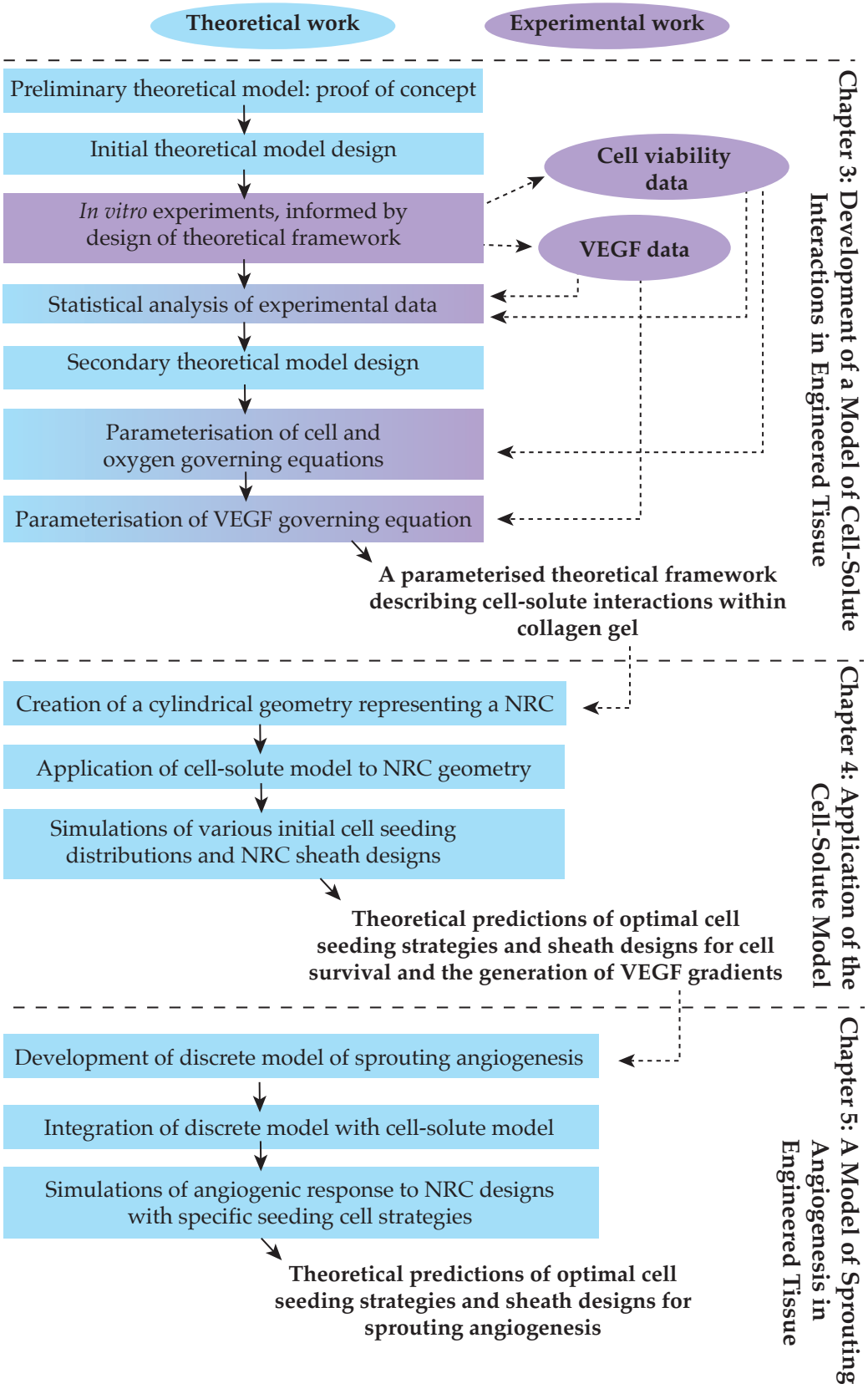

Figure 1.5: Flow chart demonstrating the structure of the work in this thesis.

Chapter 2

Literature Review

Elements of the review presented in this chapter have been published in *Tissue Engineering and Regenerative Medicine* (see [86])

The following literature review is split into two sections due to the interdisciplinary nature of this project; the first deals with the biological and tissue engineering aspects of the project and the second explores the mathematical side.

Knowledge and analysis of the biological mechanisms behind cell-solute interactions and neuronal and vascular growth, in the context of peripheral nerve repair, was required to devise a model capable of simulating seeded cell survival and the impact of cell distributions on vascularisation. The first section of this chapter initially describes the biological processes that drive peripheral nerve repair, and then examines the relationship between nerve regeneration and revascularisation, thereby providing motivation for the development of the mathematical model described in this thesis.

The second section provides a review of existing model frameworks developed to describe the processes of interest in the current project: cell-solute interactions and angiogenesis. This review was used to establish which types of theoretical framework would best suit the objectives of this research, and to finalise the choice of mathematical framework and parameter values used in this work.

2.1 Peripheral nerve regeneration and the role of blood vessels

2.1.1 Peripheral nerve regeneration

The peripheral nervous system has the ability to spontaneously regenerate after damage has occurred, although the degree of natural regeneration possible is determined by the severity of the injury. The process of nerve regeneration takes place as a series of complex and related events that begin immediately following injury, involving both neuronal and non-neuronal supportive cells and signalling molecules. After transection or a severe crush injury, the axons and myelin in the distal stump of the severed nerve which have become separated from their respective cell bodies degenerate quickly, usually beginning within 24 to 36h [403, 423]. This process is called Wallerian degeneration, first characterised by Waller after the observation of this effect in severed frog glossopharyngeal and hypoglossal nerves [398].

Around 5 to 7 days after an injury has occurred, SC proliferation increases in both the proximal and distal stumps. SCs then migrate into the nerve gap to clear the axonal and myelin debris created by Wallerian degeneration, aided by macrophages. The SCs also break down their myelin and undergo an important change in phenotype to a repair or Büngner phenotype [172]. This is marked by an increase in proliferation rate, and the secretion of factors that promote neuronal and vascular growth and support the survival of host neurons [269, 403]. These factors include brain-derived neurotrophic factor (BDNF), glial cell line-derived neurotrophic factor, nerve growth factor and VEGF [51, 121, 124, 172]. Repair-type SCs are also able to remodel the ECM via the production of basement membrane proteins such as laminin and fibronectin. Thus SCs play an important role in the process of peripheral nerve regeneration.

If a crush injury has taken place, the endoneurium remains intact.

However, if transection has occurred a bridge-like structure develops across the nerve gap, mainly composed of macrophages and neutrophils but also containing fibroblasts and endothelial cells [65, 179]. The repair-type SCs align within the endoneurial tubes to form bands of Büngner, and sprouting axons extend into the nerve gap using these bands as guidance [299]. Unaided regeneration in crush-type PNIs is generally more successful than in transection-type injuries due to the preservation of original nerve structures [273]. Transection results in the retraction of the distal and proximal stumps, prompting the need for the "nerve bridge" and forcing axons to regenerate over a longer distance. Therefore the need for surgical intervention is higher in transection type injuries.

Tissue engineered NRCs aim to support and enhance the natural process of nerve repair via the provision of mechanical and chemical cues. Designs incorporating seeded cells, as described in Section 1.3, combined with various different materials and other structural components have been tested widely both *in vivo* and *in vitro* in attempts to match the performance of the gold standard nerve autograft [416]. Research into how to support both neuronal growth and the assimilation of engineered tissue in general will need to be combined with awareness of potential commercial limitations, such as speed of manufacture, cost and storage, prior to the eventual widespread translation of these devices to the clinical setting.

2.1.2 The relationship between vascularisation and neuronal regeneration

Across the field of tissue engineering, vascularisation is recognised to be crucially important for the assimilation of engineered tissue and successful regeneration *in vivo*, and attempts have been made to boost angiogenesis through the use of specific biomaterials, scaffold properties and seeded cells and growth factors [127, 173, 208, 342]. The basic provision of nutrients and removal of potentially toxic metabolites via adequate vasculature is essential for the sustenance of implanted engineered tissue. Without per-

fusion of blood vessels, tissues must rely on limited oxygen diffusion for survival. This can be sufficient to support tissues that are relatively thin such as engineered skin and corneal tissue, or naturally not well vascularised like cartilage, but poses a major barrier to the clinical translation of "3D" engineered tissues with a greater volume, in which hypoxia can lead to the widespread death of cells seeded in the core [277]. In the case of nerve repair in particular, it has been demonstrated that SCs in autologous nerve grafts cannot survive without a blood supply for more than 7 days, underlining the importance of inducing vascularisation for the survival of SC or SC-like cell populations in NRCs [304].

Further evidence for the importance of vascularisation for nerve repair was provided by a recent study by Farber et al. that concluded that slow vascularisation of nerve grafts could limit nerve regeneration due to prolonged ischemia of the tissue [112]. They tracked changes in vascularisation over time in long (6 cm) acellular nerve allografts and isografts implanted in rat sciatic nerve gaps. Isografts are tissues transferred between two genetically identical individuals. The long acellular nerve allografts took up to 20 days to achieve complete vascular perfusion; this rate of perfusion was slower than that of the long isografts. In contrast, shorter acellular nerve allografts were previously shown to have a vascularisation period of 5-7 days [111]. Furthermore, both the shorter acellular nerve allografts and the long isografts demonstrated better regenerative outcomes than the long acellular nerve allografts, leading Farber et al. to conclude that prolonged ischemia due to relatively slow vascularisation could have a negative impact upon regeneration.

Conversely, other studies have reported no significant difference in the outcome of vascularised nerve grafts and nonvascularised grafts. In particular, Xu et al. conducted a clinical study that compared the results of phrenic nerve grafts with varying degrees of vascularisation in patients with brachial plexus injuries [414]. They observed no significant difference

in the functional results between the three types of procedures studied. This concurs with an earlier study comparing vascularised and nonvascularised intercostal nerve transfers that found no difference in the regeneration rate of the nerves or the functional outcome [285]. However, a lack of clear improvement of outcome for vascularised grafts over nonvascularised does not necessarily imply that vascularisation is unimportant, but could indicate that transplanted vasculature is not effective in promoting a renewed blood supply to the injury site. Overall, it seems likely that the provision of nutrients and oxygen by functional blood vessels is necessary for good peripheral nerve regeneration, motivating the need for fast and thorough neovascularisation of tissue engineered NRCs post-implantation.

Additionally, recent evidence suggests that the growth of blood vessels supports peripheral nerve repair not only by promoting the survival of the implanted tissue but also by directing the migration of SCs across the nerve gap, thus helping to initiate axonal growth [65]. However, the exact relationship between neuronal and vascular growth is complex, and has been a subject of debate over the past 60 years. As early as 1942, Weddell found that axonal regeneration appeared to progress fastest when the nerves were in close proximity to blood vessels [407]. Subsequently, observed increases in vessel permeability after injury were hypothesised to be linked to axonal growth [254, 361, 408], providing further evidence of a connection between vascular and neronal repair.

In 1988, Nukada investigated the impact of different types of rat nerve injury upon the number of endoneurial capillaries and the number and morphology of myelinated nerve fibers [278]. Ischemic nerve injury was found to result in delayed neovascularisation and axonal growth and myelination in comparison to crush type injury. Nukada hypothesised that "distal neovascularisation after nerve injury is dependent on two factors: (a) the success of nerve regeneration and (b) the severity of nerve ischemia", but later on suggested that delayed axonal growth after ischemic injury could

conversely be caused by delayed neovascularisation, among other factors. Thus the results of this research again suggested that the two processes are related, but the exact mechanisms behind the relationship remained unclear.

Hobson et al. published a study in 1997 that aimed to clear some of the confusion surrounding this relationship [153]. Orientated acellular fibronectin mats rolled into a cylindrical form were used to bridge 10 mm sciatic nerve gaps in rats. At the 10 and 15 day time points immunofluorescence staining revealed that a good degree of vascularisation had been achieved within the grafts, with areas of longitudinally orientated vessels appearing to precede migrating SCs and regenerating axons. The orientation of blood vessels and axons was observed to be closely related. The authors also reported that well vascularised areas with randomly orientated vessels had poor SC penetration. Hobson et al. concluded that the distance and degree of SC migration and axonal regeneration after 30 days appeared to be greatest in the areas containing the most extensive, longitudinally-orientated vessels.

These results suggest that the orientated growth of blood vessels both precedes and provides directional guidance for the migration of SCs and growth of axons, and could potentially be necessary for good axonal regeneration. However, Hobson et al. did not provide any clear evidence of direct interaction between the vessels and the SCs or axons, and therefore did not rule out the influence of a third confounding factor. Additionally, the degree of functionality of the new vasculature was not assessed and thus it is unclear whether the new vessels actually delivered significant additional nutrients to the nerve gap.

Furthermore, it remains uncertain whether material aspects of the conduit itself directly influenced the results. Firstly, the structure and metabolic needs of the acellular conduit used by Hobson et al. could differ significantly from those of an autologous nerve graft or a cellular NRC.

Hobson et al. raised the question of whether the presence of cells could lead to a greater risk of ischemia due to metabolic uptake of oxygen, and thus impact the relationship between vasculature and nerve regeneration. Secondly, the authors postulated that the fibronectin matrix itself could have had an impact upon the relationship between the vessels and the degree of regeneration. Earlier studies demonstrated that fibronectin can impact both the growth of blood vessels and axons [26, 162]. Finally, the orientation of the vessels and axons could have been influenced by the directionality of fibronectin strands. In fact, the paper mentioned briefly that unpublished experiments using mats of randomly orientated fibronectin fibres had produced inferior axonal regeneration. Therefore although this study provided a hint as to the relationship between neovascularisation and peripheral nerve regeneration, further research was required to provide clarification.

In 2015 Cattin et al. published a report on a series of *in vivo* and *in vitro* experiments that revealed more details of the relationship between SCs, peripheral nerve regeneration and blood vessel growth, and helped to corroborate some of the conclusions previously reached by Hobson et al. [65]. Immunostaining of transected rat and mice sciatic nerves revealed that the nerve gap was fully vascularised prior to any SC migration from either nerve stump, supporting the hypothesis that endothelial cell (EC) migration and blood vessel growth precedes SC migration and axonal regeneration. All the blood vessels within the nerve gap bridge were found to contain ECs labelled positively with a marker of proliferation, indicating that they were newly formed. Crucially, erythrocyte staining and immunolabeled lectin showed that most of these blood vessels were also functional. Cattin et al. also reported that "~80% of the blood vessels were orientated in the direction of subsequent SC migration".

In the same study, confocal microscopy revealed that migrating cords of SCs appeared to interact with the new vasculature as they progressed

from the proximal stump into the nerve gap, and correlative light and electron microscopy was used to "observe multiple points of direct contact between [ECs and SCs]". *In vitro* experiments corroborated this observation: SCs were co-cultured with capillary-like structures formed by human umbilical vein endothelial cells (HUVECs) in a fibrin matrix, and the majority were reported to have interacted with and migrated along the tubules. Those SCs that did not interact with the tubules were not able to migrate, providing evidence that direct interaction between vasculature and SCs could be necessary for SC migration. Overall, Cattin et al. concluded that the growth of vasculature precedes neuronal growth, and that blood vessels provide mechanical and directional support that enables the migration of cords of SCs.

Cattin et al. also altered the directionality of blood vessels via the implantation of heparin beads loaded with recombinant human $VEGF_{165}$. The beads induced vessel growth into adjacent muscle instead of into the nerve gap, and this resulted in a higher rate of abnormal regeneration after 6 days. Immunostaining showed that the misdirected blood vessels appeared to guide the SC cords and regenerating axons into the adjacent muscle, demonstrating the importance of directional blood vessels for effective directional peripheral nerve repair. The study was concluded with the suggestion that the efficacy of nerve repair constructs could be improved by "encouraging or mimicking a polarized vasculature within the grafts" to induce directional SC migration.

Although this paper by Cattin et al. provides comprehensive evidence of the importance of vascular growth for the initiation and directional guidance of neuronal regeneration during peripheral nerve repair, it does only study the case in which there is no surgical intervention. The size of the nerve gaps used in the study ranged from around 0.12 cm in the mouse model to around 0.17 cm in the rat model; these are relatively small distances that would not normally require surgical intervention to facilitate re-

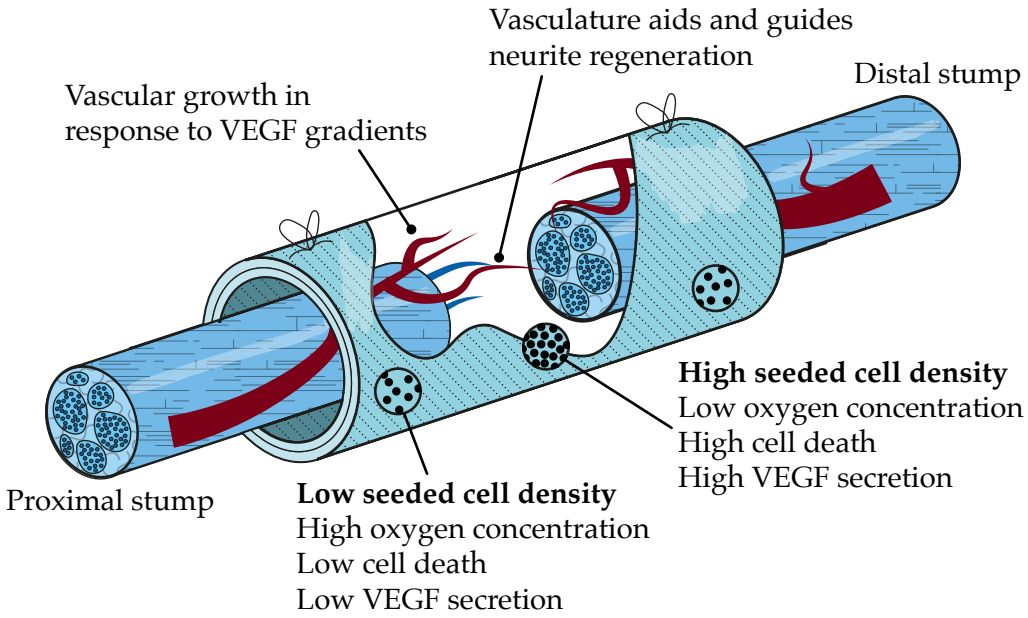

Figure 2.1: Research points towards a relationship between vascularisation and nerve regeneration after PNI. Directional neurite growth occurs from the proximal into the distal stump, possibly guided by vessels. Seeded cell density within an NRC could be altered to achieve a balance between relatively high VEGF concentrations, to encourage vascularisation, and cell survival.

generation. Interactions with the materials, cells and growth factors found within an NRC, and an increase in the length of the nerve gap, could impact the relationship between regenerating blood vessels and axons. However, on balance it is probably safe to assume that neovasculature will continue to precede and guide axonal growth in the context of an NRC until contrasting evidence is provided, particularly in light of the results provided by Hobson et al.

In conclusion, taking both historical and current research into account it appears that obtaining thorough, fast and directional vascularisation within implanted NRCs is beneficial for regeneration, although the use of vascularised nerve grafts *in vivo* do not always yield significantly better outcomes than nonvascularised controls. This could be due to the difficulty of delivering functional vascularised nerve grafts. Recent research has shed light upon the mechanisms behind the impact of blood vessels, beyond the

delivery of nutrients and oxygen, with the current prevalent hypothesis suggesting that neovasculature precedes SC migration and provides directional cues for axonal growth. Therefore, encouraging the orientated growth of blood vessels early on in the repair process by altering elements of NRC designs could potentially improve peripheral nerve repair. The use of directional elements such as rods and aligned cells is already common in nerve tissue engineering [343]; this thesis investigates the role that specific seeded cell densities and distributions could play in encouraging the growth of healthy vasculature, as well as increasing levels of cell survival post-implantation (Figure 2.1).

2.1.3 Initiation and progression of angiogenesis

Knowledge of how the growth of new blood vessels is initiated and progresses through tissue is vital for the creation of an effective mathematical model of vascularisation, and it is important to identify the most influential or limiting variables in the system as a starting point for the construction of the theoretical framework. To this end, this subsection motivates the inclusion of oxygen and VEGF as variables in the mathematical framework by describing the process of angiogenesis, defined as the sprouting of new blood vessels from existing vessels, and evaluating the relative importance of the key angiogenic factors involved.

Capillaries, such as those found in the epineurium of peripheral nerves (Figure 1.1), are often defined as blood vessels with a diameter of 5 to 10 µm or lower and are made up of an inner layer called the endothelium, consisting of ECs and typically just a single cell thick, surrounded by a basement membrane or lamina. The basement membrane is embedded with microvascular pericytes, which communicate with the ECs via peg-socket contacts [20]. Pericytes help to stabilise the vessels and regulate endothelial cell proliferation and vascular remodelling.

Hypoxic environments, such as traumatic injury sites, require blood vessel perfusion to deliver oxygen and nutrients and thereby meet the

metabolic demands of cells. Cells are equipped with oxygen sensing mechanisms, and respond to low oxygen environments by inducing Hypoxia-inducible Factor 1 (HIF-1), a transcription factor that in turn upregulates the production of angiogenic growth factors [196, 327]. For this reason HIF-1 is generally regarded as the key regulator of angiogenesis. The important role that oxygen plays in inducing HIF-1 and thus the secretion of angiogenic factors by cells, as well as its potential influence upon the death and proliferation rates and therefore survival of cells seeded in engineered tissue, means that the inclusion of the spatio-temporal oxygen concentration in the proposed mathematical model will be vital.

It is worth noting at this stage that it is widely accepted that there are two types of angiogenesis: sprouting angiogenesis and intussesceptive or splitting angiogenesis. Intussesceptive angiogenesis is still relatively poorly understood, although it is generally thought of as the formation of transcapillary pillars that result in capillary splitting, leading to increased vascular network density and complexity [57, 237, 255]. Intussesceptive angiogenesis has also been associated with vascular pruning and remodelling.

Sprouting angiogenesis, on the other hand, has been the subject of a great deal of research and is characterised by the proliferation and migration of endothelial cells from an existing vessel into the surrounding tissue to form new vascular sprouts. Tissue regeneration such as peripheral nerve repair thus relies on the invasive nature of this type of angiogenesis to restore vasculature to relatively large gaps in the vascular network. Therefore, although it is possible that intussesceptive angiogenesis could play a role in vascular regrowth and network remodelling at later time points in the nerve repair scenario, the work presented in this thesis focuses solely on sprouting angiogenesis. However, the mathematical framework presented in Chapter 5 is flexible and could be adapted to incorporate intussesceptive angiogenesis in the future.

Sprouting angiogenesis is initiated when an existing vessel senses an angiogenic factor such as VEGF or fibroblast growth factor (FGF). In response, pericytes are freed from the walls and the basement membrane of the vessel is degraded via proteolysis governed by matrix metalloproteinases (MMPs) [61]. The vessel's EC layer becomes permeable and plasma proteins are released to form the base of a new ECM. Integrins, adhesion receptors on the surface of cells, then initiate the migration of leading "tip" ECs (TECs) onto this matrix. TECs migrate towards growth factors, and are followed by "stalk" ECs (SECs) which proliferate and then assemble into tubes to form new vessels [220, 331]. The process of TEC selection and the different phenotypes and behaviour of TECs and SECs during sprouting angiogenesis are described in more detail later in Section 5.2.

In the peripheral nerve repair setting, research has so far suggested that the initiation of vascularisation occurs between 3 and 6 days post injury. Hobson et al. observed vessel growth into the central portion of their orientated fibronectin constructs after 6 days post-implantation [153]. Cattin et al. found that vascularisation of the nerve gap began within 3 days [65], and Dun et al. used whole mount staining, which is the staining of pieces of tissue without sectioning, to demonstrate blood vessel formation 5 days post-injury in a transected rat sciatic nerve gap [103].

The process of angiogenesis involves an array of angiogenic factors with different roles and varying levels of importance [196]. VEGF-A is likely the most thoroughly studied, and generally regarded as the most important, of these angiogenic molecules. VEGF-A is part of the wider VEGF signalling protein family. However, the majority of the impact of the VEGF family upon angiogenesis can be attributed to VEGF-A [61, 104], and therefore VEGF-A will henceforth be referred to simply as VEGF. When it was first discovered, VEGF was known as Vascular Permeability Factor for its ability to increase microvessel permeability, as reviewed by Bates and Harper in 2002 [32]. VEGF not only helps to initiate angiogenesis by stim-

ulating MMP production, promoting vascular permeability and basement membrane degradation, but it is also a mitogen for ECs [116]. This allows it to play a key role in the necessary proliferation of SECs to form new blood vessels during angiogenesis.

Furthermore, it has been demonstrated by a few different research groups that TECs migrate in response to gradients of VEGF [31, 282, 335]. Recently, Wu et al. found that ECs moved towards higher concentrations of VEGF when cultured on surfaces with gradient densities of immobolized VEGF [413], in contrast to the random movement exhibited by the cells on uniform VEGF surfaces. VEGF gradients were also found to induce EC alignment along the axis of the gradient. These results corroborated earlier work by Gerhardt et al., who showed that gradients of VEGF act as guidance cues for the TECs of sprouting blood vessels in the early postnatal retina, and also demonstrated that TECs sense the gradients of VEGF via filopodial extensions [134]. Additionally, Gerhardt et al. concluded that the proliferation rate of SECs depends upon the concentration of VEGF, and the authors suggested that the required balance between TEC migration and stalk EC proliferation could only be achieved "when the correct relationship between VEGF-A gradient and concentration occurs...". The influence that spatial distributions and concentrations of VEGF exert upon angiogenesis makes this cytokine a prime candidate for mathematical modelling.

Additionally, with particular relevance for the peripheral nerve repair scenario, evidence suggests that VEGF also plays a role in promoting axonal growth and supporting neuronal cells, as reviewed by Mackenzie and Ruhrberg [233]. Although the focus of this thesis is improving cell survival and revascularisation in engineered tissue for peripheral nerve repair, a natural extension to this work would be to incorporate neuronal regeneration into the theoretical framework. Thus including VEGF in the model here will help to facilitate future theoretical investigation into its impact

upon neuronal regeneration.

The platelet derived growth factor (PDGF) family activates many of the same pathways as VEGF [149, 240] and signals via two receptors PDGFR-α and PDGFR-β [122]. PDGFs play a role in encouraging endothelial cell proliferation and migration [34, 200] and upregulating VEGF expression [326, 402]. In turn, an *in vitro* study showed that VEGF and FGF2 upregulate the expression of PDGF-B and PDGFR-β respectively [182], demonstrating the close synergy between these different growth factors. Angiogenic endothelial cells and neurons are among the predominant producers of PDGF-B [13, 395].

In particular, research suggests that the spatial distribution of PDGF-B has an impact upon pericyte recruitment, similar to the importance of VEGF gradients for the initiation of TEC migration. PDGF-B, like the long-chain isoforms of VEGF, includes proteins that bind to heparan sulphate proteoglycans (HSPGs) and this allows retention of PDGF-B on the surface of the secreting cell. Lindblom et al. deleted the PDGF-B pattern of HSPG-binding proteins in mice, allowing the PDGF to diffuse freely, and found 50% fewer pericytes in the embryonic forebrain after 15.5 days of development [222]. Similarly, in an earlier study Lindahl et al. used a mouse knock-out model to demonstrate that PDGF-B and PDGFR-β play an important role in the regulation of microvascular pericyte recruitment [221]. Mouse embryos without PDGF-B exhibited microaneurysms and hemorrhaging due to poor structural integrity of microvasculature caused by lack of pericyte recruitment.

Angiopoietin 1 (Ang1) and angiopoietin 2 (Ang2) are also vascular growth factors that play different roles in the development of neovasculature, acting via the Tie2 receptor expressed by ECs [108]. Ang1 is predominantly expressed by perivascular cells, and VEGF has been hypothesised to upregulate Ang1 expression [143]. Suri et al. reported that both Ang1 and Tie2 deficient mouse embryos exhibit heart defects and gener-

ally less complex vascular networks [372], suggesting that the binding of Ang1 to Tie2 is essential for healthy vessel organisation, maturation and remodelling during development, although later research concluded that the vessel disorganisation could be a direct result of the cardiac defect [168]. Knock-out studies of developmental vasculogenesis such as this have provided insights into the roles and interactions of many of the growth factors described in this section, but it is worth noting that the mechanisms behind the process of angiogenesis in wound healing scenarios such as peripheral nerve repair may differ.

This point was illustrated by Jeansson et al., who created a conditional Ang1 allele that allowed Ang1 to be deleted at various life-span time points in an effort to explore how the role of Ang1 changes over the course of a life-cycle from development to adult [168]. This was necessary because Ang1-deficient mice die during the second week of development due to the previously mentioned vascular defects. The study found that Ang1 deletion after E13.5 (day 13.5) did not result in any obvious changes in phenotype, providing evidence that after the initial stages of development Ang1 is not vital for good vascular function, and in direct contrast to an earlier study suggesting that Ang1 was necessary to maintain the structural integrity of vessels [130]. The authors instead hypothesised that Ang1 could act as moderator of angiogenesis, helping to balance the levels of other growth factors by acting as a "brake" to prevent further injury and aid healthy vessel growth. An ear punch model of wound healing was used to test this. Ang1 deficient mice demonstrated a quicker and more extensive healing response at the injury site but with increased angiogenesis and fibrosis compared to the wild type, indicating that Ang1 acts to down regulate elevated levels of pro-angiogenic factors.

In contrast to Ang1, Ang2 is not vital for mouse embryonic survival but Ang2 deficient mice do exhibit vascular defects as adults [97]. Ang2 is produced by ECs and helps to regulate their function [61, 117]. Whilst

Ang1 appears to have a stabilising effect upon blood vessels, Ang2 acts to induce vessel permeability, pericyte loss and vessel sprouting [20, 24]. However, this behaviour appears to be dependent upon the presence of VEGF, as shown in a paper by Lobov et al. in which an ocular microvessel network was used to show that VEGF acts as a mediator of Ang2 action [226]. Injection of Ang2 into the network in the presence of VEGF resulted in the proliferation and migration of ECs and an increase in capillary diameter, whereas simultaneous injection of Ang2 and a VEGF inhibitor lead to increased levels of EC death and capillary regression.

FGFs are another growth factor family that play a role in the process of angiogenesis. FGF signalling can cause the release of other angiogenic growth factors from cells, and FGF2 induces the proliferation of ECs and helps to reduce apoptosis [36]. It has also been shown that the cellular response to VEGF can be enhanced via the addition of FGF2 [305]. However, mouse studies involving the knock out of FGF1 and FGF2 showed that this made little difference to the process of angiogenesis, suggesting that the FGF family could be largely redundant [36].

As reviewed in detail by Ljubimov [225], the various signalling factors involved in angiogenesis operate in a complex and synergistic manner, sharing signalling pathways and often combining to produce more powerful angiogenic effects via reciprocal upregulation. In an *in vivo* study of endometriotic lesions, the use of a VEGF inhibitor did result in a slight reduction in microvessel density whereas the use of a combined VEGF, FGF and PDGF inhibitor resulted in a much more effective suppression of angiogenesis [209]. In this case, it seems that VEGF inhibition alone caused a compensatory upregulation in the other angiogenic factors, although the specific pathology of endometriosis could have contributed to this effect.

The aim of this thesis is to investigate the impact of different cell seeding approaches on cell survival and angiogenesis; therefore, there is no need to capture all of the biological processes involved in the initiation and

progression of vascularisation in the peripheral nerve repair context. Instead, only the degree of detail necessary to achieve the aims of the research will be incorporated. This will reduce the number of unknown parameters that are included in the model, limit the complexity of the framework and ensure that focus is maintained on the most important and influential aspects of the scenario. Therefore, despite the evident complexity of the role of growth factors in angiogenesis, VEGF will be the only growth factor included as a variable in the framework.

Although from knock-out studies and research into anti-angiogenic drugs it appears that vascularisation is possible without the presence of VEGF via compensatory pathways [2, 209], currently it is still generally accepted that VEGF is the most important of the angiogenic molecules. In particular, the key role that VEGF plays in the guidance of migrating ECs suggests that the spatial distributions of VEGF will need to be included into the framework in order to properly model the directional development of new vessels, and thus to help identify which NRC designs and seeding cell strategies may generate VEGF gradient fields that best promote angiogenesis.

Although the production of HIF-1 is crucial for angiogenesis, it will not be explicitly included in the mathematical framework; instead, hypoxic upregulation of VEGF secretion in the model will implicitly take into account the influence of HIF-1. Similarly, the action of the angiogenic factors described here takes place via numerous receptors, but for simplicity the individual receptors will not be explicitly included in the model. Although simplifying the model in this way means that it will not be able to capture the full complexity of the biological processes involved, the development of this model is motivated by the goal of being able to make useful predictions to guide NRC design. Further complexity would introduce many more unknown parameters and variables, and this would in turn increase the difficulty of parameterisation and require a larger number and variety

of experiments.

After establishing the inclusion of VEGF in the mathematical framework, it is also important to evaluate the key factors that influence the production of VEGF by cells. As previously described, it is well established that cellular VEGF expression is regulated by ambient oxygen levels via HIF-1 [196, 315, 384]. Lafosse et al. studied the response of adipose-derived stem cells from diabetic and non-diabetic patients to varying levels of both glucose and oxygen [201]. Adipose-derived stem cells, keratinocytes and dermal fibroblasts all demonstrated significantly increased VEGF secretion under hypoxia (0.1%), but the magnitude of VEGF secretion varied between the cell types under both normoxia (5%) and hypoxia. This highlights the need for cell type-specific parameters to capture these differences.

Glucose is another factor that has been shown to have some effect upon cellular VEGF secretion. Lafosse et al. also found that dermal fibroblasts exhibited a higher level of VEGF secretion under hyperglycemia (25 mM glucose) than under normoglycemia (5 mM glucose) whilst under normoxia (5%), but did not find a similar relationship for adipose-derived stem cells or keratinocytes. Betts-Obregon et al. treated retinal endothelial cells either without glucose or with one of three different glucose concentrations for 24h, and found that VEGF secretion per cell after 24h was three times higher when the glucose concentration was 30 mM than when 5.5 mM was used [43]. The highest VEGF secretion per cell after 24h was achieved when no glucose was used, producing a secretion rate that was 13 times higher than that measured when 5.5 mM was used, demonstrating a biphasic response.

It appears that the cellular VEGF secretion response to glucose depends upon the cell type. In this thesis, the therapeutic cells included in the model are assumed to be dADSCs, in line with the design of NRCs that were under development (as explained later in Section 3.3.1), but the effect of glucose of VEGF for this cell type specifically is unknown. Furthermore,

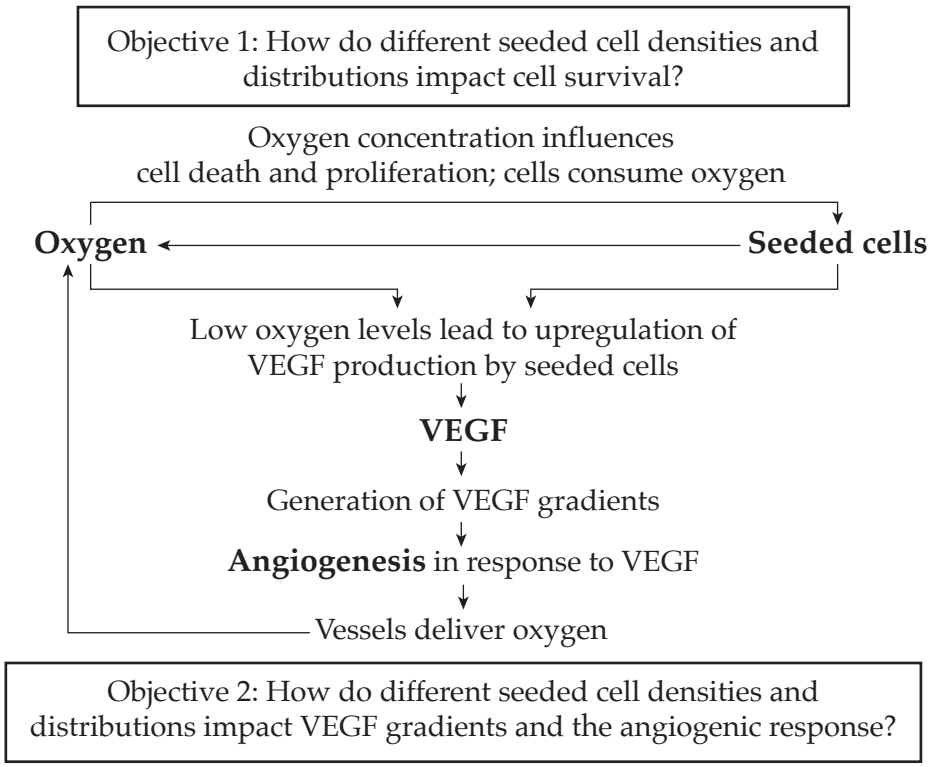

Figure 2.2: Overview of the key variables (bold) and interactions identified in Section 2.1 for inclusion into the model, with the aim of investigating the outlined objectives.

during the creation of EngNT NRCs the cell-seeded collagen construct is cultured in medium that contains relatively high concentrations of glucose (10 g/L $\approx$ 56 mM). Therefore, in this thesis it is assumed for simplicity that a state of hypoglycemia will not be reached over the studied time scale (0 to 5 days) and thus that glucose will not affect the VEGF secretion rate nor the death and proliferation rates of the seeded cells. However, glucose concentration would be a good candidate for inclusion into the framework in the future (Chapter 6).

2.1.4 Summary

The literature review thus far has established that revascularisation and neuronal regeneration of the injured peripheral nerve are closely related, and that the directional growth of new blood vessels helps to guide SC migration and axonal growth. The mathematical model must include a

variable representing the seeded cell population in order to model seeded cell survival.

Vascular growth is initiated and guided by angiogenic growth factors, of which VEGF has been identified as the most important and is therefore selected as another variable in the model. In turn the secretion of VEGF by cells is regulated by oxygen concentration, which also determines the level of cell survival, and must be incorporated into the model. Although glucose has the potential to impact both VEGF secretion rates and cell survival, it is not included under the assumption that glucose will not be a limiting factor during the time frame of 0 to 5 days. Finally, a model of angiogenesis in response to the VEGF gradients must be constructed to simulate the impact of different cell seeding strategies upon vascularisation.

2.2 Relevant mathematical and computational models

In this section, relevant mathematical models are reviewed to motivate the form and underline the novel aspects of the mathematical framework described in this thesis. The proposed model as described in Section 2.1.4 can be split into two parts: firstly a cell-solute model incorporating the seeded cells, VEGF and oxygen and their interactions, and secondly a model of angiogenesis in response to VEGF gradients and concentrations that can be layered over the cell-solute model (Figure 2.2).

In the case of the former, the chosen modelling technique needs to be able to capture the interactions between cells, VEGF and oxygen over space and time to make useful predictions about the potential impact of different cell seeding strategies upon these variables *in vivo*. Ideally, these predictions would be quantitative in nature, to allow formal validation via experimentation in the future and provide applicable insights into how to improve NRC design. However, it is not strictly necessary to model the behaviour of individual cells explicitly; the tissue level distributions of

these variables are the main features of interest.

The purpose of the model of angiogenesis is to investigate the possible effects of different cell seeding strategies, and therefore spatio-temporal VEGF distributions, on the rate, extent and directionality of revascularisation. As reviewed briefly in Section 2.1.3, sprouting angiogenesis and vessel network formation is a complex processes that involves multiple substeps and interactions. Some existing computational models of angiogenesis attempt to incorporate most of the known subprocesses to capture as much detail as possible, whereas others focus only on those processes determined to be absolutely necessary to recreate experimentally observed behaviour; alternatively, some frameworks are created with the aim of simulating just one key aspect of angiogenesis, such as endothelial cell migration, in greater detail.

In the context of peripheral nerve repair and over the time span that this thesis aims to investigate (0 to 5 days post-implantation *in vivo*), the most important features for inclusion are directional endothelial cell migration and the formation of vessels via anastomosis of sprouts. Therefore, in contrast to the cell-solute model, it will likely be necessary to model the migratory movement of individual endothelial cells explicitly as part of the angiogenesis model. The differences in the requirements for each of the two parts of the integrated model mean that the use of more than one modelling technique may be necessary.

A multitude of mathematical models describing cell-cell and cell-solute interactions, tissue growth and angiogenesis already exist. These models demonstrate a range of different approaches to problems similar in nature to the subject of this thesis. In particular, cell-solute models have been implemented to enhance the design of engineered tissues and tissue culture bioreactors [217, 238, 281, 319], to explore the process of wound healing [178], and to investigate the interactions between cancerous cells, nutrients and signalling factors [258]. Many angiogenesis and

blood flow mathematical models have been published with the long-term aim of eventually providing diagnostic capabilities, because dysfunctional angiogenesis is a fundamental part of conditions such as cardiovascular disease, arthritis and diabetes. In particular, a large number of angiogenesis models have been developed to explore the pathological tumour context [10, 242, 332]. However, the following review will instead predominantly feature models of angiogenesis in developmental or repair contexts, which are likely to be more relevant to the peripheral nerve repair scenario, although there is much overlap between these and frameworks designed to simulate tumour-induced angiogenesis.

Most of the existing mathematical frameworks relevant to this thesis can be categorised as either continuous, discrete or hybrid mathematical models, and each of these model types have specific advantages and disadvantages. Sections 2.2.1 and 2.2.2 review the application of continuous and discrete model types respectively to biomedical scenarios, to assess their suitability for use in this thesis, and Section 2.2.3 compares the approaches directly and presents conclusions.

2.2.1 Continuous models

Reaction-diffusion-advection and mechanistic continuous mathematical models are commonly used to describe spatio-temporal changes in concentrations of one or more substances, and are remarkably good at replicating the behaviour of a range of biological systems and processes including vascular development [23], tumour growth [53, 405] and cellular motility and proliferation [87, 217]. These models consist of systems of partial differential equations that determine the rates of change of the variables. Each equation usually contains terms that represent processes such as nutrient consumption or diffusion. The equations are dependent on parameter values and the functional forms used for the terms, which are usually determined by previous research or concurrent experimental work. Hypotheses can be tested by altering the functional forms, adding or removing terms

or carrying out parameter sensitivity analyses to determine the importance of different biological processes.

A few continuum models of nerve regeneration or solute transport in the peripheral nerve context have already been published. In 1993, Lagerlund and Low produced a continuous model of oxygen transport in an intact peripheral nerve, based around simulating the radial diffusion of oxygen from capillaries [202]. However, the capillaries were assumed to be straight and parallel, and vascular growth was not modelled.

Two years later, Podhajsky and Myers published a mathematical model of nerve regeneration that simulated neurite and blood vessel growth, Schwann cell proliferation, Wallerian degeneration and fibrin matrix growth as reaction-diffusion processes [318]. Two scenarios were simulated using this single generalised model: a nerve transection injury, where regeneration occurs from the proximal stump to the distal stump through a fibrin matrix nerve regeneration "chamber" (or NRC); and a nerve crush injury, where regeneration progresses from an area with no Wallerian degeneration towards a distal region with Wallerian degeneration. A combination of previously gathered experimental data and additional *in vivo* experiments were used to refine the model.

Instead of explicitly modelling the effects of hypoxia and growth factors, in the Podhajsky and Myers model Schwann cell proliferation is dependent upon the ratio of Schwann cells to vessels, representing access to nutrients, and the ratio of degenerating tissue to Schwann cells, representing the relative quantity of growth factors released by the tissue. Angiogenic factors and nerve growth factors are not modelled explicitly. The behaviour exhibited by the model was found to mimic qualitative characteristics of the experimentally observed progression of regeneration, and the authors found that the rate of vascular growth could be the limiting factor in nerve regeneration as a travelling wave of vasculature was shown to precede neuronal growth. This provides further evidence for the need to

properly investigate how to induce faster, directional vascular growth by adapting NRC design, as proposed in this thesis.

However, in contrast to the aims of this thesis, Podhajsky and Myers did not explore the potential impact of seeding additional cells within the NRC or alternative NRC designs, and the use of partial differential equations to model the progression of vascular growth meant that the development and morphology of individual blood vessels was not captured by this model.

Another mathematical model of nerve regeneration was published by Rutkowski and Heath in 2002, and consists of a reaction-diffusion model of nutrient and nerve growth factor transport within a hollow porous tubular NRC [336]. In this model, Schwann cells seeded on the internal surface of the NRC lumen produce nerve growth factor which diffuses both into the lumen and out of the construct and is consumed by neuronal cells. Both the Schwann cells and neuronal cells consume oxygen and glucose, and the diffusion of oxygen and glucose into the NRC into the lumen from the outside "bulk" material is also included.

Rutkowski and Heath investigated the impact of changing the thickness and porosity of the NRC wall by running simulations with different values for these parameters. The model predicted that the concentration of nerve growth factor within the NRC lumen is increased when porosity is decreased and the wall is relatively thick, but that the same low porosity values also result in a decrease in the oxygen concentration within the lumen which is undesirable for axon growth. This thesis will also investigate the impact of NRC wall porosity and thickness on cell survival and nutrient concentrations, but with a focus on VEGF instead of nerve growth factor. Rutkowski and Heath concluded that oxygen, not glucose, was the limiting nutrient in both their experimental and theoretical work. This further motivates the exclusion of glucose from the model proposed in this thesis.

Experiments were conducted by Rutkowksi and Heath alongside their theoretical work to enable the derivation of many of the model parameters, such as nutrient diffusion coefficients, nutrient consumption rates by Schwann cells and neurons (dorsal root ganglia) and the nerve growth factor-dependent axon growth rate. In a second paper published as part of the same project, the model simulation predictions were compared to measures of axonal growth recorded from the use of NRCs with varying porosity and wall thickness configurations *in vitro* [337]. The model predictions regarding the impact of wall porosity and thickness seemed to qualitatively approximate the experimental results. However, the predicted quantities of oxygen and nerve growth factor were not directly validated as the experimental data recorded only axonal growth metrics. Therefore although the specific parameter values used in the model are likely to be relatively accurate, there is no way of knowing whether inaccuracies could have been introduced by the forms of the constitutive relationships chosen for the study.

Rutkowski and Heath assumed that only radial diffusion was significant, thus neglecting to include diffusion of nutrients from the open ends of the NRC. This is in contrast to the work in this thesis which investigates NRCs with impermeable sheaths that permit inward or outward diffusion of solutes *only* from the open ends, as well as porous sheaths (Chapter 4). On top of this, in the Rutkowski and Heath model Schwann cells were not modelled explicitly and the cell density was approximated as being constant, thereby excluding the influence of cell proliferation and death upon the production of nerve growth factor. The influence of vascularisation upon the process of nerve regeneration, as outlined in Section 2.1.2, was also not taken into consideration, and the use of a steady-state solution meant that the model did not simulate the progression of nerve regeneration over time.

However, the work by Rutkowski and Heath, and Podhajsky and My-

ers, does demonstrate the potential of using continuous mathematical models in combination with experimental work to make predictions about the possible implications of different NRC designs upon neuronal regeneration, revascularisation and distributions of solutes.

2.2.1.1 Continuous models of cell-solute interactions

Continuous mathematical modelling techniques have been used extensively to model cell-solute interactions in engineered tissues other than NRCs, and in particular there exist numerous models of cell and tissue culture within bioreactors. With particular relevance for this thesis, some of these existing continuous models have been used to simulate oxygen gradients and their effect on spatial distributions of growth factors or cell proliferation.

For example, a reaction-diffusion model of glycosaminoglycan (GAG) production and oxygen concentration in disc-shaped cartilage constructs, cultivated in a rotating bioreactor, was developed by Obradovic et al. in 2000 [281]. This model was informed by experiments that measured spatial cell density and GAG concentration in cell-polymer constructs over time. Simulations showed that spatial variations in oxygen concentration can cause non-uniform distributions of GAG throughout the constructs, and model predictions of GAG concentrations over time and space generally agreed with corresponding experimental measurements. Parameter sensitivity analysis was used to identify particularly important parameters and to test hypotheses.

This framework modelled the chondrocyte populations of the constructs using functional fits to the corresponding experimental cell density data, thus essentially feeding the data into the model, instead of incorporating the cell interactions as an additional governing equation. The experimental data showed that cells at the periphery of the engineered constructs proliferated at a greater rate than those in the centre. This effect could be caused by insufficient oxygen in the central portion of the constructs.

In 2004, Malda et al. built upon this work by also using a continuous model to predict oxygen gradients formed by cellular consumption and diffusion within tissue engineered cartilage polymer constructs during *in vitro* culture [238]. Similarly to Obradovic et al., the authors collected experimental data to aid the development of the model: the diffusion rate of oxygen in the polymer was estimated using a diffusion cell; oxygen tensions were measured at three radial locations of acellular and chondrocyte-seeded polymer scaffolds and osteochondral explants that were cultured for up to 41 days *in vitro*; and spatial distributions of the cells within the constructs were recorded via histological samples.

The corresponding mathematical model includes a reaction-diffusion equation that governs the oxygen concentration within the scaffold, but like Obradovic et al., the authors chose to model the cell phase using experimental values instead of a separate governing equation. The chondrocyte-specific oxygen consumption rate parameter was varied to fit the model to the oxygen data for the cartilage explants and cellular scaffolds respectively. Based upon these values, Malda et al. concluded that chondrocytes cultured in polymer constructs appear to have lower oxygen requirements than those in native cartilage tissue. However, the predictive power and flexibility of this model is limited due to its dependence on cell density data.

In 2005, Lewis et al. published a continuous model in one spatial dimension of oxygen diffusion and consumption and cell proliferation within a scaffold, during a 14-day culture period, using two partial differential equations [217]. It was assumed that the cells would not migrate throughout the scaffold. In contrast to the the previous work by Obradovic et al. and Malda et al., the cell density was modelled explicitly. The model demonstrated a good fit to experimental data, although this involved assuming that the initial number of cells in the scaffold was considerably lower than expected experimentally. The results showed that scaffolds that

rely on diffusion for oxygen transport develop areas on their outer edges where oxygen concentrations are highest and cell proliferation is dominant, corroborating the results of previous research. Based upon the model predictions, the authors were able to suggest that to improve oxygen transport the rate of oxygen supply to the central regions of scaffolds should be improved beyond that of diffusion, and/or that the cellular proliferation in certain regions should be reduced.

In the same year, Croll et al. published a similar continuous reaction-diffusion model of cell proliferation and migration and oxygen diffusion in a dome-shaped poly(lactic-co-glycolic acid) (PLGA) tissue engineered scaffold with an arterio-venous loop enclosed within its base [87]. An implicit description of vascular growth eminating from the arterio-venous loop and the impact of the cell density upon the effective oxygen diffusivity were also incorporated into the model. The simulation results lead the authors to conclude that for large-scale engineered tissues, heterogeneous cell seeding distributions may be preferable to homogeneous distributions, which were again found to result in regions of hypoxia within the scaffold. However, the simulated dome-like scaffold had a diameter of between 15 and 60 mm and thus had a much larger volume than a typical NRC, and this could have exacerbated the degree of hypoxia in central portions of the geometry. Nevertheless, this again demonstrates the potential for models to highlight or provide explanation for issues and suggest practical methods for remedying them, and ties in with the investigation into non-uniform cell seeding distributions proposed in this thesis.

In contrast to the aims of this thesis, the possible impact of hypoxia on growth factor production and thus vascularisation and the delivery of oxygen were not taken into account by Croll et al., and it was assumed that the cells would not die even under very low oxygen concentrations. Furthermore, the range of seeding cell densities tested was limited to a maximum of 2×10^6 cells/ml which is lower than the typical densities

used within tissue engineered NRCs. Nonetheless, the system of partial differential equations was able to effectively model spatio-temporal oxygen and cell distributions: the models published by Lewis et al. and Croll et al. both simulate a cell population explicitly using a separate governing equation, and are therefore closer to the type of framework that will be required in this thesis than those published by Obradovic et al. and Malda et al.

Landman and Cai extended the models created by Croll et al. and Lewis et al. by incorporating the dependence of cell proliferation upon the oxygen concentration into the framework using a Heaviside step function, and studied the impact of vascular growth, cell diffusion and homogeneous and heterogeneous cell seeding on distributions of oxygen and cells over time [205]. Again the model was simulated across one spatial dimension. A value for the critical hypoxic oxygen concentration was included, below which the cell proliferation rate was set to zero, and different oxygen consumption functional forms were compared. Dimensionless parameters were used to evaluate the significance of ratios of parameters: for example, the ratio of the rate of oxygen diffusion to that of cell proliferation. As with the work of Croll et al. and Lewis et al., simulations were used to predict the length of time that cells in different regions of the construct would be exposed to hypoxia, but no attempt was made to model the impact of this exposure beyond its effect on cell proliferation.

A slightly different approach to a continuous mathematical model was demonstrated by Lemon et al. in 2007, who modelled quantities of differentiated and undifferentiated stem cells and ECM within a porous scaffold in terms of fractional volumes of the entire scaffold, rather than as mass or concentrations [213]. Cell proliferation was taken to be proportional to the volume of ECM to represent the influence of the proliferation-stimulating protein Dickkopf-1, which is secreted by the ECM. The effective carrying capacity of the scaffold was incorporated by setting the growth of both

the cells and the ECM to be proportional to the remaining empty or void fraction of the scaffold.

A least-squares fit of the analytical model solutions to experimental values for the cell volume fractions in scaffolds over time was achieved using MATLAB. Two sets of parameter values were produced for the low oxygen (2%) and normoxia (20%) data sets, and the mathematical model appeared to match the experimental cell data. However, there was no quantitative data available for comparison against the corresponding theoretical ECM volume fraction predictions. Experimental values for the volume fractions of differentiated and undifferentiated cells were also used to fit the theoretical model via a least-squares approach, and although the general difference between the hypoxic and normoxic cases was captured, the mathematical model was not able to achieve a good fit to the data over time. Dimensionless sensitivity analysis was used to evaluate the sensitivity of the model fit to small changes in the experimental data.

In 2013, Shakeel et al. presented a mathematical model which describes nutrient transport and cell proliferation in a cell-seeded porous scaffold within a perfusion bioreactor via three coupled partial differential equations, governing the changes in cell density, nutrient transport and fluid flow [349]. The authors were able to simulate the impact of different initial cell-seeding strategies and scaffold porosity distributions upon nutrient supply and the cell yield, and also incorporated aligned channels of high porosity into their model to model enhanced nutrient delivery. A similar approach can be taken to model the influence of NRC sheaths of varying porosity, and will be explored in more detail in Section 4.2.

Pohlmeyer et al. used a continuous model to study the impact of gradients of scaffold-bound non-diffusible cell growth factor upon cell haptotaxis and proliferation, in the context of a porous 2D scaffold in a perfusion bioreactor [319]. This mathematical framework consists of an explicit cell phase and a culture medium phase, incorporates nutrient perfusion

via fluid flow, and models cell proliferation and transport via advection, diffusion and haptotaxis in response to the growth factor. The presented simulation results broadly agreed qualitatively with experimental data produced using scaffolds bioprinted with FGF2, and the effect of different initial seeded cell and growth factor distributions were also simulated. The authors concluded that imposing static growth factor gradients upon scaffolds could help to increase cell proliferation and induce seeded cells to form specific desired distributions across engineered tissue, demonstrating the use of mathematical modelling to verify and add weight to hypotheses generated by experimental research.

However, due to lack of data the model could only be matched to the experimental data qualitatively. This could reduce the validity of any precise, quantitative predictions made by the model. The haptotactic coefficient and cell advective velocity factor were chosen arbitrarily due to a lack of empirical values; the values for these parameters would have to be identified experimentally for the model to make more specific, meaningful predictions. Furthermore, a continuous approximation was used to model the cell density, and the authors noted that this assumption may not be valid due to the small size of the experimental printed region. Nevertheless, this paper demonstrates how haptotaxis can be simulated using this type of framework.

A more complex continuum approach to modelling cell-solute or similar interactions has also been put forward, which involves utilising the theory of mixtures to create multiphase models that include both solid or cellular and liquid phases [58, 59, 212]. This method uses concepts such as mass and momentum balance to unify the different phases of the model. Byrne et al. showed that a two-phase model of avascular tumour growth can be reduced to a system of reaction-diffusion equations when the effects of viscosity are neglected [59]. The multiphase approach has the advantage of facilitating the addition of further phases to a model, such as the

vascular growth components proposed in the current model. However, it can be difficult to link tissue-scale mechanisms such as growth to known biological information via constitutive laws, especially in the absence of the necessary experimental data.

In 2006, Lemon et al. published a multiphase porous mixture model of the growth of engineered tissue *in vitro* [212], which used three phases to model the material of a porous scaffold, and the cells and water contained within it. In particular, the cell phase was represented as an incompressible viscous fluid, and shear forces were incorporated to represent the forces exerted by the motile cells. Certain parameter regimes representing variations in cell-cell and cell-scaffold interactions were shown to result in the formation of cell aggregates as opposed to a uniform cell distribution across the scaffold, in concurrence with experimental data, and with potential application for scaffold design. The same methods of evaluation of different parameter spaces can be used when working with other models.

This thesis will assume that the cells seeded within the engineered tissue remain stationary over the relevant time period, unlike the work of Lemon et al. (2006) which focuses on cell motility, and therefore the momentum balance techniques used in mixture models will not be required. This assumption is based on the fact that the framework developed in this thesis will aim to model cell-seeded EngNT NRCs specifically (Section 1.2): part of the manufacturing process for this NRC design involves stabilisation, which embeds the cells in the collagen matrix and prevents migration.

2.2.1.2 Continuous models of angiogenesis

Some of the earliest published mathematical models of angiogenesis are deterministic continuous frameworks consisting of ordinary differential equations with no spatial dimension. Although these models are capable of producing estimates of metrics such as average network expansion rates and vessel densities, they do not capture any of the complex branching and looping structures that are characteristic of vascular networks, and

therefore are of limited use in this setting.

An example of this type of framework is a continuum model of angiogenesis in an porous engineered tissue scaffold implanted *in vivo* published by Lemon et al. (2009) [214]. This consists of a set of coupled ordinary differential equations governing the behaviour of populations of cells modelled as volume fractions of the scaffold, including cells initially seeded in the scaffold as well as macrophages, fibroblasts, unbound and bound pericytes and immature and mature (surrounded by a pericyte sheath) capillaries. The average concentration of VEGF is described as a function of release by the cells and exogenous delivery from the surrounding tissue or experimental set up.

This model does not capture spatial inhomogeneities, and thus does not explicitly describe processes such as vessel sprouting and adaptation or individual cell migration, instead seeking to simulate tissue-scale interactions between different cell populations and the influence of VEGF upon these populations. Although this ignores much of the complexity of the scenario, it does result in a model that is significantly easier and faster to solve computationally than other frameworks that incorporate spatial dimensions, and the authors were able to show that the rate of cell infiltration influences the degree and rate of vascularisation. However, despite the reduction in complexity the model still incorporates a large number of parameters, and the values of many of these were uncertain.

Lemon et al. attempted to parameterise the theoretical framework using data from a chick embryo chorioallantoic membrane (CAM) assay. The experimental procedure involved positioning porous, cell-seeded engineered tissue scaffolds were on embryo membrane either with or without VEGF, and acquiring μCT data at three time points. Then the total tissue volume fraction was extracted from the data and used to determine the theoretical VEGF application rate and infiltration rate parameters via a least squares method. However, the experimental data was of limited use be-

cause the stain did not differentiate between cell types. Overall, although this model and other ODE models like it offer a simple way of simulating important metrics like overall rate of vascular growth, the lack of a spatial dimension makes this type of framework a poor fit for the aims of the work proposed in this thesis, which are largely centred around the impact of cell densities and distributions upon the production of spatial distributions of VEGF and directional vascularisation.

It follows that the natural way of extending time-dependent ordinary differential equation models of angiogenesis is via the introduction of spatial dimensions. The simplest examples of spatially-dependent continuum angiogenesis models include partial differential equation models of wound healing that simulate average quantities over a single spatial dimension.

For example, in the previously mentioned model of nerve regeneration published by Podhajsky and Myers, vascular growth is modelled as a continuum reaction-diffusion process along the lengthwise spatial coordinate of the nerve repair chamber [318]. The proliferation of vascular endothelium is described by three terms. The first dictates a source of growth proportional to the amount of matrix present, as the authors suggested that this could represent the amount of angiogenic factors as secreted by the matrix. However, the development of vasculature in response to this source is necessarily limited because the model does not incorporate the growth of new matrix. Secondly, a term proportional to tissue degeneration is incorporated to represent the consequential release of angiogenic factors. The third term represents upregulation of vessel growth in response to higher metabolic needs by introducing a dependence on the ratio of non-vessel cells to vessels. The response of vessel growth to specific concentrations and gradients of angiogenic factors is thus not explicitly included.

Croll et al. also incorporated the impact of vascular growth into their continuous model of engineered tissue. This was achieved via a spherical diffusion equation for oxygen, which in turn is dependent upon the

temporal radial position of a growing vascular "front" [87]. The position of the vascular front is assumed to change at a constant capillary growth rate. This formulation suits the purposes of this specific study, but effectively eliminates all complexity involved in the process of vascular growth, including potential radial inhomogeneity and variation in the capillary growth rate, and the impact of changing growth factor gradients.

Another example of a continuum model of angiogenesis with a single spatial dimension is that published by Zawicki et al. in 1981, which describes the one dimensional average radial growth of microvasculature in a soft tissue rabbit ear chamber scenario [418]. Pettet et al. later constructed a similar PDE model of angiogenesis in the same context [308]. In both papers, approximately circular two dimensional experimental rabbit ear wounds are modelled by assuming radial symmetry and by representing variables such as capillary tip density, chemoattractant concentration and blood vessel density as spatial averages, thus reducing the mathematical equations to one spatial dimension. In particular, Pettet et al. were able to replicate both normal and dysfunctionally healing responses, and they conducted sensitivity analysis to explore how cell proliferation and death and chemotaxis impact the rate of wound healing.

In 1997 Olsen et al. published a similar wound healing model, this time also incorporating ECM interactions into the PDE framework [287]. Other one dimensional models of tumour-induced angiogenesis, which simulate temporal changes in vessel cell density at various distances away from a tumour, have also been published [28, 70, 289]. However, this type of model still fails to fully reflect the spatial heterogeneity in vessel density that is often observed across vascularisation in tissue.

Consequently, continuous mathematical models of angiogenesis with two spatial dimensions were then developed. These frameworks simulate the evolution of spatial distributions of macroscale features such as endothelial cell density over time. For example, Orme and Chaplain created

a model of tumour angiogenesis to investigate the possible impact of different anti-angiogenesis strategies, in which the densities of endothelial cells, angiogenic factors and a generic adhesive ECM protein were simulated via partial differential equations over a 2D square domain [290]. Each capillary structure is represented by an area of high EC density with an elongated, sprout-like shape; the equations simulate the outgrowth of these sprouts from a parent vessel. The model simulations were able to replicate the spatial inhomogeneity of the migrating and proliferating ECs, with broader areas of high density representing branching at sprout tips, and the joining up of two areas of high EC density mimicking the process of anastomosis. Parameter values were altered to investigate the effect of, for example, inhibiting cell proliferation on the formation of the capillaries.

Levine et al. published a similar model of capillary outgrowth composed of non-linear partial differential equations, which also took into account the role of anti-angiogenic factors [216]. This model is more complex that than of Orme and Chaplain, resulting in the use of 30 parameters that required identification from the literature. Simulations run using the model approximated qualitative understanding of the formation of capillaries.

However, although both of these two models were able to describe some of the spatial heterogeneity of vascular growth, this type of continuous framework is incapable of capturing the fine-grain details of tortuous vascular networks: instead a "smoothed" view of overall cell distributions is provided. It is clear that representing the migration of endothelial cells as diffusive term, or as a moving front with a prescribed growth rate as in the case of the study by Croll et al. [87], is not sufficient to capture the tubular morphology of EC migration in angiogenesis.

In an effort to remediate this issue, Ambrosi et al. implemented a general form of the Burgers' equation in their continuum model of the organisation of endothelial cells into vessel networks on a Matrigel surface [8]. In this model, the cells are represented as a continuous density field sub-

ject to chemotactic and tensile forces exerted by the environment, paired with a corresponding velocity field. These are governed by a multidimensional Burgers' equation, which is known to accentuate heterogeneities and thus lead to organized spatial structures such as the characteristic form of vascular networks. A differential equation also determines the diffusion of chemical factors, and varying the chemical interaction radius of these generic factors resulted in networks with a coarser mesh, which qualitatively matched experimental data. However, this relatively simple model does not include processes such as cell proliferation that would be necessary for the simulation of a broader range of angiogenesis-related scenarios.

2.2.2 Discrete models

In opposition to continuous frameworks, discrete models are often used to explicitly simulate and study cell scale behaviour. Agent based models simulate the actions and interactions of a population of autonomous agents, such as animals or cells, via a series of rules that dictate how the agents behave and interact with each other and their environment [25]. They have the capacity to incorporate a large number of rules, which makes them very flexible and capable of modelling complex behaviours; however, the use of many different rules can make it difficult to understand which aspects of simulation outcomes can be attributed to which rules. Agent based models are particularly useful for evaluating whether a relatively small set of rules can produce the complex emergent behaviour of a group of agents.

Discrete models such as this are typically stochastic; the outcome of interactions depends upon probability distributions, meaning that different outcomes can result from simulations run using the same initial conditions. This is in direct contrast to the deterministic nature of many continuum models. In reality, this more closely mimics the actual behaviour of biological systems.

Random walks, which are discrete, stochastic processes that model a series of steps over a set of states (such as nodes on a lattice) are often

implemented to model cellular movement as part of a wider agent based approach, or on their own. When applied to a lattice, the random walk of the agent from one node to the next depends on a probability distribution; this can be uniform, meaning that the likelihood of the agent moving to any of the available nodes at a particular time step is equal, or non-uniform, leading to a biased or directed random walk in which movement in certain directions is more likely than others. This probability distribution can also be set as a function of some other variable.

Cellular automata are agent based models in which the discrete agents are restricted to a lattice grid and assigned "state" variables, which can be continuous or discrete and represent the properties of that particular agent. A cellular automaton evolves via a set of rules that govern the interactions between each agent and other agents in their defined neighbourhood, based upon their states, over a series of discrete steps.

A particularly well-known type of cellular automata is the Cellular Potts model. Cellular Potts models are generally characterised by two key elements: a discrete Euclidean grid with labelled lattice sites, and a Hamiltonian energy function. Each individual cell is represented by a combination of lattice sites that are assigned the same cell ID, thus forming an explicit spatial domain. Any entities other than cells, such as the ECM in the case of angiogenesis models, are represented by separate IDs and thereby inhabit their own spatial domains.

The progressive behaviour of the cells in a Cellular Potts model is determined by minimisation of the Hamiltonian function, which is a sum of energies representing both interfacial interactions, such as cell-cell and cell-matrix adhesion, and other constraints such as cell surface area and volume. Cell motion takes place stochastically: iterative attempts are made to copy the cell ID of a randomly selected site onto a randomly selected adjacent site, and for each attempt the Hamiltonian function determines the probability of accepting the lattice update. If an attempt is successful,

that particular cell has effectively expanded its spatial domain. Typically for each model time step the number of copy attempts is equal to the total number of lattice points. The use of the Hamiltonian function ensures that the cells tend to reorganise towards configurations that favour strong intercellular interactions over weaker ones.

Cellular Potts models are useful for studying biological mechanisms that involve a complex mix of cell-cell and cell-matrix interactions. Known or hypothesised cellular responses to environmental cues, such as chemical agents or mechanical stressors, can be encoded as specific rules to be obeyed by the individual constituent cells. Simulation outcomes therefore predict the emergent, collective behaviour of the cells according to these rules, and can be compared to experimental observations of multicellular tissue behaviour.

2.2.2.1 Discrete models of cell-solute interactions and tissue

Discrete, agent-based approaches have previously been used to simulate cell-cell and cell-solute interactions within regenerating or healthy tissue and *in vitro* cultures. For example, a research group based at the University of Sheffield have produced a series of papers exploring cellular behaviour in epithelial tissue using agent-based modelling. First of all, in 2003 Walker et al. published a model of epithelial cell interactions within a 2D square substrate, in which the cells interact with each other and their environment according to biologically informed rules at each discrete time step [397]. The cells are assigned different internal parameters according to their type, either stem or transit amplifying cells, and their phase in the typical cell cycle, from the G0 or quiescence phase to the M or mitotic phase. Migration, spreading, apoptosis and response of the cells to calcium concentrations are all incorporated into the framework. Simulations run using conditions representing low and physiological calcium concentrations agreed qualitatively with *in vitro* data.

Following on from this work, in 2007 Coakley et al. from the same

group described a form of an open-format agent-based model using X-machines, with the aim of encouraging understanding and the use of a clearly defined framework for agent-based studies [82]. An X-machine is a finite state machine, composed of a set of states with inputs, initial conditions and defined transitions from one state to another, with additional memory so that information about the history of states for a particular agent can be used to inform future transitions. Coakley et al. proposed the use of communicating X-machines, which have the capacity to exchange information between each other in the form of lists.

A software environment dubbed FLAME (FLexible Large-scale Agent Modelling Environment) was then developed and used in a separate paper to create an X-machine agent-based model of keratinocytes, an epidermal cell type, to study how these cells self-organize to form epithelium [370]. In this study, validation of the model was achieved using *in vitro* data, before predictions were made regarding the growth of two different types of keritinocytes and their behaviour in a scratch wound healing scenario. The wound healing predictions were then used to design a corresponding *in vitro* experiment. This effectively demonstrates how computational predictions can directly inform the design of future experimental work: this thesis also aims to provide useful predictions that can help to plan *in vivo* studies.

This model was subsequently extended by the same research group to develop a 3D multiscale model of the human epidermis, with the aim of investigating the role of Transforming Growth Factor (TGF-β1) upon cellular behaviour in epidermal wound healing [3, 371]. In contrast to previous work, this involved incorporating subcellular mechanisms into the model. FLAME was also used for this work, but this time in combination with COPASI (COmplex PAthway SImulator), another software application developed to simulate biochemical networks. COPASI was used to solve ordinary differential equations relating to biochemical networks associated

with intracellular signalling pathways, such as those involving TGF-β1, and intercellular interactions. Simulations suggested that cell migration and proliferation are crucial for effective epidermal wound healing, and that TGF-β1 helps to coordinate these processes. The authors proposed that this model could also be used in the future to investigate the influence of other growth factors and signalling molecules upon cellular interactions within tissue.

These works were able to produce some interesting insight into epithelial cell behaviour and generated testable hypotheses about the relative importance of certain processes and variables. The use of an agent-based framework facilitated analysis of the mechanisms behind cellular behaviour; such analysis is very difficult to achieve *in vitro* or *in vivo* due to the number of different cell types and factors involved, whereas computational modelling allows biological scenarios to be broken down into their constitutive parts to investigate the importance of each factor in turn.

On the other hand, much of the focus for these models was on the qualitative collective behaviour of the cells, whereas the current thesis aims to use mathematical modelling to make quantitative predictions about cell seeding within NRCs. Furthermore, the inclusion of sub-cellular processes into a model framework is likely to be unnecessary for the fulfilment of the aims of this thesis, and could over complicate the model due to the complexity of the process of peripheral nerve repair.

In another example of the use of agent-based modelling to investigate a tissue regeneration scenario, Galvão et al. produced a model of the effect of stem cell transplantation upon damaged heart tissue caused by Chagas disease (chronic chagasic cardiomyopathy) [126]. The framework consists of agent types representing fibrotic tissue, cardiomyocytes, inflammatory factors and cells, the Chagas parasite and bone marrow stem cells. Simulations were run on a 2D lattice, with state transition rules representing the processes of cell apoptosis and differentiation, as well as the spread of

fibrosis and the transformation of bone marrow stem cells into cardiomyocytes. These rules were informed by previously published experimental evidence.

The model was parameterised against the fractional areas of fibrosis and inflammatory cells obtained experimentally from cardiac tissue sections afflicted with Chagas disease at different time points after treatment. Although a relatively good quantitative fit was achieved, validation for the simulated total number of cardiomyocytes was not possible due to a lack of data, and the spatial structure of the simulated fibrotic areas was markedly less elongated than in the cardiac tissue images. The simulations suggested that the amount of fibrosis could be decreased using bone marrow transplantation, in line with the experimental evidence, and also that the concentration pattern of the fibrotic tissue and inflammatory cells is the factor that has the most influence upon stem cell mediated regeneration in this context.

Finally, a study by Scianna et al. aimed to aid understanding of cell migration within tissue and through tissue engineered scaffolds via a discrete modelling approach [344]. The researchers devised a Cellular Potts model capable of simulating cell migration on 2D and through 3D sections of extracellular matrix. In this model, the agents are cells, ECM fibers and liquid. The cell type agents are split into two subregions representing the nucleus and the cystol, which allowed the authors to assess the separate contributions of each of these components towards cell migration. As with previous models, the cells follow rules informed by experimental evidence to model migratory behaviour.

The orientation and density of the ECM fibers within the simulated matrices were varied to assess the impact of the structural composition of the geometry upon cell migration. The direction of cellular migration was found to generally align with the predominant orientation of the fibers, and it was noted that this effect has also been observed experimentally. Pore

size was varied by arranging the fibers in specific configurations, and this revealed a biphasic relationship with cell migration. A maximum in the chosen measures of cell motility occurred when the pore size was set to be approximately equal to the cellular diameter. Matrix adhesion and stiffness was also investigated, and the authors concluded with the proposal that the model could be used to help design regenerative implants, such as acellular scaffolds, by running simulations to identify the optimal the porosity and stiffness values to encourage cell migration.

This Cellular Potts model therefore demonstrates how this type of model can incorporate the influence of many different variables, in this case fiber orientation, pore size, and other matrix properties, allowing researchers to investigate the effect of various combinations of these factors. However, the model proposed in this thesis will not include the influence of mechanical factors such as matrix composition on the seeded cell population, and will focus on overall distributions of therapeutic cells as opposed to cell-level interactions and behaviours; therefore it seems that the increased computational cost of a Cellular Potts or similar agent-based model may not be worth the increase in flexibility and insight when cell-solute interactions can be simulated fairly simply via a continuous modelling approach, as described previously.

2.2.2.2 Discrete models of angiogenesis

Discrete models have already been used extensively to study the development of vasculature because they can usually capture vascular network morphology more easily than continuum approaches, and thus can be directly compared to qualitative experimental observations.

In 1991, Stokes and Lauffenburger published a two dimensional model of EC migration in culture medium as a random walk in response to chemotactic gradients [366]. This was one of the first examples of the use of a probabilistic discrete framework to describe EC movement. In this model, the movement of microvessel ECs is described using the Ornstein-

Uhlenbeck process, a stochastic differential equation model which had previously been used to model Brownian motion, with an extension to incorporate chemotaxis. Time lapse videos of cell movement in media was used to validate the model and identify key parameters such as cell migration speed and chemotactic responsiveness.

In a second paper by the same authors, the model was extended and used to investigate the role of microvessel ECs during angiogenesis [365]. In this model, the migration of TECs is described as per the previous work, but the proliferation and redistribution of microvessel ECs along each sprouting vessel is also modelled and a minimum cell density across a sprout is required for further elongation to occur. The authors concluded that chemotaxis is necessary to produce directed vascular growth, but that a degree of randomness in the migration direction of the ECs is also needed to emulate the often tortuous morphology of microvascular networks *in vivo*.

The parameters used in this model were derived from experimental observations of the migration of cells in culture medium. Although the behaviour of cells in tissue could differ due to the increased complexity of their surroundings, the model simulation results exhibited many similarities to *in vivo* measurements of values such as the average vessel length between branches and the average network expansion rate, providing some further validation for the parameters used.

The aspects of microvascular growth captured in this model align with the requirements for the model of vascular model proposed in this thesis. However, in this model Stokes and Lauffenburger assumed that the distributions of growth factor over the simulated 2D spaces were static, thus neglecting the impact of growth factor uptake by endothelial cells and growth factor decay. In reality, the process of angiogenesis responds to gradients of growth factors, and also impacts growth factor distributions both directly via growth factor uptake and indirectly via the provision of oxygen that

can inhibit cellular growth factor secretion.

Another important early 2D discrete mathematical model of (tumor-induced) angiogenesis was published by Anderson and Chaplain in 1998 [10]. Unlike Stokes and Lauffenburger, the authors derived the probabilities used to calculate the biased random walk movement of individual ECs by discretising a previously developed continuous model of angiogenesis using the Euler finite different approximation. This allows the cell density at any spatial position to be expressed as a linear combination of the densities within a single grid length at the previous time step. The coefficients of the linear combination correspond to the probabilities of a cell either remaining stationary or moving left, right, up or down at each time step, and depend upon local angiogenic factor concentrations. These coefficients, which incorporate the processes of diffusion, chemotaxis and haptotaxis as per the original differential equations, are used as weights to calculate the stochastic movement of individual cells.

In this framework, the probability of a sprout branching is determined to be a function of the angiogenic factor concentration, and the angiogenic factor distribution is modelled by a separate continuous governing equation that includes terms representing diffusion, uptake by ECs and decay. Thus in contrast to the Stokes and Lauffenburger model, the angiogenic factor distribution was able to vary over time.

In 2001, Tong and Yuan published a mathematical model of corneal sprouting angiogenesis that also incorporates the influence of time-dependent growth factor distributions [381]. A partial differential equation is used to model the growth factor concentration, including an inactivation or decay term, a diffusion term and an uptake term, proportional to the vessel density.

In this model, the direction of growth of each sprout at each time step depends upon the direction of growth at the previous time step and the direction of the growth factor concentration gradient. Additionally, the

influence of ECM structure upon the direction of endothelial cell migration is incorporated via a random deviation in the angular direction, governed by a probability distribution and limited to between $\pi/2$ and $-\pi/2$. It is also assumed that anastomosis occurs whenever two vessels meet.

Tong and Yuan chose basic fibroblast growth factor (bFGF) as the growth factor in their published simulations, and simulated the inward growth of blood vessels from the edge of a circular cornea geometry towards an implanted bFGF-releasing pellet. They were able to replicate qualitative experimental results, although the model simulations showed initial vessel sprouting occurring sooner than in the experiments. Tong and Yuan speculated that this could be because the model does not take into account a delay between growth factor sensing and sprouting.

Although Tong and Yuan had developed a flexible model that could be altered to match experimental observations via parameter adjustments, they did not incorporate vessel remodelling into their framework. But in 2013, Secomb et al. collated and adapted existing frameworks, including that of Tong and Yuan, to arrive at a theoretical model of angiogenesis in response to concentrations of growth factors that also featured vessel pruning and remodelling [347]. This approach of integrating and adjusting previously developed separate models of processes such as cell motility, vascular pruning and blood flow, and solute diffusion into a single hybrid model has become a popular approach to vascular modelling.

The Secomb et al. model incorporates oxygen transport, via blood flow in the vessel structures and diffusion through the tissue, and the production and diffusion of VEGF. It was developed based upon previous mathematical models of vessel growth and adaptation, and informed by experimental measurements of hemodynamics and vessel structure in rat mesentery tissue.

The model simulates sprouting angiogenesis according to a probability distribution dependent on the local VEGF concentration: the likelihood of

a new sprout occurring is higher if the parent vessel is in a section of tissue with a high VEGF concentration, and there is a minimum VEGF concentration threshold required for sprouting. However, unlike the other discrete models of angiogenesis mentioned thus far, this model does not incorporate the gradient of VEGF as a directional cue for the growing sprouts. The authors justified this exclusion by observing that biasing vessel growth according to VEGF gradients "interferes with formation of new flow pathways" and results in high densities of unconnected vessels in regions with the highest VEGF concentration. Nevertheless, currently the weight of experimental research suggests that there is a link between VEGF gradients and the direction of vascular growth led by TECs (as outlined in Section 2.1.3 and reviewed in more detail in Section 5.3.4), and this relationship is central to the investigation carried out in this thesis.

In 2007, Jabbarzadeh and Abrams published a model of EC migration through a porous tissue engineered membrane in response to VEGF released from embedded sources. This work is of particular relevance to this thesis as it focuses on the impact of VEGF upon the vascularisation of implanted biomaterials, although it does not include the secretion of VEGF by cells or any feedback between the vessels and the surrounding tissue. Here the authors drew upon previous work by again modelling the trajectories of developing capillaries as the pathways of migrating tip cells, governed by a biased random walk. Three different combinations of VEGF source placement were trialled, and it was found that the duration of VEGF release from the sources had an effect upon the morphology of the vascular networks, with longer durations resulting in denser networks near the primary vessel but less penetration. The authors concluded that there may be an optimal release duration that enables the vessels to reach further within the geometry, although they did not suggest a possible range of values for this optimum. However, this does again demonstrate the power of mathematical modelling to suggest testable hypotheses.

Some more complex models of angiogenesis have incorporated biological processes that occur across multiple temporal and spatial scales. For example, Owen et al. developed a lattice-based multiscale model of angiogenesis and vascular modelling that includes simulation of subcellular processes, cell population dynamics and VEGF and oxygen diffusion, as well as vascular growth and remodelling [293]. Correspondingly, the model is composed of three layers relating to different time and length scales: the tissue or vascular level, cellular level and subcellular level.

The cellular section of the model describes cell division, movement and apoptosis, as well as intercellular interactions and competition for space and resources, governed by rules that relate to the outcomes of subcellular processes such as VEGF secretion and protein production. These subcellular processes are in turn modelled by ordinary differential equations.

The vascular portion of the model involves first of all the selection of TECs from existing sites occupied by a vessel according to a probability density function dependent upon the local concentration of VEGF. TECs then migrate according to a biased random walk, dependent upon the surrounding VEGF concentration gradient, and ECs are created at all lattice sites passed through by the TECs to form vessels. This method of simulating TEC migration is very similar to that used by Anderson and Chaplain, with the exception that in this case diagonal movement is permitted.

In this model, the vessels also undergo changes in their radii according to metabolic and structural stimuli. The interdependent values of the vessel radii, haematocrit and flow are calculated iteratively at each time step until a certain tolerance is reached, using a quasi-steady state assumption. Finally, the vascular and cellular layers are coupled via reaction-diffusion equations governing oxygen and VEGF transport. The vessels take up VEGF and act as a source of oxygen, and the oxygen is in turn consumed by the other cells whilst they produce VEGF. This feedback loop between the vascular model and the equations governing the solute distributions is

an aspect that the model in this thesis will seek to emulate.

Owen et al. ran simulations of several different scenarios using their framework, demonstrating the flexibility of this type of model. First of all, angiogenesis and vessel pruning in non-cancerous tissue was simulated in the context of a 2 mm square of tissue using a range of different initial conditions and key parameters, such as the level of oxygen release from the vessels. The authors found that in this model the degree of vessel pruning was governed by the pressure drop across the network of vessels, with a smaller pressure drop resulting in more pruning. They also concluded that a strong chemotactic bias in sprout migration, determined in this model by a chemotactic sensitivity coefficient, is necessary for the formation of rapid, directed and less tortuous vessel growth, in corroboration with observed experimental results. Vascular tumour growth was also simulated by assigning tumour cells different internal parameters from normal cells, and seeding a group of them in the virtual tissue .

Overall, Owen et al. were able to produce some meaningful results from their simulations, although the section of tissue simulated was relatively small and the model operates only in 2D. The authors also neglected to include ECM interactions into their framework, which they suggested could have resulted in less tortuous vessels.

A similar complex 2D combined discrete-continuum theoretical framework of vascular development in the murine retina was devised by McDougall et al. [251]. This includes the migration of astrocytes in response to PDGF-A, the diffusion, decay and uptake by the astrocytes of PDGF-A, the diffusion, decay and secretion by the astrocytes of VEGF-A, and the migration of endothelial cells in response to VEGF-A, all via a set of coupled partial differential equations. Additional equations govern interactions between extracellular proteins and matrix degrading enzymes. As in the previously mentioned work by Anderson and Chaplain, the two cell governing equations (for astrocytes and endothelial cells) are derived via

discretisation of a continuum model.

Vessel pruning occurs in this model when three criteria are met: the local oxygen concentration must fall below a threshold, the vessel must be of at least a certain critical age, and it must not be experiencing flow-related stimuli. These conditions are based upon experimental observations, and are a good example of how qualitative experimental results can be effectively translated into rules that govern the behaviour of a discrete mathematical framework. Similar conditions for pruning are also used in the model by Owen et al.

McDougall et al. used this framework to simulate retinal capillary development, and found broad agreement with experimental imaging data taken at various time points. The simulations were able to reproduce the spatial structure of vessel networks over time, thus demonstrating an advantage over continuous modelling methods, as well as provide estimates of the rate of advancement of the cellular fronts. The authors also drew conclusions about the impact of factors such as astrocyte chemotaxis, VEGF diffusion rates and haematocrit input levels by varying the corresponding model parameters. This method of investigation leads to the generation of testable hypotheses about the relative roles of the various complex and interconnected processes involved in angiogenesis.

All the discrete models reviewed thus far are simulated over two spatial dimensions. This is likely sufficient for the approximation of vessel growth in very thin tissues ($\lessapprox 100$ μm). However, in this thesis a model of vascular growth will be applied over a cylindrical geometry with a radius of around 0.25 mm, and therefore a three dimensional model would be more appropriate.

So far, the translation of cell migration models to three dimensions has been limited [328]. One example, a three dimensional hybrid model of vasculogenesis, was developed by Perfahl et al. and could be adapted for application to the wound healing setting [307]. This framework uses an

agent-based, lattice-free approach to describe the behaviour and interactions of TECs and SECs. The cells are modelled as linearly elastic spheres under mechanical and chemotactic forces exerted by each other and their surrounding environment. Thus the TECs are simulated via a biased random walk, similarly to the other models, whilst stalk cells follow on behind according to intercellular forces.

As in the multiscale model devised by Owen et al., each cell is also assigned a phase variable representing its position over the cell cycle and governed by a differential equation. In this case, this is also linked to the degree of mechanical compression or tension experienced by each cell. In this way, the process of cell division and sprouting is connected to these forces, integrating into the model the experimentally informed assumptions that elongated cells have a higher proliferation rate and compressed cells have a higher probability of producing new sprouts.

Model simulations suggested that networks with morphology similar to those observed *in vitro* and *in vivo* could be generated when sprout formation is governed by mechanical stimuli alone. However, it appeared that the formation of directionally oriented, dense vasculature was dependent of the existence of an imposed chemotactic gradient, matching experimental observations.

The authors also found that large increases in the chemotactic sensivity of the TECs caused them to "tear off" from their attached sprout, leading to network degeneration. This behaviour was due to an imbalance between the strengths of the intercellular and chemotactic forces, and does not match the behaviour of cells *in vitro* or *in vivo*. This highlights the difficulty of assigning parameter values in a way that allows a model to produce realistic simulations across a wide range of scenarios. Additionally, the authors note that this model can feasibly only represent the very early stages of vasculogenesis prior to the introduction of blood flow, as aspects such wall shear stress, oxygen delivery, growth factor uptake and

surrounding tissue metabolism are not taken into account, although the model could be expanded to incorporate these factors.

Another 3D model of vascular growth was provided by Norton and Popel, who simulated sprouting angiogenesis in a 500 micron cube to assess the effect of SEC proliferation rate and TEC migration rates on the developing networks [276]. This study is part of a wider body of work on simulating vascular growth in 3D by Popel and colleagues [223, 325]. In this model, TECs are agents that migrate on a discrete grid according to chemotactic and haptotactic cues. SEC proliferation, sprouting, anastomosis and sprout regression are all included in the framework.

The discrete nature of the model allowed the authors to calculate various metrics relating to the morphology of the vessels, including tortuosity and the number of vascular bifurcations per unit volume of vessel, and these were then compared to corresponding metrics obtained from whole tumour imaging data. These kind of metrics cannot generally be derived from the results of a continuous mathematical model of vascular growth, yet are crucial for quantitative assessment of how simulated vascular networks compare to experimental data. Additionally, these metrics provide a method of quantifying differences in simulation outcomes. In this thesis, metrics that capture the directionality and tortuosity of new vessels could be used to assess the degree of directional guidance that the vascular growth could offer to regenerating neurons [65].

Cellular Potts models provide a different approach to the frameworks mentioned so far, which have been predominantly based around the use of biased random walks. In fact, one of the key applications of the Cellular Potts model has been in the study of the mechanisms behind angiogenesis and the formation of vascular networks. Cellular Potts models have enabled researchers to evaluate the potential of different mechanisms hypothesised to be responsible for vascular growth. For example, Merks et al. developed a Cellular Potts model that describes the behaviour of hu-

man umbilical vein endothelial cells within an *in vitro* Matrigel environment, including the secretion of VEGF and migration and elongation of the cells, in order to mimic vasculogenesis [256]. The results, which indicate that the inclusion of the elongated shape of endothelial cells can aid the *in silico* formation of vascular networks, were validated using quantitative time-resolved image analysis data from HUVEC cultures. This demonstrates how a properly validated mathematical model can highlight important variables or parameters in a system, and even delineate between those that are unnecessary, sufficient or necessary for good biological function.

Additionally, in 2008 Merks et al. developed a Cellular Potts model of the early stages of angiogenesis which simulated the aggregation of ECs [257]. This model incorporates preferential extension of pseudopods up chemoattractant gradients. Pseudopods are transient projections extended by cells, such as the filopodia that are observed to be produced by ECs in response to gradients of VEGF [134]. The chemoattractant itself was modelled using a continuum approach which included diffusion, degradation and secretion by the ECs.

In this paper, Merks et al. conducted simulations of ECs to investigate the impact of vascular-endothelial-cadherin (VE-cadherin), a molecule that regulates EC response to VEGF and mediates EC adhesion [393], upon the formation of vascular networks. *In vitro* experimental data suggested that binding between ECs via VE-cadherin causes VEGF to decrease the motility and proliferation rate of the cells, whereas a lack of VE-cadherin conversely causes VEGF to increase EC proliferation, and enhances ECs' chemotactic response to VEGF gradients. This information was used to form the hypothesis that VE-cadherin-mediated contact between ECs results in the inhibition of chemotaxis and aids vascular sprouting, and simulations of ECs using rules to represent this hypothesis did suggest that this mechanism could induce blood vessel sprouting.

This model was particularly useful for the evaluation of EC behaviour

with and without the influence of VE-cadherin because the impact of the adhesion molecule could be included or removed simply using the addition or subtraction of a section of the model algorithm, thus demonstrating the power of this type of mathematical modelling as a tool to test hypotheses.

Daub and Merks published another hybrid Cellular Potts-continuum model in 2013 that incorporated the impact of the ECM into a model of angiogenesis [93]. In this case, the ECM was represented by all lattice sites not occupied by cells, and the authors were able to show via sensitivity analysis that the formation of branching vascular sprouts is dependent upon concentrations and gradients of ECM acting as guidance cues for ECs.

However, many of the parameters incorporated into the model, such as the decay rate of the ECM, were not based on quantitative data and remained non-dimensional. The authors acknowledged that this was due to a lack of quantitative data, highlighting the need for experimental integration with mathematical modelling to identify unknown quantitative values where possible. The large number of parameters included in this model, due to the complexity of the biological scenario, does make the task of identifying parameter values more difficult.

Furthermore, although the model was able to successfully evaluate different hypotheses by comparison against experimental data, it was not able to reproduce some aspects of observed sprouting behaviour. Simulation results showed the formation of unrealistic "bulbs" at the tips of the sprouting vasculature. The authors acknowledged that the published model is still relatively simplistic, partly because it does not differentiate between TECs and SECs despite the fact that these cell types behave and respond to environmental cues in different ways. Other biological nuances were also neglected. This highlights the difficulty of successfully incorporating the many different "rules" and interactions involved in highly complex biological processes, such as angiogenesis, into agent-based models. The omission of even a seemingly minor interaction or behavioural aspect

could drastically impact the resulting emergent behaviour; conversely, the inclusion of many different rules makes it progressively more difficult to unpick which are having the most significant impact upon the results.

2.2.3 Discussion

The preceding two sections reviewed a range of mathematical and computational models of cell-solute interactions, tissue growth and repair, and angiogenesis, to highlight the advantages and disadvantages of different techniques and assess their suitability for implementation as part of this thesis.

Continuous mathematical models naturally lend themselves to the simulation of distributions of solutes, via the use of partial differential equations with a series of terms representing processes such as diffusion, decay and secretion from a cell population. The ability to simulate spatial variations in oxygen, and its effect on VEGF and cell distributions, is necessary for one part of the model proposed in this thesis: this capability is clearly demonstrated by some of the previously mentioned continuum frameworks [217, 281].

In contrast to continuous frameworks, discrete models are best suited to describing the interactions of agents like cells, and the majority rely on integration with continuous models to simulate changes in solutes such as oxygen or growth factors [165, 251, 293, 306]. They have the advantage of being able to capture cell specific responses and cell-level heterogeneity, and have been used effectively to simulate the emergent behaviour of groups of cells.

The widespread use of discrete models to investigate vascular growth scenarios is likely due to their ability to recreate the formation of specific spatial tissue structures, such as cell aggregates and vascular networks: as reviewed in Section 2.1.3, vascular sprouting in wound healing scenarios like peripheral nerve repair initially involves the production of discrete, highly structured nascent vessels composed of a relatively small number

of cells. The morphology and directionality of these sprouts are important aspects of angiogenesis that are commonly recorded as part of experimental imaging data; theoretical models that capture these structures can not only provide more detailed predictions but also allow these predictions to be compared against experimental data with greater ease, as in the work of Perfahl et al. and Galvão et al. [126, 306].

In the case of vascular growth models, simulating individual endothelial cells or vessels allows researchers to calculate representative metrics such as vascular tortuosity, bifurcation density and vessel length [276]. These metrics can be used to quantify the differences between outcomes, and to facilitate quantitative, as well as qualitative, validation of the model.

Although continuum approaches to modelling vascular growth as average endothelial cell or vascular densities are able to capture some of the macroscale properties of angiogenesis, such as changes in spatial distributions or vessels or cell densities over time [23, 308, 318], they are generally incapable of reproducing observed sprout morphology.

One of the major challenges of developing a mathematical model of a biological or biomedical scenario, regardless of whether the model is discrete or continuous, is the estimation of parameter values and the choice of functional forms to represent processes such as cell proliferation or rules that govern interactions. The complexity of many biological scenarios often demands that these models include multiple equations or rule and many different parameters. The collection and use of relevant experimental data is one of the best ways of remedying this issue. Experiments can be carried out to identify specific parameter values such as diffusion coefficients, or data that matches specific model outputs can be collected and the model parameters can be adjusted to achieve a better fit against the data.

Helpfully, parameters like oxygen diffusion coefficients [71] and cellular oxygen consumption rates [336, 367] have already been measured experimentally or derived theoretically as part of previous work on continuum

models of cell-solute interactions, which would ease the development of the proposed model in this thesis and narrow down the number of unknowns. The work of Lewis et al. [217], Croll et al. [87] and Landman and Cai [205], among others, demonstrates how continuum models can use similar previously published frameworks as a foundation prior to incorporating new aspects or refinements, aided by experimental evidence, which provide incremental improvements.

Of course, discrete models can also be built upon and improved over time: in particular, the ability to iteratively incorporate new information into an agent based model via the addition of new rules as scientific knowledge progresses was put forward by An et al. as an important benefit of agent-based models, along with their modular structure which eases the process of model modification [9]. However, the parameter values used in discrete models are often more uncertain because it is more difficult to experimentally measure interaction rates on the cellular or subcellular scale.

Due to their composition, discrete, agent-based models such as the Cellular Potts model developed by Merks et al. [257] are useful for testing hypotheses. For example the effect of knocking out a particular process upon overall behaviour can be simulated by removing that particular rule from the framework. Results can then be used to plan similar experiments that test the hypothesis *in vitro* or *in vivo*.

Additionally, as argued in a review of the use of discrete models of tissue growth by Azuaje et al., discrete, rule-based models can be useful for formalising existing knowledge of biological processes in a structured manner [25]. Agent-based models are able to test whether quantitative rules applied to collections of cells can give rise to qualitative observed emergent behaviour. However, it is worth noting that via a similar process of adding and removing terms in a set of partial differential equations, continuous models can also be used effectively to test hypotheses about which interactions are the greatest contributors to certain outcomes.

Furthermore, one of the advantages of continuous models is that analytical solutions can sometimes be found, either in a general case or within certain parameter regimes. This can facilitate comparison between numerical and analytical solutions, and accelerate the time taken to run a large number of simulations. Nevertheless, this is often only possible for simple continuum models.

Another technique often used to investigate continuous models is non-dimensionalisation, which can be used to inspect the relative sizes of reaction-diffusion model parameters. In some cases this can lead to justified simplification of the model when small terms are identified and neglected, although this requires knowledge of parameter scales. Non-dimensionalisation can also be used to reduce the number of parameters in the model prior to solving [23, 217], which can make using both numerical and analytical techniques easier.

Non-dimensionalisation can also be used to simplify some discrete models. However, the stochasticity of many discrete agent-based or random walk models means that it is necessary to run multiple simulations for each initial condition, prior to analysis using statistical techniques if possible, to properly evaluate which processes are underpinning the emergent behaviour of the system or to test hypotheses [9]. This approach is not necessarily an easy undertaking: cellular automota such as the Cellular Potts model and agent-based models in general can be computationally intensive. In contrast, deterministic continuous models need only be run once for each set of initial conditions and are relatively computationally inexpensive.

In light of the distinct advantages and disadvantages of continuous and discrete approaches, many researchers have chosen to incorporate aspects of both into their work to create "hybrid" frameworks. These include models of tumour cell migration in tissue [12] and vascular growth (or EC migration) in response to angiogenic factors [93, 251, 257, 293, 347]. In

these models, solutes such as oxygen and VEGF are typically simulated using partial differential equations, whilst cell populations are described using a discrete modelling method. In this way, the ability of discrete models to capture fine-grain cellular structures can be used whilst also taking advantage of the ease with which continuous models can describe varying spatial distributions of variables over time.

In this thesis, it is necessary to track and assess the changes in seeded cell, oxygen and VEGF distributions over time: in particular, the effect of non-uniform cell distributions on cell survival and the generation of VEGF gradients will both be important aspects of this work. However, the simulation of individual seeded therapeutic cells is not necessary as this work is concerned with making experimentally verifiable predictions, rather than with unpicking the intricacies of how the seeded cells interact and behave on the cellular level. Thus a continuous approach is a clear fit for this portion of the model.

In contrast to this, the proposed model of angiogenesis will require the ability to derive metrics relating to vessel tortuosity, directionality and length over time, due to the importance of fast and directional growth for peripheral nerve repair. This requires the ability to simulate individual vessels, and therefore lends itself to a discrete approach.

The complete framework will therefore take a similar form to previously reviewed hybrid models of Owen et al. [293] and Secomb et al. [347] by integrating continuum and discrete methods into a single hybrid framework. Note that this will require modelling one cell population, the therapeutic seeded cells, using a continuous approach, and another population, the endothelial cells that make up the vessels, via a discrete approach. The use of a hybrid model will require extra thought about how feedback between the two sections of the model can be achieved, but offers a good compromise that plays to the strengths of the two methodologies.

Although some previous studies have used mathematical modelling

to investigate aspects of peripheral nerve repair [155, 202, 318, 336], out of these only Podhajsky and Myers incorporated a model of vascular growth. However, they modelled vascularisation using a continuum method and neither VEGF nor other growth factors were incorporated. Therefore although discrete models of angiogenesis have been implemented to study other contexts, this will be the first time this technique has been applied to model the process of vascular growth in response to growth factor gradients in the peripheral nerve repair setting.

Rutkowski and Heath did simulate the effect of different thicknesses of Schwann cell layers on the inside lumen of cylindrical NRCs [337]. However, thus far mathematical models of peripheral nerve repair have not attempted to assess how different distributions or densities of therapeutic cells, seeded along the *length* of 3D biomaterial NRCs, could affect cell survival, growth factor distributions or vascularisation. This is the proposed goal of this thesis.

2.3 Conclusion

The importance of vascularisation for NRCs is twofold. Firstly, the provision of nutrients and removal of waste metabolites is crucial for the good function of any implanted engineered tissue. This point is widely agreed upon both within nerve regeneration research and the wider field of tissue engineering. Hypoxia and resulting cell death can be prevented by an ingrowth of well connected and functional vessels.

Secondly, recent research suggests that the longitudinal inosculation of these vessels could play an important role in the initiation and directional guidance of axonal growth [65]. Although the strength of this hypothesis would benefit greatly from further experimental research, the studies that do advocate this theory appear to have been conducted carefully and thoroughly.

Although plenty of work on mathematical and computational mod-

els of vascular and cellular growth in tumours has been carried out, and similar techniques have been applied to simulate cell-solute interactions in bioreactors and bone regeneration, application of mathematical modelling to the peripheral nerve repair scenario has so far been limited.

The design of NRCs offers plenty of potential as a candidate for mathematical modelling. Many of the biological mechanisms behind nerve regeneration have been investigated thoroughly experimentally as outlined in Section 2.1, providing a good knowledge base for the construction of models, and there is a clear need to accelerate progress in the field of peripheral nerve repair because the rate of translation from *in vivo* experiments to clinical application remains poor.

The effect of different seeded cell densities and distributions on both cell survival and the the growth of vasculature has not yet been simulated using a hybrid mathematical model, as proposed in this thesis. The mechanisms behind vascular growth are fairly well established, and the review presented in Section 2.1.3 helped to identify the key variables involved in this process. The next three chapters will describe the development of the continuous cell-solute part of the model (Chapter 3), present simulations of cell-solute interactions in collagen NRCs and predictions for optimal cell seeding strategies for cell survival (Chapter 4), and finally outline a discrete model of sprouting angiogenesis, coupled to the cell-solute model, and make predictions about the influence of cell seeding strategies on vascularisation (Chapter 5).

Chapter 3

Development of a Model of Cell-Solute Interactions in Engineered Tissue

3.1 Introduction

Chapter 2 outlined the key processes involved in peripheral nerve repair, and in particular, Section 2.1.4 identified VEGF and oxygen as key factors in the progression of vascularisation. However, the interactions between these factors and seeded therapeutic cells within engineered tissue are not thoroughly understood, despite the fundamental importance of cell fate under varying oxygen conditions and VEGF gradients for vascularisation and nerve repair. Section 1.4 motivated the use of mathematical modelling to explore these processes and inform repair strategies.

This chapter presents the development of a mathematical model, parameterised using *in vitro* data, to describe cell-solute interactions within collagen hydrogel. This spatio-temporal model can be used to simulate these interactions within NRCs and other engineered tissue constructs, and thus predict which initial seeded cell densities and spatial distributions are the most likely to result in cell-solute gradients that enhance vascularisation and nerve repair. This is demonstrated later in Chapter 4.

For the work in this chapter, a cross-disciplinary approach was adopted that involved feedback and iteration between experimental and theoretical work, as detailed in Figures 1.4 and 1.5. Initially, a 1D proof of concept model was developed to confirm the viability of the modelling approach, as described in Section 3.2. The *in vitro* experimental protocol was then designed and carried out specifically to collect data for the parameterisation of the mathematical model. Section 3.3 explains the experimental methods used and reports statistical analysis of the *in vitro* data. Section 3.4 provides detailed reasoning for the choice of constitutive relationships used in the model based upon existing experimental and theoretical research, and Section 3.5 describes the methods used to simulate the model and the process of parameterisation of the framework against the *in vitro* data. Finally, in Section 3.6 plots of the final parameterised model simulations and the fit to the data are provided and sensitivity analysis is conducted.

In summary, the overall aim of the chapter is the production of a mathematical model, parameterised against *in vitro* data, that can be used to test the hypothesis that initial seeding cell densities and distributions impact population cell survival and VEGF distributions in NRCs over time.

3.2 Proof of concept cell-solute model

A preliminary mathematical model of cell-solute interactions was constructed and tested as a proof of concept for the project. The functional forms used in this model were based upon existing models and knowledge of the biological system as outlined in the literature review (Chapter 2) and were used for the purposes of demonstrating the general relationships between the variables. The specifics of the constitutive relationships are further refined and discussed in detail in Section 3.4. All unscaled parameter values used in this section are listed in Table 3.1.

3.2.1 Mathematical framework

The theoretical framework consists of three coupled differential equations, developed to model changes in the distributions of VEGF concentration v, oxygen concentration c and viable cell density n as functions of time t and space z. For the proof of concept model, a cell-seeded collagen NRC was modelled in two spatial dimensions as a rectangle with length L and width w. The dimensions of the nerve construct were approximated as $w \approx 0.1$ cm and $L > 1.5$ cm, to reflect the typical size of constructs used in experimental research for long nerve gap repairs. The boundary conditions were assumed to be uniform across the width of the NRC. It was therefore possible to reduce the model to one spatial dimension $0 \leq z \leq L$, by approximating $L \gg w$.

3.2.1.1 Cells

The continuous distribution of viable therapeutic cell density $n(z,t)$ was modelled under the assumption that the cells do not migrate, as the time scale for such migration within a collagen nerve construct (days to weeks) would be longer than that of VEGF and oxygen diffusion (seconds to hours) and cell proliferation or death (days). The governing equation consists of a proliferation term and a death term as follows:

$$\frac{\partial n}{\partial t} = \beta c n \left(1 - \frac{n}{n_{\max}}\right) - \delta \mathrm{d}(c,n)\,, \tag{3.1}$$

where β is the cell proliferation rate constant, $n_{\max}$ is the maximum viable cell density and δ is the cell death rate constant. Note that $n_{\max}$ should be thought of as the carrying capacity for the cell population in the gel, rather than as a maximum cell density based on how many cells can be packed into the gel according to their volume.

The cell death function $\mathrm{d}(c,n)$ dictates the dependence of the cell death rate upon the viable cell density and oxygen. The cell death function is

given by:

$$\mathrm{d}(c,n) = \frac{n}{2}[1.05 - \tanh(k_\delta(c - c_d))]\,. \tag{3.2}$$

Here c_d is the low oxygen threshold value at which the magnitude of cell death becomes greater than the baseline value applicable to higher ambient oxygen environments. The constant k_δ dictates the gradient of the transition from the basal rate of death at high oxygen concentrations to the upper rate at low oxygen concentrations. Equation (3.2) is a convenient approximation of the relationship between the cell death rate and oxygen. This term is further refined in Section 3.4.

3.2.1.2 Oxygen

The continuous distribution of oxygen concentration $c(z,t)$ (per unit volume of fluid) is determined by a combination of diffusion and oxygen metabolism by the cell population, described by the following governing equation:

$$\frac{\partial c}{\partial t} = D_{c_g}\frac{\partial^2 c}{\partial z^2} - Mn\frac{c}{c + c_{1/2}}. \tag{3.3}$$

Here D_{c_g} is the diffusivity of oxygen in collagen gel, M is the oxygen metabolism constant which dictates the maximum consumption rate of oxygen by the cells, and $c_{1/2}$ is the concentration at which oxygen consumption is half-maximal.

3.2.1.3 VEGF

The continuous distribution of VEGF concentration $v(z,t)$ (per unit volume of fluid) is determined by a diffusion term, a secretion term and decay term as follows:

$$\frac{\partial v}{\partial t} = D_{v_g}\frac{\partial^2 v}{\partial z^2} + \alpha_0 n\,(\alpha \mathrm{h}(c) - d_v v)\,, \tag{3.4}$$

where the VEGF secretion function $\mathrm{h}(c)$ is given by:

$$\mathrm{h}(c) = \frac{1}{2}[1.05 - \tanh(k_\alpha(c - c_h))]. \tag{3.5}$$

Here D_{v_g} is the diffusivity of VEGF in collagen gel, α_0 is the VEGF net change magnitude constant, α is the basal VEGF secretion rate, c_h is a hypoxia oxygen threshold below which cells produce an increased amount of VEGF, k_α dictates the gradient of the transition from the basal rate of VEGF secretion to the upper rate at the threshold value, and d_v is the VEGF degradation constant.

3.2.1.4 Boundary and initial conditions and parameter values

Boundary and initial conditions were applied to solve the governing equations:

$$\text{Oxygen density boundary conditions:} \begin{cases} c(0,t) = c_{\text{tissue}} \\ c(L,t) = c_{\text{tissue}} \end{cases}$$

$$\text{VEGF boundary conditions:} \begin{cases} \left.\frac{\partial v}{\partial z}\right|_{0,\,t} = 0 \\ \left.\frac{\partial v}{\partial z}\right|_{L,\,t} = 0 \end{cases}$$

$$\text{Initial distributions of } n, c \text{ and } v: \begin{cases} c(z,0) = c_{\text{init}}(z) \\ n(z,0) = n_{\text{init}}(z) \\ v(z,0) = 0\,. \end{cases}$$

Dirichlet boundary conditions are assumed for the oxygen concentration, representing a constant level of oxygen c_{tissue} at the proximal and distal ends of the construct. VEGF concentration is initially set to zero along the length of the NRC, under the assumption that VEGF will not have been generated prior to the presence of cells and hypoxic conditions. The diffusive flux of VEGF is assumed via Neumann boundary conditions to be zero at either end of the construct at all time points. The initial distributions for the oxygen concentration and viable cell density, $c_{\text{init}}(z)$ and $n_{\text{init}}(z)$ respectively, can be prescribed any function. Therefore these functions can be varied to investigate the possible implications of different experimen-

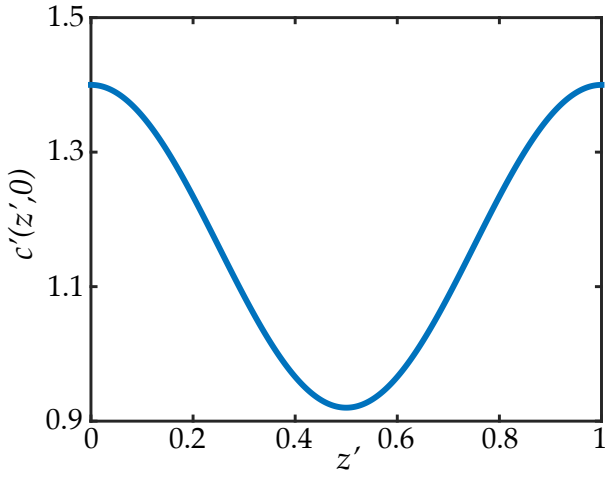

Figure 3.1: Initial non-dimensionalised oxygen concentration distribution $c'(z',0)$ used for all simulations. The maximum and minimum of the rescaled function $c'(z',0)$ correspond to dimensional values $[6.13, 9.32] \times 10^{-9}$ mol/ml. For explanation of the rescaling, see Section 3.2.2.

tal set ups and cell seeding distributions upon nutrient and cell gradients over time. After refinement of this proof of concept model, the boundary conditions and initial conditions for the oxygen and VEGF concentrations were adapted for application of the model to 3D axisymmetric geometries in Section 3.5.1 and Chapter 4.

An initial oxygen concentration distribution was chosen and applied for all subsequent simulations of this preliminary model. The functional form of the initial oxygen distribution was chosen as a cosine function of the rescaled spatial variable z' (Figure 3.1), based upon the idea that initial oxygen concentration in a construct may be higher at the open ends of its cylindrical geometry.

The model was simulated using a range of different initial cell density distributions, to explore whether this variable could have an effect upon the time dependent distributions of both the cells and the solutes.

Cell density parameters	
Proliferation rate constant	$\beta = 24$ ml/mol/s†
Maximum cell density	$n_{\max} = 3.62 \times 10^7$ cells/ml†
Cell death rate constant	$\delta = 2.27$ cells/ml/s†
Cell death gradient constant	k_δ
Cell death oxygen threshold	c_t mol/ml
Oxygen concentration parameters	
Diffusion coefficient for oxygen in collagen gel	$D_{c_g} = 4.5 \times 10^{-6}$ cm^2/s [71]
Oxygen metabolism constant	$M = 1.19 \times 10^{-17}$ mol/cell/s [367]
Concentration at which oxygen consumption is half maximal	$c_{1/2} = 6.66 \times 10^{-9}$ mol/ml†
VEGF concentration parameters	
VEGF diffusion coefficient	$D_{v_g} = 1.13 \times 10^{-6}$ cm^2/s [232]
VEGF net change magnitude constant	α_0 cm^3/mol
Basal VEGF release rate	α mol/cm^3/s
VEGF secretion gradient constant	k_α
Hypoxia oxygen threshold	c_h mol/ml
Degradation rate constant	d_v s^{-1}
Estimate of a typical VEGF concentration	$V_0 = 5 \times 10^{-11}$ mol/ml

Table 3.1: Unscaled parameter definitions, units and approximate values (where known) used for the proof of concept model. (†) denotes parameter values provided by Prof. Shipley, based upon previous unpublished research; these values were derived by fitting against published data [18]. Note that these parameter values are used only for the proof of concept model; updated parameter values are derived in Section 3.5.4.

3.2.2 Non-dimensionalisation and simulation method

The equations were non-dimensionalised via rescaling to ease the process of simulation, using the scaling factors listed in Table 3.2. The notation c', v', n', t' and z' will now refer to the non-dimensional variables.

The non-dimensional equations used for simulation of the model are as follows:

$$\frac{\partial c'}{\partial t'} = \gamma_c \frac{\partial^2 c'}{\partial z'^2} - \mu_c \frac{n'c'}{c'+1}\,, \tag{3.6}$$

$$\frac{\partial n'}{\partial t'} = c'n'(1-n') - \eta_d \mathrm{d}(n',c')\,, \tag{3.7}$$

$$\frac{\partial v'}{\partial t'} = \gamma_v \frac{\partial^2 v'}{\partial z'^2} + \mu_v n' \mathrm{h}(c') - \eta_v n'v'\,. \tag{3.8}$$

The time scale of oxygen diffusion is smaller than that of cell proliferation (Appendix A.1), represented by a relatively large value of γ_c. Therefore it is possible to use a quasi-steady assumption to reduce Equation 3.6 to:

$$0 = \frac{\partial^2 c'}{\partial z'^2} - \frac{\mu_c}{\gamma_c}\frac{n'c'}{c'+1}\,. \tag{3.9}$$

Assumptions about the approximate magnitude of the oxygen concentration can also be used to simplify the Michaelis Menten term of this equation further:

$$c' \gg 1 \Rightarrow \frac{n'c'}{c'+1} \approx c'\,,$$
$$c' \ll 1 \Rightarrow \frac{n'c'}{c'+1} \approx n'c'\,.$$

The approximation $c' \ll 1$ was used for the simulation of the proof of concept model to enable the solver to calculate the solutions more easily. The model was solved computationally in MATLAB using explicit spatial discretisation and MATLAB based ODE solvers (Appendix A.2).

Variable	Scaling factor
t	$t = \frac{1}{\beta c_{1/2}} t'$
z	$z = Lz'$
v	$v = V_0 v'$
n	$n = n_{\max} n'$
c	$c = c_{1/2} c'$

Table 3.2: Rescaling factors used during non-dimensionalisation.

Variable	Definition	Name	Possible value
γ_c	$\frac{D_{c_g}}{\beta c_{1/2} L^2}$	Oxygen diffusion parameter	≈ 12.5125
μ_c	$\frac{M n_{\max}}{\beta c_{1/2}^2}$	Oxygen uptake parameter	
γ_v	$\frac{D_{v_g}}{\beta c_{1/2} L^2}$	VEGF diffusion parameter	≈ 3.1420
μ_v	$\frac{\alpha \alpha_0 n_{\max}}{V_0 \beta c_{1/2}}$	VEGF release parameter	
η_v	$\frac{\alpha_0 d_v n_{\max}}{\beta c_{1/2}}$	Tissue degradation parameter	
η_d	$\frac{\delta}{\beta c_{1/2} n_{\max}}$	Cell death parameter	≈ 0.3923

Table 3.3: Non-dimensional parameters and their estimated values (where enough parameter values are known to give an estimation).

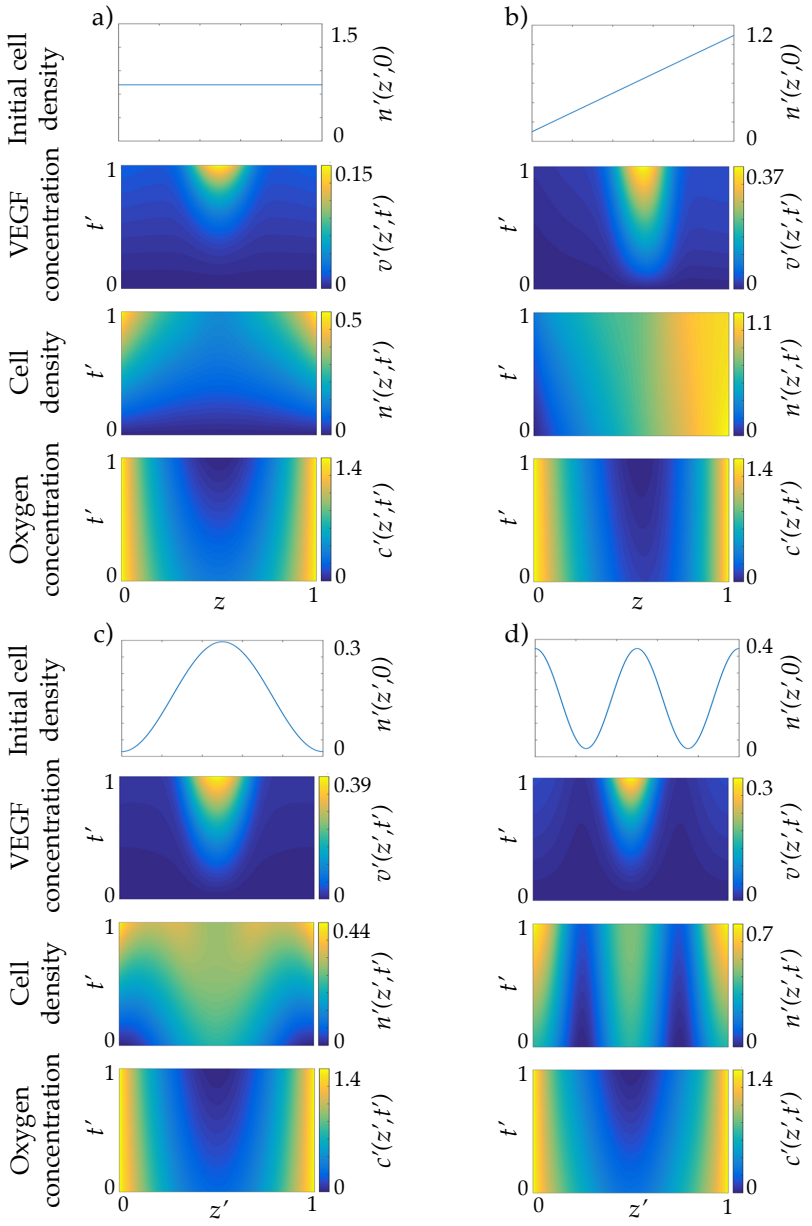

Figure 3.2: Proof of concept model simulation results: The variables c', n' and v' are the rescaled solutions, at given values of rescaled time t' and space z'. Note that $c = 6.66 \times 10^{-9} c'$ mol/ml, $n = 3.62 \times 10^{6} n'$ cells/ml and $v = 5 \times 10^{-11} v'$ mol/ml, as per Tables 3.2 and 3.1. *Figure adapted from poster for Tissue and Cell Engineering Society Annual Meeting 2015. Abstract available in eCells & Materials Meeting Abstracts 2015, Collection 3; TCES (page 42).*

3.2.3 Results and discussion

Several different simulations were run with different initial cell density distribution functions $n_{\text{init}}(z')$ to investigate the effect that the initial seeding distribution of cells could have on the distributions of VEGF concentration, oxygen concentration and cell density over time. The results are illustrated in Figure 3.2. The non-dimensional parameter values used for these simulations are listed in the Appendix A.3.

From the proof of concept model simulations, it is apparent that the distributions of VEGF concentration and cell density in particular appear to vary according to the initial cell density used. It should be noted that no attempt was made to fit this model to experimental data, and that the parameters and functional forms used for these simulations were approximations based only upon existing models and experimental knowledge. However, overall the results of this proof of concept model, coupled with experimental evidence from the literature as described in Section 2.1, suggest that the interplay between these three variables is both non-trivial and a good candidate for the application of mathematical modelling.

3.3 The *in vitro* experiments

As outlined in Section 1.5, one of the aims of this project is to demonstrate the potential of a joint theoretical-experimental approach to NRC design. Consequently, *in vitro* experiments were planned and executed with the specific aims of the theoretical work and the need for model parameterisation in mind. These experiments and analysis of the collected data were carried out after the proof of concept model was devised, and have continued alongside the expanded mathematical modelling work as the project has progressed. For information on the chronological order of work and the relationship between the experimental and theoretical sides, the reader is referred to Figure 1.5.

Experiments were planned by R. Coy, R. Shipley (UCL Department of

Mechanical Engineering) and J. Phillips (UCL School of Pharmacy). Cell culture and viability and VEGF monitoring experiments were carried out by G. Kennedy (UCL Department of Mathematics) and C. Kayal (UCL Department of Mechanical Engineering). Cell proliferation assay was carried out by C. O'Rourke (Biomaterials and Tissue, UCL Eastman Dental Institute). The VEGF ELISA was conducted by P. Kingham (Department of Integrative Medical Biology, Umeå University, Sweden), and oxygen monitoring and data analysis was carried out by R. Coy.

3.3.1 Cell type and material justification

The experiments were designed to provide data for parameterisation of the model, and to inform the functional forms of the mathematical model. Seeded collagen gels in *in vitro* wells were used to mimic the material and environment of a collagen-based EngNT NRC (for a brief description of EngNT, see Section 1.2). The cell type, Schwann cell-like differentiated adipose derived stem cells (dADSCs), and biomaterial (type I collagen) were chosen to reflect the composition of EngNT NRCs that were under development.

Adipose-derived stem cells (ADSCs), derived from adipose tissue gleaned from liposuction or abdominoplasty, are a particularly abundant [411] and widely studied source of stem cells [44]. ADSCs are capable of differentiating along multiple cell lineages [368, 424]; with particular relevance for this work, it has been demonstrated that rat ADSCs can be differentiated towards a Schwann cell-like phenotype [188] with the ability to support neuronal regeneration and produce myelin [241, 415], making them a prime candidate cell type for peripheral nerve repair.

Di Summa et al. presented an *in vivo* study on the use of fibrin nerve conduits seeded with dADSCs to bridge 1 cm sciatic nerve gaps in rats [99]. The results showed improved axonal diameter after 16 weeks for the dADSC-seeded conduits compared to an acellular control, Schwann cell-seeded conduits and Schwann cell-like differentiated bone marrow-derived

mesenchymal stem cell seeded conduits. Importantly, the dADSC-seeded conduits either matched or came close to matching the outcomes of the gold-standard autograft, including proximal and distal electrophysiological measurements taken 15 weeks post implantation and the number of motoneurons labelled after 16 weeks. However, these results do not imply that dADSCs would be the most effective choice when using an alternative base material for the conduit, particularly considering evidence that certain ECM molecules can enhance the positive neuro-regenerative effect of dADSCs [100], which demonstrates that the interaction between base material and seeded cell can have a considerable impact upon efficacy. Nonetheless, this long term *in vivo* study certainly bolsters the case for the use of dADSCs in the peripheral nerve repair context.

Other groups have also experienced success using this cell type to facilitate nerve repair: Georgiou et al. have developed collagen hydrogels with seeded, self-aligned columns of dADSCs that have been shown to increase axon regeneration in comparison to empty tube controls in rats [132, 133], and when Orbay et al. used silicon tubes seeded with dASCs in collagen to bridge 10 mm rat sciatic nerve gaps, they observed improvements in nerve conduction velocity, sciatic function index, and myelination after 6 months [288].

The potential shown by dADSCs in both clinical and pre-clinical studies, their accessible nature and in particular their continued use in the Philips lab, make them a good candidate for study as part of the proposed experimental-theoretical framework. The relative abundance of this source of stem cells from rat tissue ensures that availability will not be an issue for the proposed *in vitro* experimental section of the work, or for future validation experiments, and their well-established potential for nerve repair makes them worthy of further study in this context.

Type I collagen has a relatively long record of use in the peripheral nerve repair context, both in research and in the clinic [270], as well as in

other tissue engineering scenarios such as bone regeneration [420]. Type I collagen peripheral nerve guides and protective wraps have already received FDA approval, and it follows that the clinical translation of cell seeded NRCs incorporating type I collagen may prove to be easier than the translation of NRCs consisting of other, less well characterised material types [185].

Type I collagen is one of a range of natural materials or biopolymers currently used alongside synthetic alternatives to create NRCs, as previously reviewed by multiple authors [37, 270, 416]. Biopolymers are often more biocompatible than synthetic materials such as poly(caprolactone) (PCL) and poly(lactic-co-glycolic) acid (PLGA). Additionally, collagen is one of the key components of the ECM that surrounds peripheral nerve fibers as part of the endoneurium [138], which suggests that the mechanical, as well as biochemical, properties of collagen may be a good match for peripheral nerve repair.

Furthermore, the breadth of research that has been conducted using type I collagen also includes the characterisation of collagen hydrogel mechanics and structure [15] and the measurement of material-specific diffusion coefficients [71], which will aid the mathematical model parameterisation process. Thus for the reasons put forward in this subsection, the experimental work and the theoretical framework was planned to allow the creation of a model of dADSC-seeded plastic compressed type I collagen material specifically. This will allow the theoretical modelling work to mesh neatly with ongoing experimental work involving EngNT in the Phillips lab.

3.3.2 Methods

3.3.2.1 Culture of cells

Differentiated adipose-derived stem cells (dADSCs) were cultured in a differentiation media of modified Eagle's Minimal Essential Medium (MEM with GlutaMAX; Gibco) containing 10% (v/v) foetal bovine serum (FBS)

and 1% (v/v) penicillin/streptomycin solution, supplemented with 14 μm forskolin (Sigma), 10 ng/mL basic fibroblast growth factor (bFGF; Pepro Tech Ltd., UK), and 252 ng/ml neuregulin NR G1 (R&D Systems, UK). The cells were maintained at sub-confluent levels in a 37°C incubator with 5% CO_2 and passaged with trypsin/EDTA (Invitrogen, UK) approximately every 72 h.

3.3.2.2 Fabrication of seeded collagen gels

The dADSCs were prepared in 5 universal tubes each containing a different known number of cells in 50 µL of media in order to acquire a gel with each of the final cell densities post stabilisation. Cells were counted using a hemocytometer with an approximate error of 10%. To prepare the gels, 8 volumes of type I rat tail collagen (2 mg/ml in 0.6% acetic acid; First Link, UK) was mixed with 1 volume of 10 $\times$ Minimum Essential Medium (Sigma) and the mixture neutralised using sodium hydroxide. The neutralised collagen solution was then mixed with 1 volume of cell suspension (to give pre-stabilisation seeding densities of 0.5 to 5 $\times$ 10^6 cells/ml) and 240 µl of the resulting mixture was pipetted into individual wells of a 96-well plate.

The plate was incubated at 37°C for 15 min for the gels to set, before being stabilised by plastic compression for 15 min (RAFT, TAP Biosystems/Lonza) at room temperature. The cell densities of the gels after compression were calculated by multiplying the pre-stabilisation initial cell densities by the ratio of the pre-stabilisation gel volumes to the post-stabilisation gel volumes, giving post-stabilisation initial density values of 39, 77, 154, 231 and 385 $\times 10^6$ cells/ml, henceforth referred to simply as the initial cell densities n_0. The range of these initial cell densities were chosen to cover the range currently used in NRCs for *in vivo* experimentation, as reviewed in Section 1.3.

The gels were immersed in 200 µL media (MEM with GlutaMAX, Gibco), except the highest seeded density gels, which were transferred to a

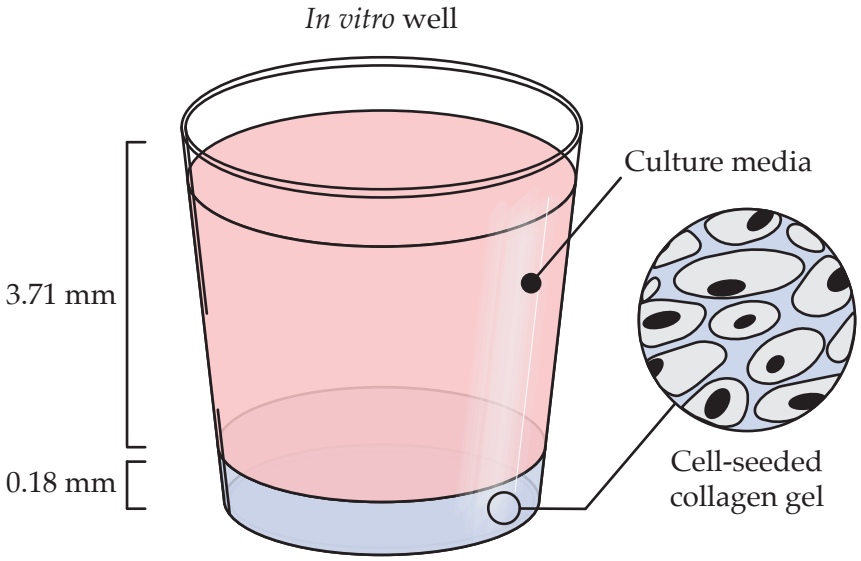

Figure 3.3: Cell culture well schematic.

24-well plate with 1 mL media. The samples were incubated at 37°C in a humidified incubator with 5% CO_2 for 24h and 5 days respectively. In both cases the oxygen level inside the incubator was controlled and maintained (using Biospherix ProOx 110) at each of the following concentrations: 1%, 3%, 5%, 10%, 16%. The controlled oxygen concentration as determined by the incubator will be referred to in this report as the ambient oxygen concentration, c_a.

The ambient oxygen concentrations within the incubator were chosen to cover ranges of oxygen concentration that could feasibly occur in tissue, found experimentally to vary from 1 to 11% across the various tissues of the human body, although measurements of many tissues appear to fall within a narrower range of approximately 3 to 7% [64]. More specifically, endoneurial oxygen tension has previously been measured at around 6 to 7.5% in non-diabetics [272]. Rat tissue oxygen measurements fall within a similar range as that of humans; in particular, skeletal muscle oxygen partial pressure has been measured as approximately 5 to 7% [6]. The unit % refers to percentage of volume as a gas, with $1\% = 1.013\,\text{kPa} = 7.6\,\text{mmHg} = 1.317\,\text{mol/m}^3$.

The gels, for each combination of ambient oxygen concentration c_a (1%, 3%, 5%, 10% or 16%), initial cell density (39, 77, 154, 231 or 385 $\times 10^6$ cells/ml) and 24h or 5 day time points, were used to conduct a metabolic viability assay, a proliferation assay and a VEGF ELISA, as detailed in the following sections. Separate gels were used to conduct oxygen monitoring experiments.

3.3.2.3 Metabolic viability assay

The viable cell density of each gel after incubation was determined using CellTiter-Glo 3D Cell Viability Assay (Promega) to generate a luminescence signal based on ATP content. The medium from each well was aspirated and frozen at -80°C for further analysis. The gels were placed in 100 µL fresh medium (MEM with GlutaMAX) in a white opaque 96-well plate, alongside two negative controls (100 µL media only), to which 100 µL reagent was added. The mixture was put on a rotary shaker for 3 min at 175 rpm and left at room temperature for a further 25 min before a stable luminescence signal was measured. Following the protocol in Section 3.3.2.2 and analysing the resulting gels immediately after plastic compression generated a standard curve, which was used to calculate corresponding viable cell density values. As these experiments were carried out in two stages, on different occasions using different reagents, there are two standard curves as shown in Figure 3.4.

3.3.2.4 Proliferation assay

The collagen gels for immunocytochemistry were fixed using 4% paraformaldehyde (PFA) overnight at 4°C. PFA was removed, gels were washed with PBS. All storage washes and dilutions were performed using PBS. Cells were permeabilised in 0.5% TritonX-100 (Sigma) for 30 min. Following 3 $\times$ 5 min washes, non-specific binding was blocked with 5% normal goat serum (Dako, Ely, UK) for 30 min. After another wash step, Ki67 antibody was diluted (rabbit IgG; 1:250 (Abcam)) and incubated overnight at 4°C. Following 3 $\times$ 10 min washes, secondary antibodies (anti-rabbit

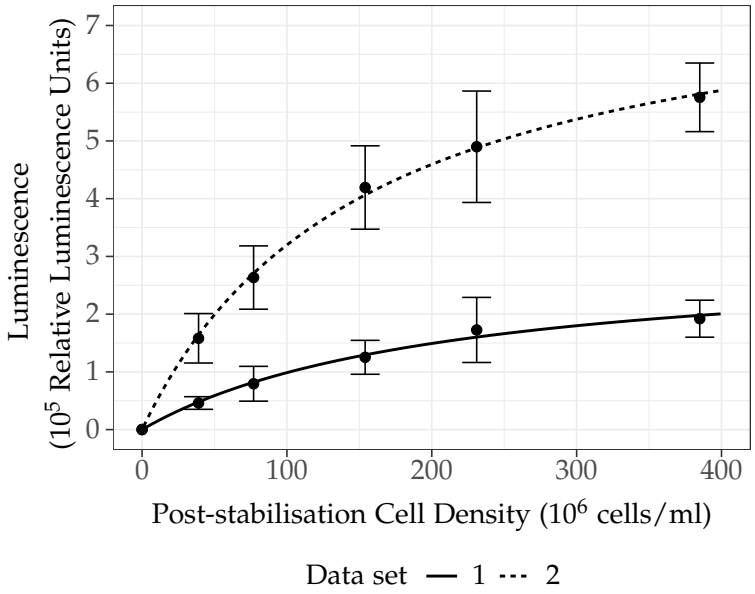

Figure 3.4: Metabolic viability assay standard curves, generated using data analysis software GraphPad Prism. Hyperbolic curves were fitted to the control values with $R^2 = 0.7573$ and $R^2 = 0.8551$ for data set 1 and 2 respectively. GraphPad Prism was used to interpolate luminescence values from the metabolic assay in order to derive viable cell densities. Black points represent means of the control values; error bars represent standard deviations. Means are calculated from 3 and 2 control data points for data sets 1 and 2 respectively.

dylight 488; 1:300 (Vector Laboratories)) were added for 90 min. Hoechst 33258 (1 µg/ml) was also added into the secondary antibody solution for cell counting. The average number of proliferating cells and cells/field was determined using fluorescence microscopy (Zeiss Axio Lab.A1) via quantification of Ki67 and Hoechst staining in 3 pre-determined areas per gel respectively.

3.3.2.5 VEGF enzyme-linked immunosorbent assay ELISA

Secreted vascular endothelial growth factor-A (VEGF-A) protein concentrations of the gels after incubation were determined by an enzyme-linked immunosorbent assay (ELISA). The cell culture supernatant from the gels was analysed with a VEGF-A sandwich ELISA kit (RayBiotech, GA, USA) according to the manufacturer's protocols. In brief, samples were placed into wells coated with a VEGF-specific antibody. VEGF present in the sam-

ples is bound and immobilised by the antibody. Subsequently the wells are washed and a second antibody with a tinted marker is added. Upon the addition of an appropriate substrate solution, the marker changes colour with an intensity proportional to the amount of bound VEGF. The amount of bound VEGF is in turn converted to a figure for average VEGF concentration over the volume of the sample using a standard curve. Samples were diluted 10-200 fold to fit the standard curve (0-80 pg/ml). All samples were analysed in duplicate and the end-absorbance was measured at 450nm (BioTek Synergy microplate reader). $n = 3$ to 6 for each condition (variable % oxygen and initial cell seeding density $\times 10^6$/ml).

3.3.2.6 Oxygen monitoring

A separate sample of 5 cellular collagen gels, 2 with a (post-stabilisation) cell density of 39×10^6 cells/ml and 3 with cell densities of 77, 154 and 231×10^6 cells/ml respectively, were prepared as described in Section 3.3.2.2. The gels were placed within the incubator set at an oxygen level of 3% (39 and 154×10^6 cells/ml) or 5% (39, 77 and 231×10^6 cells/ml). Fibre-optic needle type oxygen probes (code NX-NP/O/E, Oxford Optronix, UK) were inserted into the approximate centre of the gels, and an OxyLite Pro XL pO2 monitor (Oxford Optronix, UK) was used to conduct oxygen monitoring over a period of approximately 17 hours. Oxygen-sensitive luminescent probes are situated at the probe tips, with a tissue sampling area/volume of 1 mm^2. Molecular oxygen quenches the luminescence emitted by the probe, so that luminescence emission is extended in low oxygen environments. The luminescence lifetime thus indicates the oxygen concentration.

3.3.2.7 Statistical analysis

Means and standard deviations were calculated for all data subsets corresponding to the different initial conditions. Multiple regression analysis was carried out using SPSS Statistics to test whether the independent experimental variables, the initial cell density n_0 and the ambient oxygen

concentration c_a, effectively predict the variance in the measured viable cell densities and VEGF concentrations after both 1 and 5 days. Interaction terms were used to test moderation hypotheses, and variables were centred prior to the analysis to address any issues induced by collinearity between the interaction term and the two independent variables.

Where the independent variables were found to statistically significantly predict the dependent variable, Pearson and Spearman correlation coefficients were calculated to investigate the nature of correlations between pairs of variables. The Pearson correlation assesses the linear relationship between two variables, whereas the Spearman correlation assesses the monotonic relationship between two variables. Therefore a combination of the two tests can indicate whether any correlation is linear or non-linear.

Statistical significance thresholds were set at $^{*}p < 0.05$, $^{**}p < 0.01$ and $^{***}p < 0.001$.

3.3.3 Results and discussion

3.3.3.1 Viable cell density

For the cell viability after 1 day, data from 127 wells (Figure 3.5) was used to conduct multiple regression analysis. An interaction term was incorporated into the model to test the hypothesis that the relationship between the ambient oxygen concentration and the viable cell density is moderated by the initial cell density at each time point. The variables statistically significantly predicted the final viable cell density, $F(3, 123) = 47.0$, $p < .0005$, overall model fit $R^2 = .534$. Both the ambient oxygen concentration (standardised $\beta = .658$, $p < .0005$) and initial cell density (standardised $\beta = -.300$, $p < .0005$) added statistically significantly to the prediction, whereas the interaction term (standardised $\beta = -.081$, $p = .190$) was not a significant predictor. Therefore in this case the moderation hypothesis was rejected.

Additional correlation statistics were calculated to investigate the re-

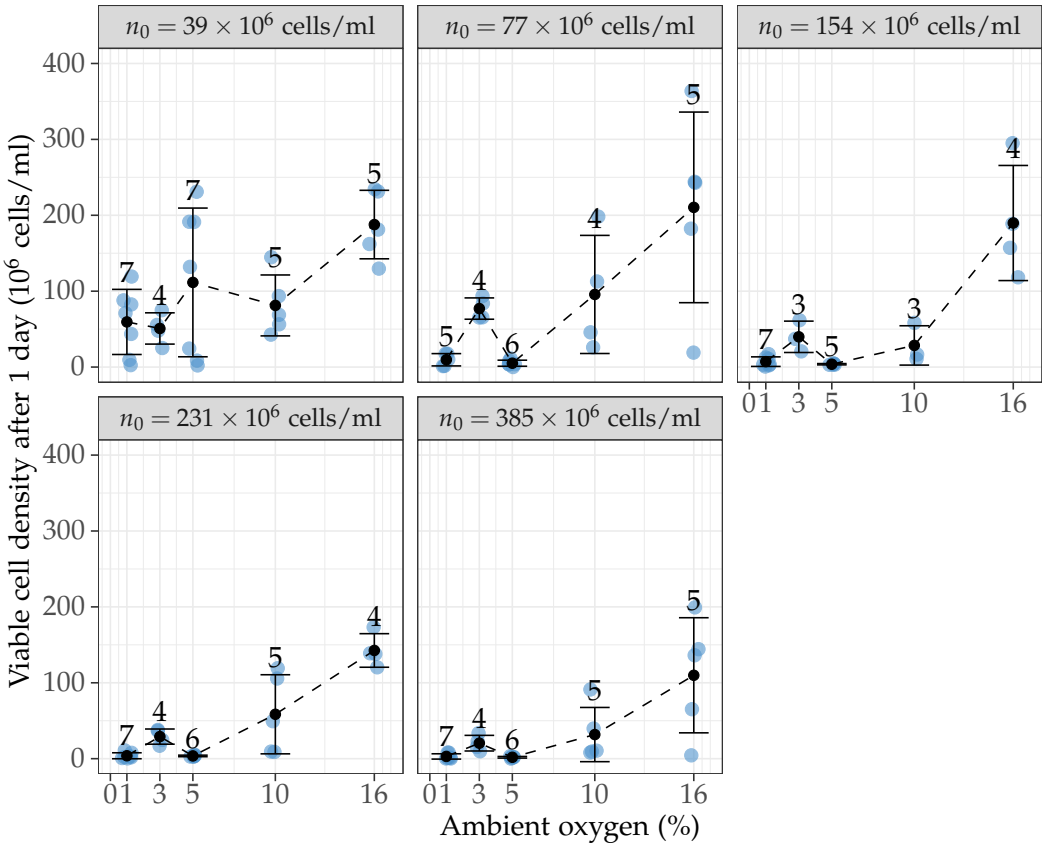

Figure 3.5: Viable cell density after 1 day is correlated with ambient oxygen concentration within the incubator, c_a. Viable cell density was measured after cell-seeded collagen gels were incubated under a range of ambient oxygen c_a conditions for 5 different initial cell densities n_0. Black points denote mean values along with the N number for each (c_a, n_0) initial condition pair, with the total N = 127. Blue points are the original data points and error bars are the standard deviations.

lationships between the viable cell density after 1 day and the ambient oxygen concentration and initial cell density (Table 3.4). As expected from the multiple regression analysis results, a negative correlation was found between n_0 and the viable cell density after 1 day, and a positive correlation between c_a and the viable cell density after 1 day. The Pearson correlation coefficient for the latter relationship has a larger absolute value than the Spearman. This suggests that a linear monotonic relationship between c_a and the viable cell density after 1 day may be more likely than a non-linear monotonic relationship. The converse is true for the relationship between n_0 and the viable cell density after 1 day.

	Test type	Correlation coefficient (3 s.f.)	p value (3 s.f.)
Ambient oxygen concentration, c_a	Pearson	0.661	2.84 e-17 (**)
	Spearman	0.559	8.62 e-12 (**)
Initial cell density, n_0	Pearson	-0.308	4.36 e-4 (**)
	Spearman	-0.402	3.00 e-6 (**)

Table 3.4: Correlation coefficients and p values indicate a positive correlation between the ambient oxygen concentration and the viable cell density after 1 day. N = 127 for all tests. (**) Indicates that the correlation is significant at the 0.01 level (2-tailed).

For the 5 day cell viability, data from 82 wells was used to conduct multiple regression analysis. The variables statistically significantly predicted the final viable cell density, $F(3, 78) = 11.9$, $p < .0005$, overall model fit $R^2 = .314$. Both the ambient oxygen concentration (standardised $\beta = .305$, $p < .005$) and initial cell density (standardised $\beta = -.467$, $p < .0005$) added statistically significantly to the prediction, but the interaction term (standardised $\beta = -.183$, $p = 0.055$) was not significant predictor. Therefore the moderation hypothesis was rejected.

The Spearman correlation coefficients for the relationship between c_a and the viable cell density after 5 days, and the relationship between n_0 and the viable cell density after 5 days, were both of a greater magnitude than the corresponding Pearson correlation coefficients (Table 3.5). This again suggests that these relationships may be non-linear.

In conclusion, both the 1 day and the 5 day cell viability data demonstrate a positive correlation with the ambient oxygen concentration. Therefore it seems likely that the cell governing equation should incorporate a dependency upon the local oxygen concentration, as this is largely determined by diffusion of the ambient oxygen concentration into the gel and media. The relationship between the spatially dependent rate of change of the distribution of viable cells and the viable cell density at any spe-

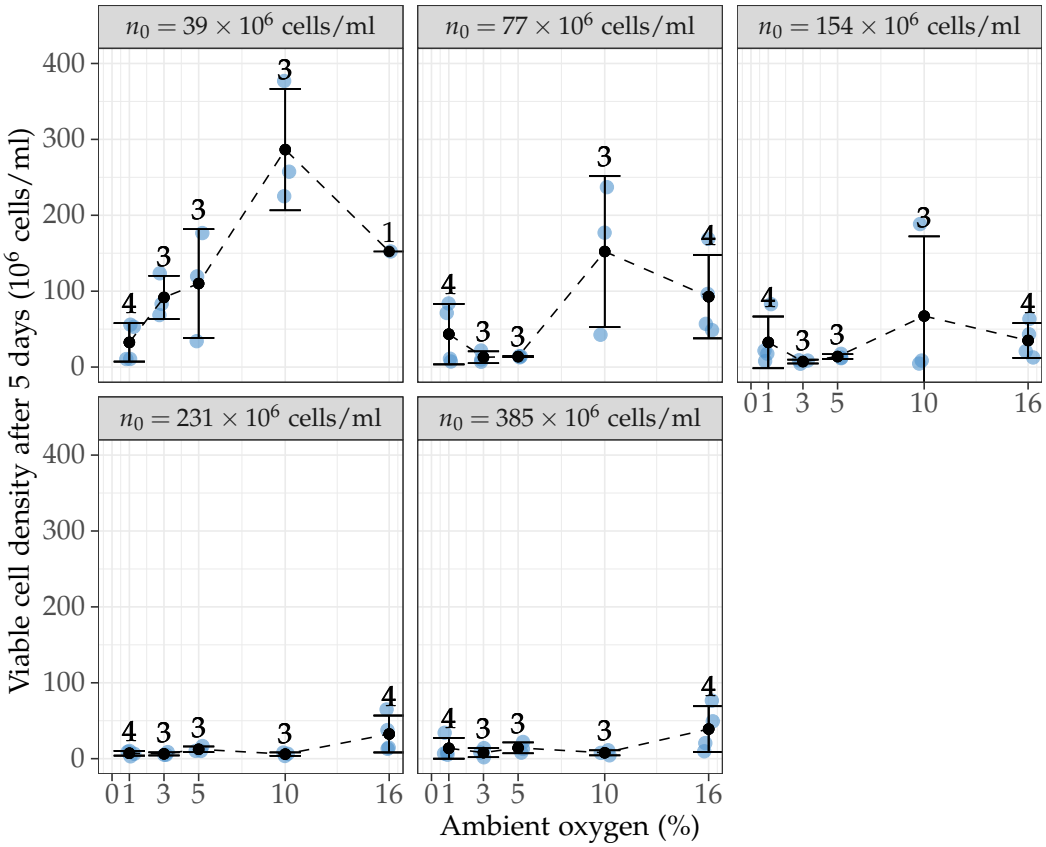

Figure 3.6: Viable cell density after 5 days is correlated positively with ambient oxygen concentration within the incubator c_a, and negatively with the initial cell density n_0, and an interaction term moderates these relationships. Viable cell density was measured after cell-seeded collagen gels were incubated under a range of ambient oxygen c_a conditions for 5 different initial cell densities n_0. Black points denote mean values along with the N number for each (c_a, n_0) initial condition pair, with the total N = 82. Blue points are the original data points and error bars are the standard deviations.

cific time point is less clear from the preceding analysis, as the correlation and regression analysis focused only on the relationship between initial cell density and final viable cell density.

In some cases, the measured increase in viable cell density achieved within the gels over 24 hours is very high. In particular, some of the gels that were initially seeded at 39×10^6 cells/ml recorded five fold greater densities of over 200×10^6 cells/ml after 24 hours (Figure 3.5). In contrast to this, typical doubling times for commonly cultured cells includ-

	Test type	Correlation coefficient (3 s.f.)	p value (3 s.f.)
Ambient oxygen concentration, c_a	Pearson	0.260	0.0182 (*)
	Spearman	0.323	3.11 e-3 (**)
Initial cell density, n_0	Pearson	-0.442	3.2 e-5 (**)
	Spearman	-0.542	1.44 e-7 (**)

Table 3.5: Correlation coefficients and p values indicate a positive correlation between the ambient oxygen concentration and the viable cell density after 5 days, and a negative correlation between the initial cell density and the viable cell density after 5 days. N = 82 for all tests. (*) Indicates that the correlation is significant at the 0.05 level (2-tailed); (**) indicates that the correlation is significant at the 0.01 level (2-tailed).

ing fibroblast-like, epithelial and tumour cells range from around 20 to 45h [224]. A slightly quicker doubling time of 17h has been recorded for mouse Schwann cells [49], and ADSCs have previously been reported to have a doubling time in culture of between 30 and 44 hours, depending on the environmental conditions [388]. The proliferation rate of Schwann cell-like dADSCs such as those used in this study has not previously been measured. Nevertheless, some of the increases in viable cell density shown in Figure 3.5 are undoubtedly high in comparison to the previously mentioned values from the literature.

The dramatic increase in density recorded in these experiments is likely to be caused in part by the use of a metabolic assay to estimate cell density, rather than cell counting. The increase in the recorded level of luminescence, which has here been converted to viable cell density, may instead reflect an increase in metabolic activity on a per cell basis rather than an overall increase in the cell population size. Better understanding of these results could be achieved by using a direct method to measure the actual number of viable cells per ml in any similar experiments in the future.

The cell viability data also exhibits a fairly large degree of variation,

both within initial seeding densities n_0 and across initial seeding densities. There are numerous possible sources for this variability. One main cause could be inaccuracies introduced during the estimation of the initial cell density when the gels were prepared. A haemocytometer was used to count a small sample of the cell suspension, and then error was likely introduced when samples of the cell suspension were then pipetted into the wells. The use of automated counting and dispensing equipment may have been able to improve this. On top of this, it is likely that variability will have been introduced by variations in the cell populations between experiments, for example due to different initial cell sources and different times in culture prior to experiments.

Finally, additional error is likely to have been caused by the indirect measure of cell viability used. The use of a metabolic viability assay to measure cell density was motivated by the fact that the gels were too densely seeded for the use of microscopy, but as previously mentioned it is likely that changes in cell density may not account for all changes in metabolic activity measured. This could have contributed to the variability of the control data points used to generate the standard curves, represented by the standard deviation values in Figure 3.4.

The metabolic activity standard curves were generated using control data encompassing densities of 0 to 385×10^6 cells/ml, and therefore extrapolating beyond this is likely to result in unreliable quantifications. However, this was not necessary to quantify the experimental data presented here.

3.3.3.2 VEGF concentration

Multiple regression analysis was run on the 1 day data (Figure 3.7), comprising of 109 measurements, to predict the VEGF concentration from the initial cell density n_0 and ambient oxygen concentration c_a. An interaction term was included to test the hypothesis that ambient oxygen concentration moderates the relationship between initial cell density and the VEGF

	Test type	Correlation coefficient (3 s.f.)	p value (3 s.f.)
Initial cell density, n_0	Pearson	0.278	3.34 e-3 (**)
	Spearman	0.347	2.20 e-4 (**)
Viable cell density after 1 day	Pearson	0.091	0.347
	Spearman	0.192	0.046 (*)

Table 3.6: Correlation coefficients and p values indicate a positive correlation between the initial cell density and the VEGF concentration in the media after 1 day, and a positive correlation between the cell density after 1 day and the VEGF concentration in the media after 1 day. N = 109 for all tests. (*) Indicates that the correlation is significant at the 0.05 level (2-tailed); (**) indicates that the correlation is significant at the 0.01 level (2-tailed).

concentration in the media after 1 day. The variables statistically significantly predicted the final VEGF concentration, F(3, 105) $= 4.64$, $p < .001$, overall model fit $R^2 = .117$. The initial cell density (standardised $\beta = .268$, $p < .0005$) added statistically significantly to the prediction but the ambient oxygen concentration (standardised $\beta = .059$, $p = .520$) did not. However, the interaction term was found to add statistically significantly to the prediction (standardised $\beta = .192$, $p = .039 < 0.05$). Therefore the moderation hypothesis was accepted.

The Spearman correlation coefficient for the correlation between n_0 and the VEGF concentration after 1 day was of greater magnitude than the corresponding Pearson correlation coefficient (Table 3.6). This suggests that the relationship may be non-linear.

Multiple regression analysis was run on the 5 day data (Figure 3.8), comprising of 81 measurements, to predict VEGF concentration after 5 days from initial cell density n_0 and ambient oxygen concentration c_a. An interaction term was included to test the hypothesis that ambient oxygen concentration moderates the relationship between initial cell density and the VEGF concentration over the media after 5 days. The variables statisti-

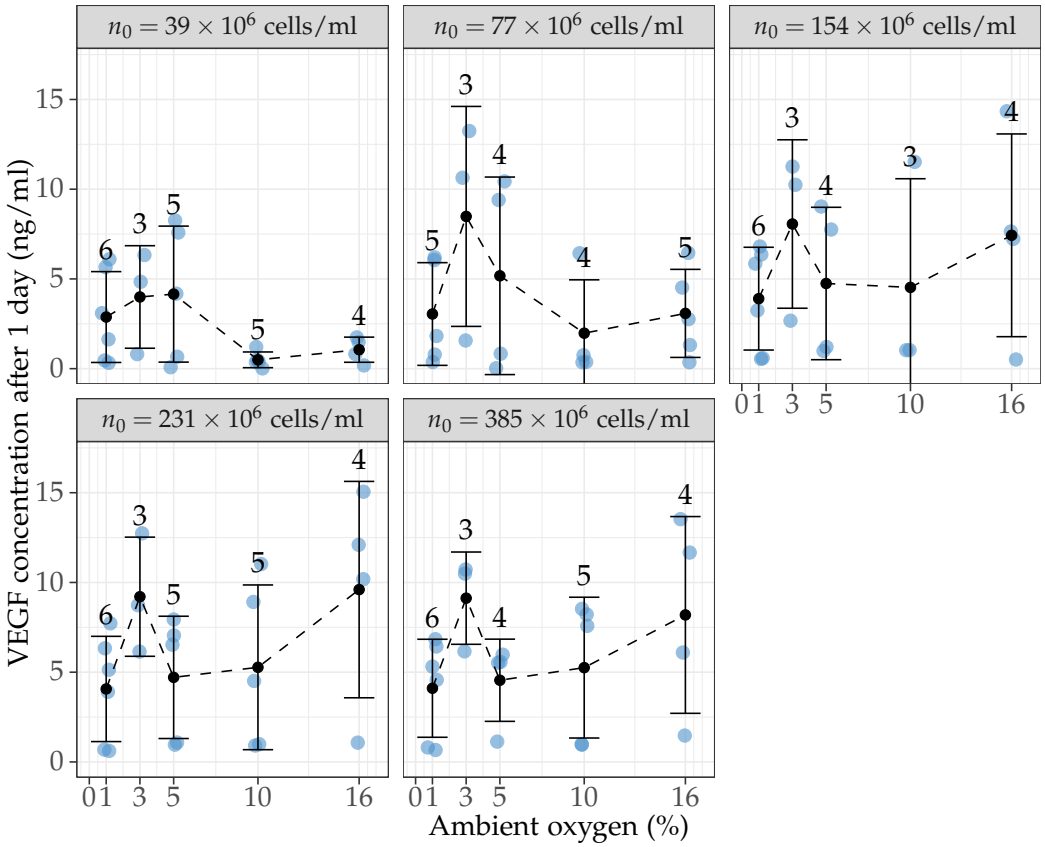

Figure 3.7: VEGF concentration in the media after 1 day is correlated with the initial cell density n_0, but not with ambient oxygen concentration within the incubator c_a. VEGF concentration was measured via ELISA after cell-seeded collagen gels were incubated under a range of ambient oxygen c_a conditions for 5 different initial cell densities n_0. Black points denote mean values along with the N number for each (c_a, n_0) initial condition pair, with the total N = 109. Blue points are the original data points and error bars are the standard deviations.

cally significantly predicted the final VEGF concentration, $F(3, 77) = 19.8$, $p < .001$, overall model fit $R^2 = .435$. The initial cell density (standardised $\beta = .626$, $p < .0005$) added statistically significantly to the prediction but the ambient oxygen concentration (standardised $\beta = -.172$, $p = .0510$) did not. The interaction term was not found to add statistically significantly to the prediction (standardised $\beta = -.138$, $p = .113$). Therefore the moderation hypothesis was rejected.

Similarly to the day 1 case, comparison of the magnitudes of the correlation coefficients (Table 3.7) again suggests that the relationship between

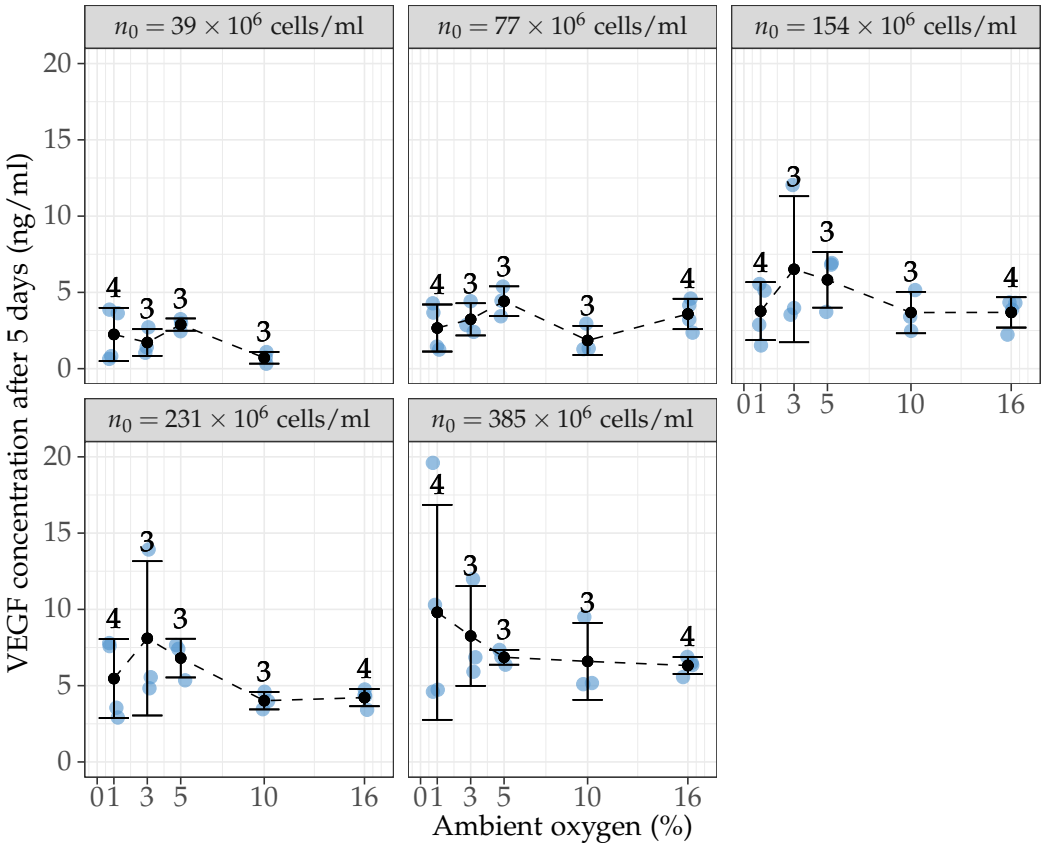

Figure 3.8: VEGF concentration in the media after 5 days is correlated with the initial cell density n_0, but not with ambient oxygen concentration within the incubator c_a. VEGF concentration was measured via ELISA after cell-seeded collagen gels were incubated under a range of ambient oxygen c_a conditions for 5 different initial cell densities n_0. Black points denote mean values along with the N number for each (c_a, n_0) initial condition pair, with the total N = 81. Blue points are the original data points and error bars are the standard deviations.

the initial cell density and the VEGF concentration in the media after 5 days may be non linear.

From the preceding statistical analysis it appears that the initial cell density positively correlates with the VEGF concentration in the media. However, this data alone does not give any information as to the mechanism behind this relationship, and thus is not particularly useful for refining the form of the theoretical model governing equations.

For this reason, further correlation analysis was conducted to investigate the relationship between the VEGF concentration data and the vi-

	Test type	Correlation coefficient (3 s.f.)	p value (3 s.f.)
Initial cell density, n_0	Pearson	0.617	8.51 e-10 (**)
	Spearman	0.744	1.77 e-15 (**)
Viable cell density after 5 days	Pearson	-0.403	1.95 e-4 (**)
	Spearman	-0.472	9 e-6 (**)

Table 3.7: Correlation coefficients and p values indicate a positive correlation between the initial cell density and the VEGF concentration after 5 days, and a negative correlation between the viable cell density after 5 days and the VEGF concentration after 5 days. (**) Indicates that the correlation is significant at the 0.01 level (2-tailed). N = 81.

able cell density data at the corresponding time points (Tables 3.6 and 3.7). These revealed a positive correlation between the VEGF concentration and viable cell density at the 1 day time point, but a negative correlation at the 5 day time point. This could indicate a complex relationship between cell density and VEGF production that may depend upon other factors. For example, after 5 days many of the cells appear to have died potentially due to competition for nutrients; the cellular response to low levels of nutrients such as oxygen often includes an increase in the production of factors such as VEGF, which could have resulted in the negative correlation between viable cell density and VEGF concentration at this time point. However, there is no way of verifying this particular hypothesis.

The lack of a statistically significant correlation between the ambient oxygen concentration and the VEGF concentration could be due to the potentially nonlinear relationship between these variables; in particular, Figure 3.7 appears to show a distinct but nonlinear pattern including a local maximum in the mean VEGF concentration at $c_a = 5\%$, and a gradual increase in mean VEGF concentration from $c_\mathrm{a} = 5$ to 16% for $n_0 \geq 154 \times 10^6$ cells/ml.

In summary, the VEGF concentration data demonstrate some interesting patterns but the exact nature of the dependence of VEGF upon the

other variables is difficult to unpick, probably due to the complexity of the problem. Thus further information from the literature will be required to develop the VEGF governing equation for the theoretical model.

3.3.3.3 Cell proliferation

Ki67 expression indicates activity in all phases of the cell cycle aside from the G0 quiescent phase, during which a cell is not dividing or preparing to divide, at the time that the sample is taken. Ki67 staining was used to assess the proliferation of the cells in the various experiments at the 1 and 5 day time points.

The number of nuclei exhibiting Ki67 in three samples of each gel were counted and averaged to give values for the % cells Ki67+, to measure the proportion of cells proliferating in each gel. Multiple samples were taken from each gel to reduce error but the individual gels, which were incubated in separate wells, are the independent experimental units. Therefore, only the mean values calculated for each independent gel are used for statistical analysis and depicted in Figures 3.9 and 3.10.

A multiple regression analysis was run upon both the 1 day and 5 day Ki67 data sets, using the same procedure as described in Section 3.3.3.1 to predict the % cells Ki67+ from initial cell density n_0 and ambient oxygen concentration c_a. An interaction term was included to test the hypothesis that initial cell density moderates the relationship between ambient oxygen concentration and the % Ki67+.

In the case of the 1 day time point Ki67 data (Figure 3.9), the variables did not statistically significantly predict the % cells Ki67+, $F(3, 56) = .972$, $p = .412$, $R^2 = .049$.

Conversely, for the five day time point (Figure 3.10), the variables statistically significantly predicted the % cells Ki67+, $F(3, 59) = 21.150$, $p < .0005$, overall model fit $R^2 = .518$. However, only the ambient oxygen concentration added statistically significantly to the prediction (standardised $\beta = .705$, $p < .0005$), whereas initial cell density (standardised

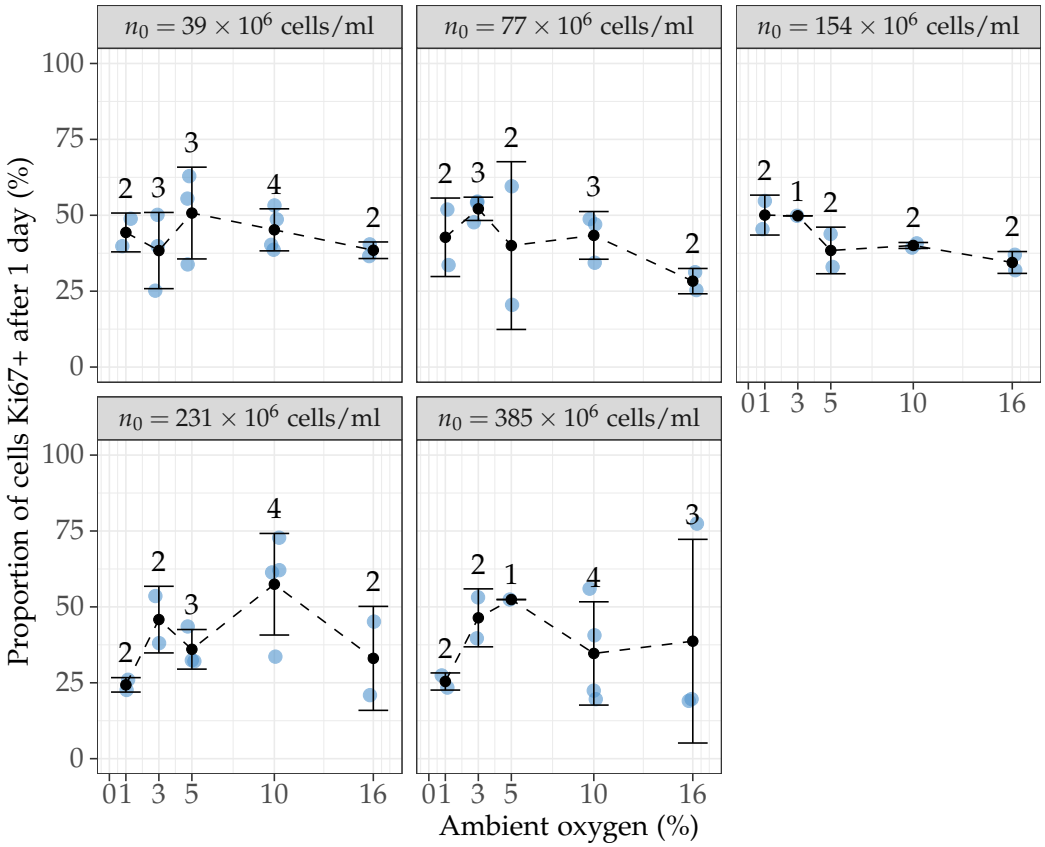

Figure 3.9: The proportion of Ki67+ cells after 1 day is not correlated with c_a or n_0. Black points denote mean values along with the N number for each (c_a, n_0) initial condition pair, with the total N = 60. Blue points are the original data points, each of which representing an average of three samples from a single gel, and error bars are the standard deviations.

$\beta = -.013$, $p = .722$) and the interaction term (standardised $\beta = -.170$, $p = .065$) were not significant predictors. Therefore the moderation hypothesis was rejected.

Pearson and Spearman correlation coefficients were calculated using the entire 5 day proliferation data (Table 3.8). Analysis was based on the assumption that the Ki67+ expression was independent of the initial cell density. The results indicate a positive correlation between the ambient oxygen concentration and the % Ki67+ expression, confirming the relationship suggested in Figure 3.10. The Spearman correlation coefficient is slightly larger than the Pearson, implying that a linear monotonic relationship is perhaps more likely than a non-linear monotonic relationship.

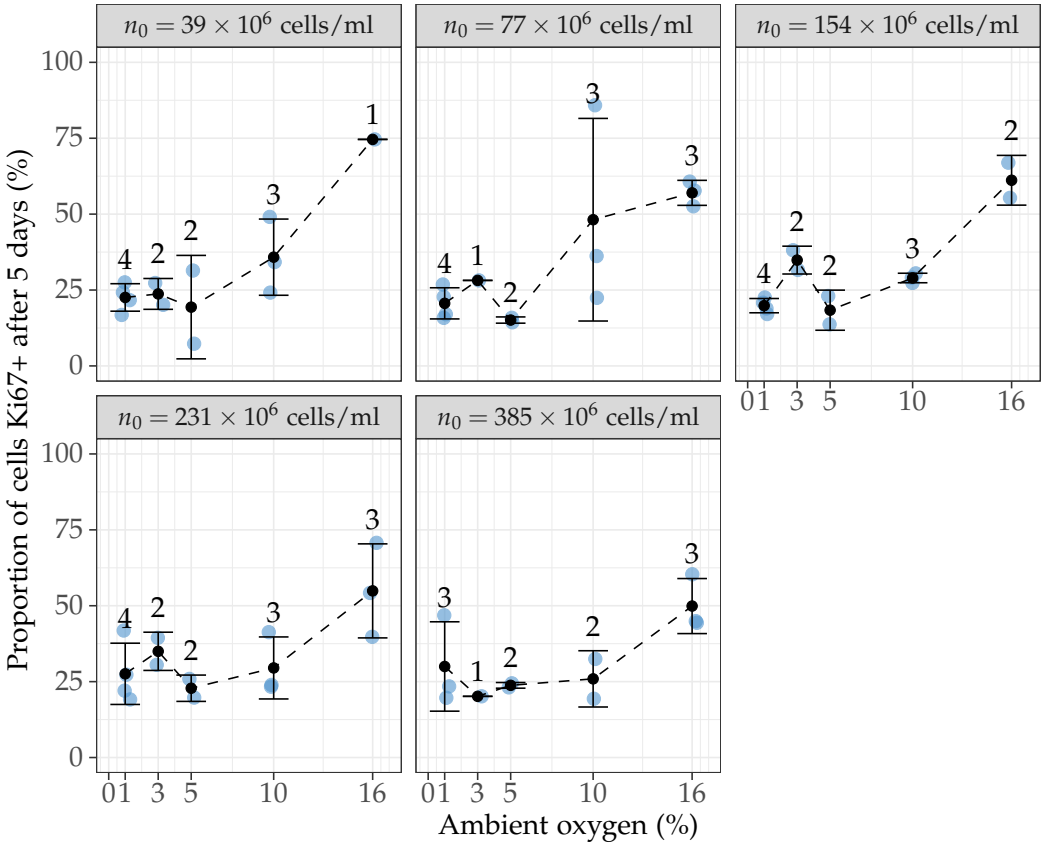

Figure 3.10: The proportion of Ki67+ cells after 5 days is not correlated with c_a or n_0. Black points denote mean values along with the N number for each (c_a, n_0) initial condition pair, with the total N = 63. Blue points are the original data points, each of which representing an average of three samples from a single gel, and error bars are the standard deviations.

	Test type	Correlation coefficient (3 s.f.)	p value (3 s.f.)
Ambient oxygen concentration, c_a	Pearson	0.699	1.93 e-10 (**)
	Spearman	0.613	9.11 e-8 (**)

Table 3.8: Correlation coefficients and p values indicate a positive correlation between the ambient oxygen concentration and the % cells Ki67+ after 5 days. N = 63.

Neither the day 1 nor day 5 proliferation data demonstrated any correlation between Ki67+ expression and the initial cell density n_0 used in the experiments. It seemed likely that the % cells exhibiting Ki67+ would be more dependent upon the cell density at the corresponding time point of measurement than the initial cell density. For this reason, multiple regression analysis was carried out using the entire Ki67 data set, including both time points to give a total of 123 observations, to predict the % cells exhibiting Ki67+ from the viable cell density at that time point and the oxygen. An interaction term was included to test the hypothesis that the viable cell density at the time point of measurement moderates the relationship between ambient oxygen concentration and the % cells Ki67+. The variables statistically significantly predicted the % cells Ki67+, $F(3, 119) = 6.540$, $p < .0005$, overall model fit $R^2 = .142$. But again, only the ambient oxygen concentration added statistically significantly to the prediction (standardised $\beta = .365$, $p < .0005$), whereas the viable cell density (standardised $\beta = .075$, $p = .542$) and the interaction term (standardised $\beta = -.146$, $p = .206$) were not significant predictors. Therefore the moderation hypothesis was rejected.

The results again demonstrated no clear relationship between cell density and proliferation. This motivates the exclusion of a dependency upon n, the local cell density at that specific time point, for the cell proliferation term in the mathematical model. However, it is clear from the cell viability data that the viable cell density at both time points does depend upon the initial cell density. Therefore it is proposed that the cell death term should include a dependency upon n to account for this.

As concluded from the preceding multiple regression analysis, the 1 day data does not show any relationship between the ambient oxygen concentration and the % of cells exhibiting Ki67+ (Figure 3.9). In contrast, the 5 day data displays a clear relationship between the ambient oxygen level c_a and the % of cells exhibiting Ki67+ (Figure 3.10). In the 1 day experiment

the ambient oxygen concentration has less time at an approximately steady state after the initial diffusion phase- it is possible that exposure to relatively low or high oxygen concentrations over 5 days instead could impact % Ki67+ expression more severely. It is important to note that any dependence upon the ambient oxygen level will be effectively indirect, with the cellular proliferation affected by the levels of oxygen in the gel which are predominantly determined by the diffusion of ambient oxygen through the media and gel in the well. Therefore it is proposed that the oxygen concentration of a cell's immediate surroundings does influence the proliferation rate, suggesting that the cell proliferation term in the mathematical model should incorporate a dependence on c.

It is interesting to note that the 5 day data reveals a distinct increase in Ki67+ expression at $c_a = 3\%$ for three out of the five values of n_0. This is especially interesting because a similar phenomenon occurs at the 3% oxygen level for the viability data. It is possible that this oxygen concentration value represents a niche for this particular cell type that is conducive for proliferation and survival.

3.3.3.4 Oxygen monitoring

The oxygen monitoring experiment took place over 17h, giving the oxygen levels in the gels time to stabilise via diffusion. The initial oxygen concentration in the gel in the standard atmosphere was 18%; the ambient oxygen concentration in the incubator was set at 3% or 5%, although this has an accuracy of +/- 1%. The final oxygen concentrations in the gels were all roughly similar. However, the rate of change from the initial oxygen concentration onwards appeared to differ according to initial cell density, with a steeper gradient for high initial cell densities (Figure 3.11). This could be due to the increased consumption of oxygen within the high initial cell density gels.

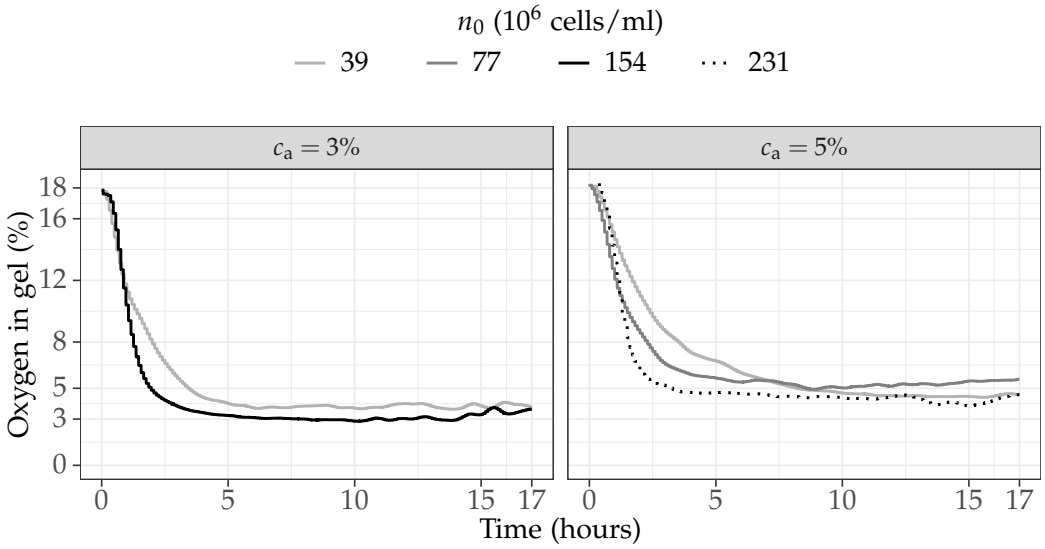

Figure 3.11: Oxygen concentration % in the collagen gels as monitored via the oxygen probes, for four different initial cell densities (n_0).

3.4 The generalised cell-solute model

In this section, the proof of concept model outlined in Section 3.2 is refined to provide general versions of the functional forms that make up the terms of the cell-solute model. This is achieved by reviewing existing published experimental data regarding the interactions between cells, oxygen and VEGF, as well as the specific functional forms used in similar continuum models. The correlations found in the preceding statistical analysis of the *in vitro* data (Section 3.3.3) are also taken into account to arrive at initial versions of the three governing equations. Parameter values are assigned subsequently in Section 3.5 according to existing values in the literature and via parameterisation against the *in vitro* data.

3.4.1 Viable cell density governing equation

In some existing continuous models of cell-solute interactions, the cell population is represented implicitly through changes in construct permeability or via nutrient consumption [84, 349]; in others, the cell phase is explicitly represented through the use of a separate governing equation. This thesis aims to make predictions about the survival of therapeutic cells *in vivo*, and

therefore it makes sense to model the cells explicitly. In this way, the number of dead cells can also be tracked to compare the amount of wastage of cells generated by different cell seeding approaches to therapy.

Generally, the viable cell density within an engineered tissue over time and space is determined by the proliferation and death rates of the cells, as well as cell migration in certain scenarios. In a collagen NRC, the impact of cell migration upon viable cell density distributions over the examined time scale is likely to be negligible because the time scale for such migration is of the order of weeks, as opposed to hours and days for oxygen diffusion and cell proliferation and death. The assumption that no seeded cell migration will take place over the simulated time period (0 to 5 days) is supported by a study that reported no statistical change in the position of seeded cells in a plastic-compressed collagen construct after 5 days *in vitro* [18].

This leaves the viable cell density governing equation with two terms for which functional forms and parameter values must be identified: the cell proliferation term, here represented by the proliferation function G, and the cell death term, a sink term represented in this thesis as the function F. So the general form of the cell density governing equation is given by:

$$\frac{\partial n}{\partial t} = G - F \,. \tag{3.10}$$

The functions G and F can be adapted to depend on different variables and parameters, as illustrated by previous work on similar cell-solute models which will be briefly reviewed in this subsection. All of the forms of cell proliferation and death terms mentioned in this subsection assume that these processes depend only on the current local concentrations of nutrients and densities of cells, and are independent of historical nutrient concentration or cell density values.

The majority of existing continuous models of cell proliferation have defined the function G to be the product of a function of the cell density n and a function of nutrient or oxygen concentration c. In the appendix

of their paper, Lewis et al. experimented with using a proliferation term with a simple linear dependence upon the cell density n, and a very simple dependence on oxygen that is constant for positive oxygen values but results in no proliferation when no oxygen is available [217]. The authors implemented this in the form of a Heaviside step function $\mathrm{H}(c)$ such that

$$G(n,c) = \beta n \mathrm{H}(c), \quad \text{where} \tag{3.11}$$

$$\mathrm{H}(c) = \begin{cases} 1, & c > 0 \\ 0, & c \leq 0\,. \end{cases} \tag{3.12}$$

Here β is the cell proliferation rate constant. This formulation allowed the governing equations to be solved analytically after non-dimensionalisation. This particular mathematical framework models chondrocytes within a porous scaffold, and the use of a proliferation term with no dependence upon positive oxygen concentrations was motivated by experimental evidence that chondrocyte growth may be unaffected by oxygen concentration [239, 244].

Conversely, evidence suggests that the proliferation rates of most other cell types are dependent on local oxygen concentrations. As reviewed by Hubbi and Semenza, this relationship is likely to be cell type-specific and mediated by hypoxia-inducible factors [161]. For example, Kakudo et al. demonstrated that ADSCs cultured under hypoxia (1%) demonstrated increased proliferation compared to cells cultured under normoxia (20%) [180], although this was assessed via cell counting and therefore did not take into account possible changes in death rates due to oxygen concentration. Furthermore, Van Pham et al. concluded that hypoxia (in this case 5% oxygen) upregulates ADSC proliferation [388]. On the other hand, alternative cell types including embryonic fibroblasts [128] and embryonic stem cells [62] have demonstrated inhibition of proliferation under hypoxia (0.1-0.5% and 2% oxygen respectively in these studies).

The analysis of the *in vitro* Ki67 data completed in Section 3.3.3.3

demonstrated a positive correlation between dADSC proliferation and the ambient oxygen concentration after 5 days. Although no correlation was found for the 1 day data, due to this result and the previous research suggesting that the proliferation of most cell types is affected by oxygen, in this thesis it is assumed that dADSC proliferation does depend upon oxygen.

A simple linear dependence of proliferation upon both oxygen and cell density was implemented by Lewis et al. in the main section of their paper [217]:

$$G(n,c) = \beta c n \,. \tag{3.13}$$

Jones et al. also used this form of cell proliferation in a model of avascular tumour growth [177], although in this case the tumour cell density was subsequently assumed to be constant and thus the cell term was not considered explicitly.

This formulation assumes that the rate of cell proliferation increases indefinitely both with the concentration of nutrient available and the number of viable cells. This does not take into account the negative effect that higher cell densities could have upon proliferation via increased competition for space (contact inhibition) and nutrients. Furthermore, this functional form does not incorporate a saturation point for the nutrient density, assuming instead that higher concentrations of nutrient will always result in a higher proliferation rate. This is unlikely to be the case due to receptor saturation.

The Michaelis-Menten function has also been used to describe the dependence of cell proliferation upon oxygen. This formulation does incorporate the concept of nutrient saturation: gradually, increases in oxygen concentration will result in diminishing increases in proliferation rate as this hyperbolic function tends towards a limit. When coupled with a linear dependence upon cell density, this gives the following:

$$G(n,c) = \beta n \frac{Mc}{c_{1/2} + c} \,, \tag{3.14}$$

where M is the maximal oxygen consumption rate and $c_{1/2}$ is the oxygen concentration at which the oxygen consumption rate is half of its maximal value. In particular, Croll et al. used the Monod model for cell proliferation which is essentially of the same form as Equation (3.14) but allows the direct coupling of cell proliferation with oxygen consumption [87]. However, the use of Equation (3.14) does not incorporate any limitation on the cell proliferation rate related to cell density.

The logistic growth function, on the other hand, has been used to describe the dependence of cell proliferation upon cell density and can be used to model the impact of competition for space and resources [205, 319, 349]:

$$G(n,c) = f(c)n\left(1 - \frac{n}{n_{\max}}\right). \tag{3.15}$$

Here $f(c)$ is a generic function of oxygen concentration. This model determines that cell proliferation is proportional to cell density at low cell densities, but that at high cell densities it is limited by the existence of a maximum cell density $n_{\max}$, which could represent the negative impact of overcrowding and competition for space and resources upon cell proliferation. This functional form is often used in population dynamics and here is applied specifically to a cell population, with $n_{\max}$ assuming the role of the carrying capacity often seen in ecological population models.

Pohlmeyer et al. used two terms to model cell proliferation: one representing the dependence of proliferation upon the concentration of a nutrient, here denoted c, and the other capturing enhanced proliferation due to the presence of a growth factor, denoted v [319]. A logistic growth function was used for the nutrient dependent proliferation term, coupled with a function W representing a dependence upon shear stress:

$$G(n,c) = Wn\left(1 - \frac{n}{n_{\max}(c)}\right). \tag{3.16}$$

Pohlmeyer et al. also defined $n_{\max}$ as a function of nutrient concentration

c to represent the dependence of the maximum cell density upon available nutrient supply, with nutrient toxicity also taken into account by letting $n_{\max}(c) \to 0$ as $c \to \infty$. The shear stress component in this case is a product of fluid flow generated by a perfusion bioreactor, which will be neglected in our case under the assumption that there will be zero flow through an avascular nerve repair construct in the first few days post-implantation.

In the same paper, the form of the growth factor dependent proliferation term was chosen to reflect a small effect for low concentrations of growth factor v, and to incorporate saturation at high concentrations:

$$G(v) = \frac{v^3}{v_{\text{sat}} + v^3} \,. \tag{3.17}$$

Here v_{sat} is a VEGF saturation constant. This term was likely informed by the established existence of growth factors such as fibroblast growth factor that upregulate the proliferation of cells. It is known that VEGF can increase the proliferation of vascular endothelial cells by directly inducing mitosis [116]. Furthermore, Sondell et al. reported that VEGF_{165} induced a statistically significant increase in the number of proliferating cells in ganglia cultured for 48 hours [360]. But the concentrations used were 50 and 100 ng/ml of VEGF; much higher than those concentrations measured in the *in vitro* experiments, which reached a maximum of around 20 ng/ml (Figures 3.7 and 3.8).

Conversely, much lower concentrations of VEGF (0.1-0.5 ng/ml) were shown to increase the proliferation of ADSCs *in vitro* in a dose dependent manner by Chen et al. [74]. Proliferation was assessed via MTT and trypan blue assays. Similarly, Van Pham et al. hypothesised that the previously reported upregulation of ADSC proliferation under hypoxia is partly due to the effect of VEGF [388].

However, Chen et al. also reported that examination of the effect of VEGF on human bone marrow MSCs and human umbilical cord stem cells did not reveal a similarly clear impact on proliferation, providing evidence

that the impact of VEGF upon proliferation is likely to be highly cell type dependent. In this thesis, any dependence of dADSC proliferation upon VEGF is neglected because there is currently no clear information on this specific relationship, and introducing a function reliant on VEGF into the cell proliferation term would increase the complexity of the model as well as introduce additional unknown parameter values.

Landman and Cai compared simulation results arising from the use of three different cell proliferation functional forms composed of a logistic growth function of cell density multiplied by different forms of dependencies upon oxygen, proportional to the consumption of oxygen [205]: firstly, a linear model as in Equation (3.15) with $f(c) = c$; secondly, a Michaelis-Menten model,

$$G(n,c) = \beta n \left(1 - \frac{n}{n_{\max}}\right)\left(\frac{Mc}{c_{1/2} + c}\right), \tag{3.18}$$

and finally a Heaviside step model:

$$G(n,c) = \mathrm{H}(c - c_p)\left(1 - \frac{n}{n_{\max}}\right). \tag{3.19}$$

This final form was found to approximate the results achieved by the Michaelis Menten function whilst permitting the use of analytical methods for further investigation of the model and derivation of important relationships.

Finally, Chung et al. used a modified Contois kinetics term to describe cell proliferation in a mathematical model of interactions between a cell population and glucose within a porous scaffold under perfusion [80]. This functional form integrates the effects of nutrient saturation and the amount of cells into one term:

$$G(n,c) = n\frac{Ac}{Bn + c}, \tag{3.20}$$

where A and B are the maximum proliferation rate and saturation coefficient respectively. This functional form determines that the cell growth

rate will be at its maximum when the nutrient, in this case glucose, is in sufficient supply. Galban and Locke found that this form achieved the best match against experimental data for chondrocyte growth in polymer scaffolds [125]. This functional form could also be applied to a scenario in which oxygen is the limiting nutrient for cell proliferation, as in mathematical model proposed in this project. However, it seems likely that the relationship between cell proliferation and oxygen concentration will be different to that between proliferation and glucose concentration.

The model developed in this thesis uses a cell proliferation term that increases linearly with oxygen concentration and incorporates a logistic function of cell density to take into account cellular competition for space and resources:

$$G = \beta c \left(1 - \frac{n}{n_{\max}}\right) . \tag{3.21}$$

Thus far, cell death has not been modelled using as wide a variety of functional forms as cell proliferation. Some authors of cell culture models have neglected to model the process of cell death explicitly [87, 205]. Lewis et al. justified this exclusion with the argument that cell death would be negligible during the initial phases of cell culture [217]. However, the viable cell density data presented in Section 3.3.3.1 clearly shows, for the higher initial cell densities, a reduction in the number of cells from the initial cell density to the 1 day and then 5 day time points. Therefore some variety of cell death function must be incorporated into the model presented in this thesis to replicate this result.

Pohlmeyer et al. used a constant cell death rate, assumed to account for all causes including natural death, low nutrient concentration, and in this specific case, very high local shear [319]:

$$F(n) = \delta n , \tag{3.22}$$

where δ is the cell death coefficient. This form was also used by Jones et al.

[177].

Another potential option for the cell death function F involves incorporating a non-linear function of nutrient or oxygen, c. This would represent increased cell death under hypoxia, for example, and could take the form of a tanh function, like Equation (3.2) used in Section 3.2. Yet this does introduce more parameters to the model.

Evidence provided by Sondell et al. suggests that VEGF could also reduce the amount of cell death [360]. TUNEL staining of mouse superior cervical ganglia and dorsal root ganglia exposed to 50 and 100 ng/ml of VEGF demonstrated a 20 to 43% reduction in the number of dead Schwann cells after 48 hours compared to controls. But as previously mentioned, the VEGF concentrations used in these experiments were higher than those observed in the *in vitro* experiments, and furthermore TUNEL staining only detects apoptotic cell death.

In line with previous work, in this thesis cell death is dictated by a linear function of n (Equation 3.22), although as detailed in Section 3.5 other cell proliferation and death functions of n and c were trialled during the course of model parameterisation. No functions of VEGF v were trialled due to a lack of information on the relationship between dADSCs survival and VEGF, as well as for simplicity. This is in line with the majority of previous similar work but could be expanded upon in the future.

3.4.2 Oxygen concentration governing equation

Spatio-temporal oxygen concentrations in tissue depend upon the diffusion of oxygen from sources such as vessels, and the consumption of oxygen by cells, which is represented in this thesis as a function Q:

$$\frac{\partial c}{\partial t} = D_c \frac{\partial^2 c}{\partial x^2} - Q \,. \tag{3.23}$$

In existing mathematical models, the oxygen consumption term Q is generally expressed as the product of a function of oxygen concentration c,

representing the consumption rate for a single cell, and the cell density n. This assumes that on average each cell consumes oxygen at the same rate, and also that this rate is dependent on the available oxygen concentration. Experimental evidence suggests that this is likely to be the case [144].

Several authors have implemented oxygen consumption as a simple linear function of both cell density and oxygen concentration [177, 205, 217],

$$Q(n,c) = Mcn\,. \tag{3.24}$$

Here M is the oxygen consumption rate parameter. Shakeel et al. also used this form coupled with a term representing shear stress [349]. However, Equation (3.24) does not take into account oxygen saturation as a rate limiting factor.

In contrast, the most commonly used function of oxygen concentration for the oxygen consumption term is the Michaelis Menten function, which enforces a limit to the increase in oxygen consumption caused by increases in oxygen concentration. Haselgrove et al. produced experimental evidence for this particular relationship between oxygen consumption and oxygen concentration, although only the oxygen consumption rate of chondrocytes was studied [144]. The Michaelis Menten function can also be coupled with a linear dependence upon the cell density:

$$Q(n,c) = n\frac{Mc}{c_{1/2} + c}\,. \tag{3.25}$$

Streeter and Cheema used a functional form similar to this to represent oxygen consumption in terms of a change in oxygen tension within a model of 3D cell-seeded collagen [367]. Combining a simple model of oxygen concentration with experimental data, they were able to derive cell type-specific oxygen consumption parameters. A number of other authors have used Michaelis Menten type oxygen consumption terms to model tissue culture within different types of bioreactor [21, 80, 84, 145, 281, 354, 421],

and this formulation was also used by Secomb et al. as part of a model of angiogenesis [347].

Some existing models assume that oxygen consumption is directly proportional to cell proliferation G, and thus have used the same function of oxygen in both of these terms [205, 217]. However, the relationship between the oxygen consumption rate and cell proliferation rate has not yet been studied in detail, and it is not necessarily the case that the two are directly proportional, especially as the oxygen consumption rate is also likely to be dependent upon other cellular processes on top of proliferation.

As previously mentioned, Landman and Cai compared the results given by linear, Michaelis-Menten and step-type functions of oxygen for both oxygen consumption and cell proliferation [205]. They found that the linear form resulted in a lower cell density throughout and consequently an absence of hypoxia in the scaffold, whereas both the Michaelis-Menten and step-type functions resulted in the appearance of a hypoxic region within the scaffold centre. Simulations run using the step function model were found to closely approximate the results of those run using the Michaelis Menten model, which suggests that the step function form could be used to simplify the mathematical framework and allow the derivation of analytical solutions, as demonstrated in the appendix of Landman and Cai's paper.

In some previous models [87, 314], the oxygen consumption rate M is directly coupled to the rate of cell proliferation to give a Monod-type model:

$$Q(n,c) = n\left(\frac{\mu_{\max}}{Y_n} + m_s\right)\frac{c}{c_{1/2}+c}\,, \tag{3.26}$$

where m_s is defined as the minimum concentration of oxygen per unit time required for cells to survive, $\mu_{\max}$ is the maximum cell proliferation rate, and the yield of cells per unit oxygen is denoted Y_n. Essentially, this is of the same form as the Michaelis Menten function but with $M = \frac{\mu_{\max}}{Y_n} + m_s$. However, this method of direct coupling does not limit cell proliferation at

high cell densities.

Finally, Pohlmeyer et al. did not incorporate oxygen specifically into their model, but did include a generic "nutrient" variable into their framework [319]. In this case, nutrient consumption by the cells was modelled by a logistic function to mirror the form of the nutrient-dependent cell proliferation term in the same framework as described by Equation (3.16), under the assumption that cell proliferation is proportional to nutrient consumption:

$$Q(n,c) = -Wn\left(1 - \frac{n}{n_{\max}(c)}\right). \tag{3.27}$$

All of the oxygen consumption terms considered in this subsection assume that the consumption of oxygen is independent of the concentrations of waste products. Cell type-specific attributes such as cell size, protein content [396] and metabolic characteristics will also affect the rate of oxygen consumption, but these differences are assumed to be incorporated into the model via the cell type-specific oxygen consumption parameters.

The Michaelis Menten form of oxygen consumption term, Equation (3.25), has been used numerous times in previous models with success, and is backed up by some experimental evidence. For these reasons, this form will also be used in the model described in this thesis.

3.4.3 VEGF concentration governing equation

Currently, there are several known mechanisms that may help to produce VEGF gradients *in vivo*, including diffusion, matrix sequestering and degradation [392]. Here it is proposed that the key elements of the governing equation for the VEGF concentration, v, should be diffusion of VEGF, a VEGF production term S, and a VEGF decay term:

$$\frac{\partial v}{\partial t} = D_v \frac{\partial^2 v}{\partial x^2} + S - d_v v\,. \tag{3.28}$$

The natural degradation of the VEGF protein is modelled in this way by most existing theoretical frameworks [23, 46, 166, 236, 391], and will also

be incorporated in the model described in this thesis.

Some models also incorporate a VEGF consumption term to represent the uptake of VEGF by tip endothelial cells during angiogenesis [23, 166]. Although this could be incorporated into the framework as part of the model of angiogenesis in response to VEGF gradients described in Chapter 5, it is assumed that the therapeutic cells seeded in the NRCs do not take up VEGF, and therefore a VEGF consumption term is not incorporated into the continuous cell-solute model described in this thesis.

As briefly mentioned in Section 2.1.3, evidence suggests that cellular VEGF expression is at least partly regulated by environmental oxygen concentration. A range of studies have demonstrated up-regulation of VEGF mRNA under hypoxic conditions [262, 266, 357], which could indicate a corresponding increase in VEGF protein. Lafosse et al. explicitly measured an increase in VEGF production under hypoxia (0.1%) for three different cell types [201]. Thus far evidence suggests that the magnitude of response to hypoxia varies with cell type. Although dADSC-specific VEGF secretion data are not currently available, existing research on other cell types can be used as a guide to inform the functional form and qualitative nature of dADSC oxygen concentration-dependent VEGF secretion.

A study by Leith and Michelson published in 1995 provides some quantitative evidence for the dependence of cancer cell line VEGF secretion upon oxygen [211]. They explored how the *in vitro* VEGF secretion rates of clone A and HCT-8 human colon tumour cells, placed in glass bottles with 50 ml of media, responded to different oxygen concentrations varying from 0.01% to 21%. The bottles were gassed for 22h in total. The cell lines were seeded in the bottles with an initial cell density of 2×10^4 cells/cm^2, and proliferation was measured and controlled for. The results suggested a sigmoidal relationship between log VEGF concentration and log oxygen concentration for both lines of cells. However, only one initial cell density was tested in this way. Furthermore, the magnitude of response differed

between the two cell lines, particularly at high oxygen concentrations. The clone A cells exhibited a 17 fold increase in VEGF secretion between the 21% and 0.01% oxygen levels, whereas the HCT-8 cells' VEGF secretion increased by a factor of 80. Therefore it is reasonable to propose that the shape of the VEGF secretion-oxygen dependency for the cell line of interest for this project, dADSCs, may be sigmoidal, but the magnitude of the increase in VEGF cannot be informed by this study.

However, in a later study Chiarotto and Hill [75] questioned the methodology of Leith and Michelson. They claimed that the depth of media used in the Leith and Michelson experiments would result in the appearance of an oxygen gradient, induced by cellular respiration, thus casting uncertainty on the exact oxygen concentration exposure of the cells. Chiarotto and Hill also set out to quantify the relationship between VEGF secretion and hypoxia, and in fact provided further evidence for a sigmoidal relationship between these two solutes during their investigation.

VEGF mRNA levels were measured at 0, 2 and 4 hours in three cervical cancer cell lines, under different oxygen concentration levels, again varying from 21% down to below 10 ppm (approximately 0%). In contrast to the Leith and Michelson experiments, oxygen levels in the medium were measured directly using an electrode. The data sets were plotted and fitted to logistic functions, and the resulting figures suggested that the VEGF mRNA level can be approximated as a sigmoidal function of the oxygen concentration, corroborating the results presented by Leith and Michelson. The rate of hypoxia-induced increase in mRNA levels, and subsequently the oxygen concentration at which the VEGF mRNA reached half of the maximal upregulation, differed between cell lines. However, it was tentatively suggested that VEGF mRNA probe inaccuracies could account for some of these differences. Additionally, the exact relationship between VEGF mRNA levels and VEGF protein levels is unclear, which limits the use of this study.

Furthermore, due to the use of cancer cell lines and the possible influence of differences between the behaviour of cancerous and healthy cells under hypoxia, these results can only be used to loosely form hypotheses regarding oxygen-dependent VEGF expression of dADSCs. However, together with existing models of VEGF secretion, they form a starting point for model development.

Existing mathematical models of VEGF secretion have used a few different functional forms for the secretion term S. Maggelakis and Savakis used a simple linear function to describe the non-uniform relationship between VEGF production and oxygen concentration c [236]:

$$\frac{\partial v}{\partial t} = \begin{cases} 1 - c_0/c, & c \leq c_h\,, \\ 0, & c > c_h. \end{cases} \tag{3.29}$$

This function determines that when the oxygen level falls below a certain threshold c_h, the VEGF production increases; otherwise, it is 0. Although this model does capture a general dependency of VEGF secretion on oxygen, it is neither informed nor validated by any experimental data.

In 2011, Aubert et al. also adopted this form of VEGF secretion function in their mathematical model of angiogenesis in the retina of a mouse, replacing the direct dependency upon oxygen concentration with a dependency upon oxygen-carrying capillary density [23].

In a 3D computational model of skeletal muscles [232], the VEGF secretion rate S from the myocytes was defined by Mac Gabhann et al. as a function dependent on the average oxygen tension PO_2 in the surrounding tissue:

$$S = \begin{cases} \alpha, & PO_2 \geq 20\,\text{mmHg} \\ \alpha\left[1 + 5\left(\frac{20 - PO_2}{19}\right)^k\right], & 1 < PO_2 < 20\,\text{mmHg} \\ 6\alpha, & PO_2 \leq 1\,\text{mmHg}. \end{cases} \tag{3.30}$$

Here the basal secretion rate is denoted α, and k determines the shape of the VEGF secretion curve. The same function was used in two further

publications [174, 231], and the shape of the function was motivated by experimental evidence [176, 375].

Equation (3.30) has a similar shape to the functions used in the Maggelakis and Savakis and Aubert et al. models, with the exceptions that VEGF secretion at high oxygen tensions remains at a low, constant non-zero rate instead of reducing to zero, and that the VEGF secretion rate is capped at a constant for oxygen tensions below the 1 mmHg threshold. A tanh function as used in the proof of concept model (Section 3.2) could also be used to approximate the same general pattern as Equation (3.30) as follows:

$$S = \alpha n \left(\frac{V_m + 1}{2} - \frac{V_m - 1}{2} \tanh k_\alpha (c - c_h) \right). \tag{3.31}$$

Here V_m is the VEGF secretion multiplier and α is the baseline VEGF secretion rate at high oxygen concentrations: the maximum VEGF secretion rate per cell per unit volume is therefore $V_m \alpha$. Whilst this function maintains the general experimentally informed shape of the VEGF secretion curve set out by Mac Gabhann et al., it is proposed that the smooth nature of this function means that it is likely to be a closer approximation to the true biological relationship than Equation (3.30). Therefore this tanh function VEGF secretion curve will be implemented as part of the model described in this thesis.

3.4.4 The impact of local cell density upon diffusion

As the cell density within an engineered tissue increases, the volume of cells could begin to obstruct the diffusion of oxygen, VEGF and other solutes through the water phase, assuming that there is no intra-cellular transport. This effect can be incorporated into the mathematical model through the use of an effective diffusion coefficient, which takes into account the impact of the cellular obstructions on diffusion.

The effective diffusivity of oxygen and VEGF in a cell-seeded scaffold can be calculated by multiplying the standard scaffold or material diffusiv-

ities D by a porosity coefficient K:

$$D_{\text{eff}} = K(\rho)D\,. \tag{3.32}$$

Here ρ is defined as the fractional volume of scaffold absent of cells, i.e. the fractional volume of unobstructed gel. The use of porosity coefficients is explained in more detail in Section 4.2.2.

Croll et al. found that altering the rate of diffusion of oxygen according to the number of cells in this manner had a negligible impact upon the results of their computational study, unless the cell density was very high [87]. The authors suggested that for cells of relatively small diameter (10-20 µm), the effect of cell density upon the diffusion coefficients could be neglected whilst the cell density remained low ($< 10^7$). Similarly, Landman and Cai also chose to neglect this effect [205].

In the case of this thesis, the maximum cell density $n_{\max}$ is set at 400×10^6 cells/ml or 400×10^{12} cells/m^3 (Section 3.5.1.1) corresponding to the maximum cell densities measured in the *in vitro* experiments. Here it is assumed that a typical spindle shaped dADSC can be modelled as an impermeable cylinder with a length of 40 µm and a diameter of 3 µm, as estimated from imaging data published by Kingham et al. [188]. The minimum fractional volume of scaffold absent of cells, $\min\rho$, can then be calculated as follows, where $\max c_{\text{vol}}$ is defined as the maximum volume occupied by cells per m^3 volume:

$$\begin{aligned}\min\rho &= 1 - \max c_{\text{vol}} \\ &= 1 - \frac{\pi \times (1.5 \times 10^{-6})^2 \times (40 \times 10^{-6}) \times 400 \times 10^{12}}{1} \\ &\approx \frac{89}{100}\,.\end{aligned}$$

This corresponds to a scaffold in which only approximately 11% of the space is occupied by cells and is therefore still predominantly unob-

structed. A commonly used form of the function $K(\rho)$ is that proposed by Millington and Quirk [261],

$$K(\rho) = \rho^{4/3} .$$

Other forms of porosity coefficient functions K are explored in more detail in Section 4.2.2 in the context of modelling a porous NRC sheaths; here the Millington-Quirk expression for K is used for illustration. Using the previous calculation for $\min \rho$,

$$\min K(\rho) = \left(\frac{89}{100} \right)^{4/3} \approx 0.86 ,$$

so the effective diffusion coefficients at the maximum cell density will be around 86% of the molecular diffusion coefficients. In fact, the recorded cell densities in the *in vitro* experiments were on the whole far less than the maximum cell density recorded, and therefore the impact of cellular obstruction on the effective rate of diffusion would be even less in the majority of cases.

In line with these calculations and in corroboration with the results of Croll et al., simulating the final parameterised model with and without the use of a Millington and Quirk model porosity coefficient K produced almost identical results. Therefore it was concluded that incorporating the effect of cellular obstruction to diffusion is unnecessary in this case, but could easily be incorporated into future versions of the framework.

3.4.5 The general mathematical framework

The functional forms of the proof of concept model were altered according to the preceding review of experimental research on the relationships between the relevant variables and existing theoretical models of similar systems (Sections 3.4.1, 3.4.2, 3.4.3 and 3.4.4), as well as analysis of the *in vitro* data (Section 3.3.3), to create a general framework for the cell-solute

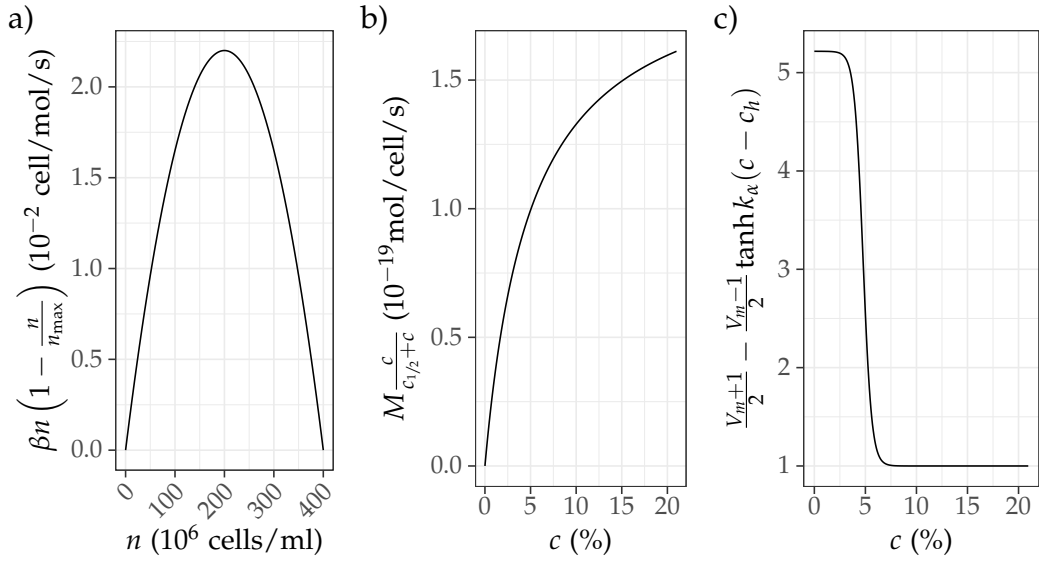

Figure 3.12: Plots of the main non-linear functions that make up the terms of the cell-solute model. All parameter values not explicitly stated here are assigned according to Tables 3.9 and 3.10. a) Cell proliferation term dependence on cell density n. b) Oxygen metabolism term dependence on oxygen concentration c. c) VEGF secretion term dependence on oxygen concentration c, with VEGF secretion multiplier $V_m = 5.217$.

model. This eventually resulted in a final general form of the mathematical framework as follows:

$$\frac{\partial n}{\partial t} = \beta c n \left(1 - \frac{n}{n_{\max}}\right) - \delta n \,, \tag{3.33}$$

$$\frac{\partial c}{\partial t} = D_c \nabla^2 c - M n \frac{c}{c_{1/2} + c} \,, \tag{3.34}$$

$$\frac{\partial v}{\partial t} = D_v \nabla^2 v + \alpha n \left(\frac{V_m + 1}{2} - \frac{V_m - 1}{2} \tanh k_\alpha (c - c_h)\right) - d_v v \,. \tag{3.35}$$

Note that the functional forms and parameters of the equations can be removed or altered respectively according to the material properties of the geometry that it is applied to, as demonstrated in the case of the *in vitro* well scenario in Section 3.5.1, and later in this thesis for a geometry representing a tissue engineered NRC (Chapter 4). Some of the key functions that make up the terms of these equations are plotted in Figure 3.12.

3.5 Model simulation and parameterisation

This section describes the parameterisation of the model framework, composed of Equations (3.33), (3.34) and (3.35), against the *in vitro* data. This begins in Section 3.5.1 with the adaptation of the framework for application to a geometry representing the *in vitro* well via the removal of unnecessary governing equation terms in specific regions of the geometry, the application of boundary conditions representing the experimental set up, and the identification of probable parameter values and ranges and key unknown parameters.

Subsequently, the finite element software COMSOL Multiphysics is introduced in Section 3.5.2, and an explanation of the built in solver used to run the model simulations is provided. Additionally, the well geometry and mesh generated in COMSOL and used for parameterisation are described in this subsection.

The general method used for parameterisation of all three governing equations within COMSOL is then explained in Sections 3.5.3. The following final subsections, Section 3.5.4 and Section 3.5.5, describe the process of parameterisation for the cell density and oxygen concentration governing equations and then the VEGF concentration governing equation respectively.

3.5.1 Application of the model to an *in vitro* well geometry

The *in vitro* well geometry is composed of two subregions: the cell-seeded collagen gel at the bottom of the well, and the media above it (Figure 3.3). The form of each governing equation within the general framework outlined in Section 3.4.5 is adapted in this subsection to match the differences between these subregions, and boundary and initial conditions are also described. Where possible, parameter values and constraints for the parameterisation of the governing equations are approximated using existing values from the literature, and key unknown parameters are highlighted in preparation for parameterisation. The final parameter values obtained via

this process are summarised in Tables 3.9 and 3.10.

3.5.1.1 Cell governing equation and parameter estimates

The cells are situated in the gel portion of the geometry only, and their behaviour is described using the following governing equation:

$$\frac{\partial n}{\partial t} = \beta c n \left(1 - \frac{n}{n_{\max}}\right) - \delta n \,. \tag{3.36}$$

A zero flux boundary condition is applied on the boundary between the gel and the media, as well as at the well walls and base. Uniform initial cell densities are used according to the experimental values; it is assumed that the cells are initially uniformly distributed throughout the gel because during the experimental procedure the cell solution was thoroughly mixed before being pipetted into the wells (Section 3.3.2.2).

The maximum cell density $n_{\max}$ is set at 400×10^6 cells/ml to approximate the maximal value observed in the experimental data (Figures 3.5 and 3.6).

Cell proliferation β and death δ rates have been estimated for other cell types in the past. These estimations are scarce but can act as a guide as to the approximate order of magnitude for these parameters. In the case of the cell proliferation rate, Lewis et al. used $\beta = 1.27 \times 10^{-5}$ $m^3/mol/s$ in their 1D mathematical model of chondrocyte proliferation within engineered cartilaginous construct [217], which was parameterised informally against experimental data. Burova et al. derived a range of 3.5 to 9×10^{-5} $m^3/mol/s$ for β by fitting a theoretical model of osteoblast growth against *in vitro* data [56]. These values correspond to maximum cell proliferation rates of 2.54×10^{-6} and 0.7 to 1.8×10^{-5} s^{-1} respectively at an oxygen concentration of 0.2 mol/m^3.

Elsewhere a maximum proliferation rate of 1.52×10^{-5} s^{-1} has been used as part of cell proliferation mathematical models [84, 349], although the method of derivation for this parameter is unclear. Similarly, Sacco et

al. used a maximum cell proliferation rate of 8×10^{-6} s^{-1} [338]. Croll et al. reviewed experimentally derived maximal cell proliferation rates and reported a range of 3 to 4.5×10^{-6} s^{-1} [87].

Cell death rates reported thus far in the literature include 1.3 to 5030×10^3 cells/m^2/s [56], and 3.3×10^{-7} s^{-1} [79]. However, the cell types and contexts used in all of these studies vary widely and none correspond directly to the scenario of interest in this thesis (dADSCs seeded in type I collagen gel). Therefore both the cell proliferation rate β and the cell death rate δ are key unknown parameters.

3.5.1.2 Oxygen governing equation and parameter estimates

The continuous distribution of oxygen is governed by two different equations, corresponding to the gel and media sub-geometries. Boundary conditions are used to enforce continuity of oxygen concentration at the interface between the gel and the media, and between the media and the external environment with its controlled ambient oxygen level, c_a. Zero flux conditions are applied at the well walls and base. Initial conditions within the gel and water are set to the initial value measured via the oxygen probe (18%). Within the media, the equation takes the form:

$$\frac{\partial c}{\partial t} = D_{c_m} \nabla^2 c \,, \tag{3.37}$$

where D_{c_m} is the diffusion coefficient for oxygen in the media. Alternatively, within the gel the additional Michaelis-Menten term governs the oxygen consumption rate by the resident cell population as follows:

$$\frac{\partial c}{\partial t} = D_{c_g} \nabla^2 c - Mn \frac{c}{c_{1/2} + c} \,. \tag{3.38}$$

In this case, D_{c_g} is the diffusion coefficient for oxygen in the gel.

Using the assumption that the diffusion rate of oxygen through culture media is approximately equal to the diffusion rate through water, D_{c_m} is assigned a value of 2.624×10^{-5} cm^2/s. This was calculated using a inter-

polation formula for aqueous oxygen diffusion coefficients [142], assuming a constant temperature of 37°C as regulated by the incubator used during the *in vitro* experiments.

Oxygen diffusion rates in acellular collagen gels, with defined collagen densities, have been explicitly characterised in experiments by Cheema et al., providing a value of $D_{c_g} = 4.5 \times 10^{-6}$ cm^2/s [71]. As expected, this rate of diffusion is slower than that through the media. It is assumed that the obstruction to diffusion caused by cells is negligible, as per Section 3.4.4.

The oxygen concentration at which oxygen consumption is half maximal $c_{1/2}$ is assigned a value of 6.66×10^{-9} mol/ml (equivalent to 0.506%) according to unpublished model fitting conducted by R. Shipley. This is in accordance with research by Chow et al. that suggests that the value of $c_{1/2}$ for human cells should lie between 0.2 and 7×10^{-9} mol/ml [78]. Streeter and Cheema used a similar value of $c_{1/2} = 5.6$ mmHg, equivalent to approximately 0.737%, in their model. As noted by Streeter and Cheema, the parameter $c_{1/2}$ only affects the rate of oxygen consumption at very low oxygen concentrations [367].

Finally, values for the maximal rate of oxygen consumption per cell M for various cell types found in the literature were used to construct bounds on this parameter in advance of parameterisation. Recorded oxygen consumption rates vary widely across cell types, including estimates of 7.91×10^{-18} mol/cell/s for human bone marrow derived stromal cells [367]; 2 to 140×10^{-19} mol/cell/s for lymphocytes [78]; 1.04 to 6×10^{-17} mol/cell/s for human dermal fibroblasts [76, 144, 147, 367]; and a range of 2.5 to 9.1×10^{-16} mol/cell/s for porcine hepatocytes [29], among other values [78, 87]. No specific value has thus far been recorded for dADSCs. Therefore the lower and upper bounds for the value of M were assigned at 2×10^{-19} mol/cell/s and 9.1×10^{-16} mol/cell/s respectively according to the available data and estimates for other cell types.

3.5.1.3 VEGF governing equation and parameter estimates

Two governing equations corresponding to the media and gel portions of the geometry are used to describe the development of the VEGF concentration distribution with time. Boundary conditions enforce continuity of VEGF concentration at the interface between the gel and the media, allowing diffusion from one into the other. Zero flux conditions are applied at the well walls and base, as well as at the surface of the media. The initial VEGF concentration was set at zero in both the gel and the media. In the media,

$$\frac{\partial v}{\partial t} = D_{v_m} \nabla^2 v - d_v v. \tag{3.39}$$

Here D_{v_m} is the diffusion constant of VEGF in the media, and d_v the decay rate of the VEGF protein. In the gel, an additional term is introduced to model the production of VEGF by the viable cell population:

$$\frac{\partial v}{\partial t} = D_{v_g} \nabla^2 v + \alpha n \left(\frac{V_m + 1}{2} - \frac{V_m - 1}{2} \tanh k_\alpha (c - c_h) \right) + d_v v \,, \tag{3.40}$$

where D_{v_g} is the diffusion constant of VEGF in the gel, α the baseline VEGF secretion rate per cell, V_m the VEGF secretion multiplier and k_α the VEGF secretion gradient constant.

The diffusivity of VEGF in the media is one of the least uncertain parameters in the VEGF governing equation due to estimates offered by various theoretical and experimental papers. Some mathematical modelling attempts have drawn upon the correlation between molecular weight and diffusivity to calculate VEGF diffusivity values [40]. In 2005 Mac Gabhann et al. used this to calculate an aqueous diffusion coefficient of 2×10^{-6} cm^2/s for VEGF [230]. In a different paper in 2007, Mac Gabhann et al. combined the correlation with the Stokes-Einstein equation to adjust values to match the desired temperature of 37°C [232]. This provided aqueous diffusivities of 1.42×10^{-6} cm^2/s for VEGF_{120} and 1.33×10^{-6} cm^2/s for VEGF_{164}, and a value in this range $D_{v_m} = 1.37 \times 10^{-6}$ cm^2/s was chosen as

the VEGF diffusivity in media for the current model. Again it is assumed that diffusion through the media is equivalent to aqueous diffusion.

VEGF protein diffusion in collagen and similar materials has also previously been calculated by fitting to *in vitro* experimental data. Kohn-Luque et al. determined the diffusion coefficient of VEGF in Matrigel absent of seeded cells to be $5.87 \pm 2.1 \times 10^{-7}$ cm^2/s by fitting to fluorescence data [191]. Experiments conducted by Nunez specifically designed to measure the diffusion coefficient of $VEGF_{121}$ in collagen also resulted in a value close to this range, 5.55×10^{-7} cm^2/s [280]. Mac Gabhann et al. predicted a diffusivity of 1.13×10^{-6} cm^2/s for $VEGF_{120}$ in skeletal muscle ECM. Overall a range of 5.55×10^{-7} to 1.13×10^{-6} cm^2/s was identified and these values were used as bounds for D_{v_g} during parameterisation.

The VEGF protein decay rate, or half life, is a result of proteolysis and does not include VEGF uptake by cells such as endothelial cells. Cited values range from a half life of 3 minutes in blood [120] to 72 hours in culture media, as measured by VEGF ELISA [191]. Other values lie in between. Kleinheinz et al. measured a half life of 90 minutes for $VEGF_{165}$ in aqueous solution, and theorized that the half life of VEGF in collagen could be around 48 hours from indirect experimental evidence [189]. Lanza et al. quote a half life of 30 minutes for VEGF in tissue [207]. These estimates indicate that the half life varies according to context, suggesting that d_v should also be derived via parameterisation. The bounds used for this were 3.85×10^{-4} and 2.67×10^{-6} s^{-1}, corresponding to half lives of 30 minutes and 72 hours respectively.

The remainder of the parameters within the VEGF governing equation relate to the secretion of VEGF by the cells, in this case dADSCs. VEGF secretion in response to oxygen is highly cell type dependent, and therefore all of these parameters need to be refined via parameterisation. However, existing values corresponding to other cell types can be used to inform this process of parameterisation.

Some of the existing secretion rates reported in the literature were not measured as secretion per cell but as secretion per mass of tissue, rendering them less useful for the purpose of this model. For example, Zhang et al. quantified the VEGF secretion rates of cells from the omentum and pituitary of rats: cells from the omentum were found to have the highest secretion rate, 362.51 ± 14.63 pg/g tissue/h, but values ranged from this to 6.45 ± 1.33 pg/g tissue/h for retroperitoneal adipose tissue [419].

Kelm et al. quantified the VEGF production rate of a variety of human cell lines and primary cells [186]. The values were calculated from both cell monolayers and microtissues, and ranged from 0.09 ± 0.011 ng/h/cell for human articular chondrocytes to 1.55 ± 0.231 ng/h/cell for human fibrosarcoma cell, both in microtissue. Mick et al. measured the VEGF secretion over 12 hours of adipocytes (294 ± 87 pg/10^6 cells/12 h, equivalent to 24.5 ± 7.25 pg/10^6 cells/h) and stromal cells (200 ± 96 pg/10^6 cells/12 h, equivalent to 16.67 ± 8 pg/10^6 cells/h) [259].

Leith and Michelson measured VEGF secretion rates for clone A and HCT-8 human colon tumour cells in a range of oxygen conditions [211]. In 21% oxygen, a secretion rate of 41.3 to 94.5 pg/10^6 cells/h was recorded for the clone A cells, and a rate of 3.7 to 6.9 pg/10^6 cells/h for the HCT-8 cells.

However, these experimental procedures do not take into account the rate of VEGF decay which is one of the mechanisms incorporated into the model, so the figures mentioned above can only act as a guide for the magnitude of the parameter α. Mac Gabhann et al. estimated secretion rates of 0.25×10^{-17} pmol/μm^2/s for $VEGF_{164}$ and 2.95×10^{-7} pmol/μm^2/s for $VEGF_{120}$ by matching a mathematical model to *in vivo* measurements of unbound VEGF in human skeletal muscle [232].

Overall, although these various estimates may give an indication as to the likely range of VEGF secretion, differences in cell type and context mean that no specific values can be taken forward for use in the model.

It is well established that VEGF secretion by cells increases in hypoxic conditions, but the degree to which this occurs is still unknown. The maximum fold increase in VEGF secretion that occurs as the oxygen concentration drops, as illustrated in Figure 3.12, is V_m as dictated by Equation (3.31). Zhang et al measured a 1.7 fold increase in the expression of VEGF protein by rat omental adipocytes under hypoxic conditions [419]. Mac Gabhann et al. incorporated a 6 fold increase into their model [232], and Tang et al. reported a fold increase in VEGF protein of 2.2 ± 0.4 under hypoxia *in vivo* [375]. Leith and Michelson reported a 7 fold and 75 fold increase in VEGF production under hypoxia for clone A cells and HCT-8 human colon tumour cells respectively [211]. From these values it is assumed that the value of V_m for the dADSCs modelled in this thesis will lie between 1 and 75, and it seems likely that $V_m < 10$ in line with values for other non-cancerous cells.

The VEGF secretion gradient constant k_α determines the rate of increase in VEGF secretion as environmental oxygen concentration decreases. This parameter is not measured quantitatively anywhere in the literature and therefore will be determined as part of the parameterisation process.

Finally, c_h determines the oxygen concentration below which VEGF secretion increases. This is again unknown, although likely to be below 5% as per the previously described research conducted using other cell types [75, 201, 211].

3.5.2 Simulation method

The finite element modelling software COMSOL Multiphysics (version 5.2a) was used to simulate and parameterise the model. This software allows the user to enter and solve systems of coupled partial differential equations, such as the model presented in this report. COMSOL has been used previously to solve other published models similar to that described in this thesis [80, 349].

The backward differentiation formula (BDF) method, implemented in-

ternally by the COMSOL software, was used to solve the differential equations that make up the model. A BDF solver approximates the derivative of a variable y at a time t_j in terms of the values of the function y at t_j and previous time steps: suppose that we have the initial value problem

$$y' = \frac{\partial y}{\partial t} = f(t,y)\ ,\ \ y(t_0) = y_0; \tag{3.41}$$

then $y(t)$ can be approximated using the Lagrange interpolation polynomial of order k, which is a function of k evaluations of $y(t)$ at t_j and earlier time points. Differentiating this polynomial and evaluating it at $t = t_j$ gives the following BDF formula in the case of constant step size $h = t_j - t_{j-1}$ for all j so that $t_n = t_0 + nh$:

$$hy'_j = \sum_{i=0}^{k} a_{ki} y_{j-i} \tag{3.42}$$

Here the coefficients a_{ki} are specific to the order of the BDF method used. BDF methods are generally known for their stability.

COMSOL Multiphysics implements a variable order and step size version of the BDF method. The solver uses the highest order up to a maximum set by the user when possible, but automatically implements a lower order BDF when an increase in stability is required. For the simulations in this thesis, the maximum order was set at $k = 2$. Default "Free" time stepping was used, which permits the solver to use variable time steps within the range specified by the user to satisfy the tolerance. For all simulations in this thesis, a minimum time step of 0.001h was used; the maximum time step was varied.

3.5.2.1 The COMSOL *in vitro* well geometry

An axisymmetric 2D geometry representative of a well from a 96-well plate, as used during the *in vitro* experiments and depicted in Figure 3.3, was created within COMSOL to enable parameterisation against the experimental data. A thin slice at the bottom of the geometry represents the seeded cell gel, with the remaining geometry representing the media-filled portion of

the well. Measurements of the gel thickness and volume of the media were used alongside known dimensions of the wells to accurately recreate the experimental set up in COMSOL.

A fine mesh was generated to cover this geometry, containing a total of 8032 triangular elements automatically generated with a maximum element size of 0.4 mm, with a more refined mesh at the geometry boundaries and in the section representing the gel (Figure 3.13). Simulations were subsequently run over this 2D axisymmetric geometry, presented as a 3D well in COMSOL. Mesh refinement at the boundaries and in the section of the geometry representing the gel was required for the model to reach convergence. Further mesh refinement studies have been performed, but made no detectable difference to the simulation values.

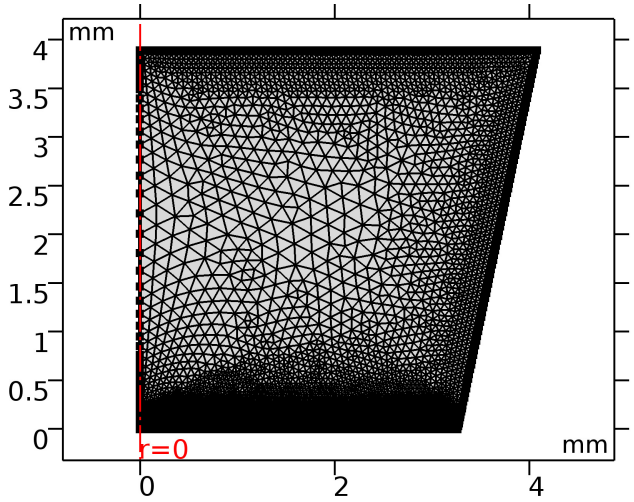

Figure 3.13: Cross section of the mesh generated over the axisymmetric well geometry in COMSOL. The maximum element size in the gel portion of the geometry was set at 0.03 mm; along the top and outside edge of the well (angled edge in this figure) the maximum element size was set at 0.05 mm. Elsewhere, in the section of the geometry representing the culture medium, the maximum element size was set at 0.4 mm. The minimum element size over the whole geometry was set at 4.61×10^{-4} mm. In total, the mesh contains 8032 triangular elements.

The size of the mesh was not prohibitive to simulation completion time. The completion time for each simulation did depend upon the time step size and the number of metrics, such as averages and standard devia-

tions of variables over the geometry, that were calculated by COMSOL. A maximum time step size of 0.1h was required to reach convergence, and this was used throughout the model fitting process. After these considerations, a typical simulation of a 24h period had a maximum run time of around 3 minutes, but more commonly the run time was under 30 seconds.

3.5.3 Parameterisation method

The *in vitro* data set for the 1 day time point was split into a training subset and a validation subset. The training subset S_T consists of the mean viable cell densities in the gel n_{exp} and the mean VEGF concentrations in the media v_{exp} for $n_0 = 39$, 154 or 385×10^6 cells/ml; the validation subset S_V consists of the corresponding data with $n_0 = 77$ or 231×10^6 cells/ml. The mean values referred to here are shown in black in Figures 3.5 and 3.7. The 5 day time point data was not used for parameterisation due to time constraints, but was used for further validation of the model in Section 3.6.

Parameterisation of the model was carried out in two stages. First, the mutually dependent governing equations for the viable cell density and oxygen concentration were parameterised, using the 15 mean viable cell density data points in S_T. Secondly, the VEGF governing equation was parameterised using the 15 mean VEGF concentration data points in S_T in conjunction with the previously attained parameterised cell-oxygen equations.

The SNOPT or sparse nonlinear optimizer solver [137] was used to minimise a different least squares objective function at each of the two stages of parameterisation (LS_n for the viable cell density and oxygen concentration equations parameterisation step, and LS_v for the VEGF concentration equation parameterisation step):

$$\text{LS}_\text{n} = \sum_{n_{\text{exp}} \in S_T} (n_{\text{exp}} - \bar{n}_\text{g})^2 \,, \tag{3.43}$$

$$\text{LS}_\text{v} = \sum_{v_{\text{exp}} \in S_T} (v_{\text{exp}} - \bar{v}_\text{m})^2 \,. \tag{3.44}$$

These objective functions are the sum of the squared differences between the 15 mean experimental data points (either $n_{\text{exp}} \in S_T$ or $v_{\text{exp}} \in S_T$) and the corresponding simulated values for the mean viable cell density over the gel, denoted $\bar{n}_{\text{g}}$, and the mean VEGF concentration over the media, denoted $\bar{v}_{\text{m}}$, after 1 day, calculated by running the model using the same initial conditions (initial cell density n_0 and ambient oxygen concentration c_{a}) as the corresponding experimental data points.

The SNOPT algorithm is commonly used to solve non-linear problems with constraints. The SNOPT solver was selected for the parameterisation of the model because it can take into account many different constraints; conversely, although the Levenberg-Marquadt solver is designed specifically for least-squares problems such as this, it cannot incorporate constraints. In this thesis, control parameters are defined as the unknown parameters that are derived via parameterisation using the SNOPT algorithm. Where upper and lower bounds for control parameters had been identified in Section 3.5.1, these were implemented as constraints for the SNOPT algorithm.

3.5.4 Cell density and oxygen governing equations parameterisation

The viable cell density and oxygen concentration governing equations were parameterised together first because they are interdependent, but are not dependent upon the VEGF concentration governing equation.

In Section 3.5.1, β, δ and M were identified as the key unknown parameters in the cell and oxygen governing equations and were therefore used as control parameters during the first stage of parameterisation. All other parameters in these governing equations were assigned values according to the previous review of the literature, as presented in Table 3.9.

Parameter sweeps were carried out over orders of magnitude of the control parameters to identify parameter spaces that would give feasible simulation results when compared to the data set. These also gave an in-

dication of the impact of individual parameters upon the results of the simulations, although it was difficult to interpret these results due to the complexity of the mathematical framework and the multiplicative interactions between some of the parameters.

Initial attempts at parameterisation revealed that the model was able to capture the relationship between the simulated mean viable cell density over the gel $\bar{n}_{\mathrm{g}}$ and the ambient oxygen concentration c_{a}, but did not demonstrate any relationship between $\bar{n}_{\mathrm{g}}$ and the initial cell density n_0. This is not in accordance with the experimental data, which did exhibit some dependence of the final viable cell density upon n_0, and it was clear that further work was needed to ensure that the model reflected this relationship.

Different functional forms with various dependencies upon n were trialled in further attempts to achieve a greater dependency of $\bar{n}_{\mathrm{g}}$ upon n_0. This included a cell death function of the form

$$F(c,n) = \delta \frac{n}{2}[1 - \tanh(k_\delta(c - c_d))] \,, \tag{3.45}$$

which incorporates greater cell death in low oxygen environments, with c_d representing the hypoxic oxygen threshold for increased cell death, but this did not provide an improvement to the model fit to the data. Consequently the cell governing equation eventually remained in the form set out in Equation (3.33).

It was therefore decided that the training data set should be split into three sets according to the three different initial cell densities, and optimisation should be run on each of these sets individually. Subsequently, any differences between the optimised values of β and δ across the data sets could give some indication of how the functional forms of the equations could be altered to give a more generalised model.

It became clear that the equations in their current form did not capture the difference in results across the different initial cell densities. Therefore

it was necessary to determine δ as a function of n_0,

$$\delta(n_0) = \delta_0 + \delta_1 n_0 \,,$$

essentially introducing an extra parameter in order to achieve a better fit to the data.

3.5.5 VEGF governing equation parameterisation

In Section 3.5.1, D_{v_g}, d_v, c_h, k_α, α and V_m were all identified as unknown parameters in the VEGF governing equation and were therefore used as control variables for the second stage of parameterisation.

Parameter sweeps revealed that in order to obtain mean VEGF concentrations across the media after 1 day close to the experimental means, the VEGF diffusion rate through the gel would have to be as large as possible within the constraints laid out in Section 3.5.1.3. This is because the VEGF, which is produced in the cellular gel portion of the geometry, needs to diffuse into the media before it decays in order to influence the value of $\bar{v}_{\mathrm{m}}$. Therefore $D_{v_g} = 1.13 \times 10^{-6}$ cm^2/s, at the upper bound of the limits set out in Section 3.5.1.3 for this parameter. Decreasing the decay rate would also facilitate higher VEGF concentrations in the media, but would result in unrealistically high VEGF concentrations in the gel.

After initial parameterisation attempts, again it was found that in order to achieve a good fit to the experimental data points v_{exp} it was necessary to introduce parameters as functions of n_0 into the governing equation.

As with the parameterisation of the oxygen and cell governing equations, the VEGF experimental data set was split into three sets corresponding to the three different initial cell densities. Parameterisation was conducted on each of these separately to assess the similarities and differences. It was found that the parameters c_h, d_v and k_α differed the least across these three sets; therefore these parameters were assigned by averaging over the three optimal values. This left only α and V_m as unknown

Cell density equation parameters	
Proliferation rate†	$\beta = 2.2 \times 10^{-4}$ m^3/mol/s
Cell death rate†	$\delta(n_0) = \delta_0 + \delta_1 n_0$ 1/s $\delta_0 = 1.1334 \times 10^{-5}$ 1/s $\delta_1 = 9.1256 \times 10^{-14}$ ml/cell/s
Maximal cell density[2]	$n_{\max} = 4 \times 10^8$ cells/ml
Oxygen concentration equation parameters	
Diffusion coefficient for oxygen in media*	$D_{c_m} = 2.624 \times 10^{-5}$ cm^2/s [142]
Diffusion coefficient for oxygen in collagen gel*	$D_{c_g} = 4.5 \times 10^{-6}$ cm^2/s [71]
Maximal rate of oxygen consumption†	$M = 2 \times 10^{-19}$ mol/cell/s
Concentration at which oxygen consumption is half maximal[1]	$c_{1/2} = 6.66 \times 10^{-9}$ mol/ml (0.506 %)

Table 3.9: Final parameter values derived from the literature (∗) and via parameterisation (†) against the *in vitro* training data sets. Where parameters are functions of n_0, here n_0 has units cells/ml.

control parameters. These two parameters were determined as functions of n_0 to incorporate the differences in experimental results across the various initial cell densities used in the experiments (Table 3.10).

3.6 Results and discussion

3.6.1 Parameterised model simulation results and comparison with experimental data

The final parameter values for the cell and oxygen governing equations are in Table 3.9, and those for the VEGF governing equation are in Table 3.10. These parameters were obtained either from the literature or during

[1]Parameter value provided by Dr Shipley, based upon previous unpublished research
[2]Based upon experimental data values

VEGF concentration equation parameters	
Diffusion coefficient for VEGF in media*	$D_{v_m} = 1.37 \times 10^{-6}$ cm^2/s [232]
Diffusion coefficient for VEGF in collagen gel†	$D_{v_g} = 1.13 \times 10^{-6}$ cm^2/s
VEGF degradation rate†	$d_v = 29.874 \times 10^{-6}$ 1/s
Hypoxia threshold for VEGF secretion†	$c_h = 6.281 \times 10^{-8}$ mol/ml (4.77 %)
VEGF secretion gradient constant†	$k_\alpha = 90$ ml/mol
Baseline VEGF secretion rate†	$\alpha(n_0) = \alpha_0 + \alpha_1 n_0 + \alpha_2 n_0^2$ mol/cell/s $\alpha_0 = 0.04596 \times 10^{-23}$ $\alpha_1 = 6.7225 \times 10^{-34}$ $\alpha_2 = 5.4325 \times 10^{-42}$
VEGF secretion multiplier†	$V_m(n_0) = V_{m_0} + V_{m_1} n_0$ $V_{m_0} = 5.217$ $V_{m_1} = -9.0375 \times 10^{-9}$ ml/cell

Table 3.10: Final parameter values derived from the literature (∗) and via parameterisation (†) against the *in vitro* training data sets. Where parameters are functions of n_0, here n_0 has units cells/ml.

the process of parameterisation outlined in Sections 3.5.4 and 3.5.5, and are used for all subsequent simulations in this chapter and in Chapters 4 and 5, unless otherwise stated.

3.6.1.1 Viable cell density and oxygen concentration governing equations

Figure 3.14 shows the simulated values of the mean viable cell density over the gel $\bar{n}_g$ after 1 day, produced by the model using the parameters in Table 3.9 and initial conditions corresponding to the experimental conditions, compared against the *in vitro* cell viability data n_{exp}. Qualitatively, the

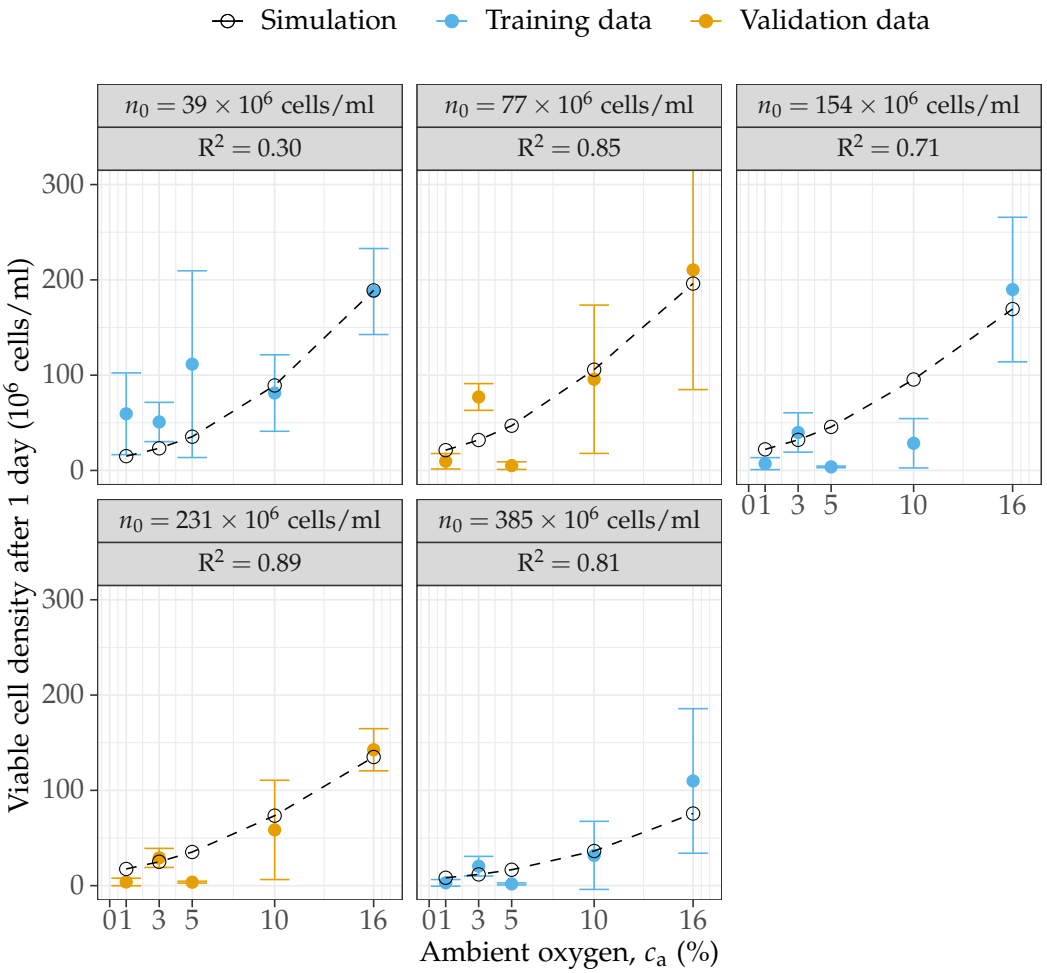

Figure 3.14: Simulated values of the mean viable cell density over the gel after 1 day, produced by the parameterised cell-solute model, approximate the general trends demonstrated by both the training experimental data S_T used during the optimisation process (blue), and the validation experimental data set S_V (yellow). Error bars represent standard deviations.

model reproduces the general trend of the experimental data, showing a clear increase in viable cell density with ambient oxygen concentration as the initial cell density increases.

The degree to which the model captures the experimental data does vary according to the value of n_0 and c_a. For initial cell densities of 77×10^6 cells/ml and above, $R^2 \geq 0.71$, providing quantitative evidence of a good model fit to these subsections of data. However, a much lower value of $R^2 = 0.30$ was produced for $n_0 = 39 \times 10^6$ cells/ml. This reflects the fact

that the model does not capture the slightly higher viable cell densities produced by this lower initial cell density at $c_a = 1$, 3 and 5%, probably because this does not match the overall trend exhibited by the rest of the data set.

Additionally, the model does not replicate the relatively low experimental values at $c_a = 5\%$ for $n_0 = 77$, 154 and 231×10^6 cells/ml. The non-linear pattern in viable cell density exhibited from 3 to 10% oxygen across these initial cell density subsets would not be possible to replicate using the model unless the proliferation or cell death functions were explicitly altered to create either an increase in cell proliferation or decrease in cell death at 3%, or the converse at 5%.

The data points at $c_a = 3$ and 5% have comparatively small standard deviations, suggesting that they are relatively precise measurements. Therefore it seems that there are three likely scenarios that explain this non-linear pattern. Firstly, a systematic error could have occurred with the experiments that were conducted using either $c_a = 3$ or 5%, resulting in a consistent increase or decrease in viable cell density. But the data collected using $n_0 = 39 \times 10^6$ cells/ml do not appear to have been affected by such an error. Alternatively, the data could be an accurate depiction of how oxygen influences cell viability, in which case either 3% oxygen provides a particularly good niche for dADSC proliferation, or 5% a particularly poor one.

However, statistical analysis of the Ki67 data set did not demonstrate a negative correlation between cell proliferation and ambient oxygen concentration (Section 3.3.3.3), and during the harvest and culturing of the cells they were not exposed to low oxygen conditions, as outlined in the dADSC culture protocol provided by Georgiou et al. [133]. Nevertheless, it is possible that $c_a = 3\%$ could correspond to the oxygen conditions that the adipose cells were exposed to in the fat tissue of the rats prior to harvesting.

Figure 3.15 shows that the simulated progression of $\bar{n}_g$ with time is

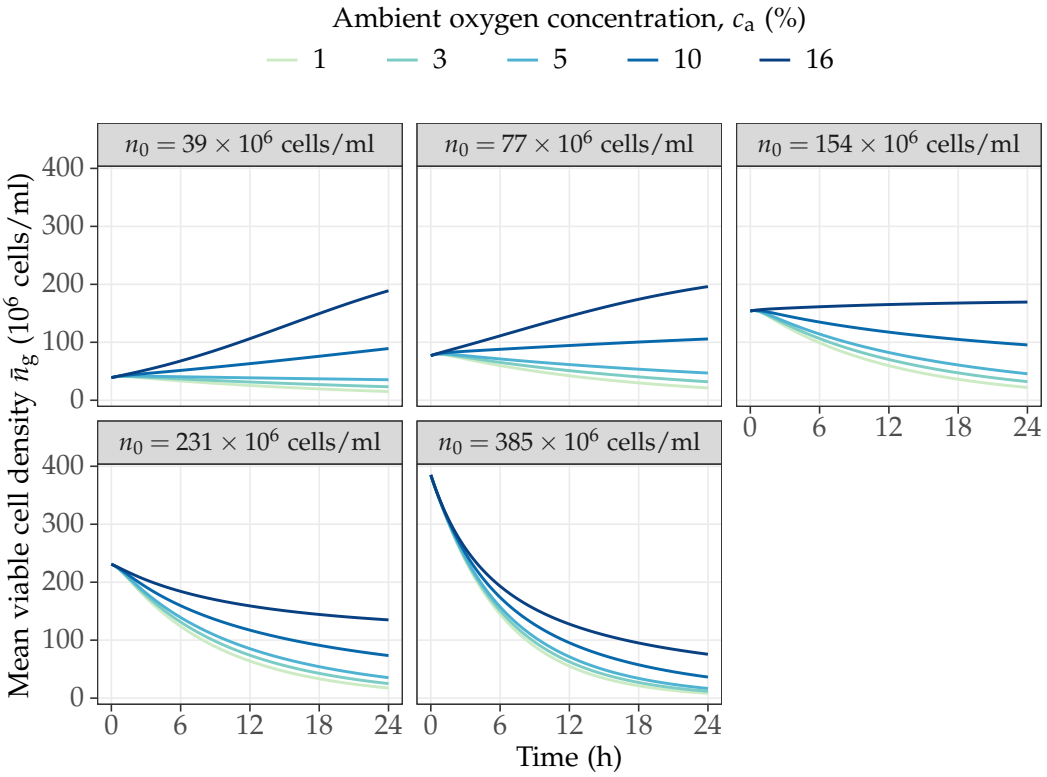

Figure 3.15: Simulated values of the mean viable cell density over the gel $\bar{n}_g$ vary gradually over time. In the majority of the simulated scenarios, the viable cell density gradually decreases, with only oxygen concentrations greater than 5% inducing increases in the viable cell density.

smooth with no discontinuities or unrealistically quick increases or decreases, although validation of these time dependent solutions would require additional *in vitro* experiments.

Although the model was not fit against the 5 day data due to time constraints, the model simulations were run up to the 5 day time point for comparison with the corresponding experimental data. Figure 3.16 demonstrates that the model does replicate the general trend of the viable cell density data after 5 days, aside from when $c_a = 16\%$. Under this condition the model tends to overestimate the mean viable cell density.

The fit again appears to be worse for $n_0 = 39 \times 10^6$ cells/ml than for the other initial cell densities. But overall the model predictions broadly match the trend of the data points despite the fact that none of the 5 day

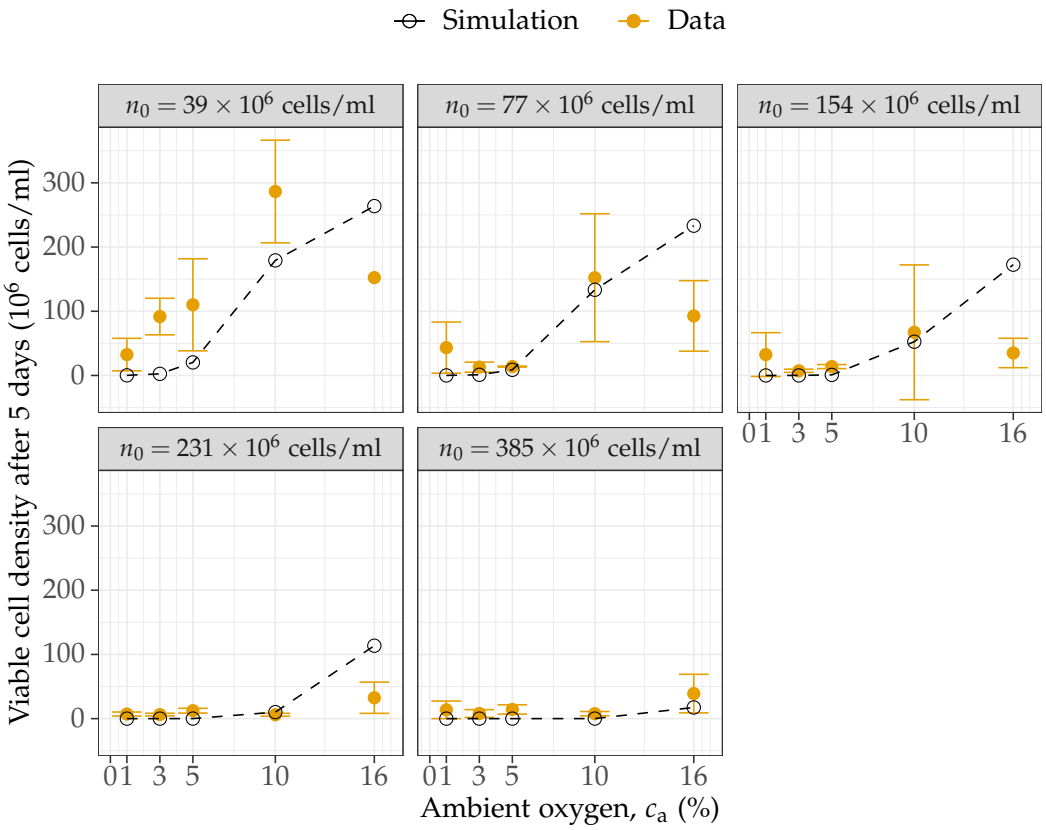

Figure 3.16: Simulated values of the average viable cell density over the gel after 5 days, produced by the parameterised cell-solute model, approximate the general trends demonstrated by both the experimental data (yellow). Error bars represent standard deviations.

data was used to parameterise the model, providing further validation of the cell-oxygen governing equations.

Although the mathematical model was not parameterised against the oxygen monitoring data, comparison of the simulated mean oxygen concentration over the gel $\bar{c}_g$ with the experimental values demonstrates that the broad shape of $\bar{c}_g$ as a function of time matches that of the data, but in the case of $n_0 = 39 \times 10^6$ cells/ml the rate of change for the oxygen concentration appears to be much quicker than the experimental values would suggest is realistic.

The solutions for $\bar{c}_g$ are highly dependent on the diffusion rate of oxygen into the gel from the media (and from the air surrounding the well into the media), but because these diffusion rates are independent of the

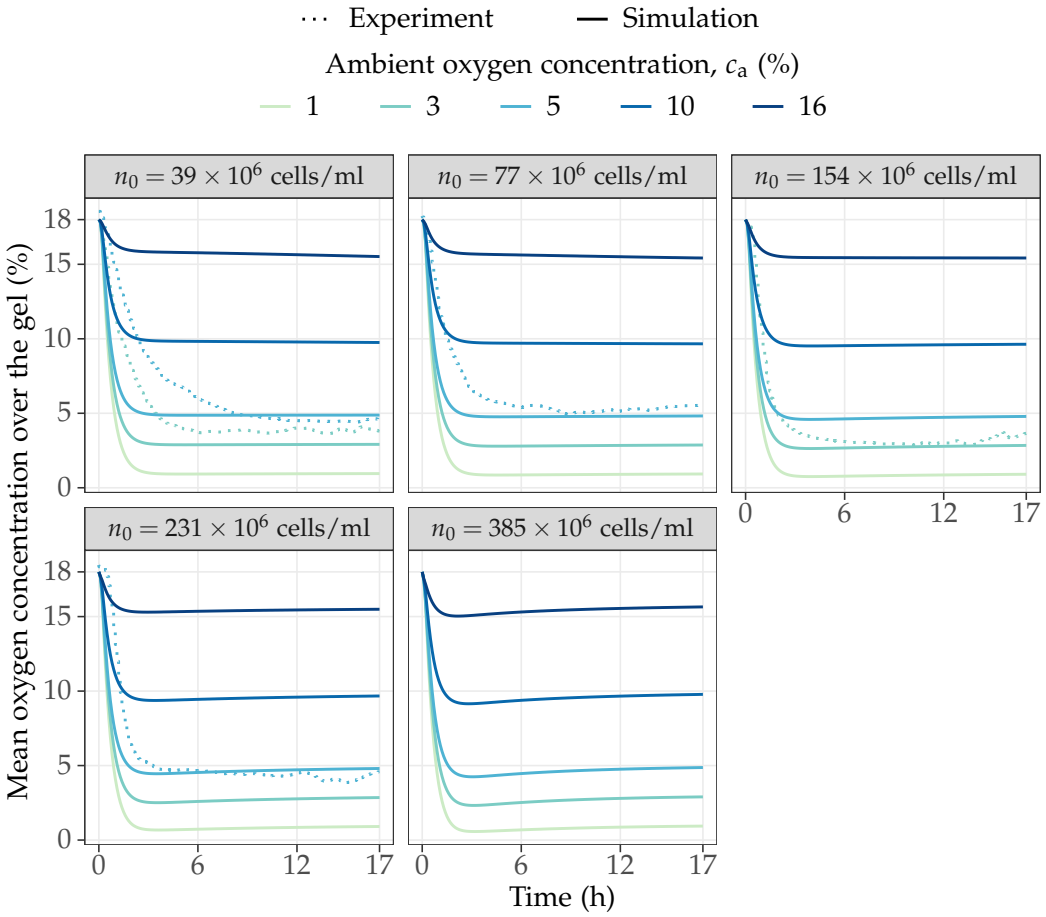

Figure 3.17: Simulated values of the mean oxygen concentration over the gel $\bar{c}_g$ are predominantly affected by the ambient oxygen concentration via diffusion through the media and gel. Simulated values $\bar{c}_g$ approximate the experimental data by reaching steady states corresponding to the imposed values of c_a.

cell density they cannot account for the difference in the experimental rate of change in oxygen between $n_0 = 39 \times 10^6$ cells/ml and $n_0 = 395 \times 10^6$ cells/ml. This would suggest that the oxygen metabolism term requires further refinement in the future. On the other hand, the oxygen monitoring experiments were not repeated or carried out across the whole range of the initial conditions used in the other experiments, and therefore could also benefit from further work in the future.

Aside from the model fit, some of the parameter values derived via least squares parameterisation against the experimental data should be re-

garded as results in their own right. The cell proliferation rate parameter $\beta = 2.2 \times 10^{-4}$ m^3/mol/s is higher than most of the values cited in the literature (Section 3.5.1.1), but cell proliferation rates in general are not widely characterised and no previous work has been done to find proliferation rate values for dADSCs specifically. Additionally, some of the existing theoretical models neglect cell death entirely, which would result in lower estimates for the rate of cell proliferation.

As explained in Section 3.5.4, the cell death rate δ was determined as a function of n_0 to produce a better fit to the experimental data. Therefore the cell death rates used by the model range from $\delta = 1.13$ to 4.65×10^{-5} s^{-1} (3 s.f.) for $n_0 = 39$ and 385×10^6 cells/ml respectively. These cell death values again appear to be larger than those currently reported in the literature (Section 3.5.1.1), but there is very little data available on cell death rates in general. Experimentally it is difficult to discern whether changes in the number of cells are due to increased cell proliferation or decreased cell death, accounting for the lack of precise data for these parameters.

The need to incorporate δ as a function of n_0 to achieve a good fit to the data may indicate that the functional forms used for the model are insufficient to explain all of the variability in the data. An oxygen-dependent cell death function was also trialled but did not result in a better fit to the data.

During the process of fitting, the oxygen metabolism coefficient was identified as $M = 2 \times 10^{-19}$ mol/cell/s. This is at the lower end of the range previously identified for this parameter in Section 3.5.1.2 (2×10^{-19} to 9.1×10^{-16} mol/cell/s). Comparison of the time dependent solutions for $\bar{c}_g$ obtained across different initial cells densities (and thus different time dependent solutions for n across the gel), as shown in Figure 3.17, leads to the conclusion that oxygen metabolism has only a small effect on the rate of change of $\bar{c}_g$ in this model.

In this thesis, cell density and oxygen concentration were modelled as

independent of VEGF concentration for simplicity. But experimental evidence suggests that VEGF increases the proliferation of certain cell types, including ADSCs (Section 3.4.1), although the exact effect of VEGF upon dADSCs could differ. Future improvements to the cell-solute model could incorporate a dependence upon VEGF into the cell proliferation term. Alternatively, glucose is another factor that can influence cell proliferation and death rates, and could be a good candidate for inclusion in the model in the future, as outlined in more detail in Chapter 6. However, it was expected that oxygen rather than glucose would be the limiting factor for cell survival over the time span simulated in this thesis, and again this effect is likely to be cell type-specific. Nevertheless, the incorporation of either or both of these aspects into the model could eliminate the need for the cell death function to depend upon n_0.

3.6.1.2 VEGF concentration governing equation

The simulated mean VEGF concentration over the media $\bar{v}_m$ after 1 day captures the general trend of the corresponding experimental data (Figure 3.20), although the R^2 values are much lower than those measuring the fit against the viable cell density data. The poorest fit was again for the $n_0 = 39 \times 10^6$ cells/ml data subset, with the model failing to capture the low VEGF concentrations at 10 and 16% in this case.

The R^2 values for the other initial cell densities all fall between 0.27 and 0.43. These lower R^2 values reflect the fact that the model tends to mimic the shape of the general non-linear relationship between c_a and $\bar{v}_m$ but does not exactly replicate the extremes; for example, at $c_a = 3\%$ and $n_0 = 77 \times 10^6$ cells/ml the model does not exhibit as great a local maximum as the experimental data.

Similarly to the viable cell density experimental data at the 1 day time point, a key aspect of the 1 day VEGF concentration data is the local maximum at $c_a = 3\%$. Interestingly, again this pattern is most evident in the data for which n_0 is greater than 39×10^6 cells/ml. This may suggest a link

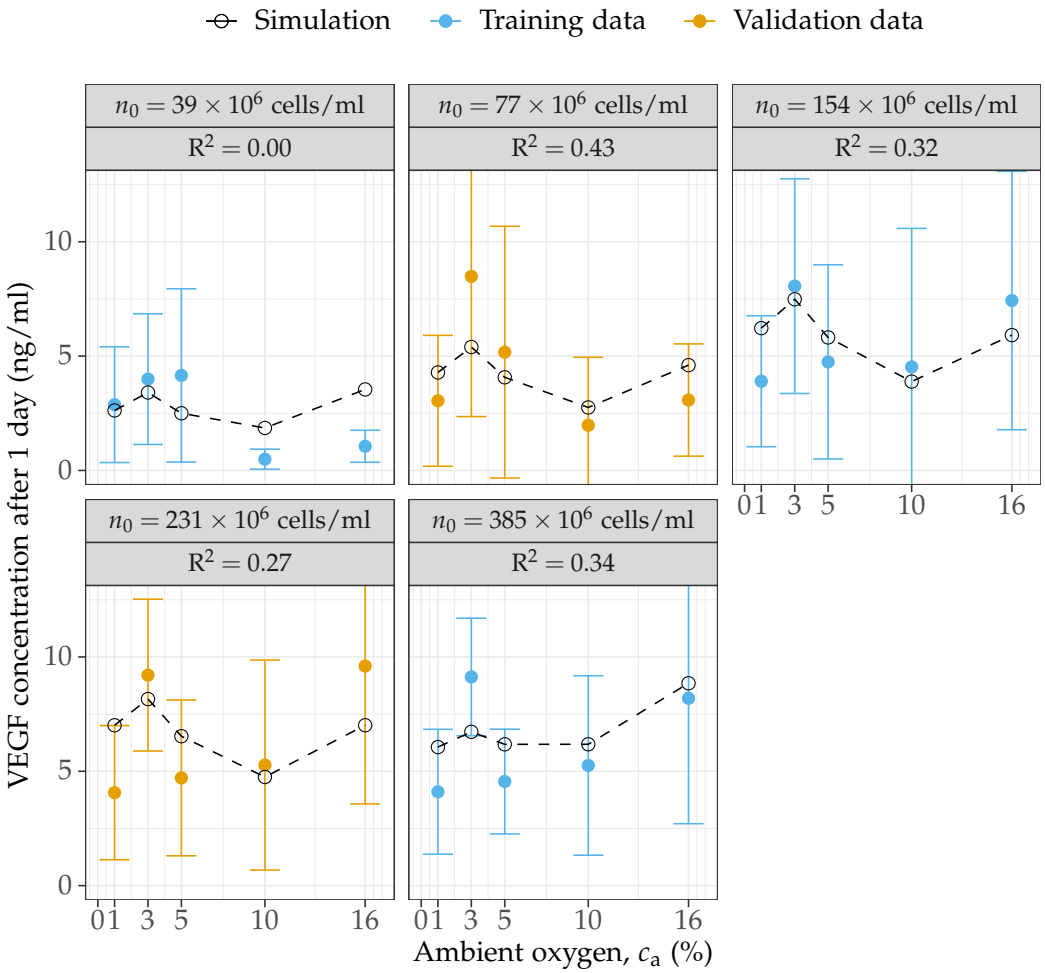

Figure 3.18: Simulated values of the mean VEGF concentration over the media $\bar{v}_m$ after 1 day, produced by the parameterised cell-solute model, approximate the general trends demonstrated by both the experimental data used during the optimisation process (blue), and the test experimental data set (yellow). Error bars represent standard deviations.

between these phenomena: the relatively large number of cells at $c_a = 3\%$ (in comparison to at 1 and 5%) at these values of n_0 could account for the correspondingly relatively high VEGF concentration. For this reason it seems likely that a better model fit to the local peak in cell viability at c_a would also improve the fit to the VEGF data.

Additionally, the difference between the recorded VEGF concentrations after 1 day for $c_a = 3\%$ and $c_a = 5\%$ could be partially accounted for by the upregulation of VEGF secretion at oxygen concentrations be-

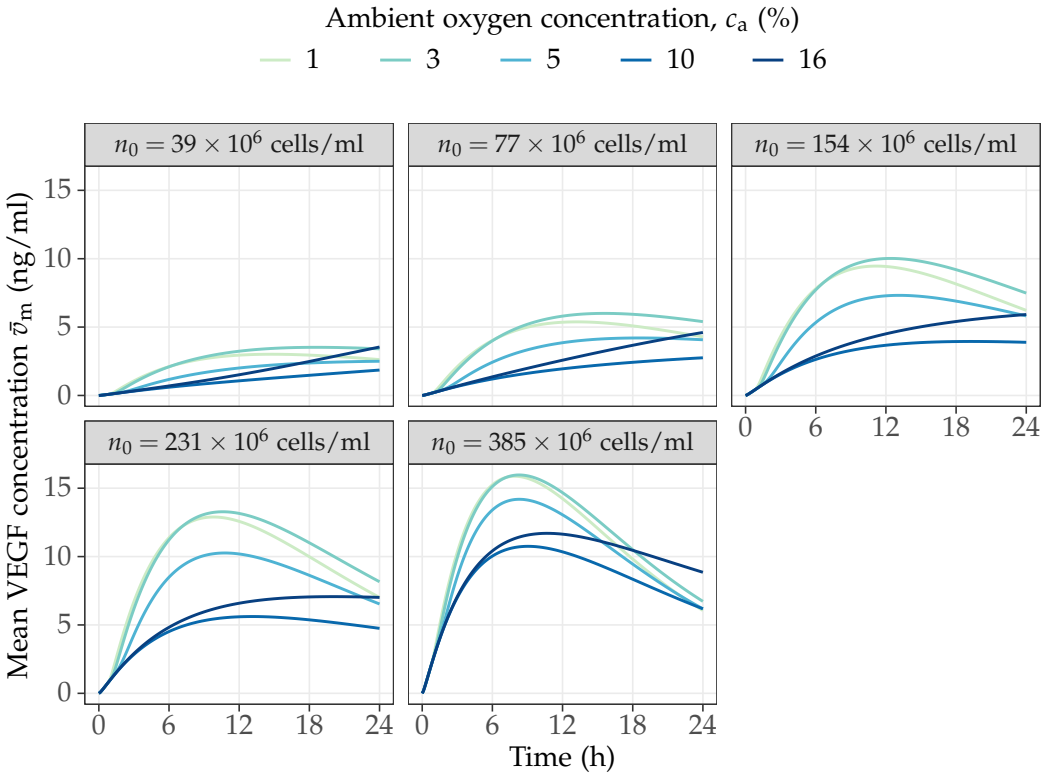

Figure 3.19: Simulated values of the mean VEGF concentration over the media $\bar{v}_m$ tend to reach their maximum between 6 and 12 hours.

low 5%; indeed, the model parameterisation process resulted in a hypoxia threshold of $c_h = 4.77\%$ for VEGF secretion, meaning that the highest rates of VEGF secretion are achieved at approximately 2.5% and below (Figure 3.12).

The time-dependent solutions for both the mean VEGF over the media $\bar{v}_m$ and the gel $\bar{v}_g$ (Figures 3.19 and 3.20 respectively) are smooth and continuous as would be expected. The simulated mean VEGF concentration over the gel has a larger range than that over the media because the model dictates that all VEGF production takes place in the cell-seeded gel portion of the geometry, and the rate of diffusion of VEGF is slower in the gel than in the media, leading to an accumulation of VEGF in the gel. Due to a lack of corresponding experimental data it is not possible to validate whether the model predictions for $\bar{v}_g$ are accurate.

Regardless of the initial conditions used (n_0 and c_a pairs), the simu-

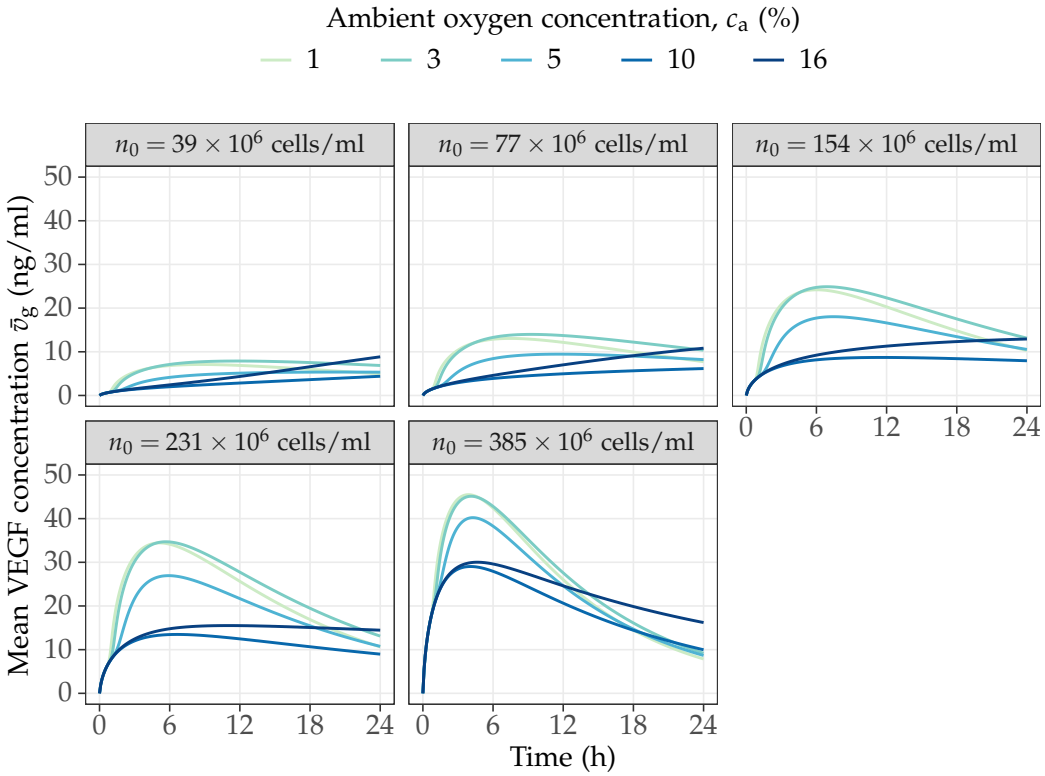

Figure 3.20: Simulated values of the mean VEGF concentration over the gel $\bar{v}_g$ tend to reach their maximum between 0 and 6 hours.

lated mean VEGF concentrations in both the gel and the media initially increase, with $\bar{v}_g$ increasing at a faster rate. This is expected because during the early stages of the simulations there is still a relatively large cell population present in the gel across all of the simulated scenarios. At later time points, changes in both $\bar{v}_g$ and $\bar{v}_m$ are directly linked to changes in the viable cell density in the gel: a decreasing cell population eventually leads to lower VEGF concentrations, with a delay due to the half life of VEGF, and vice versa in the case of increasing viable cell density in the gel.

The model predictions for $\bar{v}_m$ after 5 days do not replicate the corresponding experimental VEGF concentration data, as depicted in Figure 3.21. In particular, the simulated values of $\bar{v}_m$ for the highest two initial cell density data subsets are much closer to zero than the data points. This is because after 5 days the corresponding simulated cell densities are also nearly zero, and as VEGF secretion is proportional to the number of cells

this results in a large drop in VEGF concentration. The relatively short half life of VEGF in the model (6.45 hours) means that once the cell population is close to zero and consequently there is effectively no secretion of VEGF (as is the case around the 5 day time point for $n_0 = 231$ and 385×10^6 cells/ml, Figure 3.16), the remaining VEGF decays rapidly.

A possibly influential aspect that has not incorporated into the current model is the differences in behaviour exhibited by the various isoforms of VEGF. In the current model, VEGF is modelled as a single species in order to reduce complexity and limit the number of unknown parameters. However, different isoforms of VEGF exhibit different properties: each VEGF isoform is likely to have unique, albeit similar, diffusion, decay and secretion rates.

Additionally, the various isoforms of VEGF exhibit different ECM binding behaviour: $VEGF_{121}$ diffuses freely and does not bind to heparan sulfate proteoglycans (HSPGs) in the ECM, whereas the longer isoforms such as $VEGF_{165}$ and $VEGF_{189}$ have high HSPG binding affinities [157] and thus produce steeper spatial gradients. Chen et al. reported that long VEGF isoforms also have an affinity for collagen [73], but currently the mathematical model does not account for any binding of VEGF to the collagen matrix; explicitly incorporating VEGF ECM binding along with isoform-specific degradation and diffusion rates could be another way of improving the model in the future. VEGF binding to collagen and subsequent proteolytic release, which has been suggested by Vempati et al. to reduce degradation of VEGF and increase its spatial range [392], along with varying isoform decay rates could partially account for the relatively high VEGF concentrations measured in the media after 5 days for the highest values of n_0 (Figure 3.21), despite the low number of cells recorded at the same time point (Figure 3.16).

The diffusion coefficient for VEGF in gel was identified as $D_{v_g} = 1.13 \times 10^{-6}$ cm^2/s, which as expected induces a slower rate of diffusion through

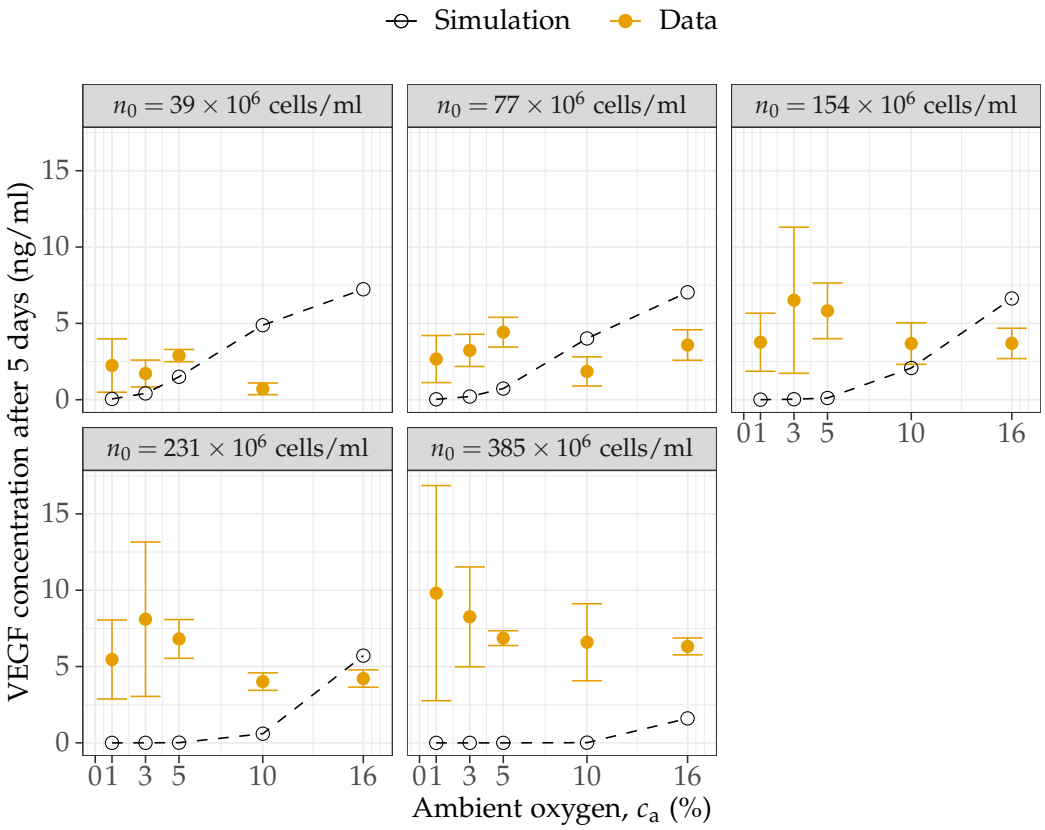

Figure 3.21: Simulated values of the average VEGF concentration over the media after 5 days, produced by the parameterised cell-solute model, generally do not approximate the experimental data (yellow). Error bars represent standard deviations.

the gel. However, the ratio $D_{v_m}/D_{v_g} \approx 1.21$ whereas $D_{c_m}/D_{c_g} \approx 5.83$. These ratios reflect the degree of impedance to diffusion caused by the collagen gel; because VEGF is a larger molecule, if anything it would be expected that $D_{v_m}/D_{v_g} \geq D_{c_m}/D_{c_g}$. The fact that this is not the case suggests that there is room for further refinement of the diffusion parameters in the future.

The VEGF degradation rate was determined via parameterisation as $d_v = 29.874 \times 10^{-6}$ 1/s, which is equivalent to a half life of 6.45 hours.

Within the VEGF secretion term, the hypoxia threshold for VEGF production was determined to be approximately 4.77%. This value could be compared against experimental results for further validation, and could be used as cell type-specific parameter in other similar models.

The baseline VEGF secretion rate (the VEGF secretion rate at high oxygen concentration levels, Figure 3.12) was determined as a non-linear function of n_0 and provides a minimum of $\alpha = 1.793 \times 10^{-3}$ pmol/10^6 cells/h at $n_0 = 39 \times 10^6$ cells/ml and a maximum of $\alpha = 5.624 \times 10^{-3}$ pmol/10^6 cells/h at $n_0 = 385 \times 10^6$ cells/ml. Assuming a molecular weight of 46 kDa for a VEGF dimer [139, 154], these values are equivalent to 82.466 pg/10^6 cells/h and 258.692 pg/10^6 cells/h. These secretion rates, although on a similar order of magnitude, are higher than those reported for adipocytes and stromal cells [259] and clone A and HCT-8 human colon tumour cells [211]. However, these experimental values likely underestimate the VEGF secretion rates of these cell types because VEGF decay is not taken into account. Additionally, some variation in VEGF secretion rates across cells types is expected. These values suggest that the Schwann cell-like dADSC phenotype produces VEGF at a relatively high rate.

The VEGF secretion multiplier V_m, which dictates the fold change in VEGF secretion at low oxygen concentrations, is also determined by a decreasing function of n_0, with a minimum of $V_m = 1.738$ for $n_0 = 385 \times 10^6$ cells/ml and a maximum of $V_m = 4.865$ for $n_0 = 39 \times 10^6$ cells/ml. These values are within the expected range based upon previous experimental and theoretical work (Section 3.5.1.3).

Finally, the VEGF secretion gradient constant was assigned as $k_\alpha = 90$ ml/mol. The model is not sensitive to this value, as explored in the next section.

3.6.2 Sensitivity analysis

The credibility of a theoretical model depends on the robustness of the parameter estimates; if model outputs are very sensitive to small changes to model inputs or parameter values, then the predictions are likely to be less reliable because experimental variations are a certainty. Sensitivity analysis can be used to measure the robustness of the model fit to the data, and help to identify which parameters may need refinement in the future.

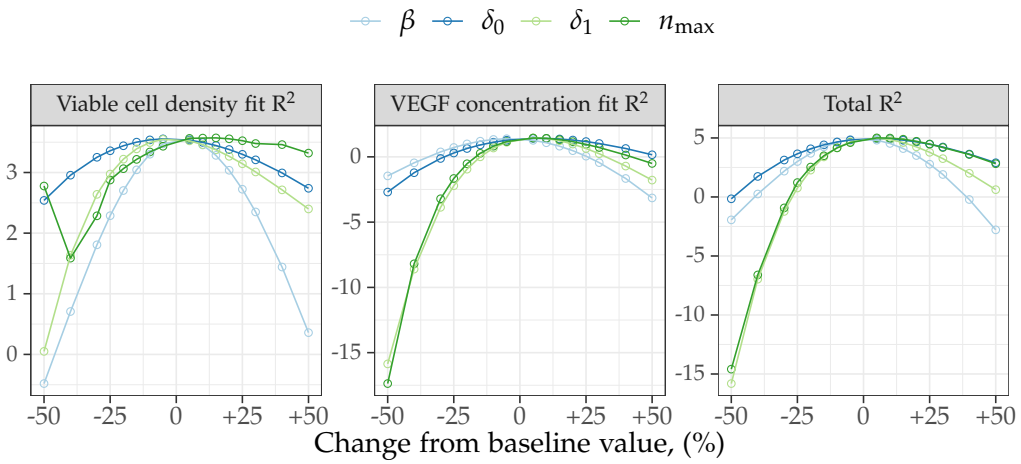

Figure 3.22: The total VEGF concentration R^2 is more sensitive to changes in the viable cell governing equation parameters than the total viable cell density fit R^2. The overall measure of whole model fit against both 1 day data sets (Total R^2) is least sensitive to δ_0.

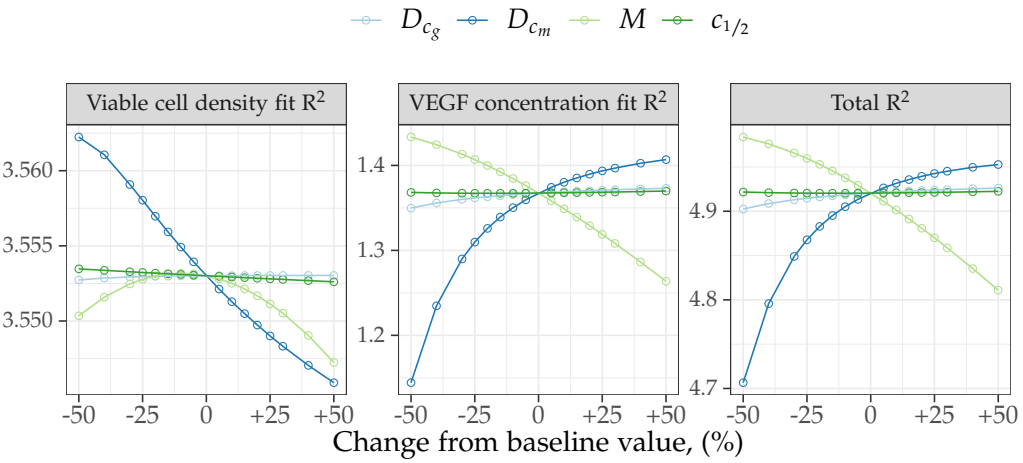

Figure 3.23: The total VEGF concentration fit R^2 is more sensitive to changes in the oxygen concentration governing equation parameters than the viable cell density fit R^2. The overall measure of whole model fit against both 1 day data sets (Total R^2) is least sensitive to $c_{1/2}$.

3.6.2.1 Model sensitivity to the parameters

Local sensitivity analysis assesses the sensitivity of the model outputs to variations in model inputs from a single specific value, referred to here as a baseline point, $\bar{x}$. In the case of the mathematical model described in this thesis, a clear candidate for $\bar{x}$ is the set of parameters derived during the process of optimisation and listed in Tables 3.9 and 3.10. Local sensitivity

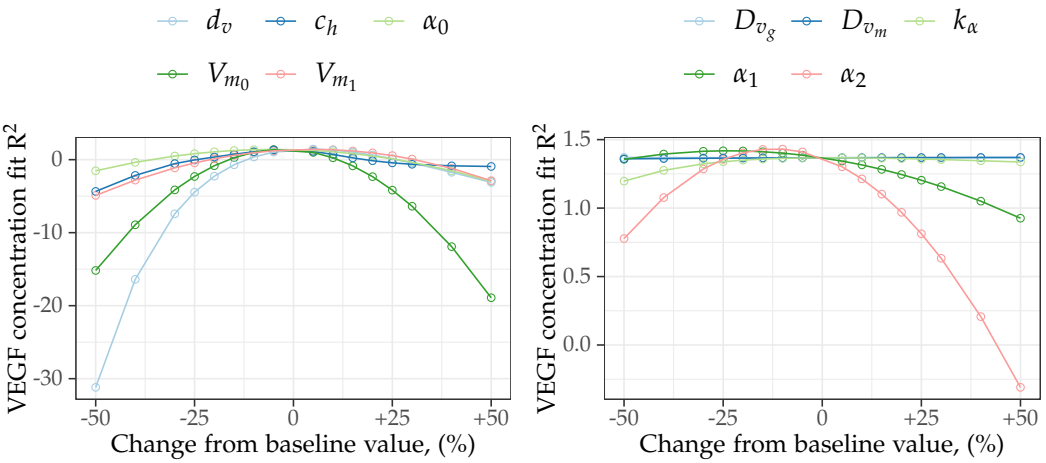

Figure 3.24: Out of all of the VEGF governing equation parameters, the VEGF concentration fit R^2 is most sensitive to the VEGF decay rate parameter d_v.

analysis usually uses the "one factor at a time" (OAT) technique, in which one parameter is varied at a time whilst all others are fixed, and thus the individual effects of the parameters upon the model output are measured.

Local sensitivity analysis was conducted for the cell-solute model by varying each parameter in the governing equations by up to 50% of their final values as recorded in Tables 3.9 and 3.10 and measuring the impact upon the total viable cell density fit R^2, defined as the sum of the R^2 values calculated for each of the initial densities n_0 as depicted in Figure 3.14, the total VEGF concentration fit R^2, and the sum of these two values, the total model fit R^2.

Out of the four cell governing equation parameters, the viable cell density fit R^2 is most sensitive to β and slightly less sensitive to δ_0 and δ_1, suggesting that cell proliferation is the process that predominantly determines viable cell density in this model (Figure 3.22). The VEGF concentration fit R^2 is more sensitive to changes in any of the cell density governing equation parameters than the viable cell density fit R^2. Both R^2 values appear to be fairly robust within variations of 5% of the baseline value.

Both the viable cell density fit R^2 and the VEGF concentration fit R^2 are much less sensitive to the oxygen governing equation parameters than

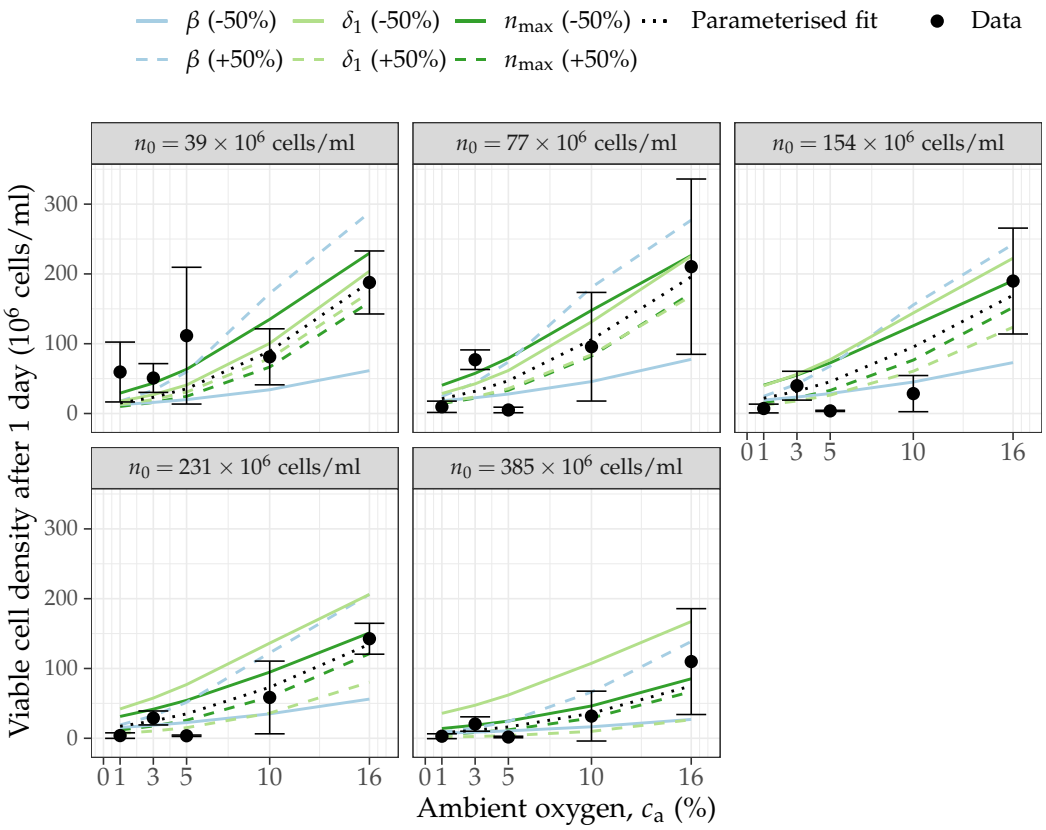

Figure 3.25: The impact of increasing and decreasing β, δ_1 and $n_{\max}$ by 50% of the values found during optimisation, on the model fit to the viable cell density data. Black dashed line indicates the final, parameterised model fit; error bars indicate the standard deviations of the viable cell density data.

to the cell density governing equation parameters (Figure 3.23). Decreasing the value of D_{c_m} by 50% induced a decrease of approximately 0.22 in the total R^2, but the value of the coefficient D_{c_m} was derived using experimental methods [142] and D_{c_m} is therefore one of the more well ascertained parameters in the model.

In this model, the viable cell density is not dependent upon VEGF and therefore varying the VEGF governing equation parameters has no effect upon the total viable cell density fit R^2. Figure 3.24 demonstrates the results of varying these parameters upon the VEGF concentration fit R^2. The R^2 value was found to be least sensitive to the VEGF diffusion coefficients, and most sensitive to the VEGF decay rate d_v.

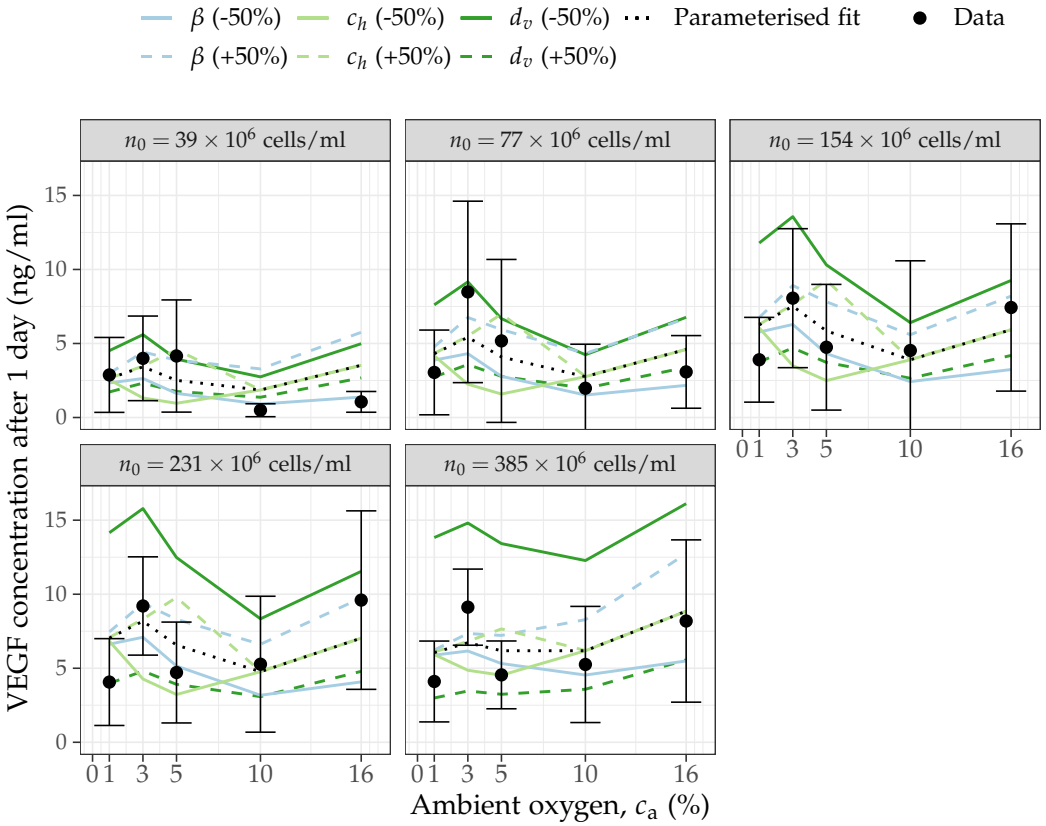

Figure 3.26: The impact of increasing and decreasing β, c_h and d_v by 50% of the values found during optimisation, on the model fit to the viable cell density data. Black dashed line indicates the final, parameterised model fit; error bars indicate the standard deviations of the VEGF concentration data.

Figures 3.25 and 3.26 illustrate in more detail the impact that increasing and decreasing a selection of parameters has on the model fit to the *in vitro* data.

Varying the proliferation rate parameter β was found to result in the largest change in the total viable cell density fit R^2, and Figure 3.25 shows how increasing β by 50% results in the model overestimating the viable cell density, especially for higher ambient oxygen concentrations.

Similarly, decreasing the value of the VEGF degradation rate d_v was found to result in the greatest changes in the total VEGF concentration fit R^2, and Figure 3.26 demonstrates that reducing d_v by 50% does induce a more drastic change in the model fit to the VEGF concentration data than

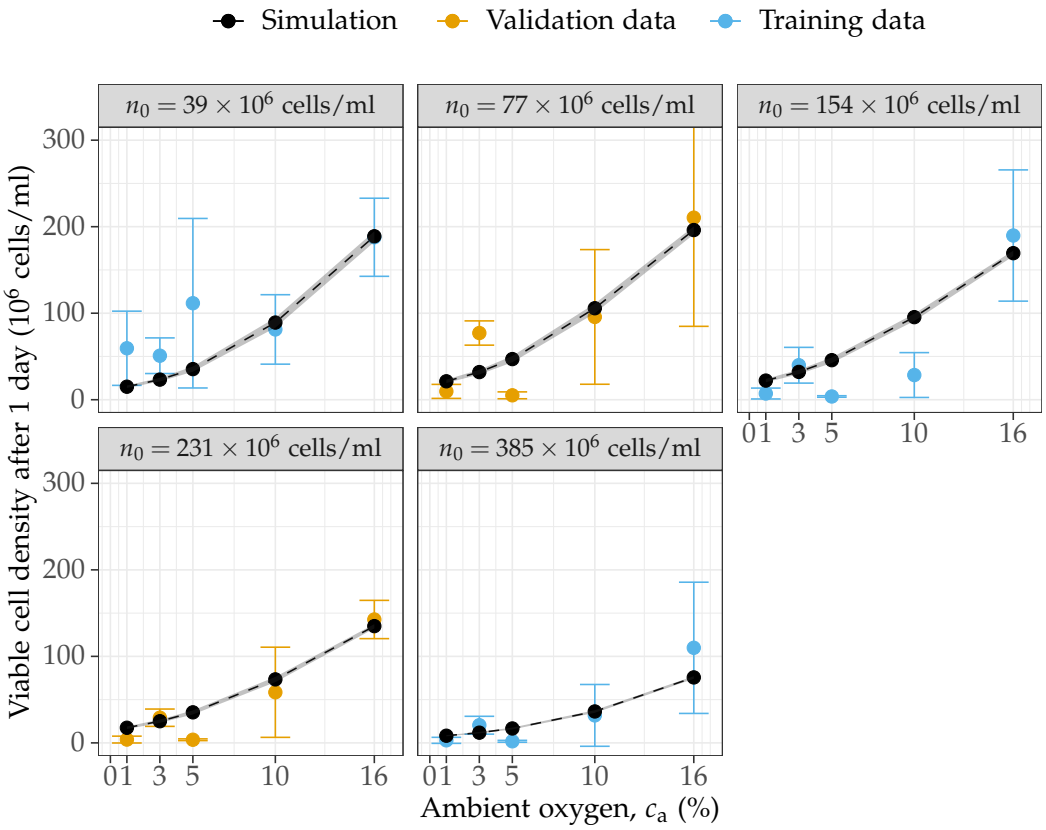

Figure 3.27: Simulated values of the mean viable cell density over the gel after 1 day. Grey ribbon represents the range of values achieved when using $n_0 \pm 10\%$ of the value indicated. Error bars represent standard deviations around the means of the experimental data.

changes on a similar scale applied to some other parameters.

3.6.2.2 Model sensitivity to the initial cell density

The experimental methods used to count and seed the cells will have introduced inaccuracies into the value of n_0. Here the initial cell densities n_0 used in the model were varied by 10% to determine how these experimental variations could affect the model fit to the data.

In the case of the viable cell density data, a variation of 10% in n_0 results in only minor changes to the value of $\bar{n}_g$ at the 1 day time point (Figure 3.27), whereas much more variation occurs in the corresponding values of $\bar{v}_g$ (Figure 3.28). The difference between the two results is likely explained by the fact that the VEGF secretion term in the mathematical

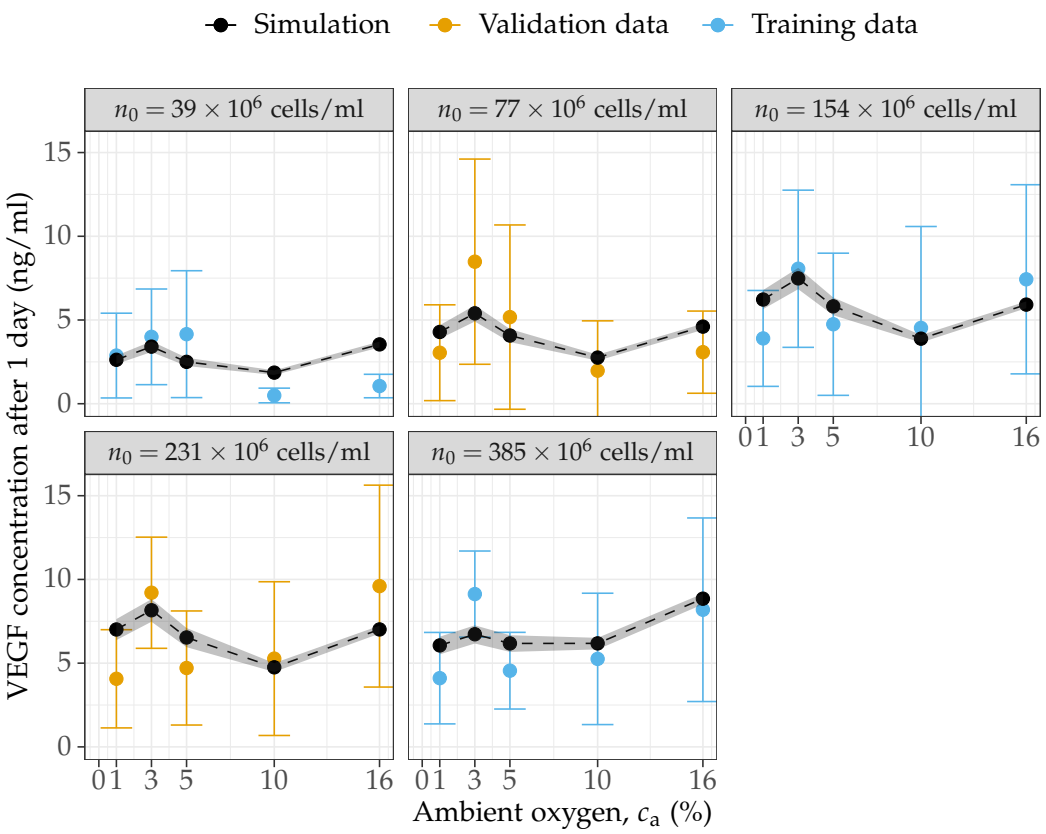

Figure 3.28: Simulated values of the mean VEGF concentration over the media after 1 day. Grey ribbon represents the range of values achieved when using $n_0 \pm 10\%$ of the value indicated. Error bars represent standard deviations around the means of the experimental data.

model is highly dependent upon parameters that are explicit functions of n_0.

3.7 Conclusion

In summary, in this chapter a continuum model of cell-solute interactions was developed, with some parameter values being assigned according to existing values in the literature and others identified via fitting against *in vitro* data collected specifically for this purpose.

The fit to the cell viability data achieved a higher R^2 value than that for the VEGF data, indicating a closer fit to the data, but in both cases the model captured the overall trend of the data. The VEGF governing equation contained a greater number of parameters than the oxygen and cell

governing equations, of which a larger proportion were unknown based upon a review of the literature. This made parameterisation of the VEGF governing equation more difficult, and it was necessary to include two parameters that were explicit functions of the initial cell density n_0 in order to achieve a good fit. The cell death rate δ was also defined as a linear function of n_0.

The incorporation of parameters that depend explicitly on n_0 does suggest that the functional forms and variables included in the model do not account for all of the variability in the data. It is worth noting that this does not mean that the predictions generated by the model will necessarily be inaccurate; the incorporation of a dependence on n_0 could implicitly represent the effect of biological interactions that were not explicitly included in the model equations. Nevertheless, three possible adjustments to the terms and composition of the mathematical model stand out as having the potential to improve the model fit to the data and better reflect the biological scenario.

Firstly, the influence of VEGF concentration on cell proliferation was neglected here due to a lack of cell type-specific data and for simplicity, but incorporating feedback between the viable cell and VEGF governing equations could reduce the need for parameters that explicitly depend on n_0.

Secondly, the model did not incorporate distinct behaviours for different VEGF isoforms, and in particular did not include VEGF binding behaviour. VEGF binding may be important during the generation of VEGF gradients, and therefore including this mechanism in to the model may improve its ability to predict VEGF distributions over time.

Finally, glucose could be incorporated as an additional variable. Glucose can influence VEGF secretion [43, 201] as well as cell proliferation, although the exact relationship between these factors in the case of dADSCs specifically is unknown. However, the introduction of another variable

would increase the complexity of the model considerably, and validation or parameterisation against glucose measurements would be highly desirable, further increasing the number of *in vitro* experiments required.

The *in vitro* data did exhibit a relatively high amount of variability, as demonstrated by the standard deviation values. The variability of the data that the model was fitted against could impact the accuracy of any simulations run using the derived parameters. This motivates the need for further validation studies in the future, as per Figure 1.4. If a similar study was to be carried out in the future, the use of higher N numbers as part of the *in vitro* experimental design could help to reduce some of the uncertainty in the mean values that were used for parameterisation.

The experimental data also restricts the range of initial conditions that should be used to run simulations. The experiments used initial seeded cell densities of between 39 and 385×10^6 cells/ml, and therefore simulations of the parameterised model should also be restricted to the use of this range. However, this range was chosen specifically to represent the range of values currently used in the Phillips lab, and therefore this does not present a significant limitation.

In the next chapter, the parameterised mathematical framework is applied to a cylindrical geometry representing a collagen, cell-seeded NRC implanted *in vivo* and simulations are run using a variety of different seeded cell densities and distributions to investigate how seeded cell strategies could influence cell survival and the generation of VEGF gradients *in vivo*.

Chapter 4

Application of the Cell-Solute Model to Nerve Repair Construct Geometries

A selection of the work contained in this chapter is currently under review for publication.

4.1 Introduction

As explained in Section 1.5, this thesis aims to use computational methods to test the hypothesis that initial spatial distributions of cells and materials within NRCs could influence cell survival and the distributions of cells, growth factors and other solutes over time, and thus impact the progression of vascular growth and neuronal regeneration. Existing research suggests that the use of specific initial seeded cell densities could maximise cell survival and neuronal regeneration (Section 1.3), motivating the use of theoretical methods to identify possible optimal values for future experimental testing.

Hypoxia can cause therapeutic cell death in central regions of engineered tissue that lie beyond the diffusion limit of oxygen. Seeding too many cells in an area of tissue unlikely to have the capacity to maintain their metabolic needs could result in unnecessary waste of cells, whereas

seeding too few cells may lead to worse regenerative outcomes. The importance of spatial gradients of growth factors like VEGF for vascular growth, and in particular for TEC migration, is also well established [31, 134, 282, 335, 413]. Spatial variations in cell density across engineered tissue could be used to enhance the generation of VEGF gradients and thereby improve the rate and directionality of revascularisation. The importance of spatial variations in oxygen and VEGF suggest that a uniform approach to therapeutic cell seeding may not maximise cell survival, vascularisation or regeneration in general.

Additionally, when implanted *in vivo* the collagen NRCs manufactured in the Phillips lab are wrapped in a sheath for protection and mechanical support [132]. This sheath can be made from a variety of materials, from impermeable synthetics such as silicone to porous materials that allow some transfer of nutrients across the sheath interface. The mathematical framework described in this thesis provides the ability to simulate how variations in sheath porosity may influence cell-solute distributions, and thereby suggest how sheath materials can be engineered to improve regeneration. Porosity ϵ is defined as the ratio of volume of void or fluid-filled space to total material volume, expressed as a decimal. The total material volume includes both fluid or void and solid parts.

In this chapter, the mathematical framework and accompanying parameters derived in Chapter 3 are used to simulate the effect of different NRC designs, including variations in therapeutic cell seeding densities and distributions and NRC sheath materials, upon cell survival and VEGF and viable cell distributions over time. The objective is to test the hypothesis that initial seeding cell densities and distributions can impact measures of cell population survival, such as the mean viable density over the NRC geometry, and VEGF distribution, such as the mean and standard deviation of the VEGF concentration, over time. The outcomes presented in this chapter are specific cell densities and distributions that achieve the high-

est simulated rates of cell survival and steepest VEGF gradients over the simulated time period; these results can help to inform and direct future experimentation.

It is assumed that all of the designs simulated in this chapter are composed of type I collagen seeded with dADSCs, thus permitting the use of the model equations and parameters that were derived in Chapter 3 using *in vitro* data corresponding to this material and cell type.

First of all, Section 4.2 describes the NRC sheath, an external supportive wrap for the NRC that can be porous or impermeable, and how to implement different varieties of sheath into a mathematical model of an NRC. Secondly, Section 4.3 describes how the mathematical model derived in Chapter 3 can be applied to the full NRC and sheath geometry and the simulation methods used.

Subsequently, Sections 4.4 and 4.5 present and discuss the outputs of a range of simulations that aim to address questions related to cell seeding strategies and NRC design. In Section 4.6, a final discussion draws together the results in the context of existing research and suggests ideas for future experimental work based upon the simulations.

4.2 The nerve repair construct sheath

The use of sheaths or tubular NRCs helps to prevent fibrous tissue from developing [353, 404], as well as providing mechanical support and preventing misdirection of growing axons [343]. Additionally, it has been speculated that impermeable sheaths and tubular NRCs improve nerve repair by averting the loss of vital growth factors and neurotrophins [92]; however, they also prevent diffusion of waste solutes out of the construct and the transport of valuable nutrients such as oxygen into the construct. On the other hand, porous materials facilitate diffusion both in and out of the construct. It has been suggested that macroporous sheaths could permit the inward diffusion of macromolecular proteins such as growth factors [187],

but large pores could also allow the invasion of inflammatory cells.

In this section, first of all the structural characteristics of existing NRC sheath materials used in the literature are collated to inform parameter ranges for the model, and existing research on the use of porous materials in tissue engineering solutions for peripheral nerve repair is discussed. Subsequently, a mathematical model of solute transport through a porous medium is outlined for the purpose of simulating oxygen and VEGF diffusion through a porous NRC sheath. This can be used in combination with the previously developed cell-solute model (Chapter 3) to assess the impact of different sheath properties upon cell survival and vascularisation, and thus inform future experimental designs.

4.2.1 Porous materials and the impact of sheath porosity upon peripheral nerve regeneration

A range of existing porous biomaterials and synthetic alternatives are suitable base materials for hollow tubular NRCs or NRC sheaths. It is possible to measure the pore size and porosity of these material scaffolds via techniques such as scanning electron microscopy and the measurement of fluid flow [380]: Table 4.1 provides a basic overview of the measured characteristics of existing viable materials, motivating the range of values investigated in subsequent sections of this chapter. It is possible to fine tune the characteristics of porous scaffolds by using different material compositions and synthesis methods, with the implication that predictions about the optimal scaffold porosity or pore size for regeneration could be tested experimentally.

Porous materials can effectively act as filters, allowing the diffusion only of molecules and cells with a diameter less than that of the pores. Molecules are typically not perfectly spherical, and therefore the kinetic diameter of molecules is often defined as the smallest dimension of a molecule. When the pores are particularly small, the pore size of a membrane or porous material is sometimes instead described as a molecular

Material	Porosity (%)	Pore size (μm)	Thickness T (mm)
Chitosan-silicate hybrids [355]	83 – 97	53 – 107	-
Collagen [218]	-	0.0125	-
PCL [192]	50 – 80	10 – 150	0.2 – 0.6
Collagen Type I (NeuroMatrix™) [417]	-	0.001 – 0.005	-
Tyrosine-derive polycarbonate terpolymer [107]	55.2 ± 1.2	35.7 ± 9	0.1
Gelatin cryogel (5%) [376]	95	150 ± 9	2.5
Poly(DL-lactide-co-caprolactone) [252]	-	10 – 20	0.3
Trimethylene carbonate/poly(ϵ-caprolactone) [394]	-	15 – 265	0.21 – 0.26
PLGA / Pluronic F127 [284]	-	Asymmetric: 0.05 and 50	0.4
Polysulfone [4]	-	≈ 0.0077 – 0.017[1]	0.9
Braided conduits [45]	-	65 ± 19	-
Genipin-cross-linked gelatin [69]	90.8 ± 0.9	-	-

Table 4.1: Published characteristics of a selection of existing tubular NRCs and sheaths, where porosity, pore size or thickness measurements are available.

weight cut off. This value is defined as the lowest molecular weight at which greater than 90% of a solute is retained by the material. Thus molecules with a greater molecular weight than the cut off value are effectively unable to diffuse through the membrane.

Oxygen and VEGF are the solutes of interest for this thesis. A molecule of O_2 has a molecular weight of 32 Da and a gaseous kinetic diameter of approximately 0.346 nm [253]. VEGF-A is secreted as a dimer [229] and most commonly exists as three key isoforms, $VEGF_{121}$, $VEGF_{165}$ and $VEGF_{189}$, that have differing molecular weights and kinetic radii. However, the model described in this thesis does not differentiate between these isoforms, so it is assumed that the molecular weight of a VEGF dimer in the model is 46 kDa [139, 154]. Varongchayakul et al. estimated the diameter of VEGF to be 4.12 nm and 5.20 nm for the monomer and dimer respectively [389]. These calculations suggest that both VEGF and oxygen molecules will not be filtered out by pore sizes of more than 0.005 µm or molecular weight cut offs of greater than approximately 46 kDa. The majority of existing porous materials currently used to manufacture tubular NRCs or sheaths have a pore size equal to or greater than this value (Table 4.1).

Type I collagen-based tubular matrices manufactured by Collagen Matrix, Inc. (Frankline Lakes, NJ), such as NeuroMatrix™, Neuroflex™ and NeuroMend™, have similar pore sizes to this and have already received FDA approval for clinical use [185]. These matrices are semipermeable and thus permit nutrient transfer, but due to the pore size are claimed to be occlusive to cells. NeuraWrap™ (Integra Life Sciences Corporation, Plainsboro, NJ) is a similar "nerve protector", designed to prevent neuromas and protect regenerating peripheral nerves and also constructed using Type I collagen. However, studies featuring the use of these commercial products are difficult to find.

Aebischer et al. found that porous tubular NRCs with a molecular weight cut off of 100 kDa resulted in larger numbers of regenerated myeli-

nated axons after 4 and 8 weeks than similar NRCs with a molecular weight cut off of 1000 kDa [4]. This suggests that smaller pore sizes could enhance regeneration: however, other studies also reported positive *in vivo* results using materials with much larger pore sizes than both of these materials tested by Aebischer et al.

For example, in 1985 Jenq and Coggeshall showed that implanting silicone tubes with two large rectangular holes (0.6 mm $\times$ 3 mm) in their walls into a rat sciatic nerve gap resulted in, on average, a greater number of axons in the gap after 8 weeks than when regular impermeable silicone tubes were used [169]. A later study by the same authors found that this type of permeable tube also increased the spanning distance of regenerating axons [170]. They speculated that these improvements could be due to the migration of supportive cells and promotion of ECM formation via the holes.

In another paper by Jenq et al., the holes in the silicone tubes were covered with filters with two different pore sizes (1.2 and 5.0 µm) before implantation into the sciatic nerve gap [171]. It was found that the 5 µm filter resulted in a higher percentage of successful regenerations (classed as cases in which at least 1000 axons span between the proximal and distal stumps). However, it seems doubtful that the "holey" silicone tubes used in these experiments are comparable to other porous sheaths materials, which are generally uniformly porous or at least porous throughout the length of the sheath. On the other hand, the authors pointed out that these results do suggest that infiltration of the conduit by some cells from the surrounding tissue may actually be beneficial to regeneration: the amount of solute diffusion would not differ between the two filter sizes but the larger pore size is likely to allow more cells to pass.

A study comparing the efficacy of a macropore collagen tube with that of semipermeable and impermeable collagen tubes found that the macropore tube produced significantly greater functional nerve regener-

ation across a rabbit sciatic nerve gap, as measured by electrophysiological analysis after 6 and 12 weeks [187]. However, the exact pore sizes used were not reported. Additionally, in both this study and the studies published by Jenq et al., the overall porosity ϵ (the ratio of void volume to material volume) was not recorded. Therefore it is unknown whether the overall porosity of the tubes could have influenced these results.

In 2009, Kokai et al. developed permeable ploy(caprolactone) (PCL) conduits with different wall thicknesses, pore sizes and porosities and investigated the impact of the structure upon glucose and protein diffusion *in vitro* [192]. They concluded that nerve guide walls 0.6 mm thick with porosity $\epsilon = 0.8$ and pore sizes of between 10 and 38 µm would provide minimal loss of lysozymes without prohibiting the diffusion of oxygen and other nutrients. With relevance for the work in this thesis, the results of this study indicated that out of the three factors tested (wall thickness, pore size and porosity), percentage porosity in fact had the biggest influence on both lysozyme and glucose diffusion.

Work by Chamberlain et al. suggests that the efficacy of porous and impermeable tubular NRCs could also be influenced by whether or not they are filled by an ECM-like material [66], similar to the EngNT manufactured in the Phillips lab. Specifically, Chamberlain et al. compared the regeneration produced by a silicone tube and both porous and impermeable collagen tubes, either left with an empty lumen or filled with a collagen-GAG copolymer, implanted in a sciatic nerve gap. The impermeable collagen tube filled with the collagen-GAG matrix produced the greatest number of large axons after 6 weeks. The authors speculated that this could have been due to the retention of important growth factors within the construct.

Similarly, in 2016 Ezra et al. studied the interaction between NRC wall porosity and the bioactivity of the central hydrogel filler in a mouse femoral nerve gap [107]. They found that impermeable constructs with a

neurite promoting filler matrix yielded better functional recovery than both the porous construct with the same filler, and impermeable and porous constructs with a standard collagen filler. These papers provide a contrasting perspective to the work of Jenq et al. and Kim et al. among others [69, 218, 394] which conclude that porosity is beneficial for nerve repair.

Asymetrically porous NRCs have also been manufactured and tested *in vivo*. For example, Oh et al. created hydrophilic porous tubes with nanopores (around 50 nm in size) on the inner surface, and micropores (around 50 µm) on the outer surface, so that approximately half way through the cross-sectional sheath the pore size changed [283, 284]. The authors showed that this design significantly improved measurements of nerve conduction velocity and myelinated axon diameter when compared to a silicone tube in a rat sciatic nerve repair model. Overall it was concluded that the hydrophilic asymmetric porous tubes achieved better results than their impermeable counterparts, and that this design could potentially improve *in vivo* outcomes by allowing vascular ingrowth through the micropores, whilst retaining growth factors but permitting nutrient diffusion through the nanopores. However, a direct comparison of asymmetric and symmetric porous structures was not undertaken.

Chang et al. found that asymmetrically porous PLGA NRCs resulted in a statistically significantly greater amount of regenerated axons in medial and distal sites compared to symmetrically porous and silicone NRCs [68]. Inflow and outflow of solutes were measured over 48h to assess the permeabilities of the materials. The asymmetric PLGA materials permitted the diffusion of glucose (with a molecular weight of 181 Da), lysozymes (14.4 kDa) and bovine serum albumin (62 kDa). Interestingly, the asymmetric materials exhibited asymmetric flow effects: in the case of glucose, the outflow rate was greater than the inflow rate until the 48h time point, and the outflow rate was greater than the inflow rate at all time points for both of the larger molecules. This effect was not observed for the sym-

metric porous PLGA. Thus Chang et al. suggested that this asymmetric flow profile could have benefited the repair process through the efficient disposal of waste materials in the early stages.

As well as the internal structure of the porous material, governed predominantly by the overall porosity and the size of the pores, the rate of flux of molecules from one side of a sheath or porous material to the other also depends upon the thickness of the sheath, denoted by T in this thesis. Early *in vivo* research concluded that thicker Silastic tubular conduits were more likely to result in neuroma formation [101]. Furthermore, work by Rutkowski and Heath found that the use of conduit wall thicknesses greater than 0.81 mm resulted in a decrease in axonal growth [337]. These results were also backed up by the previously mentioned finding by Kokai et al. that the optimal nerve guide design would include walls 0.6 mm thick [192].

NRCs currently under development [132, 133] are constructed using an impermeable silicone sheath with wall thickness $T = 0.25$ mm, or a NeuraGen™ wrap (made from collagen) with a similar thickness. Other studies have used tubular thicknesses ranging from 0.1 to 2.5 mm (Table 4.1). Based upon this and the data suggesting that large thicknesses may be detrimental for nerve repair, simulations in this chapter will explore wall thicknesses in the range of 0.1 to 1.5 mm.

In conclusion, a number of studies suggest that using porous materials to manufacture NRCs or NRC sheaths could have benefits for peripheral nerve regeneration [169, 170, 187, 218, 394]. In particular, the delivery of oxygen and nutrients is crucial for the survival of seeded cells and the success of neuronal regeneration, and this can be facilitated through the use of porous guidance constructs. Careful design of NRC sheaths could also contribute towards greater control over spatial distributions of growth factors and cells via the use of asymmetric or spatially varying porosity; it is possible that the sheath design could be tailored to complement the

chosen distribution or density of seeded cells.

However, the exact effect of introducing porosity appears to differ according to the scenario, with some studies reporting better results with impermeable sheaths or tubular NRCs [66, 107]. These contrasting results could be due to the positive effects of restricting the migration of inflammatory cells into the construct and the loss of important growth factors by diffusion out into the surround tissue. It has been suggested that porosity may be necessary for long nerve gaps, and in particular for those greater than 1 cm in length [107], whereas for shorter gaps the detrimental effect of growth factor loss and possible cell invasion could outweigh the benefits of enhanced access to nutrients. An additional consideration is whether the degree of porosity can influence the ingrowth of vasculature from the surrounding tissue; but Feng et al. reported that much larger pore sizes than those reported in the literature for NRC tubes and sheaths are required to enable significant blood vessel penetration (on the order of 400 to 700 μm) [115].

With the aim of understanding more about how spatio-temporal solute distributions within an NRC can be influenced by the characteristics of the surrounding sheath, in Sections 4.4 and 4.5 the impact of combinations of different porosities and thicknesses of NRC sheath upon cell survival and the generation of VEGF gradients will be investigated via model simulations, and the results contrasted against simulations of NRCs with impermeable sheaths.

4.2.2 Modelling solute diffusion in a porous sheath

Solute diffusion in a porous sheath is dependent upon the microstructure and porosity ϵ of the porous material. This dependency will need to be incorporated into the mathematical framework to evaluate the impact of different porosities and thicknesses of porous sheaths upon cell survival and VEGF gradients.

The transport properties of solutes in porous media can be described

in terms of macroscopic equations, derived via homogenization techniques that rely on the assumption that the pore microstructure is periodic [89], and which involve splitting the porous domain into a void or fluid phase Ω_κ and a material phase. In this thesis, this homogenised approach was chosen because it allows the simulation of porous solute transport without the need for explicitly generating and simulating diffusion through complex porous geometries. The explicit approach would likely require direct imaging of the geometry and would be far more computationally intensive.

In particular, a volume averaging approach can be used to derive the transport equations for solutes diffusing through porous material, as previously outlined by Quintard and Whitaker [323, 324]. Use of this method relies on the assumption that the porous material is homogeneous in that it can be modelled as a series of identical averaging volumes (and therefore it is also taken that the porosity does not vary spatially). Using this assumption, the homogenised solute concentration s, which is obtained by averaging over a representative volume of porous materials that includes both the fluid or void phase Ω_κ and the material phase, can be related to the solute concentration in the fluid phase s_κ via $s = \epsilon s_\kappa$.

Via volume averaging [324] (or other homogenisation techniques) the following equation for the diffusion and reaction of the generic solute in the fluid or void phase s_κ of the porous domain is obtained:

$$\epsilon \frac{\partial s_\kappa}{\partial t} = D_{\text{eff}} \nabla^2 s_\kappa + \epsilon R(s_\kappa) \,, \tag{4.1}$$

where s_κ is the solute concentration in the fluid phase, $R(s_\kappa)$ is the function determining the reactions of the solute in the fluid phase, and the effective diffusivity is given by

$$D_{\text{eff}} = K(\epsilon) D_\kappa \,, \tag{4.2}$$

where D_κ is the molecular diffusivity of s_κ in the fluid or void phase, and $K(\epsilon)$ is the porosity coefficient. In this thesis, it is assumed that the void

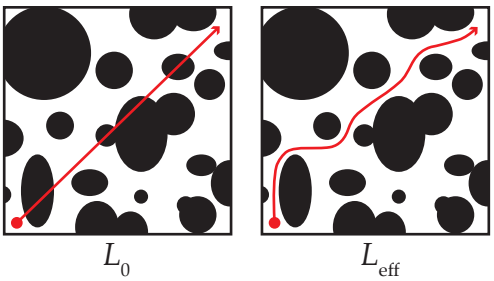

Figure 4.1: Visualisation of the straight-line path length L_0 and the effective path length L_{eff} in a porous medium.

fraction of the NRC sheath is completely filled with water-like interstitial fluid *in vivo*, and therefore the molecular diffusion coefficients for oxygen and VEGF will be equal to their respective molecular diffusivities in media or water.

Attempts have been made to determine the relationship between effective diffusivity and molecular diffusivity via both empirical and theoretical methods. Theoretical models typically incorporate two key elements: the void fraction or porosity of the porous material ϵ, and the diffusive tortuosity of the material τ. Tortuosity is defined here as the square of the ratio of the average length of the diffusive path of a molecule through a porous medium L_{eff} to the straight-line path length L_0 (Figure 4.1), which is determined by the internal geometry of the porous material [88, 106]:

$$\tau = \left(\frac{L_{\text{eff}}}{L_0} \right)^2 . \tag{4.3}$$

Typically tortuosity $\tau > 1$ because the diffusive path length of a molecule through a porous geometry will be greater than the straight-line path taken in the absence of the porous material.

The study of solute diffusion in soil, which can be modelled as a granular porous medium, led to the commonly used definition of effective diffusivity shown in Equation (4.2) and the definition of the porosity coefficient

$K(\epsilon)$ as follows [106, 382]:

$$K(\epsilon) = \frac{\epsilon}{\tau}. \tag{4.4}$$

Often the value of the porosity ϵ can be quantified for a specific material using imaging, as explained and demonstrated for various prospective sheath materials in the previous subsection and presented in Table 4.1. Tortuosity must be a function of porosity and molecular size because both of these variables will impact the diffusive path of a molecule. Boving and Grathwohl proposed that once the molecular size nears the that of the pore size, an additional constrictivity factor, κ, must be incorporated to account for the impact of pore cross sectional area upon diffusion [50]. This gives the following modified relationship:

$$D_{\text{eff}} = \frac{\epsilon\kappa}{\tau} D_{\kappa}. \tag{4.5}$$

However, in this thesis it is assumed that the pore size of the simulated sheath materials will be larger than the size of VEGF and oxygen molecules, and therefore this adjustment will not be applied. This is in accordance with the fact that the majority of sheath materials reviewed in Table 4.1 have pore sizes much greater than 0.005 µm, which was identified in Section 4.2.1 as the approximate threshold for permitting the diffusion of both VEGF and oxygen. The model of porous solute diffusion used in this thesis does not explicitly take into account pore size, instead modelling solute transport as a function of porosity and tortuosity alone.

Another consideration is the effect of percolation. The percolation threshold of a porous material here refers to the porosity value after which the connectivity of the void space of the structure increases dramatically with a small increase in porosity. In their study of tubular porous PCL nerve guides with varying porosities, Kokai et al. found that those with a porosity of 50% contained closed, isolated pores, whereas 80% porous guides consisted predominantly of interconnected pores. This suggests

that the percolation threshold, at least for porous PCL guides of this type, lies somewhere between these two values.

4.2.2.1 Modelling tortuosity

Tortuosity τ is difficult to determine empirically, and therefore expressions of diffusive tortuosity as functions of porosity have been derived from simplified models and comparison to data. In this subsection, the most relevant models will be described (Table 4.2) and compared.

The concept of tortuosity is also used to study fluid flow and electrical conductivity through porous materials. Hydraulic tortuosity τ_h is defined as the square of the ratio of the average streamline length of fluid flow through a porous medium to the straight-line streamline length; similarly, electrical tortuosity τ_e is the square of the ratio of the average path length for electrical flow to the straight-line length. Thus some existing theoretical models of tortuosity were derived by modelling or measuring the effect of porous materials on fluid flow or electrical conductivity.

Although theoretical expressions for hydraulic, electrical and diffusive tortuosity have typically been used interchangeably in the past, more recent work suggests that these parameters are not necessarily the same: Ghanbarian et al. used a Wheatstone bridge model and theoretical methods to conclude that $\tau \approx \tau_e < \tau_h$ in the case of materials with variable pore size [136]. The work in this thesis aims to model diffusive tortuosity; additionally, the majority of the materials currently used to construct NRC sheaths or tubular constructs exhibit variable pore size (Table 4.1). Therefore, following on from this result and in order to narrow the breadth of model choice, models of hydraulic tortuosity were not considered.

Evidence does suggest that electrical and diffusive tortuosity are identical or at least broadly similar [114, 129, 136]; therefore a small number of key electrical tortuosity models are also included in the following review as potential candidates for the theoretical framework described in this thesis.

Additionally, models of tortuosity are generally derived based upon

the assumption that either the porous material is saturated, so the void fraction of the material is entirely filled by fluid, or unsaturated, in which the void fraction contains both fluid and pockets of air. In this thesis it is assumed that the void fraction of the sheath is entirely filled with fluid and therefore only models relating to saturated materials will be included in this brief review.

Theoretical models of tortuosity rely on assumptions about the composition of the porous media. The assumption that the porous material can be modelled as a bed of randomly overlapping spheres, for example, is often used when modelling granular material such as soil. Weissberg et al. derived an analytical description of the upper bound of τ as a function of ϵ by assuming that the porous medium consists of a bed of randomly overlapping spherical particles [409]. The resulting expression can be written in a general form with parameter q,

$$\tau = 1 + q \ln(\epsilon), \tag{4.6}$$

where $q = 0.5$ in the Weissberg model, which applies to both uniform and non-uniform sphere diameters. This model was found to approximate experimental results, albeit imperfectly. The authors concluded that the calculated bound would serve as a useful estimate for use in predictive studies.

Tsai and Strieder derived the same expression as Equation (4.6) but with $q = 2/3$ by assuming that the porous media is composed of randomly overlapping solid 3D fibers that can be represented as cylinders [383]. Other authors also used models of oriented cylinders to investigate the transport properties of fibrous porous materials [190, 379].

Pisani et al. derived a model for tortuosity that incorporates a shape factor α_{P} that depends upon the cross section and volume of the solid objects that are assumed to make up the porous medium, as well as the "average distance necessary to by-pass" them [316]. In the case where the solid objects are assumed to be spherical, $\alpha_{\mathrm{P}} = 0.75$. For $\alpha_{\mathrm{P}} > 1$, the function

$K(\epsilon, S)$ is positive only for values of ϵ above a percolation threshold ϵ_0 where $\epsilon_0 = (\alpha_P - 1)/S$.

However, as noted by the authors, the shape factor α_P is not always easy to evaluate as it depends upon a qualitative evaluation of the average distance that a molecule is required to travel to avoid one of the solid particles assumed to make up the porous material.

In 1837, Maxwell proposed the first model of electrical tortuosity τ_e [245] (Table 4.2), which assumed that the material is composed of a dilute suspension of non-conducting spheres. This model is still commonly cited today.

One of the key drawbacks of many of the theoretical models of diffusivity is that they are generally not validated against experimental data; certainly most of them have not been compared to a large range of experimental results from different material types. In 2012, Chou et al. measured the diffusivity of three soil types at different levels of water saturation and compared the values to theoretical models [77]. They found that the commonly used Millington and Quirk model of hydraulic tortuosity ($\tau_h = \epsilon^{-1/3}$) actually resulted in the largest root mean square error values across all three solid types, providing further evidence that hydraulic tortuosity values do not apply directly to the diffusive scenario as well. However, solute diffusion in biomaterials and porous sheath materials may differ significantly from that in soils, so this conclusion can only act as a hint to the accuracy of the tested models.

Delgado recorded measurements of diffusivity in packed beds of silica sand and compared them to the corresponding diffusivities in free fluid [96]. Sand granules with average diameters ranging from 0.110 mm to 0.496 mm were used. The experimental values of τ were compared against four different theoretical models: the models proposed by Archie (Table 4.2) with $m = 0.4$ and Weissberg (Equation (4.6) with $q = 0.5$) both closely agreed with the empirical measurements.

Reference	Expression, $\tau(\epsilon)$	Derivation method	Assumption
Weissberg (1963) [409]	$1 - \frac{1}{2}\ln(\epsilon)$	Theoretical (Diffusive)	Overlapping spheres
Tsai & Strieder (1986) [383]	$1 - \frac{2}{3}\ln(\epsilon)$	Theoretical (Diffusive)	Cylinders
Beeckman (1990) [35]	$\frac{\epsilon}{1-(1-\epsilon)^{1/3})}$	Theoretical (Diffusive)	Heterogeneous catalyst
Pisani (2011) [316]	$\frac{1}{1-S(1-\epsilon)}$	Theoretical (Diffusive)	Flexible (relates to shape factor α_P)
Iversen & Jorgensen (1993) [164]	$\epsilon(1+k(1-\epsilon))$	Empirical (Diffusive)	Different sediment types (see text)
Rutkowski & Heath (2002) [336]	$\epsilon^{-4.1}$	Empirical (Diffusive)	Porous Poly-D,L-lactide (see text)
Klemens (1990) [190]	$\frac{3\epsilon}{4\epsilon-1}$	Theoretical (Diffusive)	Cylindrical
Maxwell (1837) [245]	$1 + \frac{1}{2}(1-\epsilon)$	Theoretical (Electrical)	Non-conducting spheres
Archie (1942) [17]	ϵ^{1-m}	Empirical (Electrical)	Sand formation cores

Table 4.2: Existing relevant analytical models of tortuosity as a function of porosity ϵ. The derivation method refers to to whether the model was derived using a theoretical model or via experimental/empirical means, and whether the model refers to diffusive or electrical tortuosity (which are treated as interchangeable for the purpose of this thesis). The Assumption column refers to the assumptions made about the structure of the porous material in each case.

Beeckman created a model of a heterogeneous porous material consisting of a travel process with a branching probability dependent upon the properties of the material [35]. The results of this model were used to derive an expression for τ (Table 4.2). This expression reaches a maximum value of $\tau \to 3$ when $\epsilon \to 0$, which may be insufficient to describe particularly tortuous materials.

Other authors have used empirical data to derive expressions for τ (Table 4.2). Rutkowski and Heath conducted diffusion experiments to derive the effective diffusivities of oxygen and glucose through membranes of different porosities [336]. The membranes were made of Poly-D,L-lactide, and salt crystals of size less than 106 µm were used to create pores within the material. A logarithmic plot of the experimental data against the ratio of the effective to bulk or molecular diffusivities was then plotted to derive the power law relationship between the two: $D_{\text{eff}}/D_{\kappa} = \epsilon^{5.1}$. However, in this case the authors appear only to have used materials with approximate porosity $\epsilon > 0.86$ to derive their model of effective diffusivity. This casts doubt on the validity of using this approximation for modelling materials with a lower porosity than this, and extrapolating this model into the low ϵ regime demonstrates a stark departure from the other analytical models mentioned here (Figure 4.2).

Iversen and Jorgensen measured tracer diffusion coefficients in seawater and in different sediments to arrive at a general expression for τ (Table 4.2) [164]. The free parameter k was determined to take different values according to the sediment type: $k = 3$ for clay-silt sediments and $k = 2$ for sandy sediments.

All of the theoretical analytical models of tortuosity rely on assumptions about the structure of the porous media, and the expressions that were derived via experimental techniques are also inherently dependent upon the geometry of the material that was used. Therefore when making predictions using these models it is necessary to select the most relevant

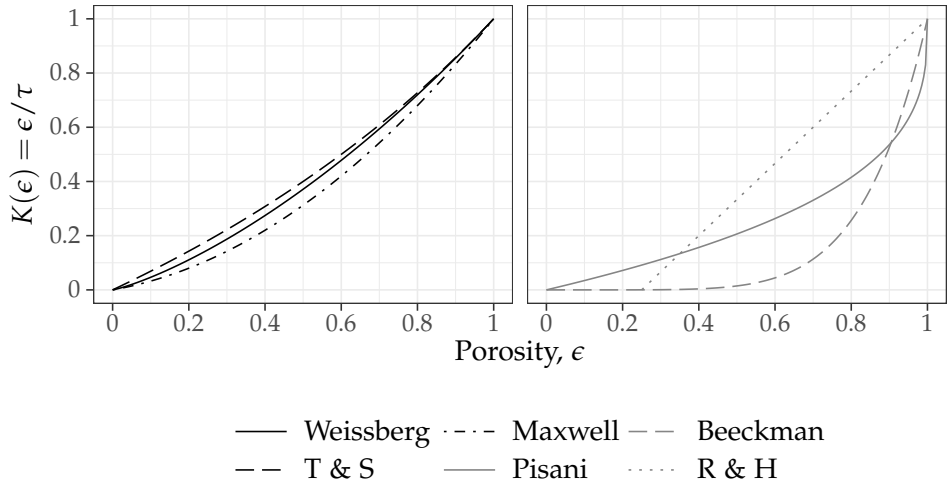

Figure 4.2: Comparison of estimates for the porosity coefficient $K(\epsilon)$ using a range of analytical models for tortuosity $\tau(\epsilon)$. Here the Pisani model uses $\alpha_P = 0.75$ corresponding to spherical obstructions. The Rutkowski and Heath (R & H) approximation differs considerably from the others, particular for $\epsilon < 0.8$. T & S denotes the Tsai and Strieder model.

expression for the given porous material of interest.

The structure of the porous materials used to construct NRCs and NRC sheaths varies widely according to the material used and method of creating porosity, as demonstrated by SEM imaging. Some appear to have a globular structure that could be approximated theoretically by a body of overlapping spheres; others are distinctly fibrous in nature.

In this thesis, the results of simulations run using a selection of the models of nutrient transport outlined in Table 4.2 to represent porous materials with different structure types are presented. In fact, it was found that the model of tortuosity used made only slight differences to the results in the specific context of the NRC sheath (Figures 4.15 and 4.16). A range of values of sheath thickness T and porosity ϵ are used to predict which parameter combinations may produce desirable cell and growth factor distributions *in vivo* for different porous structure types.

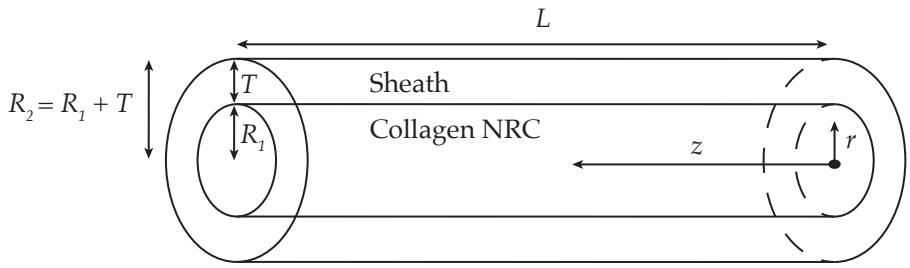

Figure 4.3: Schematic of the cylindrical NRC geometry with surrounding sheath.

4.3 A mathematical model of a complete nerve repair construct

A NRC can be represented simplistically as a cell-seeded collagen cylinder; therefore the functional forms and parameters of the previously described model (Chapter 3) that correspond to behaviour of cell and solutes in collagen gel can be applied to a cylindrical geometry to model cell-solute interactions within a NRC.

The geometry used in this thesis is composed of an inner cylinder of radius R_1 representing the collagen NRC and an outer acellular layer of thickness T representing the sheath (Figure 4.3), such that the total radius of the geometry is given by $R_2 = R_1 + T$. Radial symmetry is assumed. Details of the geometry and mesh generated in COMSOL are provided in Section 4.3.2.

4.3.1 The model equations and initial and boundary conditions

The parameterised governing equations for viable cell density n, oxygen concentration c and VEGF concentration v in the collagen gel, which were developed in Chapter 3, are directly translated to model cell-solute interactions within the cell-seeded collagen nerve repair construct ($r \leq R_1$) as

follows:

$$\frac{\partial n}{\partial t} = \beta c n \left(1 - \frac{n}{n_{\max}}\right) - \delta n \,, \tag{4.7}$$

$$\frac{\partial c}{\partial t} = D_{c_g} \nabla^2 c - M n \frac{c}{c_{1/2} + c} \,, \tag{4.8}$$

$$\frac{\partial v}{\partial t} = D_{\mathrm{v_g}} \nabla^2 v + \alpha n \left(\frac{V_m + 1}{2} - \frac{V_m - 1}{2} \tanh k_\alpha (c - c_h)\right) - d_{\mathrm{v}} v \,. \tag{4.9}$$

The parameter values used are the parameters obtained via the previously described process of parameterisation and a review of the existing literature, as per Tables 3.9 and 3.10. As in Chapter 3, this model incorporates the processes of solute transport and cell proliferation and death, but neglects cell motility. It is assumed that therapeutic cell migration through the gel over the simulated time scale of 0 to 5 days will be negligible.

As described in Section 4.2, the sheath surrounding the main NRC can be made of porous or impermeable materials. A impermeable sheath can be represented simply within the mathematical framework as a set of zero-flux boundary conditions along the curved edge of the construct, to reflect the impermeability of the material:

$$\frac{\partial n}{\partial r} = 0, \ \frac{\partial c}{\partial r} = 0 \text{ and } \frac{\partial v}{\partial r} = 0 \text{ at } r = R_1. \tag{4.10}$$

On the other hand, incorporation of a porous sheath into the model involves consideration of both the thickness T of the sheath and the transport properties of the sheath material (Section 4.2.2). In this thesis, porous sheaths are modelled explicitly by including another cylindrical outer layer of thickness T into the NRC geometry (Figure 4.3). Here c_s and v_s are defined as the oxygen and VEGF concentrations within the fluid portion of the sheath material. It is assumed that no cells are initially seeded within the sheath and that the seeded cells will not migrate into the sheath material over the studied time period; therefore the cell governing equation is not applied to the sheath portion of the geometry. Assuming that the

void fraction of the porous material is filled with interstitial fluid that has the same diffusive properties as water, the porosity ϵ is defined as the ratio of the fluid volume to the total bulk volume of the material, and the two governing equations for the sheath region ($R_1 < r \leq R_2$) are as follows:

$$\epsilon \frac{\partial c_s}{\partial t} = D_{c_s}(\epsilon, D_{c_m}) \nabla^2 c_s \,, \tag{4.11}$$

$$\epsilon \frac{\partial v_s}{\partial t} = D_{v_s}(\epsilon, D_{v_m}) \nabla^2 v_s - \epsilon d_v v_s \,. \tag{4.12}$$

The model used to define the effective diffusivities of oxygen and VEGF within the sheath, $D_{c_s}(\epsilon, D_{c_m})$ and $D_{v_s}(\epsilon, D_{v_m})$, can be varied to represent different types of porous material structure according to Table 4.2.

Boundary conditions are assigned to reflect the case in which the NRC is implanted *in vivo*. It is assumed that the proximal and distal ends of the NRC at $z = 0, L$ are left open; previously, the use of non-permeable, capped ends on autografts resulted in delayed revascularisation [42], and NRCs manufactured in the Phillips lab are not usually capped. Concentration or Dirichlet boundary conditions are applied at either end of the cylinder for both oxygen concentration and VEGF concentration:

$$c = c_{\text{tissue}} \text{ at } z = 0, L, \tag{4.13}$$

$$v = v_{\text{tissue}} \text{ at } z = 0, L. \tag{4.14}$$

Here c_{tissue} and v_{tissue} are the oxygen and VEGF concentrations in the surrounding tissue respectively. Human tissue oxygen concentrations for various tissue types (muscle, liver, intestine and lung among others) measure in the range of 4 to 7% [64] and due to a lack of corresponding data it is assumed that rat tissue oxygen concentrations will be similar; therefore $c_{\text{tissue}} = 5\%$ is used for the majority of the simulations in this chapter. However, sensitivity analysis was also carried out to investigate the possible impact of differences in c_{tissue} (Figure 4.13).

Existing measurements of tissue VEGF concentrations are generally

limited to specific tissues: for example, 9.9 to 47.1 ng/g lung tissue [1], approximately 8 to 300 ng/g in human corneal tissue depending on whether the tissue was healthy or inflamed [309], and approximately 40 ng/g to 9000 ng/g in cancerous tissue [374]. The wide variations in these values suggest that VEGF concentration is largely context specific: it would be desirable to obtain measurements of VEGF concentration in the peripheral nerve repair context in the future (see Chapter 6 for additional comments on this). VEGF concentrations in the serum (17 to 298 pg/ml) and plasma (27 to 30 pg/ml) of healthy controls have also been measured [199]. Changes in v_{tissue} of up to 1 ng/ml did not result in detectable differences in simulation outputs (Figure 4.14). Based upon this sensitivity analysis, $v_{\text{tissue}} = 0$ ng/ml was used in the majority of the subsequent simulations.

At the internal sheath-NRC boundary, boundary conditions enforcing continuity of concentration and flux are applied:

$$c_s = c \ \text{ at } r = R_1, \tag{4.15}$$

$$v_s = v \ \text{ at } r = R_1, \tag{4.16}$$

$$D_{c_s}\frac{\partial c_s}{\partial t} = D_{c_g}\frac{\partial c}{\partial t} \ \text{ at } r = R_1, \tag{4.17}$$

$$D_{v_s}\frac{\partial v_s}{\partial t} = D_{v_g}\frac{\partial v}{\partial t} \ \text{ at } r = R_1. \tag{4.18}$$

On the external boundaries of the sheath, concentration boundary conditions are applied for both oxygen and VEGF concentrations as follows:

$$c_s = c_{\text{tissue}} \ \text{ at } r = R_2, \tag{4.19}$$

$$v_s = v_{\text{tissue}} \ \text{ at } r = R_2, \tag{4.20}$$

$$c_s = c_{\text{tissue}} \ \text{ at } z = 0, L, \ R_1 \leq r \leq R_2, \tag{4.21}$$

$$v_s = v_{\text{tissue}} \ \text{ at } z = 0, L, \ R_1 \leq r \leq R_2. \tag{4.22}$$

The initial oxygen concentration $c_0 = c(t = 0)$ within the NRC and the sheath was set at 21% uniformly across the geometry to reflect storage

oxygen conditions, although sensitivity analysis was conducted to assess the impact of changing this parameter (Figure 4.11). The initial VEGF concentration $v_0 = v(t = 0)$ within the NRC and the sheath was set at 0 ng/ml. Sensitivity analysis showed that altering the value of v_0 up to 1000 pg/ml made little difference to the simulation results (Figure 4.12).

The initial distribution of the seeded therapeutic cells $n_0 = n(t = 0, z)$ was varied to assess the impact of a range of cell seeding strategies on cell survival and distributions of VEGF. Both uniform and non-uniform distributions were used in combination with different densities of cells. Non-uniform distributions were defined as functions of the lengthwise coordinate z, and therefore maintained radial symmetry.

4.3.2 The nerve repair construct geometry in COMSOL

An axisymmetric 2D geometry was created in COMSOL Multiphysics with length $L = 15$ mm and internal radius of $R_1 = 0.25$ mm to match the dimensions of NRCs under development (Figure 4.4). An assumption of radial symmetry allows the model to represent a cylindrical NRC. An additional outer layer of varying thickness T was incorporated to represent a porous sheath when appropriate; otherwise zero-flux boundary conditions were used to represent a impermeable sheath.

A fine mesh was generated to cover these geometries. The maximum mesh size was set according to convergence studies; further mesh refinement was performed but this made no detectable difference to the simulation results. Furthermore, the size of the mesh did not prohibit the simulation time. Each simulation of a period of 1 day took approximately 20 seconds, although the run time varied according to the number of metrics calculated simultaneously.

The equations were solved using COMSOL Multiphysics via the BDF method as outlined previously in Section 3.5.2.

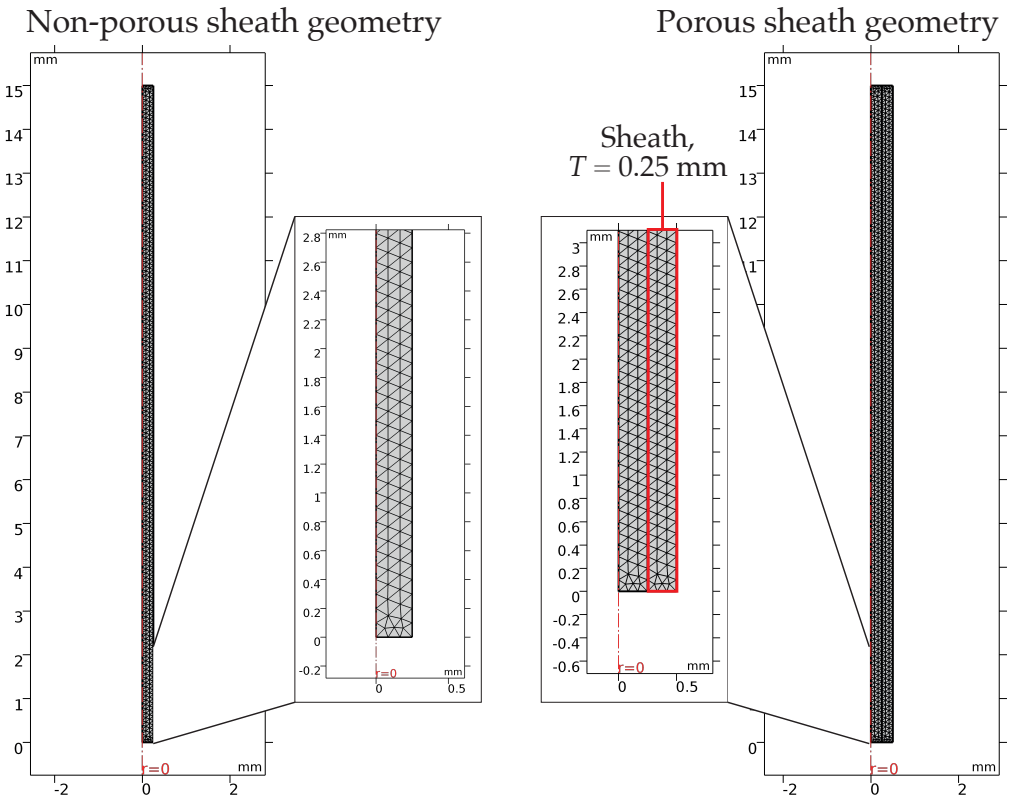

Figure 4.4: Cross section of the mesh generated over the axisymmetric NRC geometry in COMSOL. The longitudinal centreline of the cylindrical NRC was used as the axis of symmetry. The maximum element size across the geometry was set at 0.1 mm. In total, the mesh consists of 908 triangular elements, 306 edge elements and 4 vertex elements, with 608 mesh vertices.

4.4 Simulations of uniformly seeded nerve repair constructs

In this section, the impact of different uniform seeded cell densities upon cell survival and the generation of VEGF gradients is investigated in the context of NRCs with both impermeable (Section 4.4.1) and porous (Section 4.4.2) sheaths. The density at which the cells are uniformly seeded is here denoted n_0. Although some experimental work has been done to identify which densities may increase axonal regeneration during peripheral nerve repair (Section 1.3), there is currently no consensus on how the density of uniformly seeded therapeutic cells may affect cell survival and

overall repair efficacy, both for peripheral nerve repair and across tissue engineering in general.

One of the aims of this thesis is to identify cell seeding strategies that could increase cell survival and optimise VEGF gradients within NRCs. The prediction of possible optimal ranges for the initial seeding cell density n_0 in the case of uniform seeding strategies would be useful for future experimental designs and model validation.

Hence here $\arg\max_{n_0} \bar{n}$, the value of n_0 that maximises the mean cell density across the central NRC geometry $\bar{n}$, is defined as follows:

$$\arg\max_{n_0} \bar{n} = \{n_0 \mid \bar{n}(n_0) = \max_{n_0'}\{\bar{n}(n_0')\}\} . \tag{4.23}$$

The standard deviation of the cell density across the NRC geometry is denoted n_{SD}.

Similarly, the values of n_0 that maximise the mean VEGF concentration $\bar{v}$ and the standard deviation of the VEGF concentration v_{SD} across the central geometry (excluding the NRC sheath) are defined by:

$$\arg\max_{n_0} \bar{v} = \{n_0 \mid \bar{v}(n_0) = \max_{n_0'} \bar{v}(n_0')\} , \tag{4.24}$$

$$\arg\max_{n_0} v_{\mathrm{SD}} = \{n_0 \mid v_{\mathrm{SD}}(n_0) = \max_{n_0'} v_{\mathrm{SD}}(n_0')\} . \tag{4.25}$$

Both gradients and concentrations of VEGF are important for sprouting angiogenesis [134]. In this thesis, the standard deviation of the VEGF concentration values is used as a measure of the steepness of the gradients of VEGF over the construct. As demonstrated in Figure 4.10, simulated gradients of VEGF in NRCs uniformly seeded with a impermeable sheath occur predominantly in the lengthwise z direction, with a clear peak in the centre of the construct. This means that greater values of v_{SD} tend to correspond to steeper gradients of VEGF.

Figure 4.5 provides an example of the progression of typical simu-

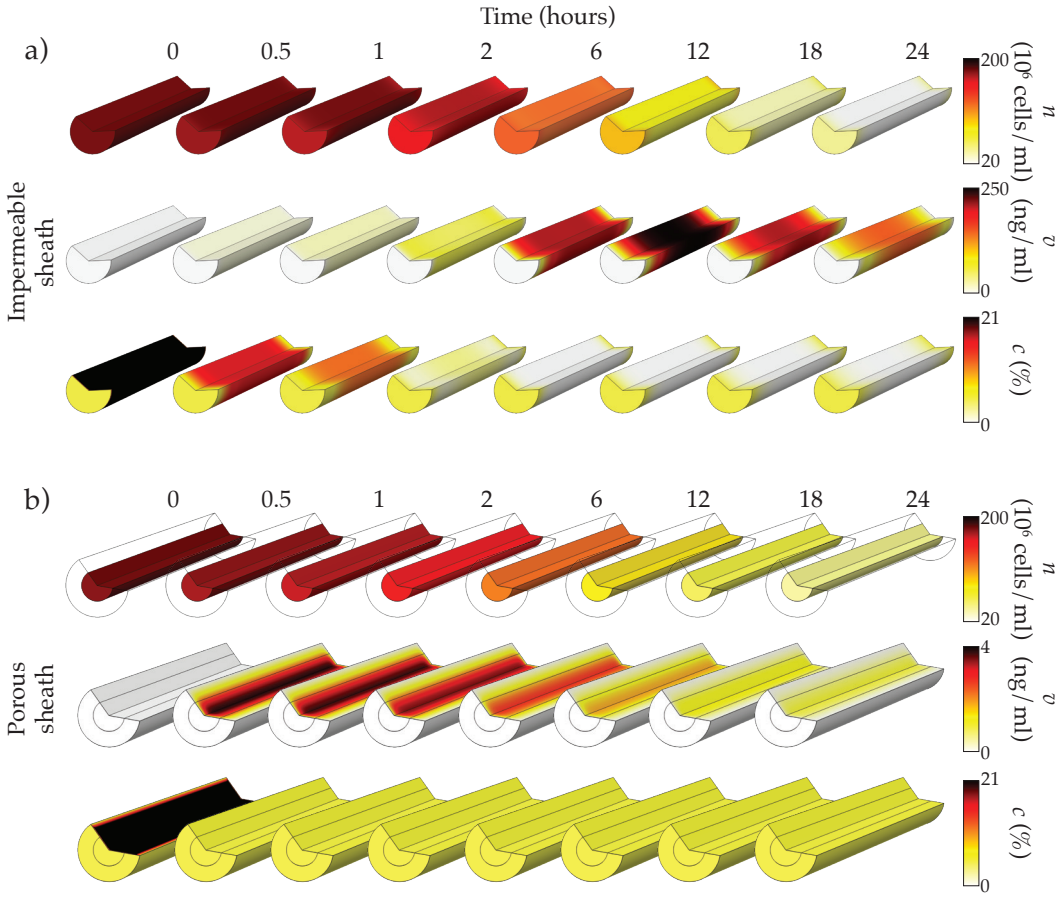

Figure 4.5: Example simulations of cell-solute interactions over time within uniformly seeded NRCs with an impermeable sheath (a) and a porous sheath (b). An initial uniform distribution of 178×10^6 cells/ml was used in both cases. a) In the NRC wrapped in an impermeable sheath, VEGF and oxygen can only diffuse in or out at the proximal and distal ends of the geometry, resulting in more distinct lengthwise gradients than in the porous sheath case. b) In the NRC wrapped in a porous sheath, the cells occupy only the central collagen NRC portion of the geometry, whereas VEGF and oxygen are free to diffuse into the outer sheath region. The porous sheath allows much quicker diffusion of oxygen into the NRC, but also permits faster diffusion of VEGF out of the NRC, resulting in much lower VEGF concentrations in the central geometry (note the difference in the scale of the VEGF legend in comparison to that of (a)). The porous sheath was simulated with porosity $\epsilon = 0.8$ and sheath thickness $T = 0.25$ mm.

lations over time for both the porous and impermeable sheath scenarios. These demonstrate how the spatial distributions of n, c and v change over time.

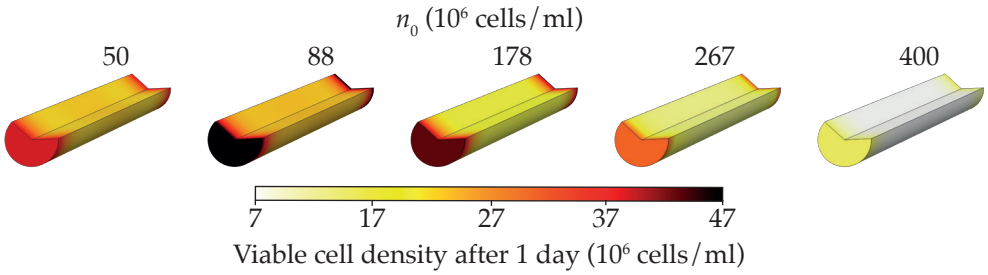

Figure 4.6: The simulated distribution of cells across the NRC geometry after 1 day is predominantly uniform regardless of the value of n_0 used for the uniformly distributed seeded cells. Higher viable cell densities at the ends of the geometry reflect greater access to oxygen via diffusion through the open ends of the NRC, as captured by the boundary conditions.

4.4.1 Impermeable sheath

First of all, a range of different uniform initial cell densities were used in combination with the model described in Section 4.3 to simulate cell-solute interactions across the NRC geometry with boundary conditions representing a impermeable sheath (Equation (4.10)). The simulated range of initial cell densities (10 to 400 $\times$ 10^6 cells/ml) was chosen to represent the range currently used in standard experimental models in the Phillips lab (100 to 400 $\times$ 10^6 cells/ml) and to cover the densities reported in the literature [141, 264, 337].

The results showed that the distribution of the cells along the length of the NRC remains relatively uniform at each time step (Figure 4.5) and for each initial cell density (Figure 4.6), apart from an increase in the density of viable cells at either end of the construct, corresponding to the higher concentration of oxygen and thus greater rate of proliferation in these regions, as determined by Equation (4.7). Therefore the mean viable cell density across the entire geometry $\bar{n}$ was used as a measure of cell survival. The observation of higher cell densities at the ends of the simulated NRCs aligns with an *in vivo* experimental study which reported a similar phenomenon around the peripheral edges of cell-seeded conduits [264], and corresponds to the regions with the greatest access to oxygen.

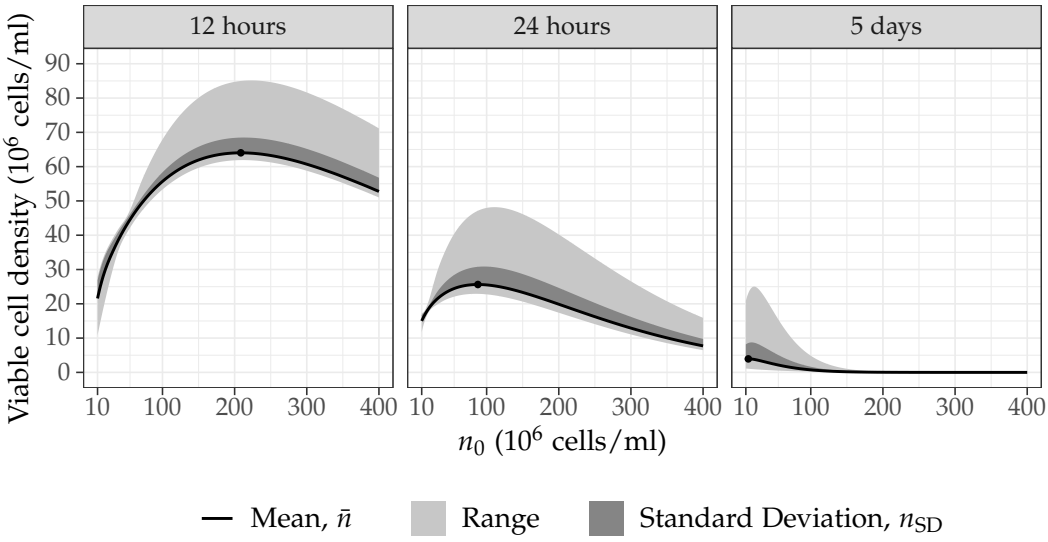

Figure 4.7: Simulated viable cell density across the NRC geometry for different uniform initial cell densities; black points indicate the positions of the maximum values of $\bar{n}$, the mean viable cell density across the geometry. After 12 hours, $\arg\max_{n_0} \bar{n} = 200 \times 10^6$ cells/ml. After 1 day, $\arg\max_{n_0} \bar{n} = 88 \times 10^6$ cells/ml. After 5 days, $\arg\max_{n_0} \bar{n} = 13 \times 10^6$ cells/ml.

Examination of how $\bar{n}$ varies over time reveals that over the initial 12 hours NRCs seeded using the highest cell densities maintain the highest values of $\bar{n}$ (Figure 4.19, red line); however, this pattern is somewhat reversed by the 1 day time point (Figure 4.7).

The simulated mean viable cell density $\bar{n}$ across the NRC after 1 day (Figure 4.7) increases monotonically as the seeding cell density n_0 increases from 10×10^6 cells/ml until a maximum is reached at 88×10^6 cells/ml. From there, $\bar{n}$ decreases to a minimum at $n_0 = 400 \times 10^6$ cells/ml.

The survival rate of the cells after 1 day (Figure 4.8) varies from around 100% for very low seeded cell densities (10×10^6 cells/ml) to less than 10% for seeded cell densities greater than 200×10^6 cells/ml. Thus it appears that seeded cell densities of 100×10^6 cells/ml or less offer the best efficiency in terms of reducing the number of wasted cells. Although very low seeded cell densities are predicted to be most efficient in terms of the survival rate, the total number of cells after 1 day is relatively low and may

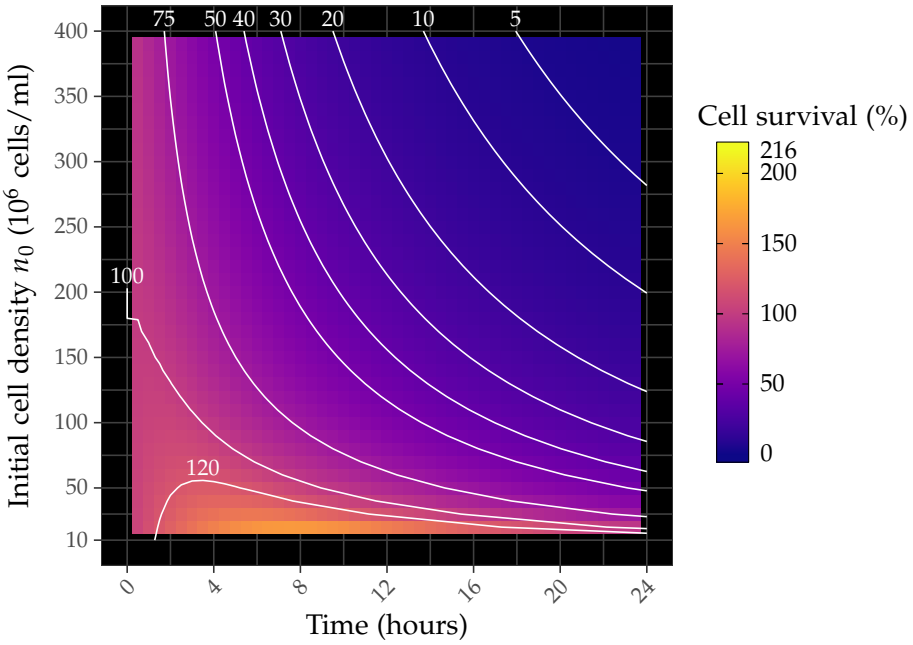

Figure 4.8: Cell survival, expressed as a % of the total number of cells initially seeded in the NRC. Low seeding cell densities result in higher % survival.

not provide the desired degree of support to the scaffold. Additionally, the model was trained and validated on cell densities with a minimum value of $n_0 = 39 \times 10^6$ cells/ml; therefore extrapolating to very low seeding cell densities may provide inaccurate results.

All the initial cell densities simulated produce 30% survival or less after 5 days. In particular, in cases where the initial cell density was greater than 100×10^6 cells/ml, the vast majority of cells have died after 5 days with only 1% or less of the original number of viable cells remaining. Experimentally measured seeded cell survival times for transplanted stem cells in peripheral nerve repair vary from around 10 days to on the order of months [400], however the simulations run in this section do not take into account the additional delivery of oxygen via new blood vessels, and therefore likely underestimate the survival of cells. This aspect is considered as part of the model of sprouting angiogenesis presented in Chapter 5.

The simulations were run up to the 5 day time point. After 5 days,

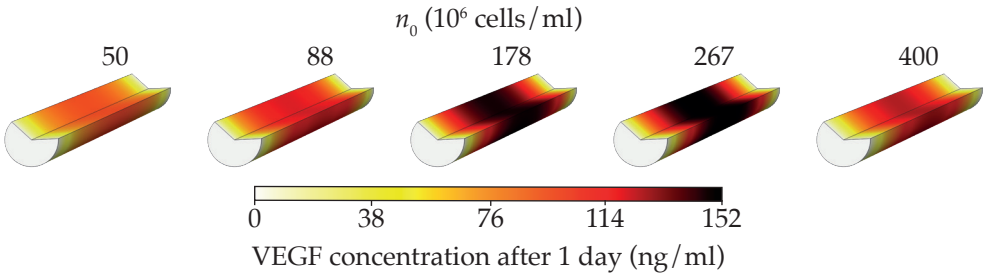

Figure 4.9: The simulated gradient of VEGF after 1 day from the ends of the NRC to the centre increases in steepness as the initial density of the uniformly seeded cells increases up to $n_0 = 267 \times 10^6$ cells/ml. VEGF concentrations of 0 ng/ml at either end of the geometry reflect the application of the boundary condition $v_{\text{tissue}} = 0$.

the cell populations have died off significantly, regardless of the density of the cells seeded (Figure 4.7). However, the model was not parameterised against data for time points beyond 1 day, casting doubt on the validity of extrapolating the model in this manner.

The VEGF concentration over the construct develops into a clearly defined gradient over time, with the largest concentration of VEGF consistently located in the centre of the construct (Figure 4.9). The simulated values of VEGF are within the range of those cited in the literature [1, 309, 374] after the cited values are converted to ng/ml using the approximate density of the compressed collagen NRC (between 0.5 and 3 g/ml). However, as previously mentioned, measurements of VEGF concentration in the peripheral nerve repair scenario have not yet been carried out and it is likely that VEGF concentrations in tissue are highly context specific.

The simulated mean VEGF concentration $\bar{v}$ across the NRC geometry after 1 day achieves a maximum at $\arg\max_{n_0} \bar{v} = 236 \times 10^6$ cells/ml (Figure 4.10). The standard deviation of the VEGF concentration v_{SD} achieves a maximum at $\arg\max_{n_0} v_{\text{SD}} = 267 \times 10^6$ cells/ml (Figure 4.10). The values of $\arg\max_{n_0} \bar{v}$ and $\arg\max_{n_0} v_{\text{SD}}$ are consistently similar in value across time, corresponding to the generation of high levels of VEGF in the centre of the construct which increase both $\bar{v}$ and v_{SD}.

Notably, at the 5 day time point almost no VEGF remains in the con-

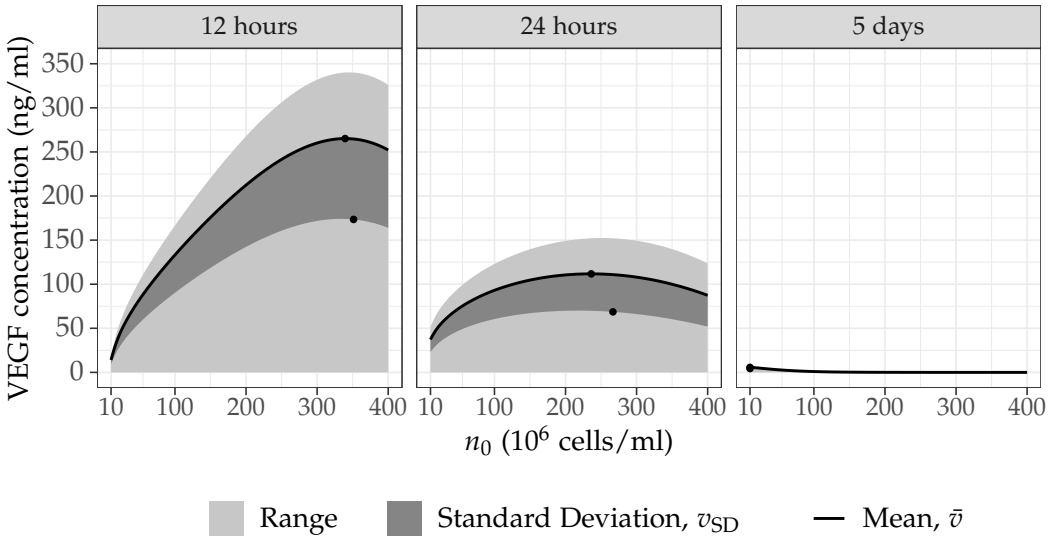

Figure 4.10: Simulated VEGF concentration across the NRC geometry for different uniform initial cell densities; black points indicate the positions of the maximum values of $\bar{v}$ and v_{SD}. After 12 hours, $\arg\max_{n_0} \bar{v} = 339 \times 10^6$ cells/ml and $\arg\max_{n_0} v_{SD} = 351 \times 10^6$ cells/ml. After 1 day, $\arg\max_{n_0} \bar{v} = 236 \times 10^6$ cells/ml and $\arg\max_{n_0} v_{SD} = 267 \times 10^6$ cells/ml. After 5 days, VEGF concentrations have decreased further, and $\arg\max_{n_0} \bar{v} = \arg\max_{n_0} v_{SD} = 10 \times 10^6$ cells/ml (the lowest value simulated).

structs. This corresponds to the fact that the number of viable cells has also dropped dramatically by this time point, resulting in a reduction in the total production rate of VEGF, whilst VEGF generated at earlier time points has decayed.

Overall, it appears that when a uniform initial cell seeding seeding strategy is used in combination with an impermeable sheath, the value of n_0 required to maximise the amount of VEGF and the steepness of the VEGF gradient after 1 day (236 to 267×10^6 cells/ml) is higher than that required to maximise the viable cell density after 1 day (88×10^6 cells/ml), suggesting that a compromise between the two is required if both high levels of cell survival and steep VEGF gradients are desired. For example, using $n_0 = 170 \times 10^6$ cells/ml generates a relatively steep VEGF gradient (Figures 4.9 and 4.10) whilst sustaining a higher density of viable cells after 1 day than initial densities of greater than 200×10^6 cells/ml (Figure 4.7).

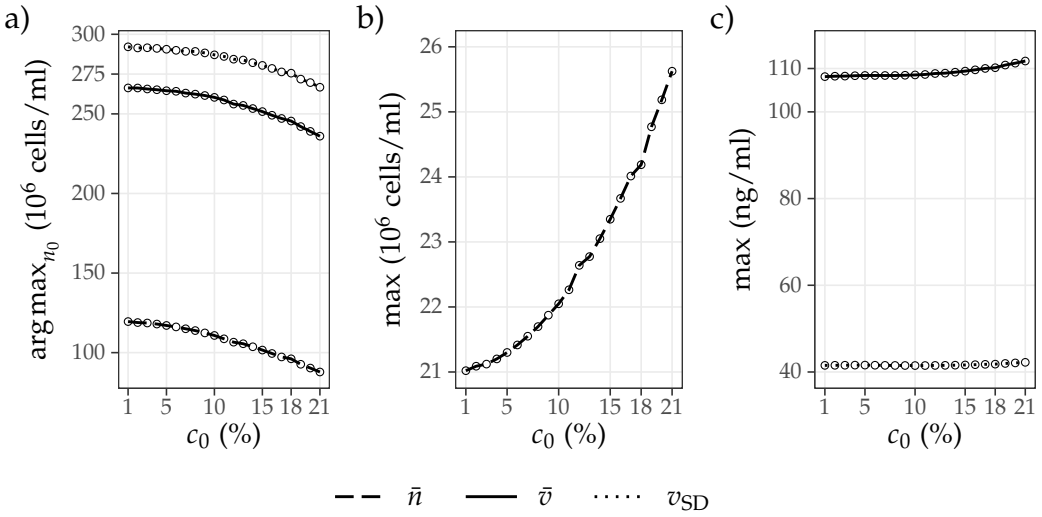

Figure 4.11: Impact of c_0 upon 1 day simulation results; empty circles denote the values of c_0 used to run the simulations. a) Varying c_0 from 1% to 21% progressively reduces the values of n_0 that produce the maximums of $\bar{n}$, $\bar{v}$ and v_{SD} after 1 day. b) The maximum value of $\bar{n}$ after 1 day over all n_0 values varies from 21×10^6 cells/ml when $c_0 = 1\%$ to 25.6×10^6 cells/ml when $c_0 = 21\%$. c) The maximum values of $\bar{v}$ and v_{SD} after 1 day over all n_0 values increase only slightly as c_0 increases from 1 to 10%.

However, it is not certain that maximising the average concentration of VEGF and the steepness of the VEGF gradient is necessarily the correct strategy to adopt to encourage vascularisation and thereby aid neuronal repair. In Chapter 5, the interplay between VEGF gradients and concentrations and their influence on revascularisation is explored in more detail: a 3D model of angiogenesis in response to VEGF in engineered tissue is described, and simulations are run in combination with the current cell-solute model to better assess the impact of different VEGF distributions upon vascular sprouting and growth.

4.4.1.1 Sensitivity of results to initial and boundary conditions: assessing the impact of oxygen storage conditions and tissue solute concentrations

The value of the initial oxygen concentration across the NRC geometry c_0 was varied from 1% to 21% to investigate its impact upon the simulation

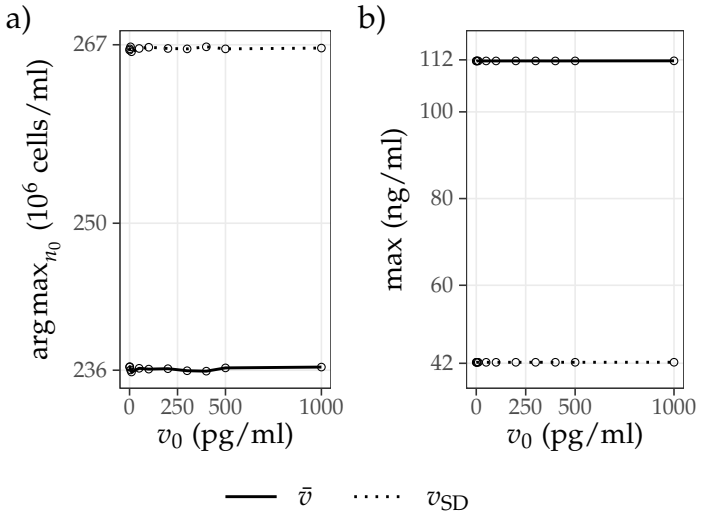

Figure 4.12: Impact of v_0 upon 1 day simulation results; empty circles denote the values of v_0 used to run the simulations. a) Varying v_0 up to 1000 pg/ml results in changes in the value of $\arg\max_{n_0} \bar{v}$ and $\arg\max_{n_0} v_{SD}$ after 1 day of less than 1% of their values when $v_0 = 0$. b) The maximum values of $\bar{v}$ and v_{SD} also change by less than 1% as v_0 is varied from 0 to 1000 pg/ml.

results (Figure 4.11). Increasing c_0 across this range decreased the value of $\arg\max_{n_0} \bar{n}$ after 1 day from 120×10^6 cells/ml at 1% to 87.9×10^6 cells/ml at 21%. Both $\arg\max_{n_0} \bar{v}$ and $\arg\max_{n_0} v_{SD}$ also decreased at a similar rate across this range of c_0. However, the corresponding maximal values of $\bar{n}$, $\bar{v}$ and v_{SD} changed by only a relatively small amount.

These results imply that cells can be uniformly seeded at a lower density within constructs with higher initial oxygen concentrations to achieve similar values of $\bar{n}$, $\bar{v}$ and v_{SD} after 1 day as constructs with a lower initial oxygen concentration seeded with a greater density of cells. This suggests that one way of minimising the number of cells required could be to incubate tissue engineered constructs within high oxygen environments prior to implantation. This hypothesis could be investigated experimentally in the future.

On the other hand, varying the initial VEGF concentration v_0 within the NRC over a range of 0 to 1000 pg/ml had no effect on any of the previously mentioned metrics at the 1 day time point. This is because any

VEGF existing in the construct due to culturing at the initial time point decays almost entirely over 24 hours: the VEGF degradation rate is set at $d_v = 29.874 \times 10^{-6}$ s^{-1}, equivalent to a half life of approximately 6.5 hours. Increasing v_0 across the designated range did not impact the simulated VEGF concentration values after 24 hours, motivating the use of $v_0 = 0$ across the simulations.

However, the initial VEGF concentration v_0 does have the potential to alter the concentration of VEGF in the construct over the first few hours after implantation. But in this case, the magnitude of v_0 is likely to be smaller than the concentrations generated by the implanted cells, and therefore may not have a great effect on signalling. Future computational studies could investigate the use of time-released VEGF delivered via capsules using a similar approach, in which case the concentration of delivered VEGF would likely be much higher than the 0 to 1000 pg/ml range simulated here, and therefore have a greater impact upon the results.

The boundary condition values for tissue oxygen and VEGF concentrations were also varied to assess their impact upon the simulation results. Values of c_{tissue} ranging from 1% to 10% were used. Changes in c_{tissue} result in minimal differences in the maximum values for $\bar{v}$ and v_{SD} after 1 day (Figure 4.13c) as well as the values of n_0 that achieve these maximums, especially within the expected physiological range identified in the literature (4 to 6%) (Figure 4.13a).

Slightly larger variations occur in the maximum value of $\bar{n}$ after 1 day, taken across the full range of the simulated initial cell densities, when c_{tissue} is varied within the physiological range of 4 to 6%: the maximum value of $\bar{n}$ varies by up to 5.1% of its value at $c_{\text{tissue}} = 5\%$. When $c_{\text{tissue}} = 10\%$, the maximum value of $\bar{n}$ is 33% greater than its value when $c_{\text{tissue}} = 5\%$, reflecting the positive effect that increased oxygen availability has on cell survival (Figure 4.13b).

However, within the approximated physiological range for c_{tissue}, the

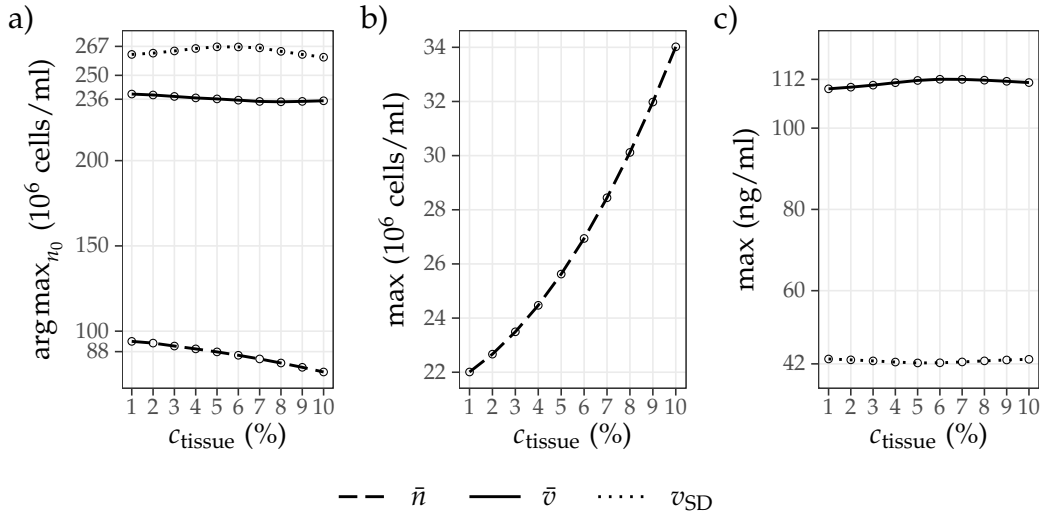

Figure 4.13: Impact of c_{tissue} upon 1 day simulation results; empty circles denote the values of c_{tissue} used to run the simulations. a) Varying c_{tissue} from the approximated physiological value of 5% results in only minor variations in the values of $\arg\max_{n_0} \bar{v}$ and $\arg\max_{n_0} v_{\text{SD}}$ after 1 day. When $c_{\text{tissue}} = 10\%$, the value of $\arg\max_{n_0} \bar{n}$ is 13% less than its value when $c_{\text{tissue}} = 5\%$. b) The maximum value of $\bar{n}$ after 1 day over all n_0 values varies from 22×10^6 cells/ml when $c_{\text{tissue}} = 1\%$ to 34×10^6 cells/ml when $c_{\text{tissue}} = 10\%$. c) The maximum values of $\bar{v}$ and v_{SD} after 1 day over all n_0 values vary by less than 3% of their values when $c_{\text{tissue}} = 5\%$.

initial cell density value at which this maximum is achieved $\arg\max_{n_0} \bar{n}$ alters by up to only 2.2% of its value at 5%, and by up to 13.4% across the entire range of simulated values of c_{tissue}. This suggests that the model's predictions for the optimal n_0 values to achieve the highest possible average cell density after 1 day are robust to potential changes in tissue oxygen concentration or error in the set value of c_{tissue}.

The concentration of VEGF in the surrounding tissue v_{tissue} was also varied in a similar manner from 0 to 1000 pg/ml. However, this had no discernible effect on the values $\arg\max_{n_0} \bar{v}$ and $\arg\max_{n_0} v_{\text{SD}}$ or the corresponding maximum values of $\bar{v}$ and v_{SD} (Figure 4.14). This is likely due to the difference in the order of magnitude between the physiological boundary condition values and the VEGF concentrations generated by the cells within the construct. As expected, varying the value of v_{tissue} did not result

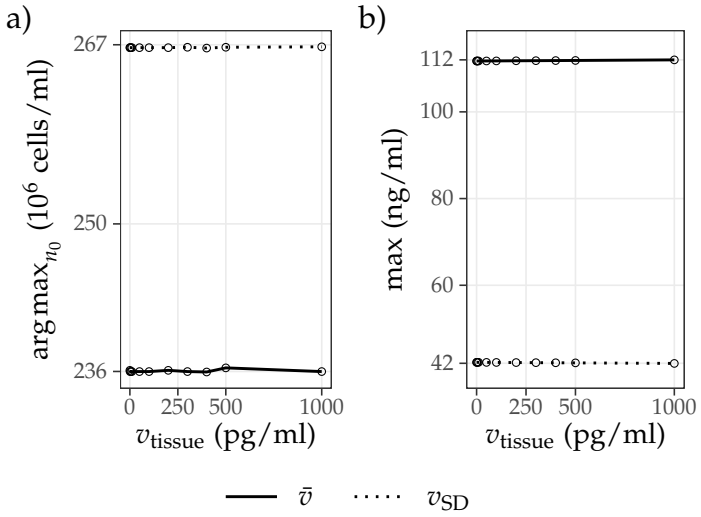

Figure 4.14: Impact of v_{tissue} upon 1 day simulation results; empty circles denote the values of v_{tissue} used to run the simulations. a) Varying v_{tissue} up to 1000 pg/ml results in changes in the value of $\arg\max_{n_0} \bar{v}$ and $\arg\max_{n_0} v_{\text{SD}}$ after 1 day of less than 1% of their values when $v_{\text{tissue}} = 0$. b) The maximum values of $\bar{v}$ and v_{SD} also change by less than 1% as v_{tissue} is varied from 0 to 1000 pg/ml.

in any changes in the simulation values of n as the viable cell governing equation is independent of VEGF concentration. This motivates the use of $v_{\text{tissue}} = 0$ ng/ml as the boundary condition in the majority of the simulations of an NRC geometry in this thesis.

4.4.2 Porous sheath

The simulations and analysis run in the previous subsection were repeated, this time modelling NRCs with porous sheaths of varying porosities ϵ and thicknesses T. An example of a simulation of cell-solute interactions over time within both the NRC and surrounding porous sheath is provided in Figure 4.5. It is evident that in this case, use of the porous sheath greatly improves access to oxygen for the cells seeded within the central collagen NRC, but also results in loss of VEGF via diffusion.

Figure 4.15 demonstrates that the maximum mean viable cell density $\max \bar{n}$ over the central construct after 24 hours, as well as the initial seeding density that achieves the maximum, changes very little across porosities ϵ

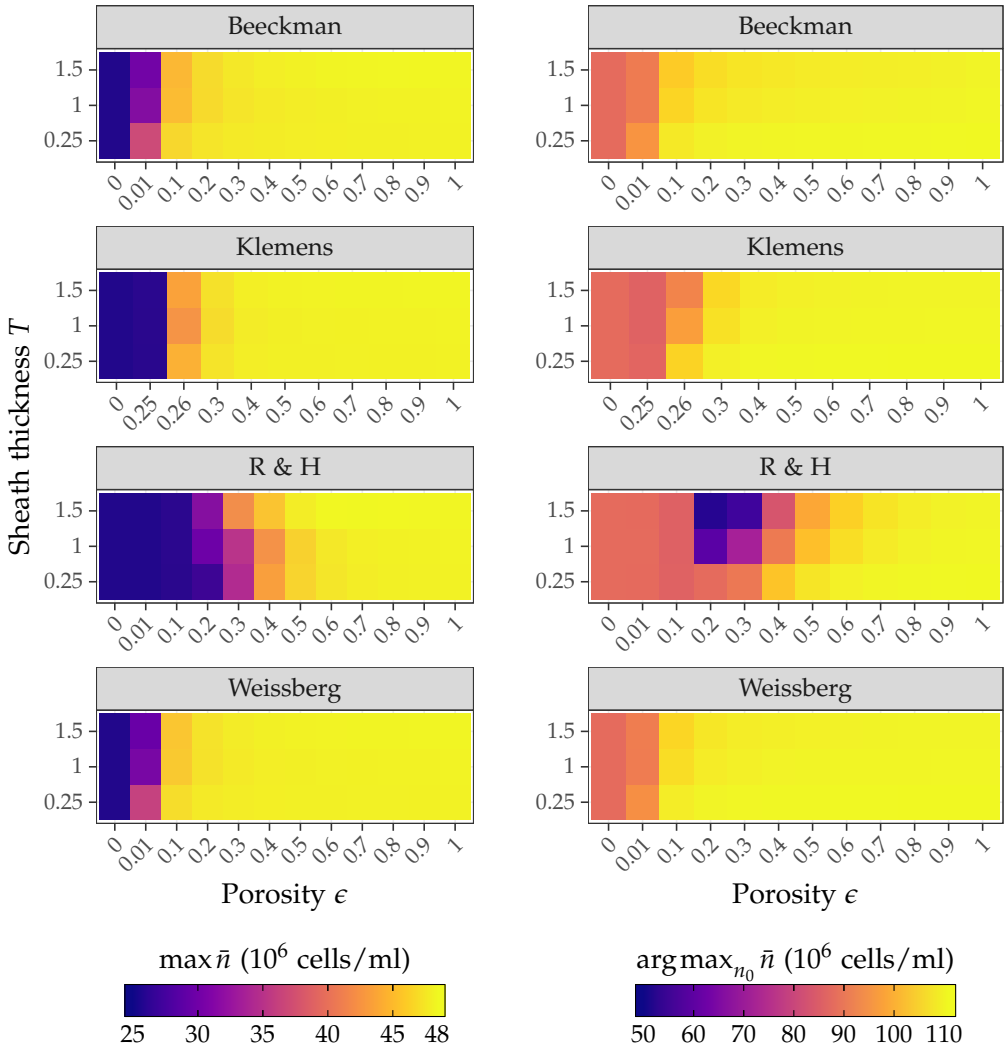

Figure 4.15: Impact of sheath porosity ϵ, thickness T and tortuosity model used upon the values of $\max \bar{n}$ and $\arg\max_{n_0} \bar{n}$ after 24 hours.

in the range of 0.6 to 1 regardless of the model of tortuosity used. The thickness of the sheath, which was varied up to 1.5 mm, also had no effect on these values when ϵ remained in this range. A similar pattern occurs in the case of the standard deviation of the VEGF concentration (Figure 4.16). This suggests that the rate of diffusion of solutes through sheaths with characteristics corresponding to these parameter ranges does not vary enough to affect these metrics.

This result can be explained by considering the approximate time scales of diffusion for various values of T and ϵ. Note that the coeffi-

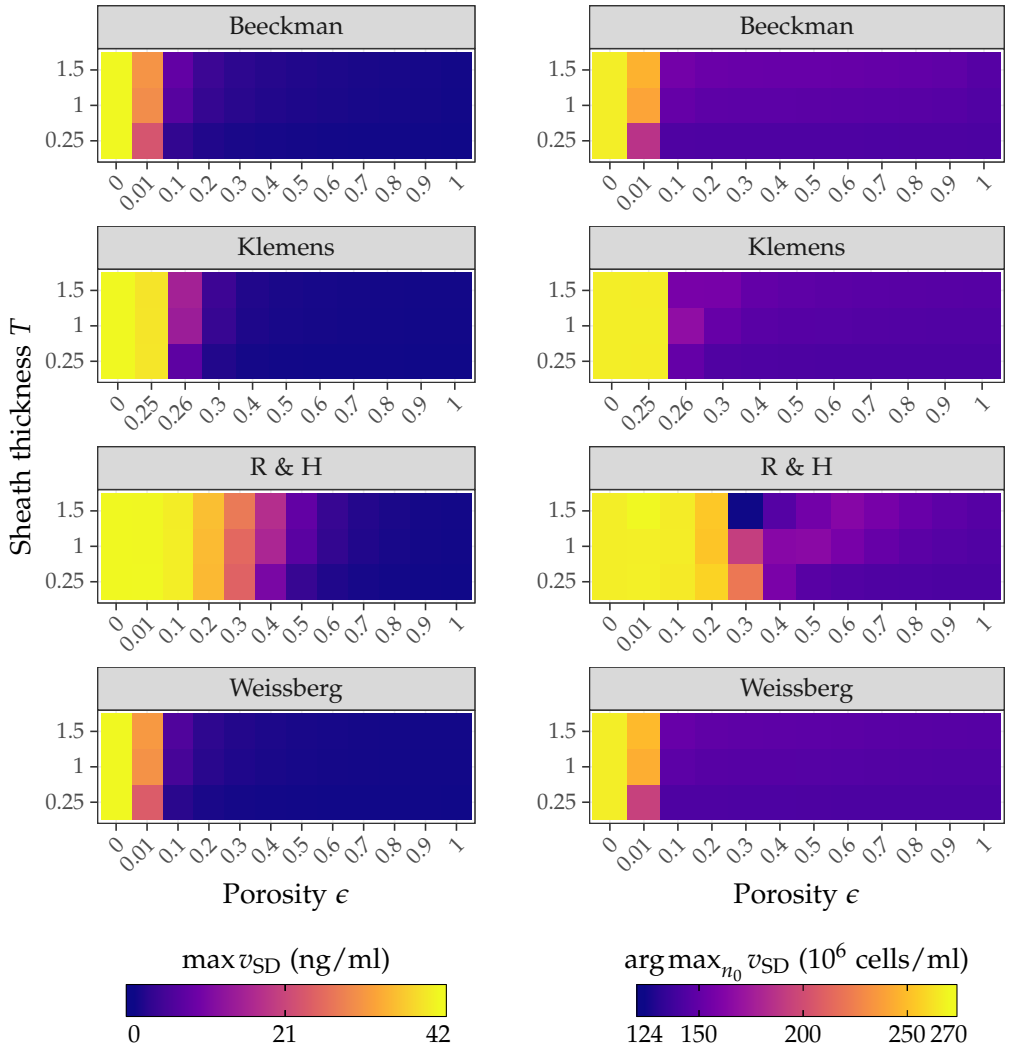

Figure 4.16: Impact of sheath porosity ϵ, thickness T and tortuosity model used upon the values of $\max v_{SD}$ and $\arg\max_{n_0} v_{SD}$ after 24 hours. Tortuosity models are listed in Table 4.2.

cient D_{eff} as defined in Equation (4.1) is not the "true" effective diffusion coefficient of the homogenised solute concentration s: this can be seen by considering the case where $R(s_\kappa)$ is linear in s_κ. Under this assumption, Equation (4.1) can be reduced to give an effective transport equation for the homogenised quantity s via the relationship $s = \epsilon s_\kappa$:

$$\frac{\partial s}{\partial t} = \frac{D_{\text{eff}}}{\epsilon}\nabla^2 s + R(s)\,. \tag{4.26}$$

This form of the equation is convenient because it allows the experimen-

tal measurement of the "true" effective diffusion coefficient of the homogenised solute concentration, $\tilde{D}_{\text{eff}} = D_{\text{eff}}/\epsilon$, and subsequent simulation of diffusion processes, without explicit knowledge of the porosity of the material ϵ.

This scaled version of the effective diffusion coefficient can be used to investigate the time scales of diffusion of the solute through the porous sheath. In this model, the maximum value of T considered was 1.5 mm, and the minimum value considered was 0.25 mm. The approximate time scale of diffusion of oxygen $t_c(\epsilon, T)$ and VEGF $t_v(\epsilon, T)$ through a sheath of thickness T can be estimated as follows:

$$t_c(\epsilon, T) = \frac{T^2}{\tilde{D}_{\text{eff}}(\epsilon)} = \frac{T^2}{(1/\tau)D_{c_m}}, \tag{4.27}$$

$$t_v(\epsilon, T) = \frac{T^2}{\tilde{D}_{\text{eff}}(\epsilon)} = \frac{T^2}{(1/\tau)D_{v_m}}. \tag{4.28}$$

Using the Weissberg model of tortuosity (Table 4.2) with $T \in [0.25, 1.5]$ mm and $\epsilon \in [0.01, 0.9]$, this gives ranges of between 25 seconds and 47 minutes for t_c and between 8 minutes and 5 hours for t_v. The difference between these diffusion times is relatively small, and all are much less than 24 hours (the time point featured in figures 4.15 and 4.16). This goes some way to explain why varying porosity and sheath thickness appears to have little impact on the model results displayed in these Figures. It seems likely that the difference in porosity will only have a clear influence on the model results at very early time points (up to 6 hours).

At very low porosity values, some variation occurs in the values of $\arg\max_{n_0} \bar{n}$, $\max \bar{n}$, $\arg\max_{n_0} v_{\text{SD}}$ and $\max_{n_0} v_{\text{SD}}$, especially when the Rutkowski and Heath (R & H) model of tortuosity is used. But at very low levels of porosity, percolation effects could influence the rate of the diffusion. It is unclear whether the chosen theoretical models take these effects into account. Additionally, most relevant manufactured porous materials have a porosity $\epsilon \geq 0.5$ (Table 4.1). For these reasons, the rest of

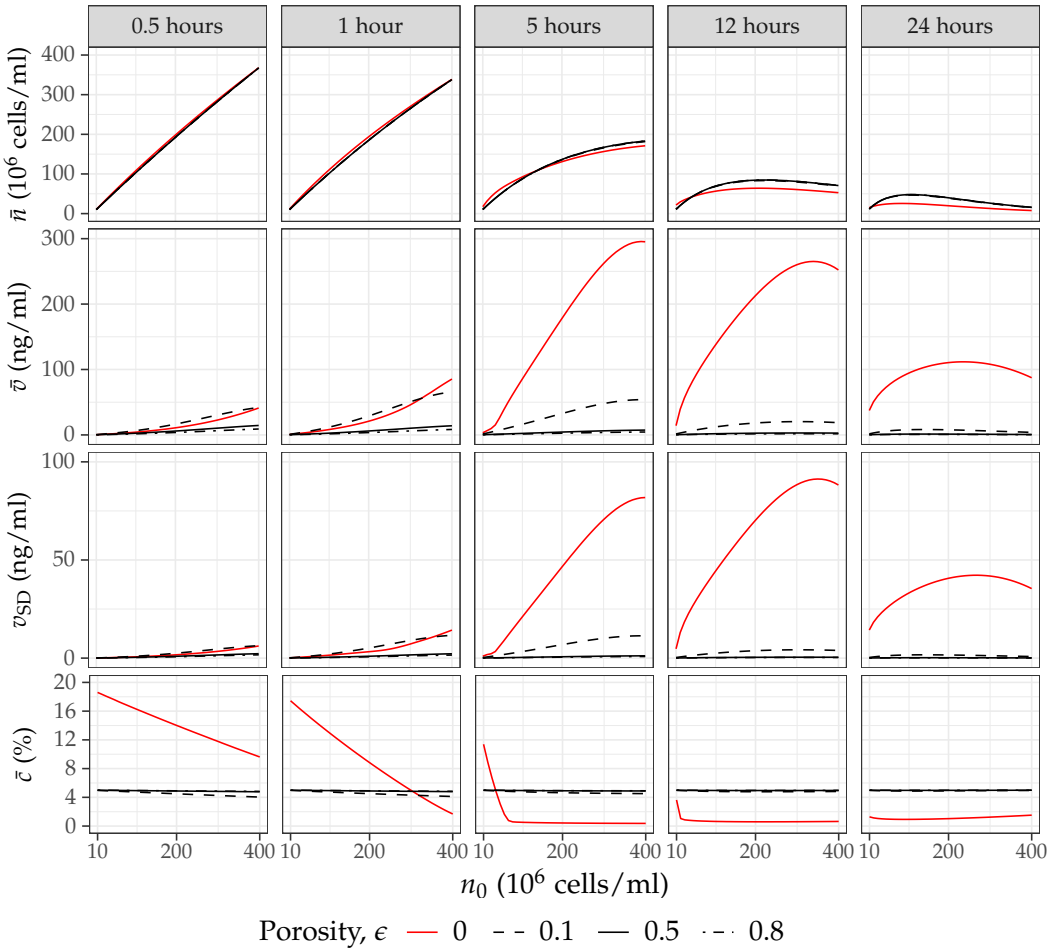

Figure 4.17: Simulated mean viable cell densities and oxygen and VEGF concentrations across the central nerve repair construct geometry at a range of time points. The Weissberg model of tortuosity and $T = 0.25$ mm were used for these simulations. The mean viable cell density over the construct is higher after 12 and 24 hours when a porous sheath ($\epsilon > 0$) is used than when an impermeable sheath ($\epsilon = 0$) is used. This is likely to be due to the increased supply of oxygen, as represented by the panels in the bottom row, and applies across all of the values of n_0 that were simulated. However, the use of an impermeable sheath results in better VEGF retention.

the analysis here will focus predominantly on simulations using a porosity values within this range, and the Weissberg model of tortuosity will be implemented.

Despite the lack of porosity and thickness dependent variation, there are clear differences in both cell survival and solute concentrations between the impermeable and porous sheath model simulation results. Figure 4.17

demonstrates that the density of viable cells at the 12 hour and 1 day time points is higher for porous sheath models than in the impermeable sheath model ($\epsilon = 0$).

As porosity is increased from 0.1 to 0.8, the mean oxygen concentration $\bar{c}$ alters only slightly. These changes in oxygen concentration are not large enough to impact cell survival, and therefore the degree of porosity has almost no effect upon cell survival as assessed by $\bar{n}$.

In contrast to the impermeable sheath model, by the 12 hour time point there is only a relatively small quantity of VEGF remaining in the NRCs with porous sheaths. Figure 4.17 demonstrates that at very early time points (0-1 hours) more VEGF is present within these constructs, especially when they are seeded with high uniform densities of cells. This may be because at this point the cell density is relatively high, and therefore the combined production rate of VEGF of the cell population is likely greater than the rate of diffusion of VEGF out of the construct into the sheath. At initial time steps (0.5 to 5 hours), low porosity sheaths ($\epsilon = 0.1$) enable greater VEGF retention within the central construct than higher porosity sheaths ($\epsilon = 0.5$, 0.8), but the effect of this upon the value of $\bar{v}$ becomes less apparent at later time steps when the overall rate of VEGF production has dropped due to the decrease in cell population.

This behaviour is demonstrated in Figure 4.17 in the case of a construct with a porous sheath modelled according to the Weissberg model of tortuosity with sheath thickness $T = 0.25$ mm, but similar results are produced with using the other models of tortuosity and values of T up to 1.5 mm.

Although previous simulations of a porous scaffold by Croll et al. demonstrate changes according to the porosity of the scaffold, in that case the thickness of the simulated porous scaffold was much greater- between 7.5 mm and 30 mm [87], which would significantly increase the time taken for oxygen and other solutes to diffuse in and out of the construct.

In terms of optimising NRC cell seeding strategies, as demonstrated

in Figure 4.15 the value of n_0 that maximises $\bar{n}$ after 24 hours when a porous sheath ($\epsilon = 0.8$) is used is approximately 110×10^6 cells/ml, which is greater than in the case of the impermeable sheath ($\arg\max_{n_0} \bar{n} = 88 \times 10^6$ cells/ml), but also results in almost double the density of viable cells at this time point.

Therefore these results suggest that a higher seeding cell density should be used when implanting NRCs with a porous sheath than with an impermeable sheath in order to take advantage of the increased access to oxygen and thereby maximise cell survival.

The fact that porous sheaths are clearly able to increase cell survival but also result in the loss of VEGF that is crucial for vascularisation suggests that a sheath with spatially variable porosity could be a potential future avenue for exploration: the creation of a sheath with both porous and impermeable sections could allow targeted VEGF retention in certain regions whilst still permitting increased diffusion of oxygen into the construct in contrast to the purely impermeable sheaths. This idea will be explored computationally in the next section.

Additionally, the use of a porous sheath material with a molecular weight cut off between 46 kDa and 32 Da could be optimal in terms of improving VEGF retention whilst improving the supply of oxygen to seeded cells. This material composition would allow the inward diffusion of oxygen whilst prohibiting VEGF diffusion out of the NRC (Section 4.2.1).

4.4.2.1 Partially porous sheath

A partially porous sheath was implemented to investigate whether some of the benefits of increased oxygen diffusion into the construct could be retained whilst preserving a gradient of VEGF within the construct.

Based upon the previous simulations of NRCs with porous sheaths, it was hypothesised that to preserve a concentration of VEGF in the centre of the sheath it would be necessary to have an impermeable sheath covering that region. However, to enhance cell survival a small section of porous

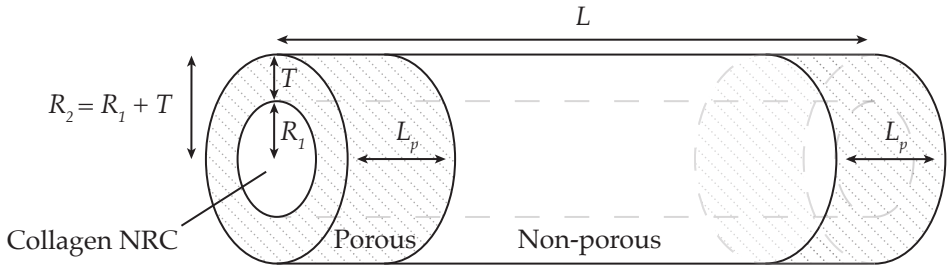

Figure 4.18: Schematic of the cylindrical NRC geometry with a partially porous sheath.

material could be incorporated at either end of the construct sheath, to enhance the inward diffusion of oxygen (Figure 4.18). This length of porous material is here denoted L_p.

All simulations were run using $L = 15$ mm, $T = 0.25$ mm and $\epsilon = 0.8$, along with the Weissberg model of tortuosity because these configurations have been shown to be representative of the majority of other porous sheath designs within the parameter ranges of $\epsilon \gtrapprox 0.6$ and $0.25 \leq T \leq 1.5$ (Figures 4.15 and 4.16).

As demonstrated in Figure 4.19, simulating an NRC geometry with a partially porous sheath with $L_p = 2$ mm results in greater cell survival ($\bar{n}$) as well as a greater value of v_{SD} after 24 hours than the entirely impermeable sheath geometry ($L_p = 0$). However, as demonstrated in Figure 4.20, the increase in both concentration and gradient steepness of VEGF is isolated to the region covered by an impermeable sheath. This means that the VEGF concentrations at the ends of the construct are much lower, with potential implications for the initiation of sprouting angiogenesis at the interface between the construct and the surrounding tissue at these locations.

Previously, Jenq et al. used holes in tubular conduits covered with different filters to create a similar partially porous scaffold, although in those studies the holes were located more centrally along the length of the tube [171]. Sheaths with non-uniform porosity in the radial direction have also been developed, but in general the lengthwise variation of the

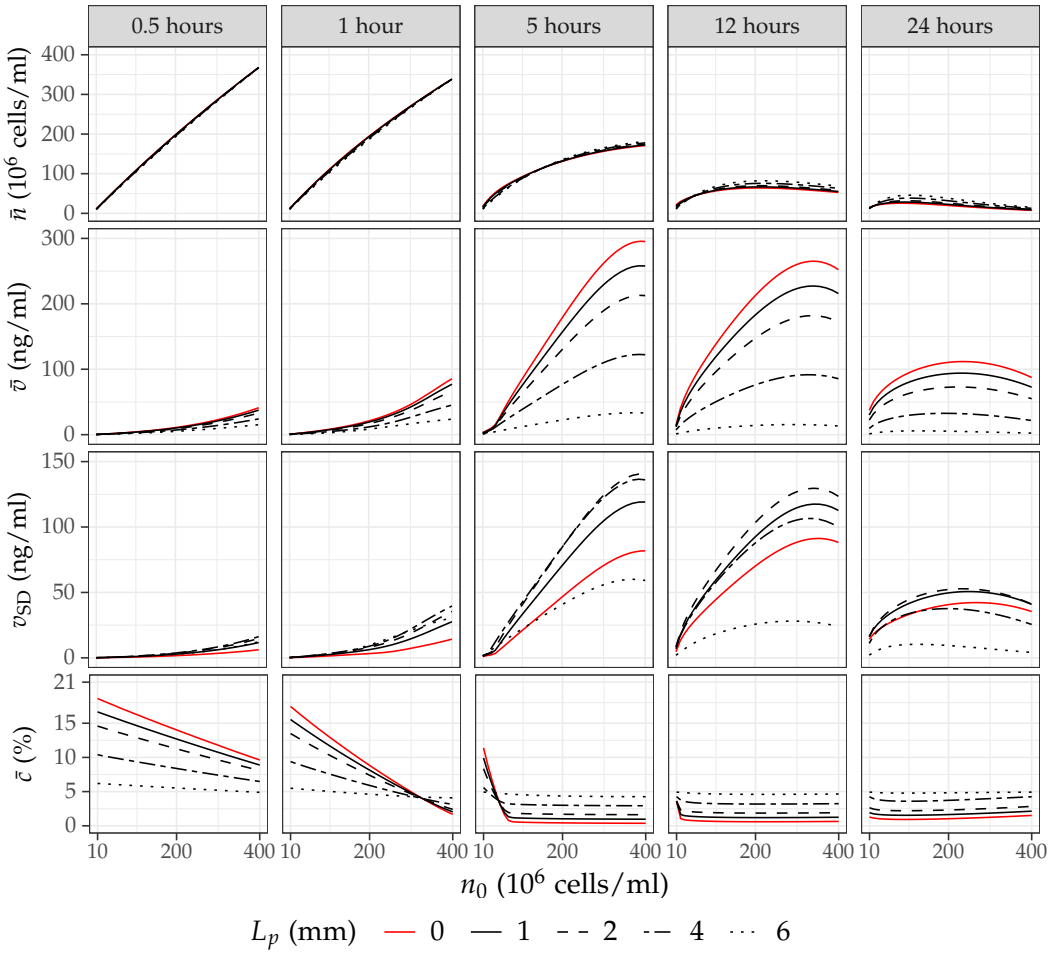

Figure 4.19: Use of a partially porous sheath can limit the loss of VEGF from the construct whilst permitting diffusion of oxygen and thus enhancing cell survival. As L_p, the length of porous material at either end of the construct sheath, decreases the results tend towards that of the impermeable sheath (represented here as $L_p = 0$).

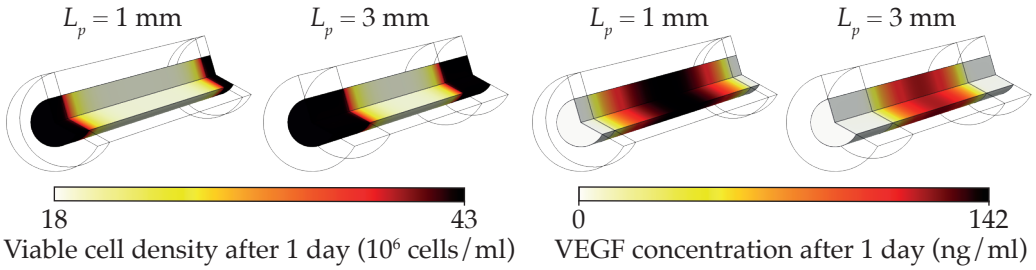

Figure 4.20: The spatial distribution of cells within NRCs with partially porous sheaths is highly influenced by availability of oxygen, with areas of much greater viable cell density occurring adjacent to the porous ends of the sheath. Conversely, these regions contain relatively low concentrations of VEGF after 1 day due to outward diffusion.

porosity has not been investigated experimentally thus far. These results suggest that this could be a worthwhile avenue to explore, although the feasibility of manufacturing these designs is uncertain.

4.5 Simulations of non-uniformly seeded nerve repair constructs

In this section, the effect of different non-uniform initial cell distributions upon cell survival and VEGF secretion within NRCs is investigated, with the aim of understanding whether moving away from the current uniformly distributed approach could reduce waste of cells and improve the generation of VEGF gradients. In particular, it is hypothesised that non-uniform distributions of cells could increase the steepness of VEGF gradients by encouraging denser populations of cells in certain regions of the engineered tissue, thereby increasing the overall rate of VEGF production in those regions relative to others.

First of all, a step-like function of initial cell density was created (Figure 4.21). This divides the length of the geometry into thirds, assigning the cell density over the middle third to be a specified multiple ζ of the cell densities of the end thirds, which are equal:

$$n_0(z) = \begin{cases} \frac{3n_{\text{tot}_0}}{(2+\zeta)\pi R_1^2 L}\,, & 0 \leq z < \frac{L}{3}\,, \\ \zeta\frac{3n_{\text{tot}_0}}{(2+\zeta)\pi R_1^2 L}\,, & \frac{L}{3} \leq z \leq \frac{2L}{3}\,, \\ \frac{3n_{\text{tot}_0}}{(2+\zeta)\pi R_1^2 L}\,, & \frac{2L}{3} < z \leq L\,. \end{cases} \tag{4.29}$$

Here n_{tot_0} denotes the total number of cells seeded within the NRC. This form of non-uniform distribution was used because it is simple and therefore feasible to manufacture. A range of designs with different (ζ, n_{tot_0}) parameter pairs were then simulated using both the impermeable and porous sheath models. Note that each value of n_{tot_0} can be related to a uniform cell seeding density n_0 that would deliver the same number of cells via the

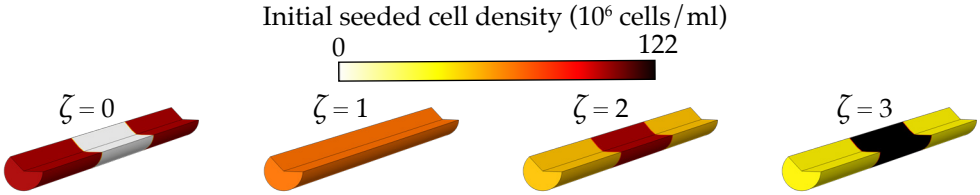

Figure 4.21: Examples of non-uniform distributions; here the total number of cells seeded remains constant whilst their distribution alters according to ζ. The case $\zeta = 1$ corresponds to a uniform distribution. Here the total number of cells $n_{\text{tot}_0} = 200,000$.

following equation, based on the volume of the NRC:

$$n_0 = \frac{1}{\pi R_1^2 L} n_{\text{tot}_0} \,. \tag{4.30}$$

Thus using $R_1 = 0.25$ mm and $L = 15$ mm, uniform cell densities of $n_0 \approx$ 170, 102 and 34×10^6 cells/ml provide a total number of $n_{\text{tot}_0} = 5$, 3 and 1×10^5 cells respectively.

In the case of the impermeable sheath, the simulation results suggest that varying the distribution of a fixed number of seeded cells does impact the number of viable cells within the construct after 12 hours and 1 day (Figure 4.22). However, the amplitude of this effect varies according to the total number of cells seeded and the value of the distribution scaling constant (Figure 4.23).

As the initial number of seeded cells increases from 50,000 to 500,000, the value of ζ that produces the greatest number of viable cells after 1 day also increases from 0.6 to 1.1, indicating that when fewer cells are seeded it may be beneficial to seed a greater proportion at the ends of the construct, potentially to maximise exposure to oxygen and therefore cell survival. A similar pattern emerges at the 12 hour time point.

However, values of n_{tot_0} in the range of 200,000 to 300,000 cells appear to result in the greatest number of viable cells after 1 day regardless of the distribution of the cells, with the exception of distributions corresponding to $\zeta \approx< 0.5$. This aligns with the previously identified optimal uniform

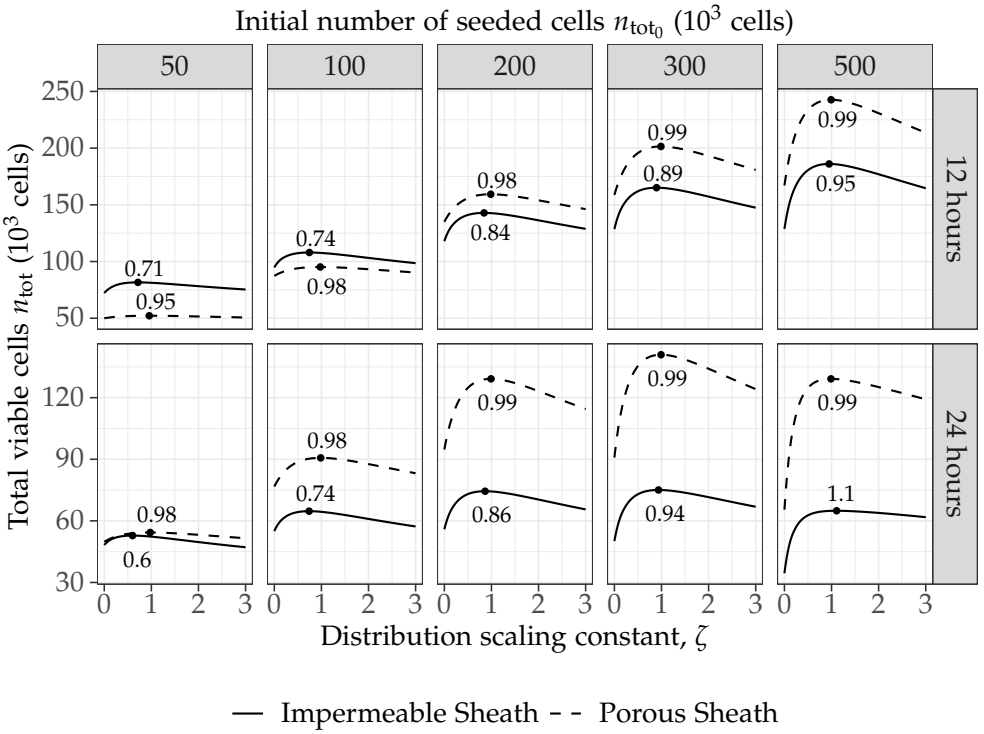

Figure 4.22: Simulations suggest that changing the distribution scaling constant ζ whilst maintaining the total number of cells seeded causes differences in the total number of viable cells n_{tot} at different time points. Here the black points and numbers refer to the maximum points and the values of $\arg\max_\zeta n_{tot}$ respectively. The optimal distribution for maximising n_{tot} after 1 day changes according to the total number of cells initially seeded.

seeding density for maximising the viable cell density after 1 day, $n_0 = 88 \times 10^6$ cells/ml, which delivers a total of approximately 260,000 cells. Futhermore, for these values of n_{tot_0} approximately uniform distributions achieve the highest number of viable cells over time.

The same general patterns emerge in the results of simulating non-uniformly seeded NRCs with porous sheaths. For $n_{tot_0} \geq 100{,}000$, it is clear that the use of the porous sheath again increases cell survival at the 1 day time point (Figure 4.22), consistent with the results presented in Section 4.4.2.

The simulation results also indicate that in the case of an NRC with a impermeable sheath, the initial distribution of the cells could have the potential to alter the values of both the mean VEGF concentration across

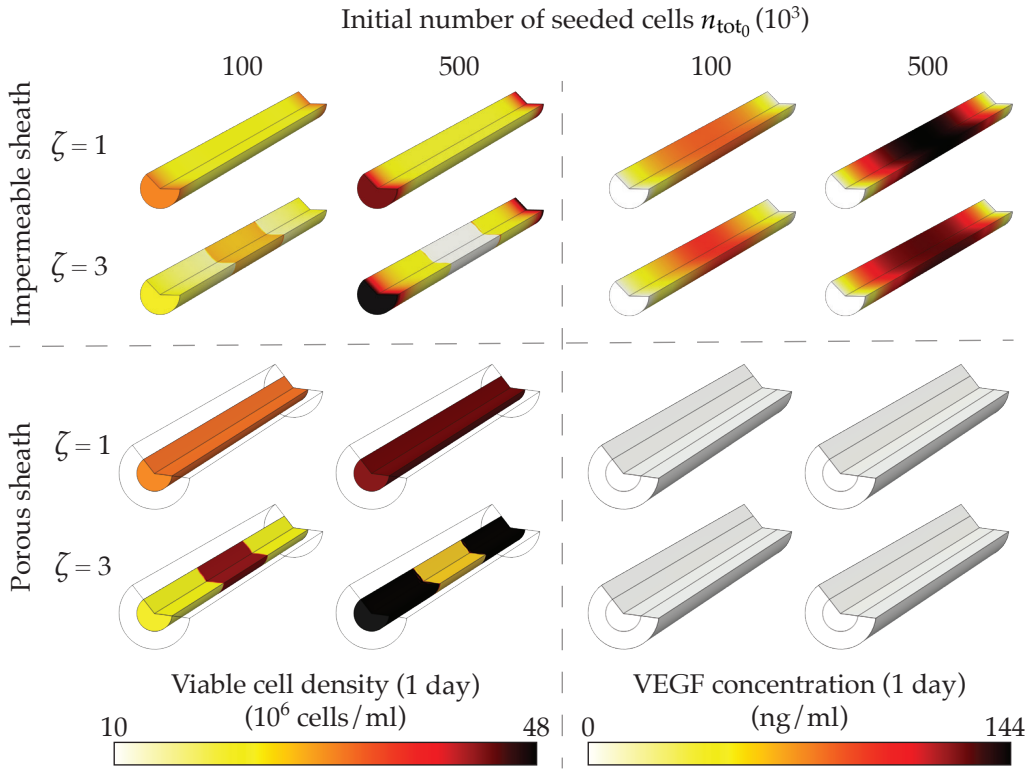

Figure 4.23: Simulations suggest that the impact of the initial seeded cell distribution upon the VEGF and viable cell density distributions after 1 day varies according to the total number of cells seeded. Seeding 500,000 cells uniformly ($\zeta = 1$) generates a steeper VEGF concentration gradient than if more cells are seeded in the centre ($\zeta = 3$); whereas the converse is true when seeding 100,000 cells.

the construct $\bar{v}$ and the standard deviation of VEGF across the construct v_{SD} (Figure 4.24). In particular, seeding more cells in the centre of the construct ($\zeta > 1$) results in consistently higher values of $\bar{v}$ and v_{SD} across all values of n_{tot_0} and for both the 12 hour and 1 day time points, although the magnitude of variation in $\bar{v}$ is small.

However, use of the porous sheath again results in the diffusion of VEGF outwards into the surround tissue, resulting in negligible concentrations ($\bar{v} < 1$ ng/ml) within the NRC.

4.6 Conclusion

The results presented in Sections 4.4.1, 4.4.2 and 4.5 suggest that cell survival can be optimised through the selection of specific seeding cell den-

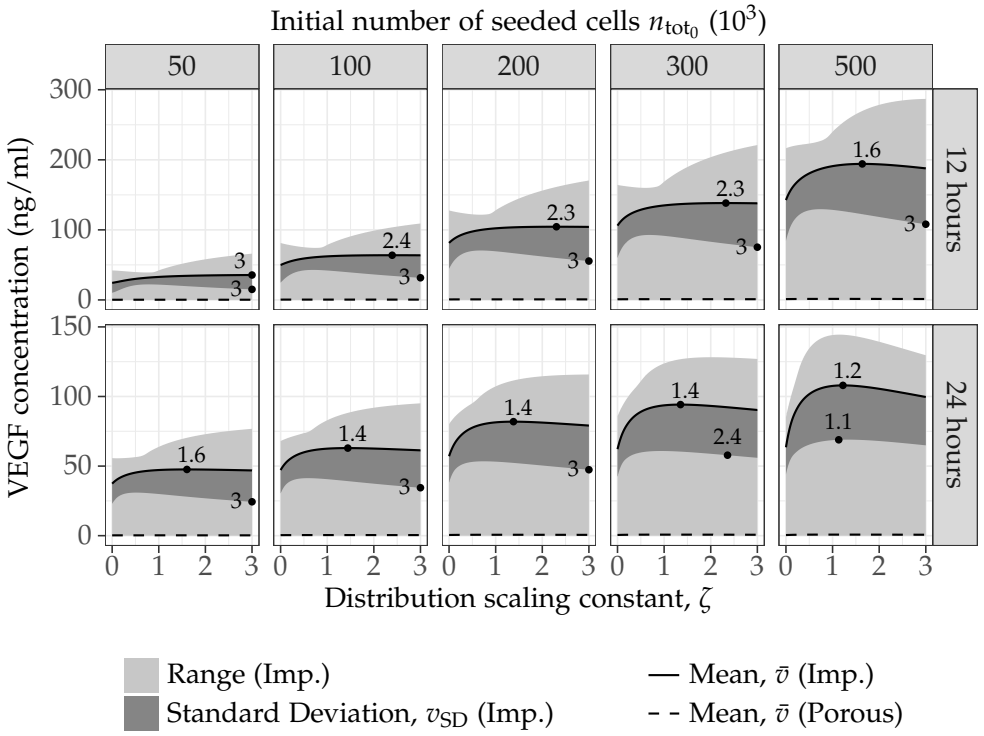

Figure 4.24: Impact of distribution scaling constant ζ on the VEGF distribution in NRCs with impermeable and porous sheaths. Here the black points and numbers refer to the maximum points and the values of $\arg\max_\zeta \bar{v}$ and $\arg\max_\zeta v_{SD}$.

sities and distributions, and that seeding more cells in engineered tissue constructs such as NRCs does not necessarily lead to higher densities of viable cells within the engineered tissue at later time points *in vivo*. This runs contrary to the reasoning previously used in many experimental studies, which either neglects to consider the effect of seeding cell densities and distributions entirely, or assumes that seeding more cells will necessarily result in a greater number of viable cells over time. These results suggest that in fact using fewer cells in engineered tissue could result in better cell survival, whilst reducing waste of cells.

The accuracy of the model predictions will be influenced by the quality of the fit of the model to the experimental data. Although the parameterised model does match the overall trends of the *in vitro* data as shown in Figures 3.14 and 3.18, it does not capture all of the variation in the

data. The model fit to the data in the low oxygen ambient oxygen concentration regime ($c_a \leq 10\%$) is particularly relevant because, as shown in Figure 4.20, the mean oxygen concentrations across the simulated NRCs are largely within this range, mimicking the *in vivo* repair environment. Figure 3.14 shows that the model is actually likely to underestimate viable cell density after 24 hours when $n_0 = 39 \times 10^6$ cells/ml within this regime. Therefore, although discrepancies between the model simulations of the *in vitro* scenario and the corresponding data indicate that there are likely to be inaccuracies in the model predictions presented in this chapter, the hypothesis that seeded cell densities of less than 100×10^6 cells/ml is also consistent with the *in vitro* experimental data presented in Chapter 3.

Although the model predicts that cell survival at the 5 day time point will be poor, especially when uniform cell densities of greater than 100×10^6 cells/ml are used, this may not necessarily correlate with poor outcomes *in vivo*. One of the key purposes of the cell population is to provide growth factors that will aid and accelerate the regeneration process; therefore, optimising cell survival as far as possible over early time points can still be beneficial, regardless of the long-term survival rate of the cellular population.

As shown in Figure 4.7, the model predicts that the optimal density for uniformly seeded cells in terms of achieving the highest possible viable cell density after 24 hours is around 88×10^6 cells/ml when using an impermeable sheath. Interestingly, this falls close to the figure of 80×10^6 cells/ml found by Mosahebi et al. to produce on average the greatest length of axonal regeneration after 3 weeks *in vivo* [264]. Increasing the cell density beyond this showed a decrease in regeneration in the experimental study. Guénard et al. also produced similar experimental results, concluding that 120×10^6 cells/ml produced the greatest number of myelinated axons after 3 weeks, although in this case the luminal diameter was altered along with the seeding cell density [141].

Thus the results of the simulations presented in this thesis support the hypothesis that the degree of axonal regeneration is linked to the density of viable cells in the construct over time. It is worth noting, however, that both of these experimental studies used a different cell type to that modelled in this this study (Schwann cells instead of dADSCs), and neither of them measured viable cell density over time and therefore they cannot be used to directly validate the model predictions.

Furthermore, the mathematical model is currently only parameterised against data from a single time point (1 day). Improving the model to allow simulation up to the 3 week time point, in line with the previously mentioned experimental studies, would require the incorporation of other biological processes likely to impact viable cell density on this time scale, such as cell migration, the influence of various other cytokines aside from VEGF, and vascular and neuronal growth. Additionally, model parameterisation up to this time point would require further *in vitro* or *in vivo* experimentation. In fact, many of the additional biological processes that occur over longer time scales in peripheral nerve repair are not easily modelled *in vitro*, so *in vivo* models would be necessary to inform and validate the inclusion of features such as host cell infiltration (vascular and neuronal growth).

In Section 4.4.1.1, additional simulations of a uniformly seeded NRC with an impermeable sheath with varying initial oxygen concentrations suggested that culturing engineered tissue at relatively high oxygen concentrations prior to implantation could enhance cell survival. The simulations predicted that using an initial oxygen concentration of 21% resulted in higher cell survival rates after 24 hours. This raises the question as to whether short term culture of engineered tissue at high oxygen concentrations prior to implantation could improve cellular survival.

Incorporating a porous sheath into the model resulted in increased numbers of viable cells when compared to the model with the imperme-

able sheath, especially at later time points when cell survival becomes highly dependent upon the diffusion of oxygen into the construct from the surrounding tissue. The length of the simulated construct is 15 mm, which means that cells seeded in the centre of the construct in particular can be as far as 7.5 mm from the ends of the construct, much further than the diffusion limit of oxygen in tissue; thus introducing porosity along the lengthwise edges of the cylindrical construct increases the cells' access to oxygen considerably.

However, the use of a porous sheath in the simulations also results in a rapid loss of VEGF to the surrounding tissue regardless of the initial seeding cell density or distribution used, (Figures 4.17 and 4.24). This is due to the difference in the order of magnitude between the VEGF generated by the cells within the construct (ng/ml) and the concentration in the surrounding tissue (pg/ml). The concentration of VEGF in a peripheral nerve injury gap during regeneration has not been measured experimentally: obtaining experimental values for tissue VEGF concentrations in peripheral nerve injuries would help to validate the boundary condition for tissue VEGF v_{tissue} used in this model.

As reviewed in Section 4.2.1, the reported efficacy of porous sheaths varies across the experimental literature: some studies record increased neuronal regeneration using porous sheaths [169, 170, 187], and thus offer the hypothesis that this could be a result of increased oxygen diffusion and infiltration of supportive cells; whereas others have observed poorer results when using porous materials [66, 107], and have suggested that this could be caused by loss of growth factors and infiltration of host immune cells.

The model results presented in this thesis actually partially corroborate both of these hypotheses: the simulations show that porous sheaths increase oxygen diffusion into the NRCs, enhancing cell surival, but also result in loss of growth factors. However, the model presented in this chapter does not include neuronal growth or cell infiltration in general. Further

research would be needed to unpick the impact of the use of porous materials upon nerve regeneration: on a case by case basis other variables such as NRC material properties, seeded cell type and the animal model used could all influence the outcome, meaning that it is difficult to directly compare the results of existing experimental studies.

The simulation of constructs with non-uniform seeding cell distributions showed that approximately uniform distributions of cells result in the greatest number of viable cells after 1 day (Figure 4.22). However, seeding more cells in the centre of the construct ($\zeta > 1$) resulted in greater values of v_{SD}, reflecting steeper VEGF gradients, particularly in cases where the total number of cells seeded was 300,000 or less (Figure 4.24). This suggests that when relatively few cells are seeded in the construct, a non-uniform distribution could be used to enhance the generation of VEGF gradients and potentially increase the rate and directionality of vascularisation.

In this chapter, simulations using various cell seeding strategies and sheath designs have predicted corresponding changes in VEGF distributions. Here the focus has been on increasing the total mean VEGF concentration over the collagen construct and increasing the steepness of the gradient, under the assumption that this will enhance vascularisation as informed by previous experimental work (Section 2.1.3). In Chapter 5, a 3D model of sprouting angiogenesis is developed and used in combination with the work presented here to investigate the degree to which these changes in VEGF distribution may impact the rate and extent of vascularisation.

In conclusion, the simulation results presented here corroborate the hypothesis that seeding cell densities and distributions can be tailored to enhance cell survival within the first 24 hours post-implantation and to increase the steepness of VEGF gradients across engineered tissue. The model presented in this thesis does now require further validation via experimentation: the predictions made in this chapter can help to achieve this

goal in the future through the suggestion of specific seeded cell densities and distributions for testing *in vivo*.

Chapter 5

A 3D Discrete Model of Sprouting Angiogenesis

5.1 Introduction

In this chapter, a stochastic model of sprouting angiogenesis is presented, designed for integration with the previously described continuum model of cell-solute interactions within engineered tissue (Chapters 3 and 4). The model is combined with the previously presented continuum model of cell-solute interactions to simulate the effect of different cell seeding strategies on vascularisation in engineered tissue NRCs, and in turn the impact of that vascularisation on cell survival.

In particular, the combined mathematical framework is used to test the hypothesis that cell seeding strategies that induce steeper VEGF gradients will result in more extensive vascularisation. The response of vascular growth to VEGF is measured through the quantification of factors such as vessel and sprout density, vessel branching density and vascular penetration distance. The outcomes of the chapter are specific cell seeding densities or distributions that achieve maximal simulated vascular density and penetration distances after 5 days, and the identification of whether vascular growth in the initial period post-implantation could increase cell

survival. Additionally, the model described in this chapter, which is derived based on existing models and published experimental data, has the potential to be improved via parameterisation against specific data in the future and then used to run more extensive investigations.

Angiogenesis is an important part of tissue regeneration, and vascularisation of engineered tissues can aid assimilation and improve seeded cell survival. Importantly, in the specific context of peripheral nerve repair, evidence suggests that the growth of new blood vessels not only improves the supply of oxygen and nutrients to cells, but also precedes and provides directional guidance for neuronal regeneration. Section 2.1.2 provides a more detailed review of the role of angiogenesis in peripheral nerve repair.

In the previous chapter, a parameterised continuum model of cell-solute interactions was used to make predictions about the effect of different cell seeding strategies upon VEGF concentrations and distributions within NRCs. Specific cell seeding strategies resulted in steeper gradients and/or higher concentrations of VEGF. However, it is not immediately apparent whether the predicted differences in VEGF profiles over time would translate to significant differences in the rate, directionality and extent of vascularisation. This motivates the construction of a 3D model of angiogenesis to simulate vascular growth in response to the spatio-temporal VEGF distributions produced by the cell-solute model.

The first section of this chapter provides a brief description of the process of sprouting angiogenesis, focusing on the roles of the different endothelial cell (EC) phenotypes involved. Subsequently, Section 5.3 introduces the various components of the discrete 3D model of angiogenesis and motivates the use of particular functional forms, mathematical techniques and parameter values by referring to published experimental and computational work. Section 5.4 describes how the model is solved in combination with the existing continuum model to provide an integrated mathematical description of vascularisation within a cell-seeded tissue engineered NRC,

and presents the results of a variety of simulations. Finally, conclusions and ideas for future work are summarised in Section 5.5.

5.2 Endothelial cell behaviour during sprouting angiogenesis

A brief description of how sprouting angiogenesis is initiated and progresses was provided in Section 2.1.3, with the aim of motivating the choice of solute-type variables for the continuum model based on their role during vascular growth: VEGF was identified as the key angiogenic factor and therefore selected for inclusion in the model, whilst a multitude of other variables were excluded from the model for simplicity. The current section will focus instead on the behaviour of ECs during sprouting angiogenesis.

As briefly described in Section 2.1.3, sprouting angiogenesis is initiated when angiogenic factors like VEGF are sensed by an existing vessel. The vessel dilates and vascular permeability increases, permitting the release of plasma proteins that form a scaffold for the subsequent migration of ECs [63]. The pericytes that surround the vessel ECs detach and the inter-endothelial cell contacts weaken, eventually allowing ECs to detach and migrate into the surrounding tissue, guided by growth factor gradients. The migrating ECs proliferate and form a solid cord that subsequently develops a lumen. Eventually, anastomisation of separate sprouts creates closed, functional capillary loops.

During angiogenesis, the ECs undergo transient phenotypic changes that broadly divide them into three categories: tip endothelial cells (TECs), stalk endothelial cells (SECs) and phalanx ECs. TECs lead the process of migration; it is commonly accepted that each sprout contains one TEC at its apex [134], although recent research suggests that in some scenarios sprout tips are instead led by two overlapping TECs [303]. TECs are highly polarised, and extend long thin projections called filopodia to sense angiogenic stimuli and other aspects of their environment, such as the presence

of other sprouts [95]. This process is aided by the presence of receptors on the filopodia, including VEGFR2; TECs have high expression of both VEGFR2 and VEGFR3. TECs also express matrix metalloproteinases, which help to clear a channel for the sprout to grow into [387].

In contrast to TECs, SECs do not have filopodia and have far fewer VEGFR2 and VEGFR3 receptors. Thus instead of moving according to angiogenic cues, they follow behind the leading TECs in a chain. SECs are more proliferative than TECs, particularly when stimulated by VEGF. They are also capable of forming a lumen, and create capillary basement membrane as the sprout grows [312].

The third EC phenotype involved in angiogenesis are phalanx ECs: these largely quiescent ECs line newly formed vessels, aid in the formation of the basement membrane and help to create a tightly structured lumen [95, 246].

Upon initiation of angiogenesis, the selection of the EC that will become the leading TEC for the new sprout is mediated by the expression of delta-like ligand 4 (Dll4): TEC exposure to VEGF results in higher expression of Dll4, which binds to Notch pathway receptors on neighbouring ECs, which in turn induces VEGFR1 and suppresses the the expression of VEGFR2 and VEGFR3, thus preventing adjacent ECs from also becoming TECs [151]. Downregulation of VEGFR2 in these cells in turn decreases their expression of Dll4. Notch signalling also prevents the formation of adjacent TECs on an existing vessel, instead inducing sprouts to occur at intervals along the vessel length [47].

However, although the VEGF-Dll4/Notch regulatory feedback loop helps to preserve the position of the TEC leading the directional growth of a sprout, the position of this TEC is still only transient: in fact, during the process of vascular growth, SECs can move to the tip of the sprout, alter phenotype, and exchange position with the original TEC [167].

One of the the key features of capillary networks is their intercon-

nected, mesh-like structure. Exactly how this structure emerges is yet to be fully understood, but it is apparent that it is a result of both the initial development process and later remodelling according to metabolic and mechanical cues. This thesis, which focuses on modelling the first 5 days of vascular growth, is predominantly concerned with the former: sprout bifurcation and anastomosis during the initial stages of sprouting angiogenesis.

Note that the terms "sprouting" and "branching" have often been used interchangeably in previous work to refer to the formation of new vascular sprouts from existing, perfused vessels. However, in this thesis this process shall be referred to exclusively as "sprouting", whereas "branching" shall be used to describe the formation of a new sprout at the location of TECs, i.e. via birfurcation of an unperfused sprout at the tip. In the remainder of this section, details of the biological processes behind branching and anastomosis, and the role of filopodia, are summarised with reference to the literature, prior to the development of the mathematical model in the following section.

Previously, an *in vitro* model of sprouting angiogenesis showed newly formed sprouts beginning to branch around 4 days after their first appearance [267]. Another study suggested that the division of TECs, and thus creation of daughter branches from the original sprout, is initiated by the inhibition of notch signalling [339]; this aligns with the converse negative regulation of TEC formation caused by Dll4/Notch activation [150]. In a further *in vitro* study, Anderson et al. placed VEGF-bound nanoparticles within HUVEC-seeded fibrin gel and found that high density clusters of the nanoparticles produced a greater number of endothelial tube branch points than homogeneous distributions of soluble VEGF [11]. However, these *in vitro* models are not able to capture the full spectrum of signalling factors and environmental cues that new vessels are exposed to *in vivo*.

Studies of branching morphogenesis, embryonic sprouting and

branching, can also provide clues as to the mechanisms behind sprout branching. For example, Kearney et al. studied the impact of VEGF receptor VEGFR1 (Flt-1) on embryonic blood vessels via a gene knock out study and found that the loss of VEGFR1 induced a decrease in vascular branching [184], again suggesting a role for VEGF in branching. It seems feasible that VEGF, which plays such an integral role in other areas of angiogenesis, would also influence the degree of TEC branching; but the effect of other factors and mechanical cues cannot be discounted.

Anastomosis, the joining of two vessels or sprouts, is a crucial part of the development of connected and fully functioning vasculature. Yet current understanding of the mechanisms behind anastomosis is less developed than understanding of the initiation of sprouting angiogenesis. Two types of anastomosis can occur: tip-to-sprout, where a TEC collides with a neighbouring sprout or vessel, or tip-to-tip, where a TEC joins with another TEC.

Experimental evidence has suggested that filopodia play a role in anastomosis, with ECs interacting via their filopodia prior to forming stable contact. In embryonic zebrafish studies, Phng et al. reported that an absence of filopodia resulted in the loss of contact formation between ECs [313], and Lenart et al. observed that filopodia contact occurred prior to both tip-to-tip and tip-to-sprout anastomosis [215]. Other recent research also suggests that ECs make transient contact with other sprouts prior to stable anastomosis, and that the process is regulated by VEGFR1 [271]. This again underlines the importance of VEGF across many aspects of sprouting angiogenesis.

In the following section, this knowledge of the basic behaviours of and relationships between the EC phenotypes involved in sprouting angiogenesis is used to inform the structure of the discrete model angiogenesis model.

5.3 Development of a discrete model of sprouting angiogenesis

As reviewed in Section 2.2, existing computational and mathematical models of angiogenesis range from simple continuum models with no spatial component, to complex multiscale hybrid frameworks that encompass processes ranging from the subcellular up to tissue scale interactions. The aim of the model of angiogenesis described in this thesis is not to provide further understanding of the underlying mechanisms behind sprouting angiogenesis, but rather to integrate current experimental knowledge of angiogenesis into a descriptive framework that will help to investigate the effect of different cell seeding strategies, and thus different time dependent VEGF distributions, on the rate, directionality and penetration distance of vascular growth in the context of peripheral nerve repair.

For this reason, the influence of subcellular processes such as the secretion of certain proteins and individual cell life cycles will not be incorporated into the framework, in contrast to previously published models by Owen et al. [293, 294] and Perfahl et al. [307] which use differential equations to govern the internal processes of individual cells and track their evolution through the cell cycle.

It is necessary only for this model to mimic the observed behaviour of growing vasculature; consequently, the number of parameters and processes incorporated was kept to a minimum to ease the implementation and usability of the model. Previously published descriptive mathematical frameworks, along with experimental evidence, are drawn upon to inform the functional forms and parameters of the model: this is described in detail in Sections 5.3.3, 5.3.4 and 5.3.5.

The key features of angiogenesis that this framework aims to capture are as follows:

1. Initiation of sprouting angiogenesis via the selection of TECs from

existing vessels. In the specific case of vascular growth into an NRC as modelled here, this is represented simplistically by the creation of TECs on the circular faces of the NRC geometry to reflect the inward "invasion" of sprouts across the boundary of the NRC (Section 5.3.3.1).

2. The migration of TECs in response to VEGF gradients, sensed by filopodia extending from the TECs, and the formation of nascent vascular structures (vascular sprouts) composed of SECs (Sections 5.3.2 and 5.3.4).

3. Branching of sprouts to create the characteristic "tree-like" structure of vasculature (Section 5.3.3.2).

4. Anastomosis of sprouts to form closed loop vessels. This can occur via "tip-to-sprout" anastomisis, where a TEC anastomises with a nearby sprout, or "tip-to-tip" anastomosis, where two TECs collide (Section 5.3.5.1).

5. Provision of oxygen to the engineered tissue by blood-perfused vessels. Note that this element of the model involves direct feedback between the discrete angiogenesis framework and the continuum cell-solute model (Sections 5.3.5.2 and 5.4).

Thus there are some well-established elements of sprouting angiogenesis that this framework omits. The time scale of sprouting angiogenesis in peripheral nerve repair was an important consideration when identifying which processes to incorporate into the model. As mentioned in Section 2.1.3, experimental work suggests that in the peripheral nerve repair setting angiogenesis is initiated within 3 to 7 days [65, 103, 153, 304]. In line with the simulations run in Chapter 4, the maximum length of time simulated in this chapter is 5 days. Beyond this point it is expected that additional factors such as vascular network pruning and remodelling, where vessels

regress in response to shear stress and metabolic signals, would need to be taken into account: the framework described here does not attempt to capture these processes.

Another key aspect of sprouting angiogenesis that is not incorporated into the framework described here is the impact of Dll4/Notch signalling on the selection of TECs as reviewed in Section 5.2. Changes in EC phenotype or the exchange of positions between TECs and SECs within the same sprout that have been observed experimentally are also neglected [151, 167]. Inclusion of these processes would add detail and complexity to the model that is unnecessary for the aims of this thesis.

Additionally, some previously published models have incorporated a VEGF consumption term to represent VEGF binding to TECs [23, 166]. However, accurate values for VEGF binding rates are unknown. Furthermore, it is assumed that the rate of VEGF uptake by the relatively small number of cells present in the sprouts will be negligible in comparison to the rates of production by the seeded cells, and also the VEGF decay rate. For these reasons, VEGF binding to ECs is neglected in this model, although the framework could be adapted to include this aspect in the future.

The impact of oxygen concentration on the ECs that make up the sprouts, and their metabolism of oxygen, will also be neglected in this model. Implicitly this assumes that oxygen has no impact on the viability of the ECs; this assumption is based on studies that suggest that ECs only show decreased viability when exposed to prolonged (>24h) severe hypoxia (<5%) [27, 118, 362], and in fact increase in viability under exposure to mild hypoxia. In general, evidence suggests that ECs are less prone to cell death under hypoxic conditions than other cell types. The consumption of oxygen by ECs is neglected using the reasoning that the density of ECs modelled in this thesis is much less than the density of the therapeutic cells; therefore, it is assumed that their impact on the oxygen local oxygen

concentration will be negligible in comparison.

Finally, it is assumed that only TECs are sensitive to VEGF. In fact, experimental evidence shows that SECs also have a proliferative response to VEGF dependent upon the concentration of the growth factor [134]. This effect has been incorporated into previous models of angiogenesis by imposing sprout growth rates and branching probabilities that are dependent on EC density [10, 23, 365]. However, here the EC density of the sprouts is not tracked and sprout elongation is modelled by TEC migration alone, without an explicit dependence upon the proliferation of the cells in the body of the sprout. Instead, a dependence on VEGF concentration is included into the branching probability distribution and the rate of TEC migration, with larger concentrations of VEGF inducing a higher probability of branching as well as a greater speed of migration and therefore higher rate of sprout elongation. This implicitly incorporates the effect of VEGF on SEC proliferation and thus sprout elongation.

In the the following subsections, first of all the basic structure of the mathematical model is outlined in Section 5.3.1, then details are provided for the different components of the model in Sections 5.3.2, 5.3.3, 5.3.4 and 5.3.5, including explanations for the choice of parameters and functional forms. The parameters used in the model are listed in Table 5.1. In Section 5.4, model simulation results are presented to explore the impact of different cell seeding strategies, and corresponding VEGF distributions, on the rate and directionality of vascularisation over time.

Sprouting angiogenesis model parameters	
Spatial grid spacing	$\Delta x = 10$ µm
Time step length	$\Delta t = 1$ h
Filopodia sensing radius	$r_f = 100$ µm [134]
VEGF averaging radius	$r_a = 20$ µm
Maximum sprout formation probability	$s_{\max} = 8 \times 10^{-5}$ µm^{-1}h^{-1} [347, 381]
TEC sprouting exclusion radius	$r_{\text{ex}} = 20$ µm
Maximum branching probability	$b_{\max} = 0.001$ h^{-1}
Threshold age for branching	$T_{\text{branch}} = 0.75$ days [10]
Directional persistence angular deviation parameter	$\sigma = \pi/6$ [276, 381]
Maximum TEC migration rate in absence of VEGF gradient	$\text{R}_{\max} = 20$ µm/h [386]
Minimum TEC migration rate in absence of VEGF gradient	$\text{R}_{\min} = 10$ µm/h [386]
Anastomosis distance	$r_{\text{ana}} = 20$ µm
Representative VEC sphere radius	$r_s = 3$ µm
Concentration of oxygen in blood	$c_b = 10\%$ [64]
Vessel wall thickness	$t_v = 1$ µm
Vessel radius	$r_v = 5$ µm
Vessel wall permeability	$k_w = 1.115 \times 10^{-12}$ µmol/(µm s mmHg) [109]
Bunsen solubility coefficient	$B_s = 1.27 \times 10^{-15}$ µmol/(µm^3 mmHg) [109]

Table 5.1: Parameter values used for the model of sprouting angiogenesis.

5.3.1 Overview of the structure of the discrete model

It was decided in Section 2.2 that a discrete framework should be used for the angiogenesis model, motivated by the need to model the behaviour of individual migrating TECs and to evaluate the morphology of vessels and sprouts: a continuum approach would not provide the ability to assess vessel directionality or tortuosity. The discrete framework uses the continuous output of the cell-solute model as an input variable.

In this model, at every discrete time new TECs are formed at randomly selected nodes on the circular faces of the cylindrical geometry, according to a probability distribution of the local VEGF concentration, to simulate the process of vascular sprouting. The subsequent growth of the vascular sprouts is described using a discrete lattice-based approach in which vascular sprouts are defined as the trace or "snail-trail" of the migrating TECs. The TECs move via a random walk process biased according to directional persistence and VEGF gradients (Section 5.3.4). The lattice is composed of nodes on a regularly spaced grid with spacing $\Delta x = 10$ μm (Figure 5.11c), and the model operates in discrete time steps of length Δt. The spatial lattice spacing reflects both the diameter of endothelial cells, which is in the range of 5 to 10 μm at their widest point [131], and the diameter of new sprouts which has also been found to be between 5 and 10 μm in the early stages of development [279], prior to exposure to flow and consequent vascular adaptation.

The model features three cell types which exhibit different behaviour according to the rules of the framework: TECs, SECs and vessel endothelial cells (VECs). Note that VECs are not analogous to phalanx ECs, but instead are used as a "placeholder" to denote the position of blood-perfused vessels; SECs are re-labelled as VECs when they become part of a closed, blood perfused vascular loop. Each EC occupies a single node and is assumed to fill the corresponding cubic voxel surrounding it. Any variation or asymmetry in the shapes and sizes of ECs or sprouts is neglected. Although all

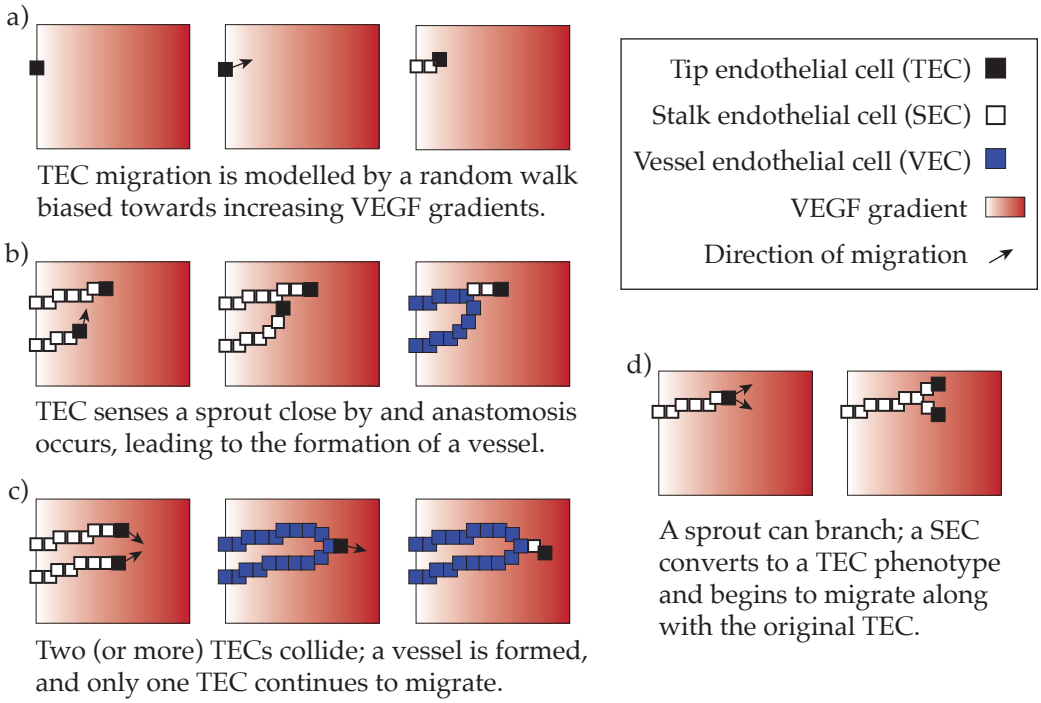

Figure 5.1: Illustration of the key behaviours and cell type characteristics incorporated into the discrete model. TEC cells migrate across a 3D lattice; here the diagrams are drawn in 2D for simplicity, but the same principles apply in 3D. Note that the VEGF distribution is determined by the cell-solute model and therefore varies over time.

three of these cell types would metabolise both oxygen and VEGF, these effects are neglected as the total amount of VEGF and oxygen consumption generated by the ECs would be negligible in comparison to the solute changes brought about by the seeded cells.

Figure 5.1 conveys the main behaviours and roles of the cell types within this mathematical framework. Nodes that have previously been occupied by TECs are subsequently assumed to be occupied by stalk endothelial cells (SECs). Sprouts, defined here as unperfused chains of SECs led by TECs, are formed and branch according to probability distributions that are functions of local VEGF concentration (Section 5.3.3). Blood-perfused vessels capable of delivering oxygen are created when TECs anastomise with other TECs or SECs to form a closed vascular loop composed of VECs (Section 5.3.5).

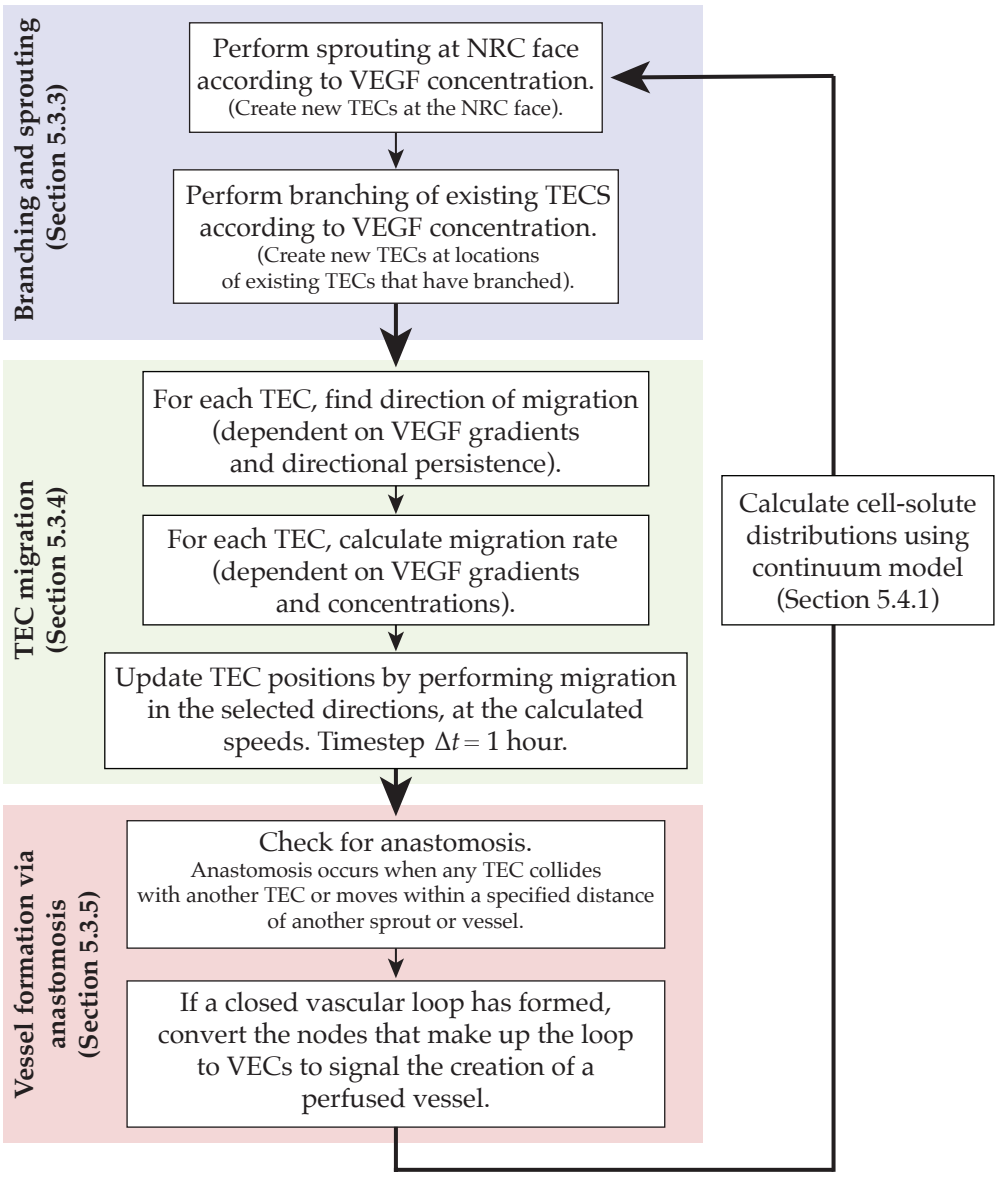

Figure 5.2: Overview of the 3D sprouting angiogenesis model. Specific details of the algorithms and functions used to carry out the three main processes that make up the model- branching and sprouting, TEC migration and vessel formation- are provided in Sections 5.3.3, 5.3.4 and 5.3.5 respectively.

At every time step, the model calculates whether new sprouts have occurred at the circular faces of the NRC and whether TECs have branched, updates the positions of the migrating TECs according to the directional cue of the VEGF distribution, and determines whether anastomosis and vessel formation have taken place (Figure 5.2). The angiogenesis model is integrated with the cell-solute model: at each iteration the VEGF distribution over the geometry is calculated using the continuum cell-solute model, and in turn the distributions produced by the cell-solute model are influenced by changes in oxygen concentration caused by diffusion from blood-perfused vessels, modelled in the discrete framework. The computational methods used to solve the model of angiogenesis and combine it with the cell-solute model are described later in Section 5.4.1.

5.3.2 Tip endothelial cell sensing of VEGF

The formation of the vascular network in this framework is governed by gradients and concentrations of VEGF. Work by Gerhardt et al. suggests that TECs sense gradients of VEGF via the extension of filopodia [134]; therefore the model must include a mechanism to mimic this process. This suggests the use of a filopodia sensing radius r_f, which represents the range of the filopodia and thus determines the distance from which each TEC can sense VEGF.

In a previous model, Qutub and Popel restricted sensing of VEGF to voxels adjacent to that occupied by a TEC [325], where each voxel has a volume of 1 μm^3; however, simulations run with this relatively small "sensing radius" and without the incorporation of strong directional persistence resulted in highly tortuous networks. The authors hypothesised that this either underlines the importance of directional persistence mediated by the structure of the extracellular matrix, or suggests that VEGF sensing should occur over longer distances.

The latter explanation is corroborated by experimental data suggesting that the filopodia of retinal endothelial cells have variable lengths predomi-

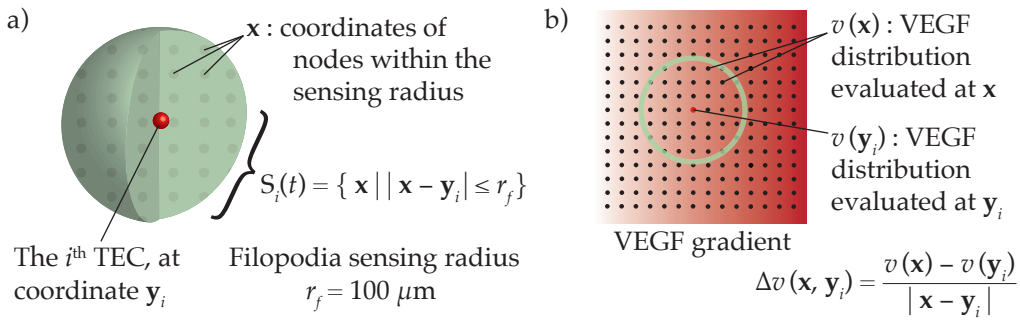

Figure 5.3: Model mechanism for VEGF sensing by tip endothelial cells. a) A sphere in 3D space with radius r_f is used to represent the set of nodes that a TEC is able to sense via its filopodia. b) Representation in 2D of the sensing radius of the i^{th} TEC and TEC evaluation of VEGF gradients within the model. The same concept is extrapolated to 3D.

nantly within the range of 0 to 100 µm [134]. Other models of angiogenesis have implicitly incorporated the effect of the filopodia by assuming that TECs can sense VEGF concentrations and gradients within 10 µm [399] or 100 µm [347] of the cell body. In line with the results produced by Gerhardt et al., in the current model the filopodia sensing radius parameter r_f is set at 100 µm.

Thus at each time point t, the i^{th} TEC occupies a node with position $\mathbf{y}_i(t)$ in the 3D lattice, and can sense the VEGF concentrations at nodes in the neighbourhood set S_i defined by the sensing radius r_f (Figure 5.3):

$$S_i(t) = \{ \mathbf{x} \mid |\mathbf{x} - \mathbf{y}_i| \leq r_f \}. \tag{5.1}$$

The local concentration of VEGF $v(\mathbf{y}_i, t)$ is the VEGF concentration field evaluated at the position of the i^{th} TEC at that time point. The gradients of VEGF $\Delta v(\mathbf{x}, \mathbf{y}_i)$ within each neighbourhood S_i can be sensed by TECs and are calculated as follows:

$$\Delta v(\mathbf{x}, \mathbf{y}_i) = \frac{v(\mathbf{x}) - v(\mathbf{y}_i)}{|\mathbf{x} - \mathbf{y}_i|} \; \forall \, \mathbf{x} \in S_i. \tag{5.2}$$

These variables are used to calculate the direction and rate of migration of TECs, as explained in 5.3.4.

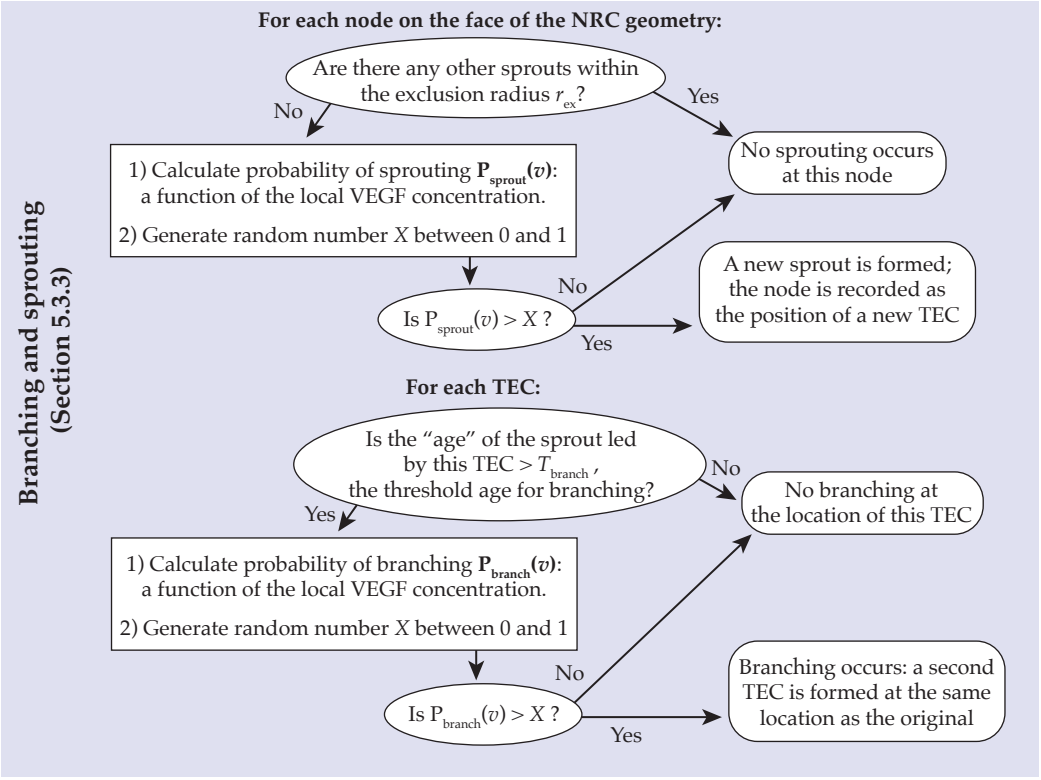

Figure 5.4: Flow diagram of the vessel sprouting and branching algorithms.

5.3.3 Sprout formation and branching

5.3.3.1 Sprout formation

There has been some debate about whether the direction of revascularisation- and therefore the origin of new vascular sprouts- during peripheral nerve repair is predominantly lateral (originating from the tissue bed and growing inwards from the sides of an approximately cylindrical graft or NRC) or longitudinal (originating from the stumps at either end of a graft or NRC, as shown in Figure 2.1), or some more equal combination of the two.

Early studies found that some vascularisation did originate laterally from the tissue bed when nerve grafts were used to repair rabbit sciatic and tibial nerve injuries [7, 304] and dog sciatic nerve injuries [377]. However, in some of these studies it was found that vascularisation also occurred longitudinally, with Algren et al. noting that vessel ingrowth from the ends of grafts appeared to precede that from the surrounding tissue in

some cases. In 2002, Hobson et al. also observed vascularisation from both the surrounding muscle bed and the proximal and distal nerve stumps in rat sciatic nerve injuries repaired using tubular fibronectin conduits [153].

However, for the model presented in this thesis it is assumed that due to the use of a protective sheath vascularisation will occur only longitudinally, via sprouting from the distal and proximal ends. This assumption is based upon studies that have used capped [42] and entubulated [322] grafts which demonstrate that impermeable materials such as silastic tubing can effectively block vascularisation.

The time scale of the simulations conducted in this thesis is 0 to 5 days, and previous work has assumed that a degree of vascular maturity is required prior to the formation of additional sprouts from the newly developed perfuse vessels: for example, in their model McDougall et al. introduced a minimum vessel age threshold of 4 days for vascular sprouting [250]. Therefore in this thesis it is assumed that any new vessels formed during each simulation will remain too immature to produce further sprouts; therefore sprouting in the current model occurs only from the circular faces of the NRC, representing the inward invasion of new sprouts that have formed from existing vessels residing outside of the NRC construct. The incorporation of sprouting from newly formed vessels could be incorporated into future iterations of the model via some relatively simple adaptations.

In the model presented here, a probability distribution is implemented that at each time step determines the probability of sprouting occuring, represented by the formation of a new TEC, at each of the nodes located on the circular faces (Figure 5.11c). The use of a sprouting probability distribution is widespread among existing theoretical models [250, 293, 307, 347, 381], although there is considerable variation in the forms of these probability distributions and the variables that they take into account.

For example, McDougall et al. determined that vessel sprouting could

not take place unless the stimuli of wall shear stress induced by blood flow was present, and then the probability of sprouting was set to increase linearly with the degree of wall shear stress [250]. However, vascular adaptation and explicit modelling of blood flow is not included in the current framework.

The other important variable often included in models of vascular sprouting is growth factor concentration. As reviewed in Sections 2.1.3 and 5.2, VEGF plays a critical role in initiating sprouting angiogenesis. This motivates the use of a sprouting probability distribution that is a function of VEGF. Due to the boundary conditions applied to the cylindrical NRC geometry described in Section 4.3.1, the VEGF concentration on the circular faces of the geometry is always 0 ng/ml. However, this is where the initial sprouting occurs. Therefore for each node on these circular faces, the average of the non-zero VEGF concentrations at local nodes (within a specified averaging radius $r_a = 20$ µm) is taken as the value of $v(\mathbf{y}_i)$ and used to determine the probability of sprouting and to calculate the gradients in the surrounding directions as per Equation (5.2), as opposed to the concentration at the node itself.

A key parameter that features in many sprouting models is a threshold VEGF concentration required for sprouting. Secomb et al. [347] used a value of 0.8 nM for this, approximately equivalent to 37 ng/ml. However, results published by Chen et al. and Nakatsu et al. suggest that sprouting can occur upon exposure to much lower VEGF concentrations of 1 to 35 ng/ml [72, 268]; therefore the current model does not impose a VEGF threshold for sprouting, instead using a probability distribution to ensure that very low VEGF concentrations result in a lower chance of sprouting.

The exact form of this probability distribution was informed by some experimental studies which have sought to quantify the relationship between VEGF and EC sprouting. A 3D *in vitro* model was used by Chen et al. to measure VEGF-induced MEC sprouting from beads in a fibrin gel

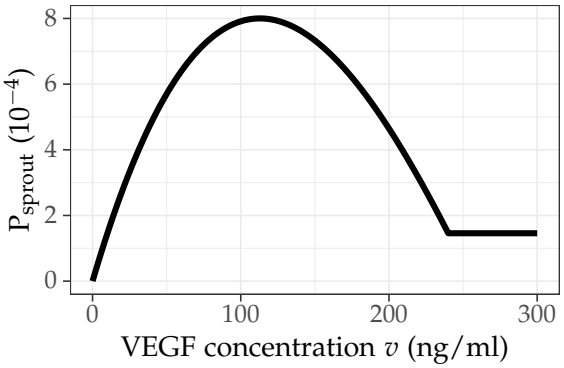

Figure 5.5: Probability of sprout occurrence P_{sprout} at any node on the NRC circular face as a function of the local VEGF concentration v over one time step. Here parameter values of mesh size $\Delta x = 10$ µm and time step $\Delta t = 1$ hour were used to calculate the values of the function P_{sprout}.

[72]. The authors found that although some sprouting occurred when the beads were exposed to low VEGF concentration (5 to 10 ng/ml), a peak in the number of sprouts was observed at around 100 ng/ml. Beyond this concentration, the number of sprouts declined until reaching similar levels at 250 to 300 ng/ml as recorded for 0 to 50 ng/ml.

Conversely, work by Shamloo et al. suggests that the dependence of sprouting upon VEGF concentration is sigmoidal [350]. In this study, beads coated with adult human dermal microvascular ECs were seeded in collagen matrices of varying densities and exposed to gradients and concentrations of VEGF via a microfludic device. Some sprouting was observed at VEGF concentrations of 25 ng/ml and a saturation threshold of around 125 ng/ml of VEGF. However, concentrations of less than 25 ng/ml or greater than 175 ng/ml were not tested. In approximate agreement with Chen et al., the optimal concentration for sprouting was 125 ng/ml.

The functional form of the sprouting probability distribution (Figure 5.5) used in the model presented in this thesis is based upon the *in vitro*

data presented by Chen et al.:

$$\mathrm{P}_{\mathrm{sprout}}(v) = \begin{cases} (1.161\mathrm{e}{-7}v^3 - 1.047\mathrm{e}{-4}v^2 + 0.0192v)s_{\max}\Delta t\Delta x \\ \qquad\qquad\qquad\qquad\qquad\qquad v \leq 240\,\mathrm{ng/ml}, \\ \mathrm{P}_{\mathrm{sprout}}(240), \;\; v > 240\,\mathrm{ng/ml}. \end{cases} \tag{5.3}$$

The value at which the probability of sprouting achieves its maximum is $v \approx 113$ ng/ml, which is within the range of the values found in the two previously mentioned experimental studies.

The maximum sprout formation probability $s_{\max} = 8 \times 10^{-5}$ $\mu\mathrm{m}^{-1}\mathrm{h}^{-1}$ is assigned in line with previous computational studies [347, 381]. This value of $s_{\max}$ approximates the probability of sprout formation per unit length of existing vessel per hour based upon experimental data measured in the rat cornea [356]. Thus these values assume that sprouting occurs from existing vasculature; however, in the peripheral nerve repair scenario modelled in the current thesis, the positioning of existing vasculature is unknown. Instead, it is assumed that sprouting could occur from any node at located at the stump interface (nodes on the circular face of the cylindrical geometry), and the parameter for vessel length is replaced with the grid spacing parameter Δx. Values for the approximate rate of sprouting that are specific to peripheral nerve repair could be obtained via future experimentation.

Finally, a TEC sprouting exclusion radius $r_{\mathrm{ex}} = 20$ µm is used to reflect the fact that new TECs (and thus sprouts) do not form in close proximity to each other. Thus at each time step, new sprouts are unable to form within this distance of the base of an existing sprout on the circular face of the NRC. Figure 5.4 shows the complete algorithm used to determine at which nodes new TECs form on each iteration.

5.3.3.2 Sprout branching

Similarly to vascular sprouting, in existing models probability distribution functions that depend on a range of different variables have been implemented to describe TEC branching: the same approach is taken in this thesis.

Milde et al. implemented a method of sprout branching that imposes TEC branching events when the local anisotropy in the joint directional cue provided by VEGF and fibronectin gradients and collagen fibers exceeds a certain threshold [260], thus combining chemotactic, haptotactic and mechanical cues. Similarly, Sun et al. included a thresholding condition upon the perpendicular component of the velocity vector of the TECs, which is dependent upon the directionality of the ECM as well as chemotactic growth factors [369]. Other models have also applied a minimum EC density condition on TEC branching [10, 365].

For the purposes of this thesis, the effects of mechanical forces and cues generated by the structure of the NRC are not considered, with the expectation that these effects could be integrated into the framework at a later date. Similarly to the sprouting probability distribution, here the branching probability distribution is therefore set as a function of the local VEGF concentration only: due to a lack of quantitative experimental evidence on the exact nature of the relationship between VEGF and branching, the shape of this function is informed by previous computational work.

Previously, models of cancerous vascular growth in response to generic tumour angiogenic factors (TAFs), which include VEGF, have defined the TEC branching probability to be an increasing function of the local TAF concentration [249, 363]. This is motivated by the observation of increased branching frequency at the edge of vascular networks in close proximity to tumours, dubbed the "brush border effect".

Some models of developmental and wound healing angiogenesis have also included TEC branching probability distributions that are increasing

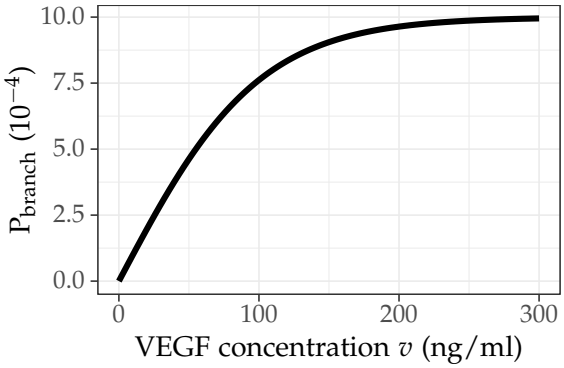

Figure 5.6: TEC branching probability P_{branch} as a function of VEGF concentration v, over a time step of length $\Delta t = 1$ hour.

functions of VEGF concentration [251, 406], although it appears that the precise functional forms of these relationships have not been based on any experimental evidence.

The branching probability distribution function (Figure 5.6) used in the current framework is defined as follows:

$$P_{branch}(v) = b_{max}\Delta t \tanh(v/100), \tag{5.4}$$

where b_{max} is the maximum probability of branching per hour and $v = v(\mathbf{y})$ is the local VEGF concentration in ng/ml for a TEC at a node with coordinates $\mathbf{y}$. As in the previously mentioned models, the functional form of this relationship is not based on experimental data and is a good candidate for further refinement in the future. The value of $b_{max} = 0.001$ was estimated in order to produce qualitatively realistic sprout morphology, but further quantitative parameterisation against experimental data would be useful for future work.

Additionally, in the model presented in this thesis the parent sprout of a TEC must exceed a threshold age before branching becomes possible to prevent unphysiological premature branching. Estimates for this threshold age used by previous mathematical models lie in a range of 0.71 to 2.1 days [10, 251, 260, 369, 406]. As per the model developed by Anderson and Chaplain, a value of $T_{branch} = 0.75$ days was chosen for use in the cur-

rent model [10]. Previously this value was shown to produce qualitatively similar morphologies to *in vivo* networks.

During a TEC branching event, a secondary TEC forms at the node location of the TEC that has branched (Figure 5.1). In the subsequent TEC migration step, the primary TEC continues to migrates as before (governed by the functions set out in Section 5.3.4.2), whereas the direction of movement of the secondary TEC is restricted to directions that form an angle of 90deg with the previous direction of growth of the parent TEC. The age of secondary TEC sprouts is set to zero when they are first formed, thus permitting them to branch again only once the age threshold has been exceeded for a second time.

5.3.4 Tip endothelial cell migration

5.3.4.1 Biological background

The direction and rate of TEC migration is influenced by haptotactic, mechanotactic and chemotactic cues [204]. Haptotaxis is the directional movement of cells in response to gradients of ECM proteins. In the context of EC migration, *in vitro* evidence suggests that gradients of fibronectin can induce directional cellular motion [359], and that collagen density may affect EC spreading and migration speed [159]. Other material aspects of engineered tissues such as collagen fibril alignment have also been shown to affect the directionality of EC migration [203], and previous models of angiogenesis have included terms that allow the ECM to influence the direction of TEC migration [93, 369].

Experimental results also indicate that fluid shear stress has an influence on the migration of TECs [385, 386]; Albuquerque et al. found that exposure to shear stress increased the degree of endothelial cell wound closure *in vitro* and induced faster cell migration velocities than in the static case [5]. Additionally, fluid shear stress may act as a directional guidance cue for migrating ECs [292].

However, the influence of chemotactic, not haptotactic or mechanotac-

tic, cues are the focus of this thesis. In line with the continuum cell-solute model presented in Chapter 3, the influence of shear forces caused by fluid flow is neglected in this model and the effect of cues provided by the collagen EngNT is restricted in this framework to the incorporation of directional persistence (as described later in Equation (5.9)). It is assumed that the structural properties of the engineered tissue are homogeneous and have no effect on TEC migration speeds or directions. The incorporation of these aspects would be a natural next step for this integrated mathematical framework for modelling peripheral nerve repair.

As reviewed in Section 2.1.3, it is well established that EC migration during angiogenesis is regulated by angiogenic factors, with VEGF being the most studied and likely the most important chemoattractant [31, 282, 335, 413]. The effect of VEGF on the migration of ECs can be separated into chemotaxis, the directional response that prompts the cells to move towards higher concentrations of the growth factor, and chemokinesis, a more general non-directional change in migratory behaviour that includes changes in the speed of migration.

Microfluidic chemotaxis chambers have been used to study chemotaxis *in vitro*. For example, Barkefors et al. used such a chamber to study the migratory response of HUVECs and human umbilical cord vein endothelial cells (HUVECs) to "hill-shaped" gradients of VEGF and FGF2 [31]. These stable symmetrical gradients were created via the use of different flow rates, and closely resemble the gradients that arise during simulation of NRCs in this thesis (for example in Figure 4.9), with a pronounced maxima in the middle of the channel.

The movement of individual cells was tracked via time lapse microscopy over 200 minutes, and the authors found that decreasing the steepness of gradients of $VEGF_{165}$ resulted in a reduced chemotactic response of the HUVECs. The highest chemotactic response was induced by a gradient ranging from 0 to 50 ng/ml over the same distance (an average

of 0.125 ng/ml/μm), although steeper gradients than this were not studied. A similarly steep gradient of $VEGF_{121}$ also induced positive chemotaxis, although at a slower rate. Conversely, upon the use of a gradient of $VEGF_{165}$ that increased from 6 ng/ml to 27 ng/ml over 400 μm (an average of 0.0525 ng/ml/μm), the movement of the cells appeared to become close to random migration.

In a set of similar experiments, Shamloo et al. found that a gradient of 0.002 ng/ml/μm resulted in no chemotaxis of HUVECs in 2D regardless of whether the absolute VEGF concentration used was low (20 ng/ml) or high (30 ng/ml), whereas a steeper gradient of 0.014 ng/ml/μm did induce chemotaxis [351].

Additionally, in their study of MEC sprouting in 3D [72], Chen et al. found that sprout alignment increased with increasing VEGF concentration gradients. Gradients of over 0.025 ng/ml/μm induced the greatest percentage of aligned sprouts.

Overall, these papers suggest that steeper gradients of VEGF induce a more pronounced directional chemotactic response in migrating ECs. They also provide evidence that there could exist a threshold gradient steepness (in the approximate range of 0.014 ng/ml/μm to 0.0525 ng/ml/μm) below which EC movement is close to random migration. The work of Chen et al. also shows a sigmoidal relationship between the gradient steepness and the % of aligned sprouts. These pieces of evidence can be used to inform the choice of functional forms used to model chemotaxis in the theoretical model. However, some of these studies track the migration of ECs in 2D only, and further work to clarify the relationship between VEGF and EC migration in 3D would be desirable [48].

Recently, gradients of oxygen have also been found to induce directional EC migration, with cells moving preferentially towards areas of low oxygen concentration [352]. This study was also carried out using a microfluidic cell migration assay using gradients of approximately 18%/mm.

However, to reduce model complexity the chemotactic effect of oxygen will not be included in the current model. It is assumed that this will not impact the overall outcomes of the model because areas of low oxygen generally coincide with areas of high VEGF, as demonstrated later in Figure 5.15. Furthermore, there has been no experimental work to examine how combinations of VEGF and oxygen gradients could affect EC migration.

It has also been demonstrated that EC migration is directionally persistent over time. In their study on the effect of fibronectin gradients on EC migration, Smith et al. also measured the persistence time of the cells, defined as the amount of time ECs would migrate in one direction before turning [359]. This metric was found to be unaffected by the fibronectin gradients, remaining at around 1.1 hours. Although this value was derived via *in vitro* experimentation and therefore may not represent the persistence time *in vivo*, it does give a useful approximation as to how long it is expected that the ECs should travel in a single direction, and motivates the use of a time step Δt of around 1 hour.

Aside from directionality, the other important aspect of cell migration in this descriptive model is the speed at which the cells move. The effect of VEGF concentrations and gradients on the rate of cell migration has also been recorded in *in vitro* studies.

The impact of $VEGF_{165}$ on the chemokinesis of HUVECs was assessed by Barkefors et al. by measuring the total 2D distance migrated by the cells [31]. In the absence of flow, a constant concentration of 50 ng/ml of $VEGF_{165}$ caused a reduction in the total migration distance achieved over the time of 200 minutes, resulting in an approximate mean migration speed of 27 µm/h, as compared to a control with no VEGF stimulation, which achieved a mean speed of 42 µm/h.

Conversely, a gradient of 0-50 ng/ml of $VEGF_{165}$ created via the use of fluid flow induced a migration speed similar to that of the control (approximately 42 µm/h). Additionally, the authors found that the rate of

chemotaxis was highest in the region where the gradient was approximately exponential (at the lower end of the gradient) as opposed to the linear region (close to the peak of the gradient).

In contrast to the findings of Barkefors et al., van der Meer et al. found that the migration rate of HUVECs in a microfluidic wound healing assay was significantly higher (approximately 18 μm/h) upon exposure to $VEGF_{165}$ at a concentration of 100 ng/ml than in a control wound assay with no VEGF application (approximately 13 μm/h) [386]. They also demonstrated that a gradient of 100 ng/ml of $VEGF_{165}$ across a distance of 150 μm (an average gradient of 0.667 ng/ml/μm) resulted in a 30% increase in the migration rate of the cells when compared to the uniform application of 100 ng/ml of VEGF [386]. Lastly, Li et al. measured migration speeds of around 12 to 30 μm/h for EC on micropatterned collagen matrices [219]. These values are used in the next section to estimate functional forms for the TEC migration mathematical framework.

5.3.4.2 Model formulation

TEC migration direction

In this model, chemotactic effects and directional persistence contribute to the directionality of TEC migration: the direction of migration taken by each cell at each time step is determined by a probability distribution function dependent on the VEGF gradients sensed by the filopodia (Section 5.3.2) and the direction taken by each cell at the previous time step. Both experimental evidence and the approaches taken by previous models have been used to inform the exact functional form of this probability distribution.

The effects of VEGF-induced directional chemotaxis and persistence are combined multiplicatively as follows to calculate the probability of the i^{th} TEC moving in the *direction* of the node within the local neighbourhood

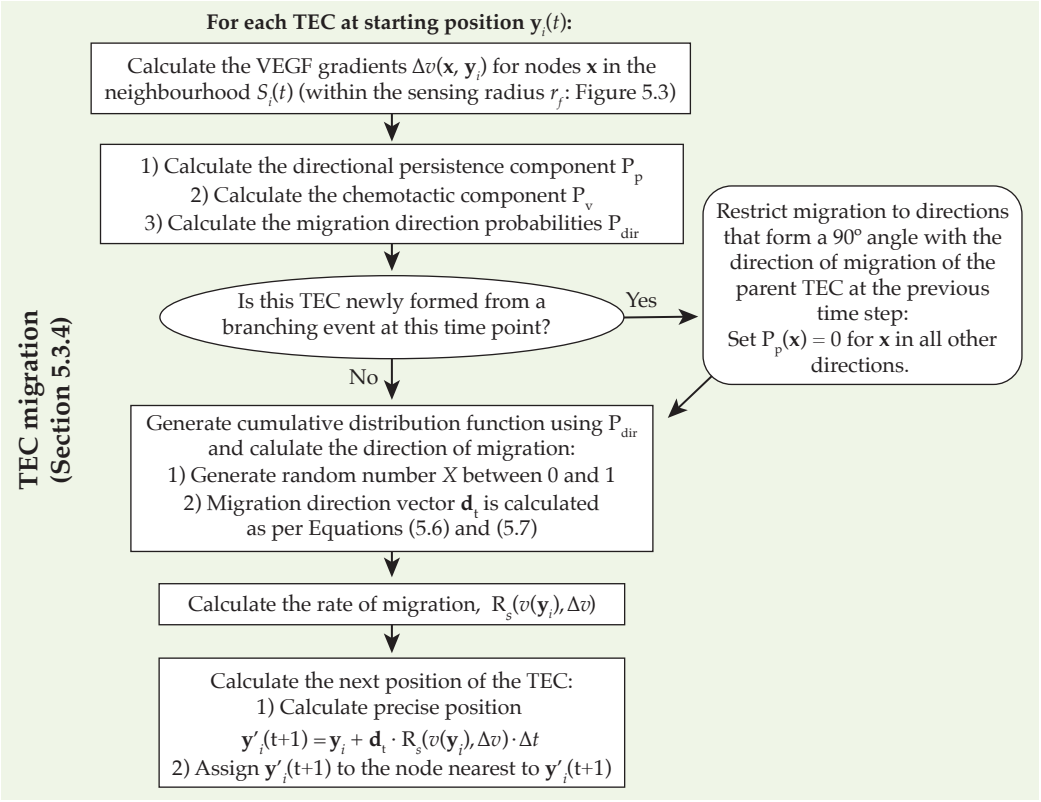

Figure 5.7: Flow diagram of TEC migration algorithm.

S_i (as defined by Equation (5.1)) with coordinates $\mathbf{x}$:

$$\mathrm{P}^i_{\mathrm{dir}}(\mathbf{x}) = \frac{\mathrm{P}^i_{\mathrm{v}}(\mathbf{x})\mathrm{P}^i_{\mathrm{p}}(\mathbf{x})}{\sum_{j=1}^{N_{S_i}} \mathrm{P}^i_{\mathrm{v}}(\mathbf{x}_j)\mathrm{P}^i_{\mathrm{p}}(\mathbf{x}_j)} \quad \forall\, \mathbf{x} \in S_i\,, \tag{5.5}$$

where $\mathrm{P}^i_{\mathrm{v}}$ is the chemotactic component dependent on the VEGF gradient, and $\mathrm{P}^i_{\mathrm{p}}$ is the directional persistence component, which is dependent on the unit vector in the direction taken by the TEC at the time step at which it last moved. Here N_{S_i} denotes the number of nodes within the neighbourhood S_i; thus the probabilities $\mathrm{P}^i_{\mathrm{dir}}$ are normalised such that their sum is equal to 1.

The probabilities $\mathrm{P}^i_{\mathrm{dir}}$ are converted into a cumulative distribution function which is used to select the direction of movement for each TEC via the generation of a uniformly distributed random variable X. The unit

vector for the direction of migration of the i^{th} TEC at time t, denoted $\mathbf{d}_t^i$, can be expressed as

$$\mathbf{d}_t^i = \frac{\mathbf{x}_k - \mathbf{y}_i(t)}{|\mathbf{x}_k - \mathbf{y}_i(t)|}, \tag{5.6}$$

where $\mathbf{x}_k$ is the node within the neighbourhood S_i selected at time t via the cumulative distribution as follows:

$$\sum_{j=1}^{k-1} \mathrm{P}_{\text{dir}}^i(\mathbf{x}_j) < X \leq \sum_{j=1}^{k} \mathrm{P}_{\text{dir}}^i(\mathbf{x}_j). \tag{5.7}$$

The chemotactic component P_{v}^i is based on the experimental studies of EC chemotaxis in response to VEGF gradients:

$$\mathrm{P}_{\text{v}}^i(\mathbf{x}) = \exp\left(50\Delta v(\mathbf{x}, \mathbf{y}_i)\right). \tag{5.8}$$

Here $\Delta v(\mathbf{x}, \mathbf{y}_i)$ is the gradient of VEGF between the current position of the i^{th} TEC $\mathbf{y}_i$ and the position of the node at $\mathbf{x}$, as defined in Equation (5.2). The exponential functional form ensures that TEC movement is weighted towards the steepest gradients of VEGF, and also dictates that as the value of the maximum local VEGF gradient increases the relative weighting in that direction in comparison to the alternative directions also increases. This effect is induced by the increasing gradient of the exponential function. Note that if the VEGF gradient is similar in all directions, the weighting will be almost uniform across opposing directions.

Directional persistence is included via the following term (Figure 5.8):

$$\mathrm{P}_{\text{p}}^i(\mathbf{x}) = \frac{\exp\left(\cos\left(\theta_i(\mathbf{x})\right)/\sigma^2\right)}{\exp\left(1/\sigma^2\right)} \; \forall \, \mathbf{x} \in S_i \,, \tag{5.9}$$

$$\text{where } \theta_i(\mathbf{x}) = \arccos \frac{\mathbf{d}_{t-1}^i \cdot (\mathbf{x} - \mathbf{y}_i)}{|\mathbf{d}_{t-1}^i| \cdot |\mathbf{x} - \mathbf{y}_i|}. \tag{5.10}$$

Here $\theta_i(\mathbf{x})$ is the angle between the previous migration vector for the i^{th} TEC, $\mathbf{d}_{t-1}^i = \mathbf{y}_i(t) - \mathbf{y}_i(t-1)$, and the prospective migration vector in the direction of the node at position $\mathbf{x}$. Here a value of $\sigma = \pi/6$ is assigned, lim-

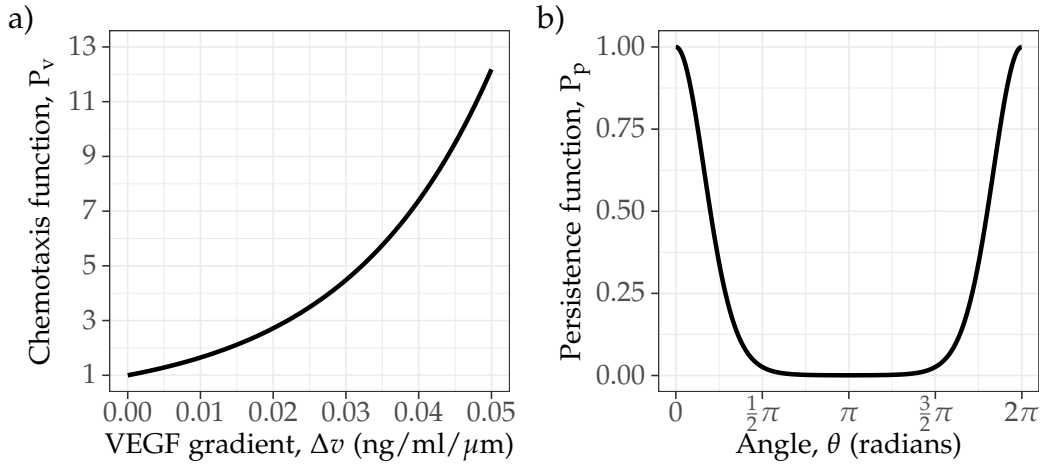

Figure 5.8: a) Chemotaxis function dictates that TEC migration will be biased towards the highest gradients of VEGF. b) The persistence function ensures that the probability of a TEC changing its direction of migration by a very large angle remains low or, in the case of complete reversals of direction, zero. This limits the degree of sprout tortuosity.

iting the angular deviation of sprout direction to between approximately $\pi/2$ and $-\pi/2$, as per previous theoretical models [276, 381]. This term prevents unphysiological vascular tortuosity.

If the TEC has been formed via branching at the current time step, then the direction of migration is limited to directions that form a 90° angle with $\mathbf{d}_{t-1}$, the migration direction of the parent TEC at the previous time step. This is to avoid collision of the two TECs that are within close proximity to each other after a branching event.

Other models of EC chemotaxis in response to VEGF have also incorporated the effect of VEGF receptor saturation [166, 260], in which the cells' ability to sense VEGF gradients decreases when their receptors become occupied. This aspect could be considered in future extensions of the model but will not be included here.

TEC migration speed

Previous models have implemented various types of functional forms and mechanisms to represent the migration speed of ECs or vascular sprout growth rates. Anderson and Chaplain, and later other authors, used a diffusion coefficient approximately equivalent to a migration speed of 8.5

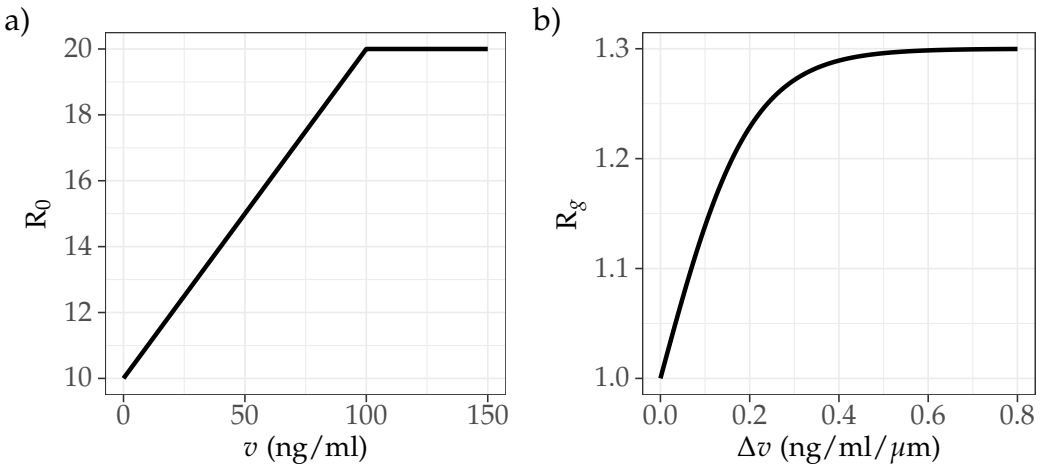

Figure 5.9: a) Baseline TEC migration rate R_0 is an increasing function of the VEGF concentration at the current position of the TEC $v(\mathbf{y})$ until a maximum is reached at $v(\mathbf{y}) = 100$ ng/ml. b) TEC migration rate multiplier function R_g increases the rate of migration according to the VEGF gradient in the direction of migration.

µm/h to model the random motility of capillary tips [10, 23, 251].

Tong and Yuan defined the sprout elongation rate to be dependent on the local angiogenic factor concentration, with a threshold concentration required for elongation for take place [381]. In this case, as the local concentration increases beyond the threshold, the rate of sprout elongation also increases, until reaching a maximum rate set at 20 µm/h.

Qutub and Popel set a maximum velocity of 6.2 µm/h in the absence of VEGF [325]. In the presence of VEGF, the migration rate was set to be proportional to the VEGF concentration, $R_s = 6.2 + 0.4v$ µm/h. Other parameter values used for the migration rate of ECs or speed of capillary sprout growth in existing models range from around 2 µm/h to 40 µm/h [28, 276, 347, 366, 399]

In this model, the rate of migration $R_s(v(\mathbf{y}), \Delta v)$ is defined as a function of both the VEGF concentration evaluated at the TEC's position prior to migration $v(\mathbf{y})$, and the VEGF gradient in the direction of movement, which is chosen prior to the migration step according to the probability distribution defined in Equation (5.5). In the absence of a gradient of VEGF in the direction of movement, the rate of TEC migration $R_0(v(\mathbf{y})) = R_s(v(\mathbf{y}), \Delta v = 0)$

depends only on the local concentration of VEGF with a minimum rate $R_{min} = 10$ µm/h at $v = 0$ ng/ml and a maximum rate $R_{max} = 20$ µm/h:

$$R_0(v(\mathbf{y})) = \begin{cases} R_{min} + \frac{R_{max} - R_{min}}{100} v(\mathbf{y}), & v(\mathbf{y}) < 100\,\text{ng/ml}, \\ R_{max}\,, & v(\mathbf{y}) \geq 100\,\text{ng/ml}. \end{cases} \tag{5.11}$$

This formulation is based upon the work of van der Meer et al. [386] and the functional form used by Qutub and Popel [325]; however, conflicting evidence provided by Barkefors et al. suggests that constant concentrations of VEGF result in slower migration speeds than no VEGF at all.

In the presence of a VEGF gradient in the direction that has been chosen for migration, this function is multiplied by an amount dependent on the steepness of the gradient to mimic the experimentally observed increase in migration speed induced by gradients of VEGF:

$$R_g(\Delta v) = \frac{\tanh(5\Delta v) + (1/0.3)}{1/0.3}, \tag{5.12}$$

$$\Rightarrow R_s(v(\mathbf{y}), \Delta v) = R_0(v(\mathbf{y}))R_g(\Delta v)\,. \tag{5.13}$$

The function $R_g(\Delta v)$ creates a maximum increase in the speed of migration of up to 30% of the baseline values determined by $R_0(v(\mathbf{y}))$ as the VEGF gradient increases, as demonstrated in Figure 5.9. This is in line with the work conducted by van der Meer et al. [386]. It is assumed that TEC velocity is unaffected by its attachment to the rest of the sprout, or other mechanical forces generated by the surrounding matrix.

Calculation of new TEC positions

At each time step, the new position of each TEC is calculated firstly by multiplying the rate of migration by the time step size to find the distance travelled, and then multiplying that by the direction unit vector $\mathbf{d}_t$ to find the next location of the TEC:

$$\mathbf{y}_i'(t + \Delta t) = \mathbf{y}_i(t) + \mathbf{d}_t^i \cdot R_s(v(\mathbf{y}_i(t)), \Delta v(\mathbf{x}_k, \mathbf{y}_i(t)) \cdot \Delta t. \tag{5.14}$$

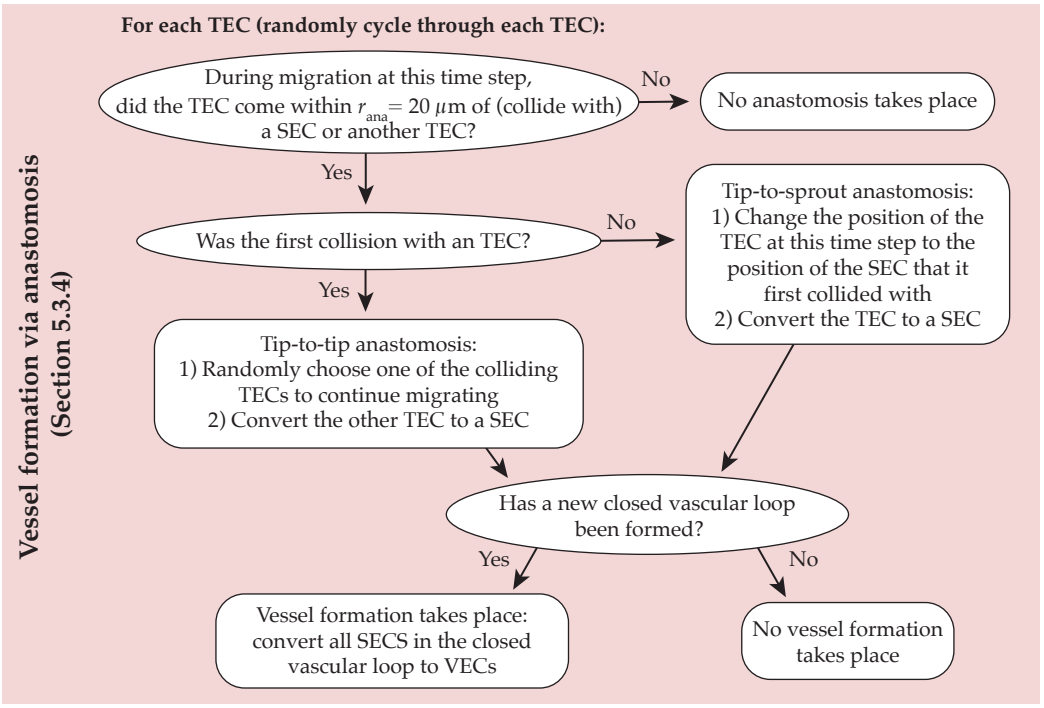

Figure 5.10: Flow diagram of anastomosis and vessel formation algorithm.

The precise coordinates $\mathbf{y}'_i(t + \Delta t)$ are then mapped to the closest node in the discrete lattice, to provide the location of the TEC at the next time step, $\mathbf{y}_i(t + \Delta t)$.

TEC migration is limited to the bounds of the geometry representing the collagen NRC; TECs cannot migrate out of the NRC. This represents the use of a sheath with a pore size that does not permit cellular infiltration. Thus when a TEC is located near the outer edge of the NRC geometry, its directional migration is biased towards the inside of the cylinder because it cannot sense nodes beyond the bounds of the NRC.

5.3.5 Anastomosis and oxygen provision

5.3.5.1 Anastomosis and perfuse vessel formation

The descriptive model of angiogenesis described here does not attempt to capture the complex interactions that occur between cells during anastomosis. Instead it is simply assumed that anastomisation takes place if a TEC comes within $r_{\text{ana}} = 20$ µm of another SEC or TEC. This mechanism was

introduced because the current model is simulated in three dimensions, which significantly decreases the likelihood of TECs colliding directly. In contrast to this, Secomb et al. countered this problem by incorporating an additional bias into their theoretical model of TEC migration that allows TECs to sense the presence of other ECs and migrate towards them [347]; this mechanism is not included into the current model but could be incorporated in the future.

In the current framework, when tip-to-sprout anastomosis occurs the colliding TEC stops migrating and changes type to SEC or VEC. In tip-to-tip anastomosis, one of the colliding TECs is chosen at random to continue migration; the other is considered to have anastomised and changes phenotype (Figure 5.1).

If an anastomisation event has occured between two cells from different "branches" of the network, a closed vascular loop is created (Figure 5.1) and all SECs that make up the loop are converted to VECs to form a vessel. A closed loop is defined as a pathway of ECs that has two root nodes on the circular face of the NRC, thus theoretically permitting flow in and out of the system.

In this model, it is assumed that upon creation of a closed loop all of the connected vessels are immediately perfused with blood and are then able to deliver oxygen to the surrounding tissue. Many existing models of angiogenesis incorporate the transport of oxygen via blood flow, but for simplicity this aspect is neglected in the current framework. Instead, it is assumed that once a vessel is formed, the oxygen concentration in blood remains at a constant value, $c_b = 10\%$ [64]. This means that the model does not take into account other factors that influence oxygen delivery via blood flow, including the vessel radius. However, this does allow the framework to illustrate the qualitative spatial effects that functional blood vessels can have on cell survival and distributions of oxygen within engineered tissue NRCs over time.

5.3.5.2 Oxygen delivery to surrounding tissue

One of the first attempts at using mathematics to describe the delivery of oxygen to tissue via microvasculature was the "cylinder model" developed by Krogh in 1919 [197]. In this model the capillaries are assumed to be evenly spaced and running parallel to each other as part of an array, with each capillary supplying oxygen to a cylinder of tissue surrounding it. A zero flux condition is imposed on the outer edge of the cylinder and thus each volume of tissue is supplied with oxygen by one capillary only.

The assumption that the capillaries are structured in this way was based on the observation that the arrangement of capillaries within muscular tissue is largely regular, with vessels running mostly in parallel to each other with some cross linking. In fact, similar patterns of vasculature are also observed in the peripheral nerve, with vessels mainly running in the lengthwise direction of the nervous tissue [227]. However, although the patterning of vasculature in the peripheral nerve appears regular in comparison to other tissues it would still be unusual to observe uniform spacing of capillaries. Furthermore, the Krogh model assumes no longitudinal diffusion of oxygen (only radial), is time-independent, and does not take into account variations in oxygen consumption across tissue, meaning that it provides a poor fit to the previously described continuum model of cell-solute interactions. Nevertheless, this model has been adapted, extended and used to simulate oxygen delivery in a range of scenarios [195, 320].

When working with a complex vascular geometry that does not necessarily conform to the regular assumption, the provision of oxygen can be modelled through a flux boundary condition applied on the vessel surface. The difficulty then is solving this in combination with the oxygen governing equation, which describes diffusion and consumption in the surrounding tissue.

Secomb and Hsu developed a Green's function method to aid the simulation of oxygen delivery to tissue from 3D vascular networks [158, 345,

346]. In these papers, the vascular geometries mapped from imaging data are divided into many short segments and Green's functions are used to described the oxygen concentration fields caused by a series of oxygen sources on the surface of each vessel segment, whereas oxygen consumption in the tissue is modelled by a series of sinks. A method of iteration is used to ensure that the supersition of the fields created by these sources and sinks satisfy boundary conditions and conservation laws.

However, this method is relatively mathematically complex and difficult to integrate into the the existing continuum model of cell-solute interactions. Alternatively, the finite element methods that were used in Chapters 3 and 4 to solve the cell-solute model within COMSOL can also be used to simulate the delivery of oxygen via the application of flux boundary conditions as sources of oxygen into the tissue domain on the vessel walls. However, Secomb et al. did caution that a finite element approach can result in slower computation times than the Green's function method due to the need to use a relatively fine mesh to allow accurate calculation of the steep gradients that can occur in the region of vessels [346]. Nevertheless, it was decided that this was the best method considering that the vascular networks were not expected to be particularly dense and that the dimensions of the NRC geometry are relatively small.

In the current mathematical framework, vessels that have formed via the anastomisation of sprouts are recorded in the discrete angiogenesis framework as a network of nodes across the three dimensional space of the NRC. Within the cell-solute model, the supply of oxygen provided by each segment of vessel of length l_v is then represented by spherical oxygen sources located at these node locations (Figure 5.11). Spheres were used instead of cylindrical segments to simplify the process of geometry creation and meshing in COMSOL.

To ensure that the total flux of oxygen into the tissue provided by each sphere is approximately equal to that provided by the vessel segment it

represents, the ratio of the spherical surface to the surface are of a cylindrical vessel segment is incorporated into the expression for the diffusive oxygen flux across the vessel wall governed by Fick's law:

$$J = \frac{2\pi r_v l_v}{4\pi r_s^2} k_w \frac{c - c_b}{B_s t_v}. \tag{5.15}$$

Here r_v is the vessel radius, r_s is the radius of each representative sphere, k_w is the vessel wall permeability, t_v is the thickness of the vessel walls, and B_s is the Bunsen solubility coefficient [109]. The parameter values used are listed in Table 5.1. The concentration of oxygen in the blood is represented by c_b, and as previously mentioned for simplicity this value is assumed to be uniform and constant across all the vessels over time. This does not take into account any chemical reactions taking place within the blood.

5.4 Angiogenesis model simulations

5.4.1 Computational methods

The model of angiogenesis was programmed in MATLAB and run in iteration with the previously described continuum cell-solute model (Figure 5.11a) using the LiveLink for MATLAB product by COMSOL Multiphysics, which allows MATLAB scripting to be integrated with COMSOL simulations. Iteration between the continuous cell-solute model and the discrete angiogenesis was facilitated by the separation of timescales between these two processes: the migration of endothelial cells occurs on a longer timescale than solute diffusion. This can be seen by comparing the minimum EC migration rate used in this model, 10 μm/h or 2.78×10^{-7} cm/s, with the rate of diffusion of oxygen through collagen gel, 4.5×10^{-6} cm^2/s.

Initial and boundary conditions for the continuum model were applied as described previously in Section 4.3.1. As shown in Figure 5.11a, the hybrid model begins with the continuum model simulation. This is because Equation (5.3) dictates that no angiogenic sprouting can take place when

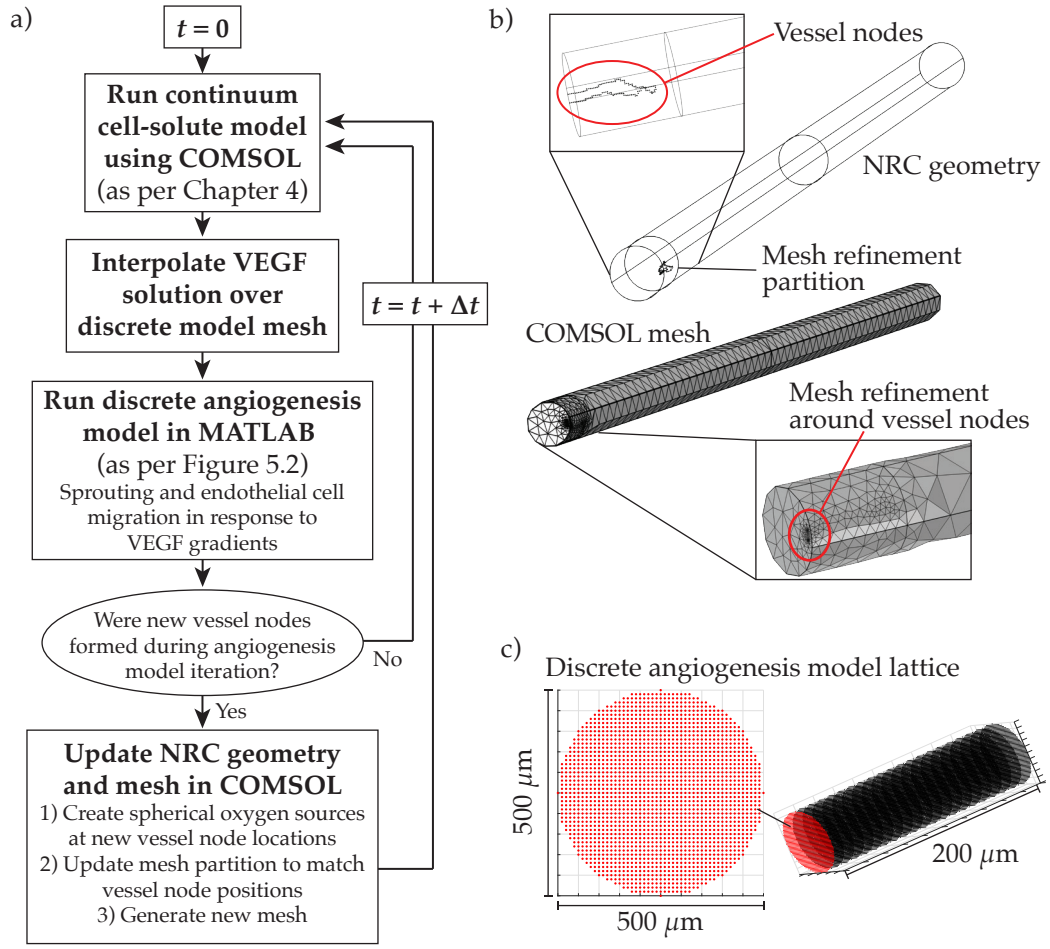

Figure 5.11: a) Hybrid model flow diagram demonstrating the feedback loop between the cell-solute model and the angiogenesis model. The hybrid model iterates between the two frameworks at each time step according to this diagram. b) Geometry and mesh generated within COMSOL for simulation of the continuum cell-solute model. Mesh refinement is carried out in the region of the vessel structures. c) Lattice used to simulate the angiogenesis model. The lattice covers one end of the NRC geometry and extends a total length of 5 mm: a truncated version of the lattice with length 200 μm is shown here, along with the cross section to demonstrate the density of the lattice.

$v = 0$, and $v = 0$ is used as a uniform initial condition for VEGF across the construct geometry. A time step of $\Delta t = 1$h was chosen because this permits the discrete model to simulate TEC migration on a relatively fine scale, but doesn't prohibit the time taken to run each simulation.

Different meshes were used for the continuous model, run using COMSOL, and the discrete model, run using MATLAB, to decrease the time

required for the simulations to complete and to match the required spatial scales. For simulation of the discrete angiogenesis model in MATLAB, the mesh consisted of a regularly spaced lattice with spacing $\Delta x = 10$ μm. As previously mentioned in Section 5.3.1, this reflects the diameter of endothelial cells and new sprouts. Additionally, this mesh size facilitates the minimum migration rate of 10 μm/h outlined in Section 5.3.4.2 when used in combination with a discrete time step size of $\Delta t = 1$h. Further refinement of the vascular model mesh would be computationally prohibitive.

The COMSOL mesh was initialised with a maximum element size of 0.006 m. In this mathematical framework, feedback occurs from the discrete model to the continuous model only once vessels have formed, at which point the vessel nodes are defined as spherical sources of oxygen within the continuous COMSOL model. The formation of vessels requires further localised mesh refinement in COMSOL due to the small scale of the spherical vessel structures (6 μm diameter). Therefore after the first occurrence of vessel formation, the COMSOL geometry is partitioned such that the mesh size in the region of the oxygen sources can be refined, leaving the rest of geometry with the original, relatively course mesh to mitigate the required increase in computational time (Figure 5.11b). The mesh in the refined region was assigned a maximum element size of 0.01 m and a minimum of 5 μm. The total number of mesh elements varied at each time step according to the number and position of the spheres used to represent the vessels within COMSOL. Further COMSOL mesh refinement was computationally prohibitive and did not significantly alter the simulation output.

For the simulations presented in this thesis, the sprouting angiogenesis model was applied only to one end of the representative geometry, to reduce the computational time required for each simulation; thus sprouting can occur at only one of the circular faces (Figure 5.11c). This assumes that the simulated vascular growth in one half of the construct does not

affect the distributions and concentrations of solutes in the other. Comparison between the simulated solute distributions of nerve repair constructs with and without the inclusion of the vascular growth model validated this assumption. A symmetry plane boundary condition could also have been used at the longitudinal midpoint of the geometry, but tests using this configuration showed no apparent difference in the time taken for the simulations to complete nor in the results achieved.

Seven different sets of initial conditions representing contrasting cell seeding strategies were used for the simulations, as presented in Table 5.2. These initial conditions were chosen based upon the results presented in Chapter 4: a uniform cell density of 88×10^6 cells/ml produced the highest viable cell density after 24h, and a uniform cell density of 267×10^6 cells/ml produced the highest standard deviation in VEGF after 24h, reflecting the generation of relatively steep VEGF gradients. A mid-point value between these two densities (178×10^6 cells/ml) was also chosen to determine whether this could induce a greater degree of vascularisation without compromising cell survival.

For comparison, simulations using a higher initial cell density of 385×10^6 cells/ml were also run to represent the higher seeding densities currently used in some *in vivo* work. Non-uniform distributions of the same number of cells as the NRCs uniformly seeded at $n_0 = 88$ and 267 million cells/ml were also selected (simulations 5 and 6 in Table 5.2). Finally, a simulation was run using a uniform $n_0 = 178$ million cells/ml with a porous sheath, for comparison with the non-porous sheath simulations.

Due to the stochastic nature of the theoretical model of angiogenesis, it was necessary to run multiple simulations for each set of parameters to allow the extraction of representative statistics. Thus each initial condition was simulated a total of 40 times.

In each case, the model was run to simulate up to the 5 day point, giving a total of 120 iterations between the continuous and discrete frame-

Label	n_0 (10^6 cells/ml)	n_{tot_0} (10^5 cells)	ζ	Sheath
1	88	2.59	1 (Uniform)	Non-porous
2	178	5.24	1 (Uniform)	Non-porous
3	267	7.86	1 (Uniform)	Non-porous
4	385	11.34	1 (Uniform)	Non-porous
5	-	2.59	3 (Non-uniform)	Non-porous
6	-	7.86	3 (Non-uniform)	Non-porous
7	178	5.24	1 (Uniform)	Porous

Table 5.2: Initial conditions simulated using the hybrid discrete-continuum model of vascular growth and cell-solute interactions.

works for each run; the simulations were terminated when $t > 120$h (Figure 5.11). The total run times for the simulations varied between 9 and 83 minutes, with a median time of 12.7 minutes. Simulations that resulted in a larger number of vessels and sprout nodes took longer to complete due to the requirement for a more complex COMSOL geometry and the need to simulate the migration of a greater number of TECs respectively.

5.4.2 Vascular network metrics

As outlined in the literature review (Section 2.1.2), the directionality of new vessels and the rate of vascular growth are important for aiding peripheral nerve repair. Fast and dense revascularisation also enhances the supply of oxygen to the NRC, with potential benefits for seeded cell survival. In this thesis, quantitative metrics are calculated to track properties such as the rate of vascular growth, vessel penetration distance and EC density, and thereby compare the theoretical outcomes of the different simulated NRC designs.

In this model, ECs are labelled and tracked as either TECs, SECs or VECs, with each EC occupying a node in the discrete 3D mesh. At each time point, the sprout and vessel densities are tracked by summing the

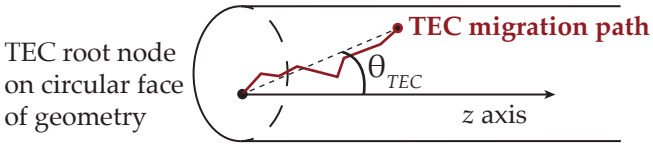

Figure 5.12: Illustration of the TEC angle, θ_{TEC}.

number of nodes occupied by SECs and VECs respectively at each z position along the length of the discretised NRC geometry. This method allows longitudinal spatial variations in sprout and vessel density to be investigated. The total number of each type of EC across the whole geometry at each time point is also recorded. Sprout and vessel penetration distances, defined as the greatest z coordinate positions obtained by SECs and VECs respectively at each time point in a simulation, are also calculated.

Sprout directionality is quantified by calculating two metrics: sprout tortuosity τ_s and TEC angle θ_{TEC}. The first of these is again defined as the ratio of the straight line distance from the TEC "root" (the node at which it first sprouted) to its current position, and the actual length of the path taken by the TEC (the length of the sprout). The TEC angle is defined as the angle between the vector position of a TEC relative to its "root" node, and the longitudinal z axis (Figure 5.12). Thus TECs that have not deviated as far in the x and y directions will have smaller TEC angles.

Vascular network branching density is calculated at each time point as the number of branching points (nodes at which a TEC branching event has taken place) divided by the total length of the vascular network. This gives an indication as to the overall structure of the developing network.

Finally, the impact of vascular growth on cell survival is assessed by calculating the mean viable cell density over the NRC at each time point and comparing it to the results of the continuum model run without the angiogenesis model (Section 5.4.3.6). Note that these means are taken over only *half* of the NRC construct- that which contains the vascular network- instead of the whole construct as in Chapter 4. This is because as previously

mentioned the simulations presented in this chapter incorporate vascular growth from only one end of the cylindrical construct.

Means, and in some cases confidence intervals, of the metrics described in this section are calculated over the outputs of the $N = 40$ simulations run for each case in Table 5.2 to assess the average outputs of each set of initial conditions.

5.4.3 Simulation results

As presented in Table 5.2, a set of 40 simulations were run using a uniform cell density of $n_0 = 178 \times 10^6$ cells/ml in combination with a porous sheath with porosity $\epsilon = 0.8$, sheath thickness T = 0.25 mm and using the Weissberg model of tortuosity. However, in 90% of these simulations no TECs sprouted at the circular face of the NRC by the 5 day time point, and in the remaining 10% only one TEC-led sprout was produced over this time span. This is likely due to the loss of VEGF out of the NRC, as demonstrated in Figure 4.17. Therefore no further analysis was carried out using these simulation results; the remainder of this section is devoted to analysis of simulations run using boundary conditions representing an impermeable sheath.

5.4.3.1 Example simulation results

Examples of the progression of the integrated angiogenesis and cell-solute model are presented here to provide a sense of the qualitative results of the simulations. Note that these are randomly chosen individual simulations, and therefore cannot be used in isolation to draw conclusions about the effect of the different cell seeding strategies due to the stochastic nature of the model.

Figure 5.13 illustrates how the migration of TECs occurs in response to the VEGF distributions provided by the continuum cell-solute model. Initially, the gradient of VEGF at the end of the construct is relatively high, resulting in fast and directional vascular growth; decay of VEGF over time

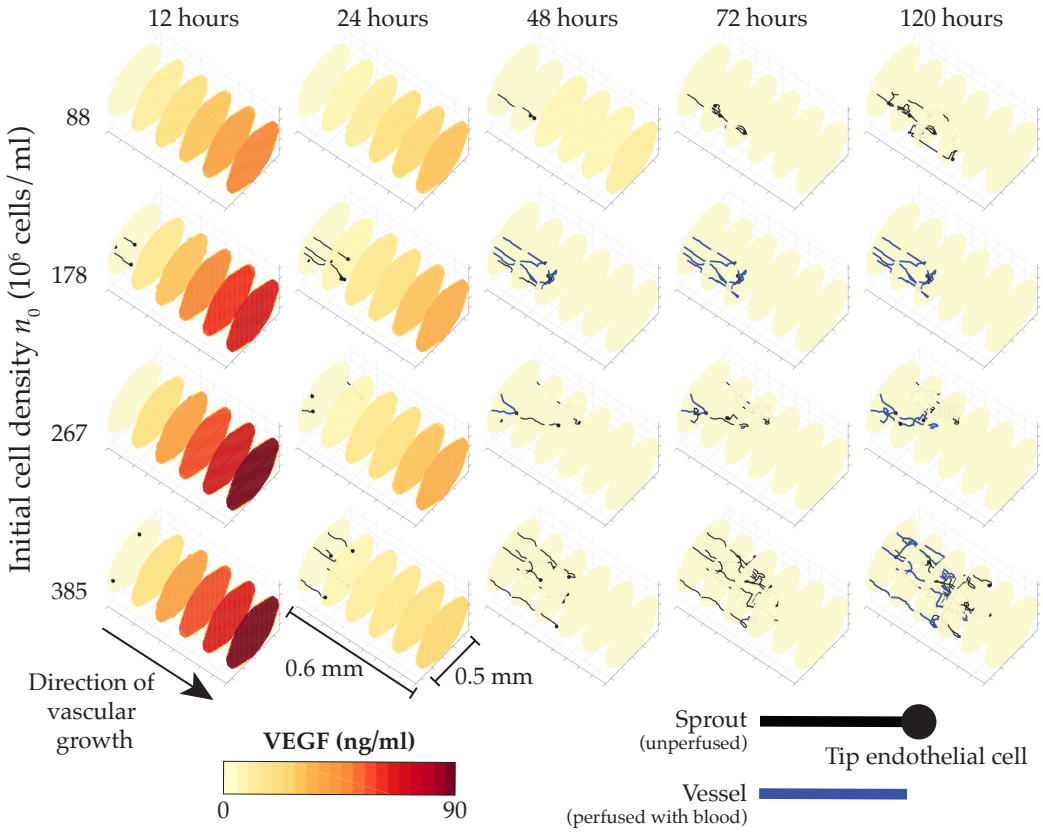

Figure 5.13: Example simulations of angiogenesis in response to VEGF gradients within an NRC, using four different initial cell densities. The distribution of VEGF over time affects both the rate and directionality of sprout growth: at relatively early time points (up to 24 hours), the gradient of VEGF within the NRCs is steeper than at later time points, resulting in the development of less tortuous sprouts. At later time points, TEC migration is almost purely random due to a decrease in the strength of the directional chemical cue provided by VEGF.

and a decrease in the VEGF-producing viable cell population results in reduced concentrations and gradients of the growth factor at later time points, which in turn leads to slower and more tortuous sprout growth.

Figure 5.14 demonstrates the impact of the formation of vessels on the spatial distribution of oxygen over time: in particular, the presented example of a simulation run with an initial uniform seeding density of $n_0 = 267 \times 10^6$ cells/ml demonstrates how when only a few perfused vessels exist, the effect on the oxygen distribution is predominantly local (48 hour time point), with the highest oxygen concentration closest to the vessels

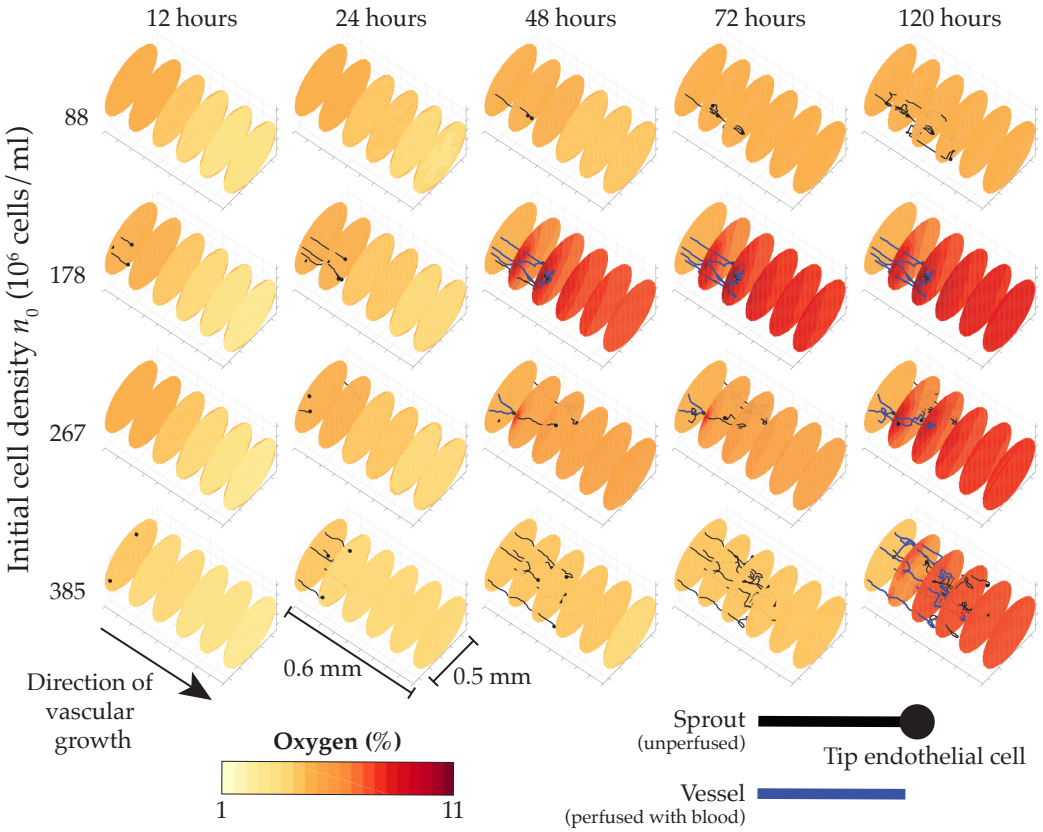

Figure 5.14: Example simulations of the interaction between angiogenesis and oxygen distributions within NRCs, using four different initial cell densities. At early time points, oxygen is consumed by the seeded cells and therefore remains at relatively low levels. Once perfused vessels have formed via anastomosis and begin to provide oxygen to the tissue, oxygen concentrations begin rise within the NRCs.

and diffusion resulting in a gradient spreading radially outwards. The formation of a greater number of vessels results in a more widespread increase in oxygen concentration throughout the engineered tissue (72 and 120 hours).

The impact of the provision of oxygen to the engineered tissue on the spatial cell density is demonstrated in Figure 5.15. Local regions of high cell density develop in close proximity to vessels.

5.4.3.2 Sprout and vessel density

Figure 5.16 demonstrates how sprout growth progresses from the stump along the NRC over time by plotting the mean number of nodes occupied

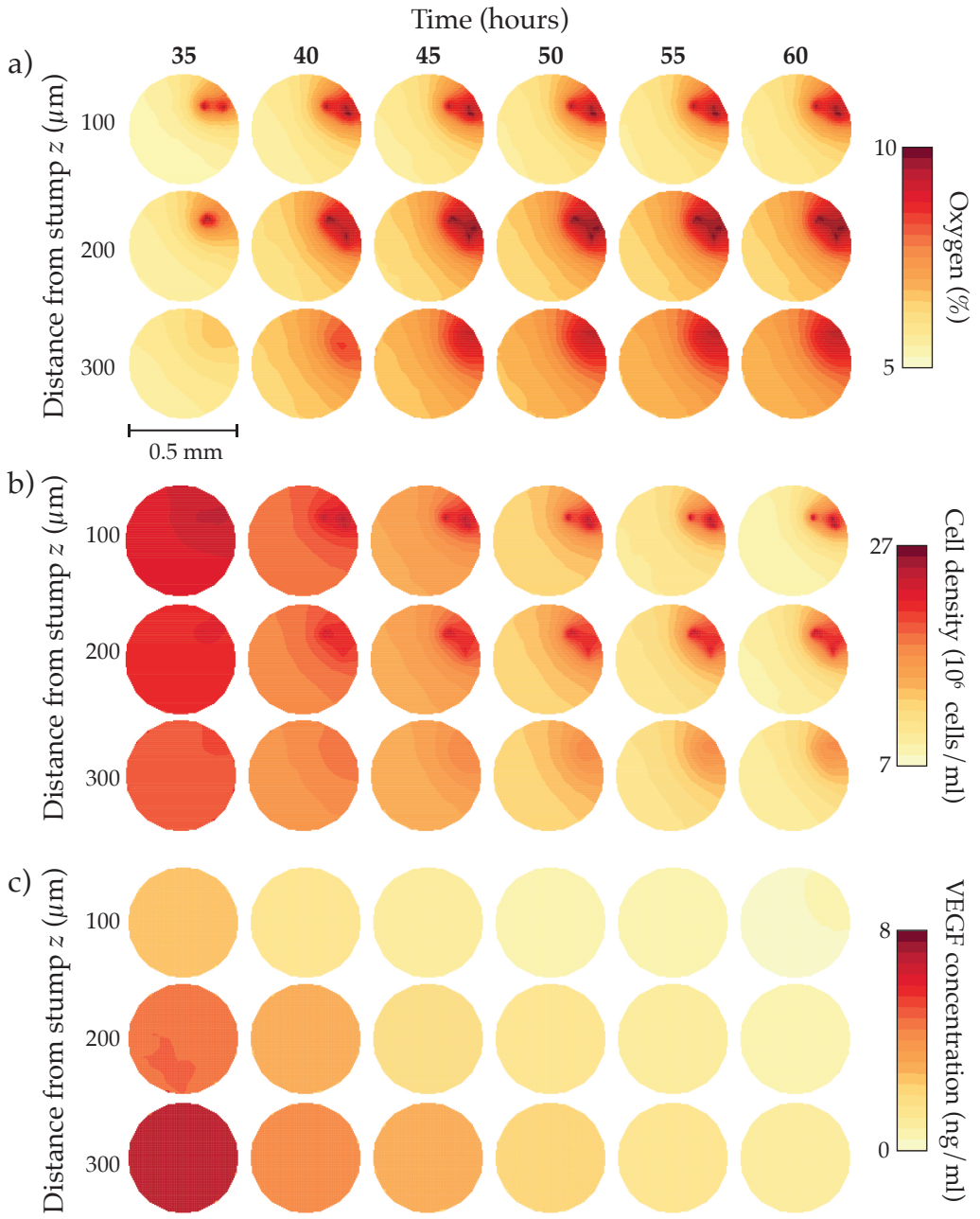

Figure 5.15: Example cross sections of oxygen (a), viable cell (b) and VEGF (c) distributions at three different values of z (distance from the stump), plotted from approximately the first time a vessel is formed. The displayed simulation used $n_0 = 178 \times 10^6$ cells/ml and corresponds to the example simulation for this value of n_0 in Figures 5.14 and 5.13. Increases in local oxygen concentration caused by vessel formation result in corresponding increases in the local cell density. The VEGF distribution is less affected by the oxygen concentration; there appears to be a delayed, small increase in local VEGF at 100 µm after 60 hours in response to the increase in cell population and decrease in oxygen.

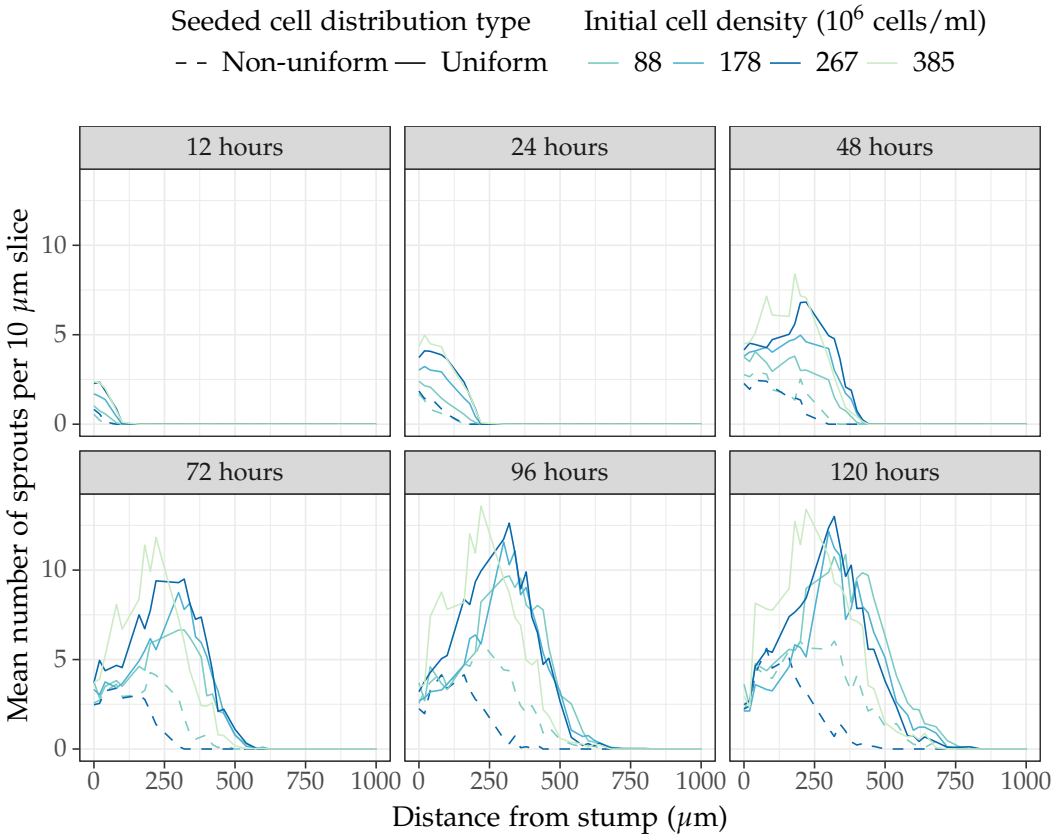

Figure 5.16: Uniform seeding cell strategies promote faster migration of TECs and induce sprouts to reach a greater distance into the NRC than non-uniform strategies. A total of $N = 40$ simulations were used to calculate the means for each initial cell seeding strategy; note that there was a large degree of variability in these results. Means are displayed here without confidence intervals for clarity.

by SECs at each cross section along the NRC in each of the simulated cases. It appears that using a uniform seeding density of $n_0 = 178$, 267 or 385×10^6 cells/ml results in very similar sprout distribution and density patterns over the initial 48 hours, but the uniform seeded density of $n_0 = 88 \times 10^6$ cells/ml appears to produce a lower density of sprouts across the length of the vessel than the other uniform seeding strategies over this time span.

From 72 to 120 hours, the rate of growth in the longitudinal direction appears to slow across all of the cases, and large peaks appear in the mean sprout density distributions in the uniformly seeded cases. This could reflect the loss of directional VEGF cues: as shown in Figure 5.13, regardless

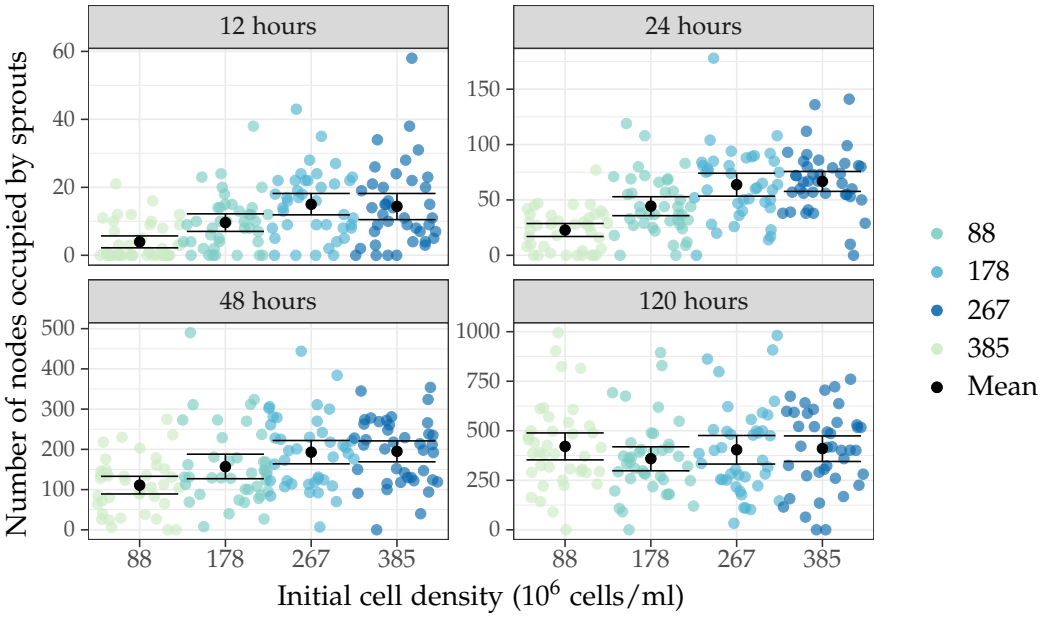

Figure 5.17: The simulated total number of nodes occupied by sprouts increases with the initial cell density at early time points (12 and 24 hours), but is broadly similar at 120 hours. Here each point represents an individual simulation, and error bars depict a 95% confidence interval for the mean in each case. All simulations use uniform initial seeding distributions.

of the uniform seeding density used, by the 48 hour time point the steepness of the VEGF gradient has reduced dramatically, causing a build up of dense vasculature as sprouts begin to migrate more randomly.

Over the whole time period, the mean sprout densities for the non-uniformly seeded construct simulations are consistently lower across the whole construct than the uniformly seeded.

However, Figure 5.16 refers only to mean values without indication of confidence intervals for this mean. For the uniformly seeded cases, the mean *total* number of nodes occupied by sprouts over the entire geometry was plotted along with 95% confidence intervals in Figure 5.17 along with the values for individual simulations, to provide a better sense of the variance in the simulations and how this could skew the results. It is apparent that the density of sprout nodes for $n_0 = 88 \times 10^6$ cells/ml is significantly different from the other three densities at the 12, 24 and 48 hour marks,

in line with the results from Figure 5.16. At the 120 hour mark all of the seeding densities produce very similar results.

The same analysis was conducted in the case of vessel density. Across all of the simulations, very few vessel structures were formed within the first 24 hours (Figures 5.18 and 5.19). From 48 hours onwards, the number of nodes occupied by vessels recorded along the length of the NRC increases with time, following a similar pattern of progression as the sprout densities. These simulation results suggest that the first formation of perfuse vessels occurs at around the 48 hour mark, with the density of vessels increasing steady from then onwards. This is on a similar time scale to the vascularisation observed by Cattin et al. [65].

The spatial distribution of sprout and vessel densities over time presented in Figures 5.16 and 5.18 suggests that the simulated vascular growth could be modelled by a travelling wave. This aligns with experimental work published by Podhajsky and Myers that shows vascular growth progressing as a travelling wave through a silicone NRC [317].

5.4.3.3 Sprout and vessel longitudinal penetration

In corroboration with Figure 5.16, Figure 5.20a demonstrates that the rate of sprout penetration was very similar for the three highest uniform cell densities over the first approximately 36 hours, with a uniform seeding density of $n_0 = 88 \times 10^6$ cells/ml producing a slightly slower penetration rate on average.

The speed of longitudinal sprout penetration slows significantly at around the 36 hour time point, as reflected by the change in the plot gradients. From Figure 5.20b, this is also the approximate time point at which some sprouts begin to anastomise and form vessels, suggesting that some of the decrease in the migration rate could be explained by SECs changing into VECs and therefore no longer having the ability to migrate further into the tissue or branch to produce other migrating TECs.

It is interesting to note that although $n_0 = 88 \times 10^6$ cells/ml initially

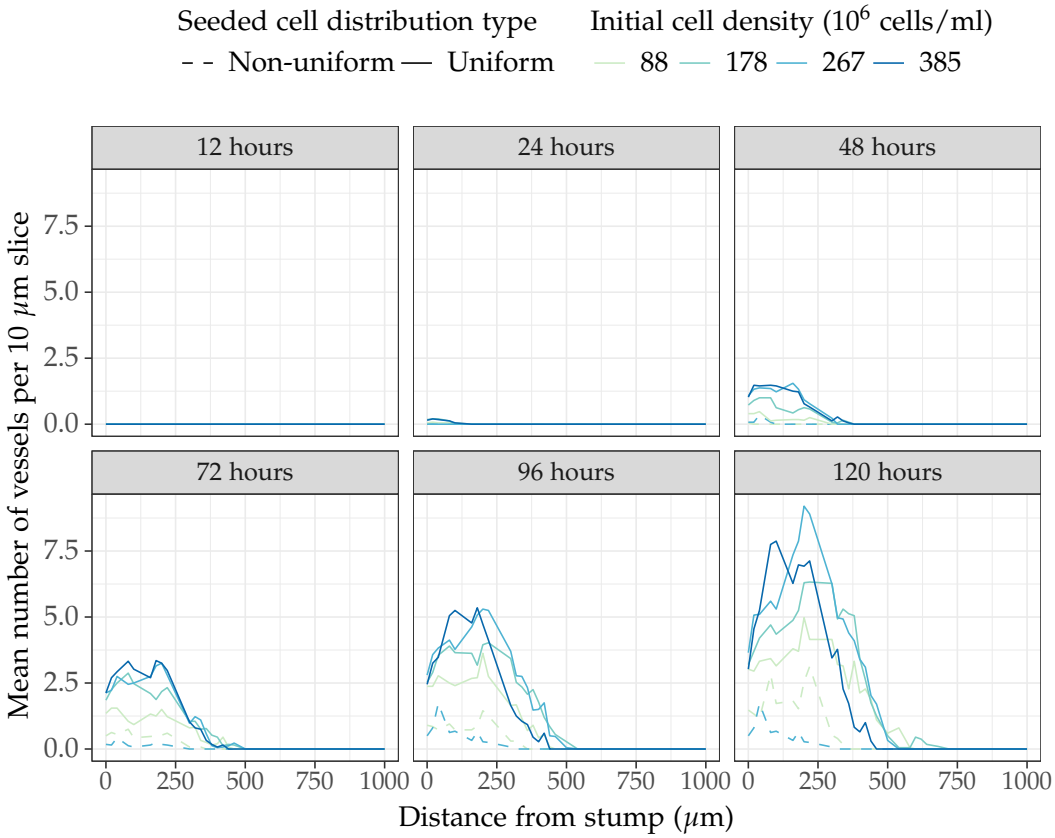

Figure 5.18: Mean spatial distribution of vessels over time, calculated as an average of $N = 40$ simulations in each case.

produced the slowest rate of sprout and vessel penetration, by the later time points the rate of directional sprout growth is higher than that of the other cases, as demonstrated by the gradient of the line. The vessel penetration rate for $n_0 = 88 \times 10^6$ is again slower than for the other uniformly distributed seeding cell densities, particularly over the first 96 hours.

The simulated non-uniformly seeded constructs result in much smaller penetration distances over time than their corresponding uniform counterparts.

5.4.3.4 Sprout directionality

Figure 5.21 provides an overview of the morphology of the simulated growing vascular networks over time. Means for both the sprout tortuosity τ_s and TEC angle θ_{TEC} were calculated over all 40 simulations for each of the

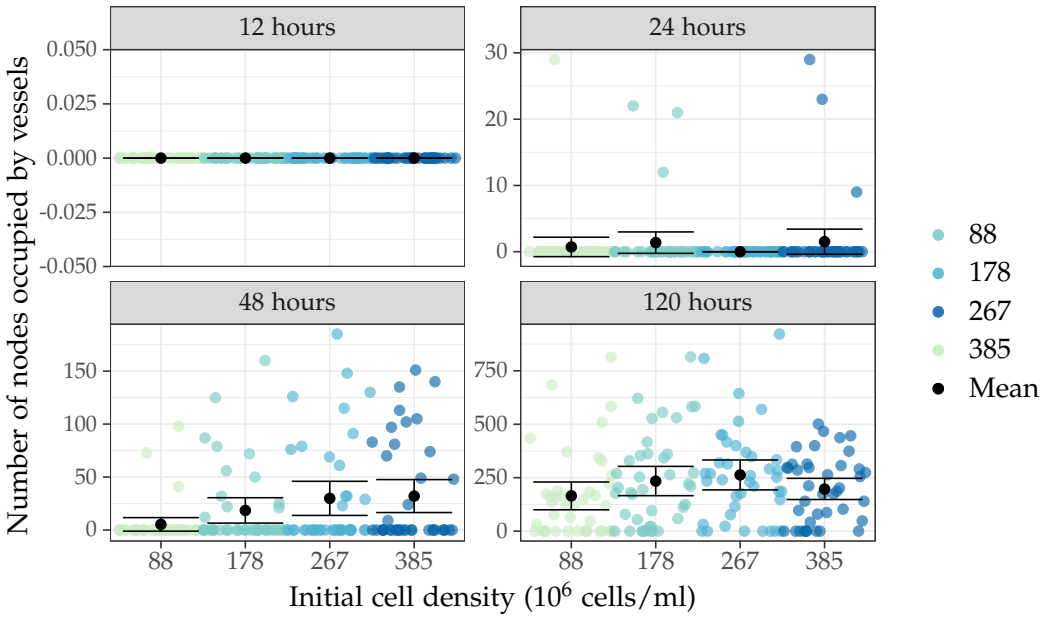

Figure 5.19: The simulated total number of nodes occupied by vessels is predominantly close to 0 at early time points (12 and 24 hours). At 48 hours, a select number of simulations exhibit the formation of vessels, especially for the highest three initial cell densities, but at 120 hours there appears to be less difference between the results for each of the four simulated scenarios. Here each point represents an individual simulation, and error bars depict a 95% confidence interval for the mean in each case. All simulations use uniform initial seeding distributions.

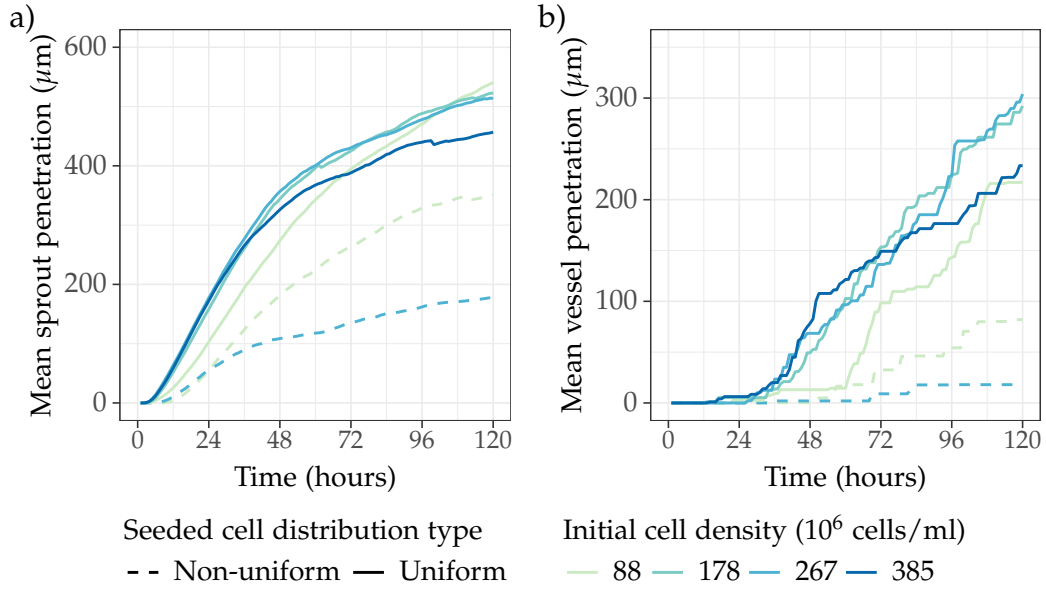

Figure 5.20: Mean sprout and vessel penetration distance over time, calculated as an average of $N = 40$ simulations in each case.

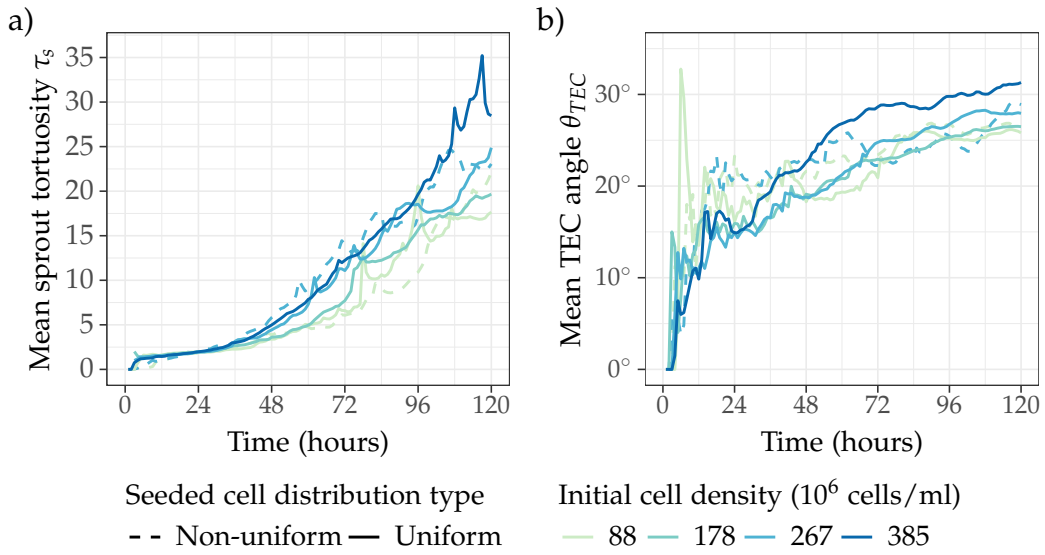

Figure 5.21: Mean sprout tortuosity and directionality over time, calculated as an average of $N = 40$ simulations in each case.

cell seeding strategies that were investigated.

The mean sprout tortuosity remains relatively constant for the first approximately 48 hours across both uniform and non-uniform seeding strategies and all four seeding densities, with only a slight increase occurring over the time period after the sprouts first begin to develop. This indicates that sprout growth during this phase is more directed, guided by the steeper VEGF gradients that occur over this time period (Figure 5.13). However, from 48 to 120 hours the rate of increase in the mean tortuosity is higher, indicating that sprout growth over this latter period of time is more tortuous.

The plot of mean sprout directionality shows a gradual increase in the TEC angle beyond the 48 hour time point across the various simulated scenarios; again, the more random migration that occurs after this time point would lead to TECs becoming more spread out across the cross section of the construct. Although the results across the different cell seeding strategies are very similar, the highest uniform seeding density $n_0 = 385 \times 10^6$ appears to result in the most tortuous networks with the largest mean values for θ_{TEC} over time.

Together, these results indicate that the initial period of sprout growth led by TEC migration is more directional (remains closer to the z axis of the constructs) and less tortuous than the later growth from approximately 48 hours onwards. This correlates with the existence of strong VEGF cues; as previously mentioned, by the 48 hour time point the directional cue provided by VEGF is far less pronounced.

Figure 5.13 illustrates this behaviour in four individual simulations: initial sprout growth predominantly follows along the z axis of the construct, in response to steep VEGF gradients and relatively high overall VEGF concentrations, whereas at later time points branching occurs and the cue from VEGF is much less strong, resulting in a localised dense and tortuous mass of vessels.

5.4.3.5 Vessel branching

As shown in Figure 5.21a, the mean number of branching points per μm of the total vascular network length increases rapidly between the 18 and 24 hour time points. This corresponds to the threshold branching age $T_{\text{branch}} = 0.75$ days, equal to 18 hours; during this time period, TECs that sprouted during the first few hours of the simulation begin to branch.

The simulations predict that a uniform seeding density of 385×10^6 cells/ml results in the lowest branching density consistently over time. In contrast, although uniform seeding densities of 88, 178 and 267×10^6 cells/ml produce similar branching densities over the first 48 hours, by the 120 hour time point the simulations run with $n_0 = 88 \times 10^6$ cells/ml result in higher branching densities than the other simulations.

5.4.3.6 Impact of vascularisation on cell survival

As expected, for each simulation the solutions for the viable cell density n, oxygen concentration c and VEGF concentration v were unaffected by the incorporation of the vascular growth model until the formation of vessels. As shown in Figure 5.18, vessels do not begin to form until at least 24 hours post-implantation.

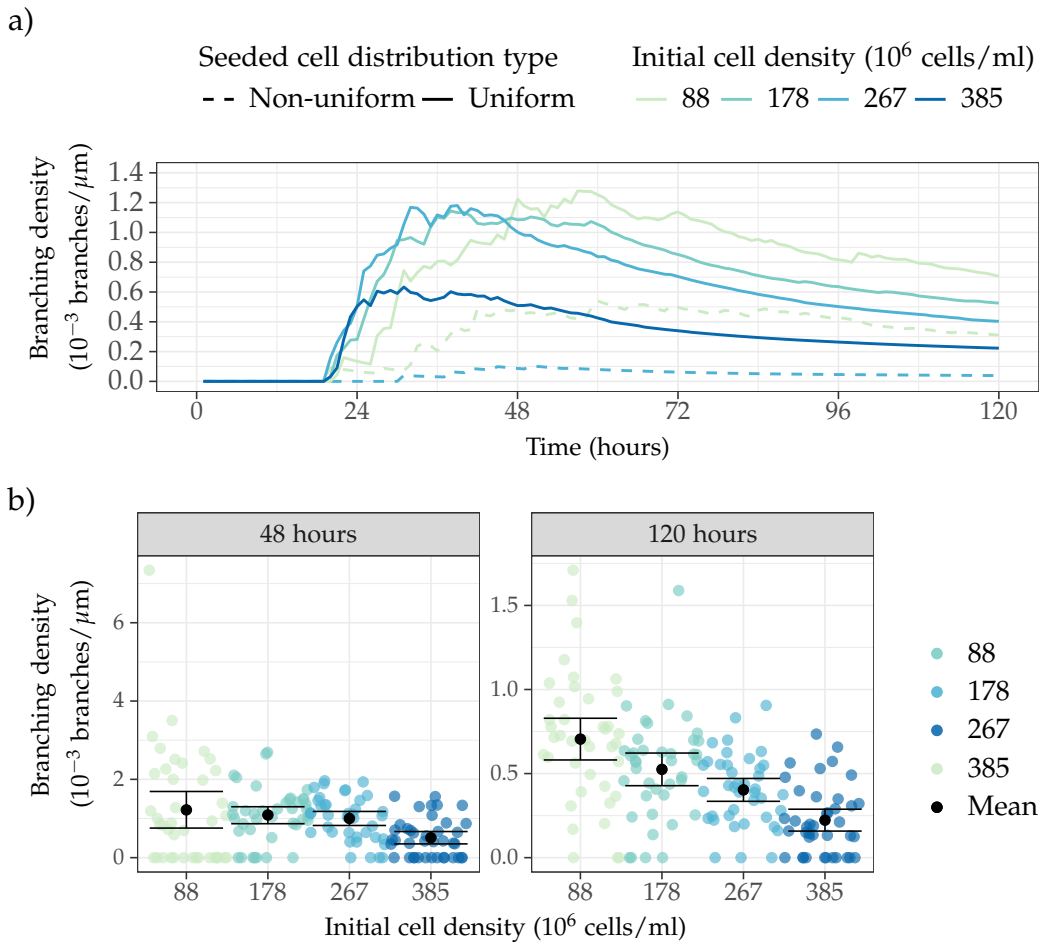

Figure 5.22: a) Mean network branching density over time, calculated as an average of $N = 40$ simulations in each case. b) Branching densities for individual simulations at 48 and 120 hours. Here each point represents an individual simulation, and error bars depict a 95% confidence interval for the mean in each case. All simulations in b) use uniform initial seeding distributions.

After the first vessels are created, they begin to supply oxygen to the adjacent area of engineered tissue. This causes an increase in the local oxygen concentration, and also impacts the mean oxygen concentration over that half of the NRC (Figure 5.23). From this figure, it is clear that in all four uniformly seeded scenarios a number of simulations achieved a dense enough vascular network to increase the average oxygen concentration over the vascularised half of the NRC geometry by as much as 4% in comparison to simulation results provided by the cell-solute model alone.

Despite this, Figure 5.24 suggests that across the four cases the pre-

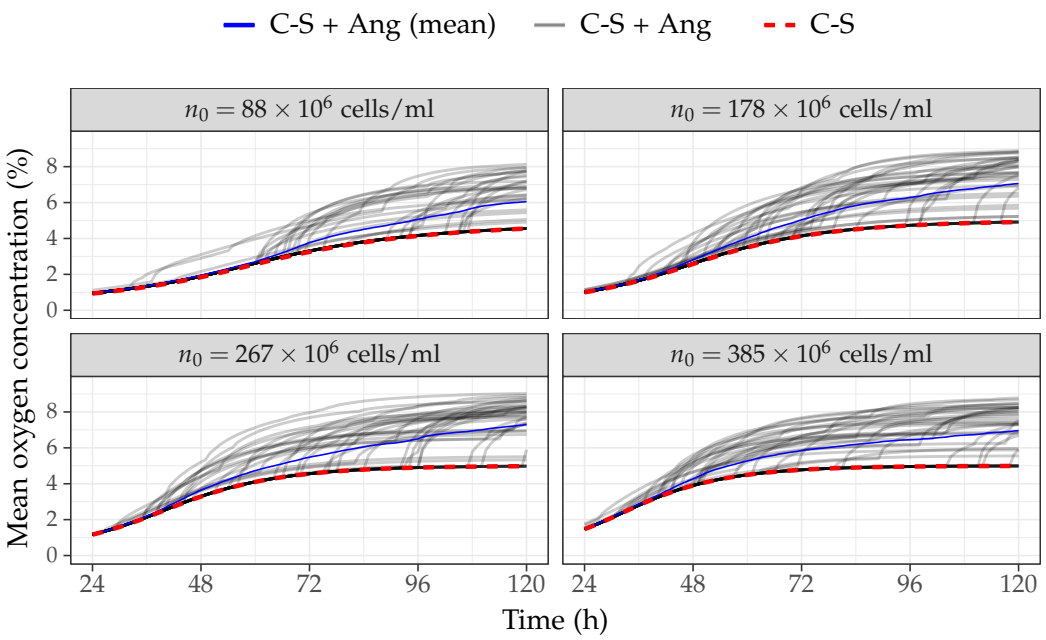

Figure 5.23: Formation of vessels increases the mean oxygen concentration over the construct. Here the model predicts "jump" increases in the mean oxygen concentration as new perfuse vessels are created. "C-S" denotes the results of the cell-solute (continuum) model only, "C-S + Ang" the individual simulation results of the combined cell-solute and angiogenesis model, and "C-S + Ang (mean)" the mean of these simulations for each initial cell density.

dicted effect of vascularisation upon the cell density is minimal over the simulated time period, with the exception of when $n_0 = 88 \times 10^6$ cells/ml. For the other three initial cell densities simulated (and in particular for $n_0 = 267$ and 385×10^6 cells ml), by the time enough vessels have formed to create an impact on the local oxygen concentration the cells in the construct have nearly all died, meaning that it is far more difficult for the cell population to recover.

Conversely, when $n_0 = 88 \times 10^6$ cells/ml the viable cell density at later time points is relatively high, enabling the cell population to recover more easily once the oxygen supply has increased. In addition to this, the form of the cell death parameter δ derived in Chapter 3 is an increasing function of initial cell density n_0; therefore, when $n_0 = 88 \times 10^6$ cells/ml, the cells die less quickly than when higher initial seeding densities are used. This

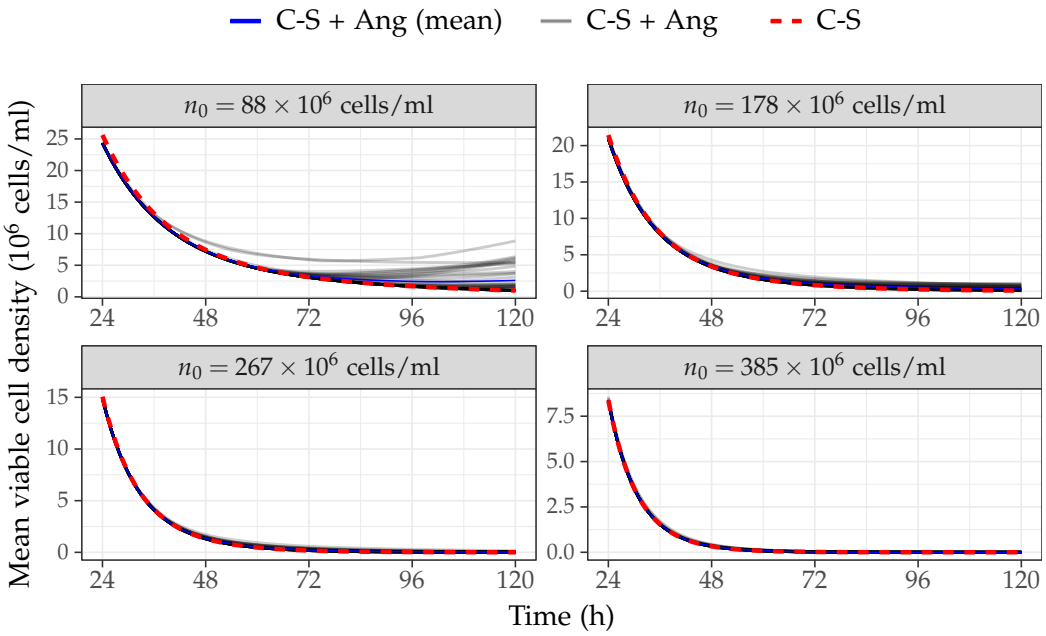

Figure 5.24: Formation of vessels and consequent increase in oxygen supply does increase the mean viable cell density over the construct in a limited number of simulations when $n_0 = 88 \times 10^6$ cells/ml. A similar but less obvious effect is predicted by the model for $n_0 = 178 \times 10^6$ cells/ml. C-S denotes the results of the cell-solute (continuum) model only, C-S + Ang the individual simulation results of the combined cell-solute and angiogenesis model, and C-S + Ang the mean of these simulations for each initial cell density.

means that increases in cell proliferation induced by higher local oxygen concentrations are more likely to tip the balance between cell proliferation and death in favour of proliferation, thus allowing the viable cell density to begin to increase once perfuse vasculature has begun to form and deliver oxygen.

Although, as previously mentioned in Section 3.7, the dependence of the cell death parameter on n_0 does not explicitly model a biological process, it can be regarded as being implicitly representative of cell-solute interactions that have not been included in the mechanistic model equations. Therefore, although it would be preferable to remove parameter dependencies on initial conditions, the inclusion of δ as a function of n_0 does not completely invalidate the results of the model. Overall, these simula-

tions suggest that if long term survival of cells is required, then cells must survive until the point where oxygen and nutrients can be provided by vasculature; the model suggests that lower seeding cell densities could help to achieve this. These are both valid and testable hypotheses that have been generated by this work.

Interestingly, these conclusions suggest that although the use of $n_0 = 88 \times 10^6$ cells/ml produced less dense vascularisation with smaller penetration distances over most of the simulated time period, the vessels that did grow had a more positive effect on cell survival. The higher branching density exhibited by simulations run using this initial cell density (Figure 5.22) may also have resulted in more interconnected vascular networks, which could have enhanced the delivery of oxygen to the cells.

5.5 Conclusion

The simulations conducted in this chapter have underlined the complexity of the linked problems of cell survival and vascularisation: although seeding cells at a higher density into an NRC can help to generate steeper VEGF gradients, if the cell population is very small by the time a perfuse vascular network has formed this may not necessarily aid cell survival. Instead of optimising for VEGF concentration, it appears that the aim should be a balance between providing the directional cues necessary for sprouting angiogenesis and ensuring that a sufficient cell population survives until the point of vessel formation.

In particular, the model simulations predict that a uniform seeding density of $n_0 = 88 \times 10^6$ cells/ml will result in vascular growth that is slower to penetrate the length of the NRC construct (Figure 5.20), but less tortuous (Figure 5.21) and with a denser branched structure (Figure 5.22) than vascular growth in constructs seeded with a higher density of cells ($n_0 = 385 \times 10^6$ cells/ml). The predictions for the mean vessel penetration and density could be validated experimentally using imaging, although

tortuosity would be more difficult to measure.

The use of step-like non-uniform seeded cell distributions as simulated in this thesis were predicted to result in slower and less dense vascular growth. This is likely to be because although non-uniform distributions of this type were predicted to increase the VEGF gradient over the whole of the construct in some cases (Section 4.5), during the early stages of vascularisation only the VEGF gradients at the ends of the NRC affect the progression of angiogenesis. In the future non-uniform seeding distributions that induce higher VEGF gradients and concentration in these specific regions could be investigated using the model.

Additionally, individual simulation results show a fairly high degree of variability across simulations that use the same initial conditions. This is a result of the stochastic nature of the model formulation, but mimics the variation that is often observed in experimental data.

However, the results provided by the model described in this chapter must be treated with caution. Many of the parameter values used in the framework are derived from previous experimental work or similar to those used in existing computational studies, and the functional forms and components of the model are based on current knowledge of the process of sprouting angiogenesis, but additional experimental clarification of some of the model relationships and model validation is required.

For this reason, statistical tests have not been carried out on the angiogenesis model simulation data. The angiogenesis model developed here is intended to explore the mechanisms that underpin angiogenesis during nerve injury repair, and the model results presented in this chapter can be interpreted as broad indicators of how vascularisation may be affected by cell-solute distributions *in vivo*. However, the results of statistical tests of hypotheses regarding the outcomes of specific scenarios are likely to be inaccurate, because the model of angiogenesis is yet to be parameterised or validated against experimental data.

In order to validate and improve this model, imaging of vascular networks during peripheral nerve repair over time would be hugely beneficial. This would enable both quantitative and qualitative validation, as well as potentially allow the derivation of more accurate parameter values and the refinement of the functional forms used throughout the model. Although some imaging data of vascular nerve repair exists [65], imaging of repair of peripheral nerves with cell-seeded EngNT NRCs would be necessary for rigorous validation purposes due to the varying impact of different repair materials.

Furthermore, as outlined in Section 5.3, the model currently neglects to include potentially important aspects of angiogenesis such as the impact of material mechanical cues upon the growth of sprouts, and the influence of vessel radius and haematocrit on the oxygen concentration in the blood and the rate of blood delivery to the tissue. In the case of the former, the exact nature of the relationship between parameters such as the rate of branching and various material factors such as fibronectin, collagen density and VEGF gradients is currently unknown. On the other hand, a more detailed model of blood flow would be relatively easy to implement because many models of this form already exist.

Additionally, processes neglected here based on the simulated time scale such as intussesceptive angiogenesis and vascular remodelling, would need to be considered for incorporation if the model was to be used to simulate longer periods of time. Experimental work could again outline whether these aspects are truly necessary. Furthermore, sensitivity analysis has not yet been carried out due to the computational time required, but would be a necessary part of further refinement of the model to identify which parameters have the greatest effect on the simulation outcomes.

Chapter 6

Conclusions and future work

6.1 Key results

The overall objectives of this work, as laid out in Section 1.5, were to investigate the impact of therapeutic cell seeding densities and distributions upon cell survival, VEGF distributions and vascularisation in engineered tissue (specifically, NRCs), via the use of a parameterised mathematical model. The key results of this thesis are summarised below.

1. A continuous mathematical model of cell-solute interactions in dADSC-seeded type I collagen gel was developed and parameterised against *in vitro* data, collected specifically for this purpose (Chapter 3).

2. The cell-solute model was applied to a geometry representing a NRC and used to simulate the effect of a variety of initial seeded cell densities, distributions and NRC sheath compositions on cell survival and VEGF generation over time (Chapter 4). This work culminated in the following theoretical predictions:

    a) Simulation results indicated that a uniform initial cell density of 88×10^6 cells/ml would obtain the highest mean viable cell density across the NRC after 1 day. Additionally, a uniform initial cell density of 267×10^6 cells/ml was found to maximise the

standard deviation of the VEGF concentrations across the NRC after 1 day.

b) Simulations that implemented a porous sheath resulted in higher viable cell density predictions than those run using an impermeable sheath, but also resulted in loss of VEGF. Altering the porosity of the sheath within experimentally viable bounds was predicted to have only a very slight effect on the overall results.

c) Simulations run using non-uniform sheath porosity along the length of the NRC geometry indicated that non-uniform sheath porosity could be used to attenuate the degree of VEGF loss, whilst maintaining the benefits of increased oxygen diffusion for cell survival.

d) Non-uniform seeded cell distributions, with more cells seeded at the ends than in the centre, were predicted to improve overall cell survival after 1 day when the total number of cells seeded in the NRC was approximately $< 200,000$. On the other hand, seeding more cells in the centre than at the ends was predicted to increase the standard deviation of VEGF across the NRCs after 1 day when the total number of cells seeded was approximately $< 500,000$. Thus the total number of seeded cells appeared to modulate the effect of different cell seeding distributions on both cell survival and VEGF distributions.

e) Incubation of constructs in high oxygen environments could potentially improve cell survival over early time points post-implantation *in vivo*.

3. A discrete mathematical model of 3D sprouting angiogenesis was developed based upon previously published frameworks and experimental evidence, and combined with the continuous model to create a hybrid model of vascular growth in response to VEGF gradients

(Chapter 5).

4. Simulations of *in vivo* vascularisation of NRCs over 5 days post-implantation were run using the full hybrid framework. The effect of a specific set of cell seeding strategies, chosen based on the results of Chapter 4, upon vascular growth rates and vessel density, tortuosity and directionality were simulated. These simulations provided the following key outcomes:

   a) Variations in the VEGF concentration profiles along the length of the NRC over time produced by different (uniform) cell seeding densities result in slightly different rates and densities of vascular growth during the initial 48 hours, but no significant effect is predicted by the end of the simulated time period of 5 days.

   b) A uniform cell density of $n_0 = 385 \times 10^6$ cells/ml produced lower branching density values over time than the other three tested uniform initial cell densities.

   c) Out of the four uniform cell seeding densities simulated, $n_0 = 88 \times 10^6$ cells/ml produced on average the lowest densities of sprouts and vessels over the first 48 hours. However, this initial cell density also resulted in the greatest average increase in viable cell density at later time points (48-120 hours), whilst the majority of the simulations run using the other three values of n_0 showed no increase in viable cell density.

   d) The use of step-like non-uniform seeding distributions was predicted to produce slower and less extensive vascular growth than uniform distributions using the same number of cells, although only two such distributions were tested.

Although a small number of mathematical models of peripheral nerve repair have been published previously [318, 336], in contrast in the work described in this thesis, none so far have been used to investigate the impact

of different densities and distributions of seeded cells on viable cell and VEGF distributions, over time, and across multiple spatial dimensions.

Furthermore, the use of cell and material type-specific parameters, derived by parameterisation against *in vitro* data, means that the predictions made by the model presented in this thesis could be directly validated in the lab in the future. Part of the novelty of this research lies in its position as part of a wider programme of multidisciplinary work centred around peripheral nerve repair that involves overlapping experimental and mathematical/computational research groups. Sometimes multidisciplinary collaboration is instead confined to an exchange of data, rather than encompassing day-to-day collaboration.

Additionally, the application of a cell-solute model in combination with a 3D model of angiogenesis to the peripheral nerve repair setting is novel. Previously, Lagerlund and Low produced a continuous model of oxygen transport in healthy peripheral nerve [202], yet this did not incorporate vascular growth. The model of nerve repair published by Podhajsky and Myers did include vascular growth [318], but vascularisation was modelled in one dimension only using a continuous approach, and thus the framework does not capture any morphological details- in contrast to the 3D angiogenesis model presented in this thesis. The inclusion of vascular morphology in the model is important because, as reviewed in Section 2.1.2, directional vascular growth during peripheral nerve repair is important for the stimulation of axonal growth. Therefore, encouraging more direct vascular growth could enhance peripheral nerve repair outcomes.

6.2 Discussion and future work

As outlined above, the work in this thesis has generated several quantitative and qualitative hypotheses. In particular, the prediction that the use of lower seeding cell densities (e.g. 88×10^6 cells/ml) may actually result in a higher density of cells within the first few days post-implantation than

the use of much higher densities (around 385×10^6 cells/ml), especially when vascularisation is taken into account, underlines the potential importance of cell seeding densities for cell survival. This result aligns with previous experimental work reporting that the optimal cell transplantation density for axonal regeneration is 80×10^6 cells/ml [264], and challenges the idea that the use of high seeding densities in engineered tissue results in better outcomes such as increased cell survival and vascularisation, and consequently tissue assimilation.

Furthermore, the results of the complete hybrid cell-solute and vascular model broadly suggest that maximising the gradient or concentration of VEGF alone is not necessarily the correct strategy if the goal is to increase therapeutic cell survival via vascularisation. The simulations suggest that although higher seeding densities could induce faster and more dense vascularisation, in order for this to have a pronounced effect on cell survival enough cells have to survive over the first 48 hours prior to the formation of perfuse vessels capable of oxygen delivery. This highlights the complexity of the problem and motivates further research into the link between cell survival and vascularisation.

The use of *in vitro* experimental data collected specifically for the purpose of parameterisation of the model means that the parameters that inform the simulation results relate directly to the cell and material types used in the Phillips lab. Although the experimental data was highly variable and would have benefited from further repeats for each experimental condition to reduce error, the overall trends in the experimental data were clear and matched by the model fit to the data. Therefore, the simulations and predictions made by the model can still be used to direct further research.

The simulations of NRCs presented in this thesis have provided a range of explicit hypotheses that can now be used to inform the design of future experimental work. Data from future experiments will provide

essential validation of the model framework applied to the NRC geometry, as well as advance understanding of the how cell seeding strategies can influence vascularisation. A plan for future experimental work is outlined in Section 6.2.2.

6.2.1 Potential model adaptations, extensions and applications

The aim of the model described in this thesis was to allow researchers to predict the effect of different cell seeding distributions on cellular survival and vascularisation, rather than to capture and investigate the all of the intricacies of cellular signalling in this context. Therefore, the processes incorporated explicitly into the model equations, such as VEGF secretion, cellular metabolism of oxygen and cell proliferation, were selected according to the need to capture sufficient biological detail to model cell survival and angiogenesis, without including a superfluous amount of detail that would act only to complicate the model and introduce more unknown parameters.

The biological processes that were included in the model were chosen according to careful evaluation of their relative importance to the aims of the research, based on existing experimental and theoretical work. This meant that many of the signalling molecules and their interactions identified in Section 2.1.3 were neglected to maintain focus on simulating only the essential components of the highly complex peripheral nerve repair scenario. The addition of many more variables would also have required further experimental work.

Nevertheless, there is potential for extension and improvement of this model, although many of the obvious avenues for extension would increase the complexity of the model and/or require the collection of more comprehensive data to enable parameterisation.

One of the most pressing areas for improvement is the need to incorporate more time dependent data into the model. In this thesis, parame-

terisation was carried out against data at only one time point (24 hours), although data was collected for the 5 day time point as well. Time dependent relationships between the variables were deduced from existing models and experimental hypotheses. Although the simulated cell density values approximated the *in vitro* values at the 5 day point, the VEGF concentration values did not (Section 3.6), suggesting that the model does not capture all of the necessary processes or variables that influence VEGF distributions at later time points. As the time post-implantation increases, a greater number of complex biological processes will affect both cell-solute interactions and the progression of NRC vascularisation. The assumptions made to enable simplification of the scenario via reductions in the number of variables are likely to hold only for early time points post-implantation.

As explained in Chapter 3, it was necessary to introduce parameters that were explicit functions of the initial cell density n_0 to enable the continuous cell-solute model to provide a relatively good fit to the *in vitro* data at the 1 day time point. Again, this suggests that the governing equations and parameters may not currently include all of the processes and variables required to account for the variability in the data. In Chapter 3, three key "ingredients" were identified as potentially important processes for future inclusion into the cell-solute model; these will be briefly recapped in the following paragraphs.

Firstly, in this thesis the governing equations used to model the viable cell density and oxygen concentration distributions were mutually dependent but did not depend on the VEGF concentration. However, VEGF has been shown to influence the proliferation rate of cell types including endothelial cells and ADSCs, as mentioned in Section 3.4.1. A dependence of dADSC proliferation on VEGF was not included in this work due to a lack of cell type-specific evidence and for simplicity, but this relationship could help to explain some of the variation in the data that the model cannot currently capture. Further *in vitro* experiments could be used to explore the

specific relationship between dADSC proliferation and VEGF.

Additionally, in this study VEGF is simulated using a single governing equation with a defined diffusion coefficient and decay rate. This essentially homogenizes the behaviour of the various isoforms of VEGF by modelling them as a single population, but in fact it is known that the different isoforms of VEGF exhibit different behaviour. Certain isoforms bind to heparin residues in the extracellular matrix, which can influence the generation of VEGF gradients, and each isoform has distinct decay and diffusion rates. The exclusion of binding behaviour and isoform-specific diffusivities and degradation rates could partially account for the need to introduce functions of n_0 into the VEGF governing equation. However, incorporation of separate equations to model the various isoforms would increase the complexity of the model considerably and result in a far larger number of relatively unknown parameters. In turn, this would again require more extensive experimental work to achieve parameterisation and/or validation.

Finally, the framework presented in this thesis does not include glucose as a variable. This decision was taken based on the assumption that over the simulated time frame oxygen, rather than glucose, would be the limiting factor for cell survival but this assumption has not been strictly verified. Based on the fact that glucose concentration has been shown to have an influence on the proliferation of various cell types, the exclusion of glucose from the cell-solute model could account for some of the discrepancies between the simulation results and the experimental data. Furthermore, other previously published models have included glucose into similar continuum cell-solute frameworks. Thus glucose is a good candidate variable for future inclusion in the model.

Regarding the discrete model of angiogenesis, the framework presented in this thesis has not been parameterised or validated using experimental data, and is therefore still in a relatively early stage of development. This means that the results of simulations of the combined, hybrid model

can be used only as qualitative indications of general trends, rather than as quantitative predictions. Although there are many aspects of angiogenesis that are not incorporated into the model currently, including the role of macrophages and other cells, the impact of growth factors other than VEGF and the influence of the material cues on the migration of TECs, at this point further experimental work is required to aid parameterisation of the existing framework and inform the direction of further extensions to the model.

The model described in this thesis has so far only been applied to a geometry representing a specific type of NRC with particular dimensions. It is not necessarily the case that the predictions made in this work about the optimal seeding densities and distributions for maximising cell survival and VEGF production will extrapolate to other engineered tissue types or even dimensions of NRC, due to the impact of various boundary conditions and length scales. However, it would be easy to vary the shape, dimensions and boundary conditions of the geometry in COMSOL in order to simulate other engineered tissues, composed of the same cell and material types, using the model and parameters derived in this thesis. Furthermore, it would be relatively easy to investigate the impact of the use of time-released VEGF using the framework set out in this thesis; capsules containing the VEGF could be modelled as 3D sources of VEGF.

The main limitation of the application of the model provided in this thesis to other systems is the cell and material type-specific parameters; simulations of alternative cell and material combinations would require the model to be parameterised against corresponding representative *in vitro* data. Additionally, the model is not currently valid for conducting simulations over long time periods- as previously mentioned, this could be improved by incorporating experimental data from different time points into a second iteration of the parameterisation process.

It is anticipated that in the future the model described in this thesis

will be combined with a model of neuronal growth. Neuronal growth progresses in a similar manner to angiogenesis, with leading "growth cones" sensing and migrating in response to chemotactic, haptotactic and mechanical cues, and therefore can be modelled via a similar biased random walk process. The integration of these two models would also enable a theoretical investigation into the theory that Schwann cell migration, and thus axonal regeneration, is guided by directional cues provided by preceding vascular growth.

6.2.2 Directions for future experimental work

In this thesis, the mathematical model was parameterised using cell and material type-specific *in vitro* data measured at the 1 day time point; the framework was applied to a geometry representing a cell culture well to achieve this. A degree of validation of the model was carried out against additional data measured at the 5 day time point in Section 3.6.1. The parameterised model was then translated to a geometry representing a NRC implanted *in vivo*, under the assumption that the same parameters and constitutive relationships could be used because the NRCs modelled in this work are composed of the same material and cell type as used in the *in vitro* experiments. As previously mentioned, a crucial next step in this work would be to conduct *in vivo* experiments to verify the ability of the model to make useful predictions when applied to this scenario.

In particular, the simulations presented in Chapter 4 predicted that a uniform seeding cell density of 88×10^6 cells/ml is optimal for cell survival after 1 day. Furthermore, the combined hybrid model results also suggested that this seeding cell density would, on average, achieve the highest mean viable cell density after 5 days once the growth of vessel was taken into account. Therefore it is proposed that dADSC-seeded EngNT NRCs, created using three different uniform seeding densities $n_0 = 20$, 88 and 400×10^6 cells/ml, could be used in an *in vivo* study to validate these results. The focus on lower cell densities is based on the quantitative re-

sults of the model, with the highest seeding cell density used as a control representing the current, more densely seeded approach.

Ideally, these NRCs would need to be harvested at a minimum of two different time points within 5 days post-implantation to enable assessment of cell survival via histological staining and imaging. Cell survival measurements could then be used to validate the model. Aside from the quantification of cell survival, this experiment could simultaneously be used to gather other vital information that could greatly improve other aspects of the model:

1. VEGF measurements: validation of the VEGF gradients predicted by the model over time would be facilitated by measurements of VEGF from sections of engineered tissue at varying longitudinal positions along the NRCs, at different time points.

2. Measurement of *in vivo* oxygen levels: currently the boundary conditions for oxygen used in the model are based on oxygen concentration measurements of other tissues. Peripheral nerve-specific oxygen concentration values could be collected via oxygen probes similar to those used in Section 3.3. Additionally, oxygen concentration measurements taken at different time points and spatial locations along the length of an implanted NRC could be used to validate model predictions for oxygen concentration distributions over time.

3. Assessment of endothelial cell migration: EC staining can be carried out in sections, permitting the number of ECs at different positions along the length of the NRC to be counted.

4. Imaging data for assessing the progression of vascular growth into the NRC: metrics such as growth rates, penetration distances and vessel densities could be extracted from such images and used to parameterise the model of angiogenesis presented in Chapter 5. Additionally, imaging data could provide further evidence to test the hypoth-

esis that higher uniform seeding densities induce lower branching densities over the vascular networks. Photoacoustic imaging could potentially be used to obtain imaging data for the same sample over several points in time.

It is important to note that validation of the mathematical model does not violate the explicit aim of the joint experimental-theoretical method to reduce the number of animal experiments. If the mathematical work contained in this thesis had not been completed, experimental techniques would have been required to investigate the same problems regarding cell seeding strategies. Effectively, the model predictions act to refine the scope and aid the design of the experimental research by suggesting which NRC designs are likely to produce the most informative results. The experiments not only act as vital validation of the mathematical model, but the results can also be used and analysed in their own right to inform future NRC design.

Further in the future, it would also be worthwhile to repeat the *in vitro* experiments to allow extrapolation of the model to other cell and material combinations. A database of cell and material-type specific parameters could be collated by repeating the *in vitro* experiments using different design combinations; combined with the mathematical model, this would allow researchers to simulate a wide variety of different engineered tissue configurations. The *in vitro* experimental data showed quite a large amount of variation; therefore in future experiments it would be advisable to use greater N numbers if possible.

6.3 Thoughts on the multidisciplinary method

A broader aim of this work was to attempt to use and assess a multidisciplinary method for the development of engineered tissues. Although this thesis goes some way towards demonstrating the potential of a multidisciplinary approach in this field via the generation of a range of testable hy-

potheses, the mathematical model presented here still requires validation, which is a crucial step in the multidisciplinary method set out in Figure 1.4.

Nevertheless, the process of working in close collaboration with experimental researchers has highlighted considerations that are important for the effective implementation of multidisciplinary work. It is hoped that the following brief assessment of these may aid future research in this area that seeks to adopt a similar approach. Although some of the recommendations and observations made here are not individually novel, often calls are made for closer collaboration between disciplines without outlining the specifics of how that can be achieved effectively. Therefore, it is still worth documenting in explicit terms the issues encountered during the course of this project relating to the multidisciplinary nature of the work.

Good communication between researchers working together on a multidisciplinary project is absolutely paramount. Although this statement is true for all research conducted as part of a team, multidisciplinary research offers some unique challenges. In particular, experimental scientists must be thorough in their explanations of experimental techniques, making sure to provide the following:

1. The specifics of the experimental procedures involved. For example, sometimes the exact compositions of materials or experimental set ups are taken for granted by experimental scientists, who may be unaware of the implications for modelling the same scenario *in silico*.

2. Details of possible sources of inaccuracy.

3. Descriptions of precisely what is being measured or can be measured.

In turn, those conducting the mathematical and computational aspects of the may benefit from these pointers:

1. Prior to the planning of experimental work, a comprehensive list should be prepared consisting of the exact measurements required

to facilitate model parameterisation or validation, and the variables that it is anticipated that the model will include. This enable experimental researchers to check the feasibility of data-driven validation or parameterisation.

2. If possible, theoretical researchers should observe the experimental procedure first hand at least once. This can highlight variables that could impact the mathematical modelling set up that otherwise would not necessarily come up in conversions with experimental colleagues.

3. Any assumptions that are made as part of the mathematical model should be double checked with experimental colleagues.

Much of the modelling work done in tissue engineering so far has produced interesting results that match experimental data qualitatively, and in this way model simulations are able to generate general hypotheses. However, in this thesis one of the aims was to make more precise predictions to aid the specific design of experiments. This requires that the results are presented in dimensional, experimental units, or that the necessary parameters for conversion from non-dimensional units to dimensional units are provided clearly. It is important that experiments are planned carefully; often experimental work relies on measuring "fold" increases or decreases in a measurement, and although this can certainly indicate a biological effect, parameterisation of dimensional models against this type of data can be difficult.

Finally, a commitment must be made on both sides to carry the work forward. The real benefits of multidisciplinary research emerge through feedback and iteration between experimental and theoretical work over time. When conducted in this manner, a joint theoretical-experimental approach to tissue engineering has the potential to direct and speed up research, and thus aid the move towards clinical translation.

Appendix A

Proof of concept model

A.1 Analysis of time scales

An analysis of the time scales involved in the processes included within the governing equations was necessary to justify the quasi-steady assumption used for the oxygen concentration governing equation. Here it is assumed that the characteristic length scale is 0.75 cm, i.e. half the length of a 1.5 cm long NRC.

Oxygen diffusion time scale:

$$\frac{0.75^2}{D_{c_g}} = \frac{0.75^2}{4.5 \times 10^{-6}} \approx 1.25 \times 10^5 \text{ s}$$

VEGF diffusion time scale:

$$\frac{0.75^2}{D_{v_g}} = \frac{0.75^2}{1.13 \times 10^{-6}} \approx 5 \times 10^5 \text{ s}$$

Cell proliferation time scale: (used to rescale the variable t)

$$\frac{1}{\beta c_{\frac{1}{2}}} \approx \frac{1}{24 \times 6.66 \times 10^{-9}} \approx 6 \times 10^6 \text{ s}$$

Note that cell proliferation occurs on a time scale that is a magnitude greater than that of VEGF diffusion and oxygen diffusion, justifying the quasi-steady assumption.

A.2 Mathematical/computational methods

Equations (3.7), (3.8) and (3.9) were solved using a combination of explicit discretisation and MATLAB based ODE solvers. The spatial elements of the cell density and VEGF concentration equations were discretised, through the use of second order central approximations, with truncation errors $O((\Delta z')^2)$:

$$\left.\frac{\partial^2 c'}{\partial z'^2}\right|_{z'=z'_i} = \frac{c'_{i+1} - 2c'_i + c'_{i-1}}{(\Delta z')^2}$$
$$\left.\frac{\partial^2 v'}{\partial z'^2}\right|_{z'=z'_i} = \frac{v'_{i+1} - 2v'_i + v'_{i-1}}{(\Delta z')^2}$$

Here $v'_i = v'(z'_i)$ and $v'_{i+k} = v'(z'_i + k\Delta z')$; the same notation applies to c'. Boundary conditions were applied in a similar manner, using ghost points where necessary. Initially the algorithm calculates the solutions for c' and n', which involves solving a matrix of linear equations in the case of c'; the solution for v' is calculated afterwards.

A.3 Parameter values

Table A.1 lists the parameter values used for the proof of concept model simulations (results of these simulations are displayed in Figure 3.2).

Parameter	Simulation a)	Simulation b)	Simulation c)	Simulation d)
μ_c	450	200	450	450
γ_c	12.5125	12.5125	12.5125	12.5125
η_d	0.3923	0.3923	0.3923	0.3923
γ_v	8×10^{-4}	8×10^{-4}	8×10^{-4}	8×10^{-4}
μ_v	3	3	3	3
η_v	2	2	2	2

Table A.1: Non-dimensional parameters used for simulations. Simulation labels refer to Figure 3.2.

Bibliography

[1] Y. Abadie, F. Bregeon, L. Papazian, F. Lange, B. Chailley-Heu, P. Thomas, P. Duvaldestin, S. Adnot, B. Maitre, and C. Delclaux. Decreased VEGF concentration in lung tissue and vascular injury during ARDS. *European Respiratory Journal*, 25(1):139–146, January 2005.

[2] S. E. Abdullah and R. Perez-Soler. Mechanisms of resistance to vascular endothelial growth factor blockade: VEGF Resistance Mechanisms. *Cancer*, 118(14):3455–3467, July 2012.

[3] S. Adra, T. Sun, S. MacNeil, M. Holcombe, and R. Smallwood. Development of a Three Dimensional Multiscale Computational Model of the Human Epidermis. *PLoS ONE*, 5(1):e8511, January 2010.

[4] P. Aebischer, V. Guénard, and S. Brace. Peripheral nerve regeneration through blind-ended semipermeable guidance channels: effect of the molecular weight cutoff. *Journal of Neuroscience*, 9(10):3590–3595, October 1989.

[5] M. L. C. Albuquerque, C. M. Waters, U. Savla, H. W. Schnaper, and A. S. Flozak. Shear stress enhances human endothelial cell wound closure in vitro. *American Journal of Physiology-Heart and Circulatory Physiology*, 279(1):H293–H302, July 2000.

[6] I. Almendros, R. Farré, A. M. Planas, M. Torres, M. R. Bonsignore, D. Navajas, and J. M. Montserrat. Tissue Oxygenation in Brain, Muscle,

and Fat in a Rat Model of Sleep Apnea: Differential Effect of Obstructive Apneas and Intermittent Hypoxia. *Sleep*, 34(8):1127–1133, August 2011.

[7] K. G. Almgren. Revascularization of free pheripheral nerve grafts: An experimental study in the rabbit. *Acta Orthopaedica Scandinavica. Supplementum*, 154:1–104, 1974.

[8] D. Ambrosi, A. Gamba, and G. Serini. Cell Directional and chemotaxis in vascular morphogenesis. *Bulletin of Mathematical Biology*, 66(6):1851–1873, November 2004.

[9] G. An, Q. Mi, J. Dutta-Moscato, and Y. Vodovotz. Agent-based models in translational systems biology. *Wiley Interdisciplinary Reviews: Systems Biology and Medicine*, 1(2):159–171, September 2009.

[10] A. R. A. Anderson and M. A. J. Chaplain. Continuous and discrete mathematical models of tumor-induced angiogenesis. *Bulletin of Mathematical Biology*, 60(5):857–900, September 1998.

[11] S. M. Anderson, S. N. Siegman, and T. Segura. The effect of vascular endothelial growth factor (VEGF) presentation within fibrin matrices on endothelial cell branching. *Biomaterials*, 32(30):7432–7443, October 2011.

[12] A. R. A. Anderson. A hybrid mathematical model of solid tumour invasion: the importance of cell adhesion. *Mathematical Medicine and Biology: A Journal of the IMA*, 22(2):163–186, June 2005.

[13] J. Andrae, R. Gallini, and C. Betsholtz. Role of platelet-derived growth factors in physiology and medicine. *Genes & Development*, 22(10):1276–1312, May 2008.

[14] D. Angius, H. Wang, R. J. Spinner, Y. Gutierrez-Cotto, M. J. Yaszemski, and A. J. Windebank. A systematic review of animal models used to study nerve regeneration in tissue-engineered scaffolds. *Biomaterials*, 33(32):8034–8039, November 2012.

[15] E. E. Antoine, P. P. Vlachos, and M. N. Rylander. Review of Collagen I Hydrogels for Bioengineered Tissue Microenvironments: Characterization of Mechanics, Structure, and Transport. *Tissue Engineering. Part B, Reviews*, 20(6):683–696, December 2014.

[16] J. B. Aquino, J. Hjerling-Leffler, M. Koltzenburg, T. Edlund, M. J. Villar, and P. Ernfors. In vitro and in vivo differentiation of boundary cap neural crest stem cells into mature Schwann cells. *Experimental Neurology*, 198(2):438–449, April 2006.

[17] G. Archie. The Electrical Resistivity Log as an Aid in Determining Some Reservoir Characteristics. *Transactions of the AIME*, 146(01):54–62, December 1942.

[18] A. G. Ardakani, U. Cheema, R. A. Brown, and R. J. Shipley. Quantifying the correlation between spatially defined oxygen gradients and cell fate in an engineered three-dimensional culture model. *Journal of The Royal Society Interface*, 11(98):20140501, September 2014.

[19] J. P. Armstrong and M. M. Stevens. Emerging Technologies for Tissue Engineering: From Gene Editing to Personalized Medicine. *Tissue Engineering Part A*, 25(9-10):688–692, May 2019.

[20] A. Armulik, A. Abramsson, and C. Betsholtz. Endothelial/Pericyte Interactions. *Circulation Research*, 97(6):512–523, September 2005.

[21] M. A. Asnaghi, P. Jungebluth, M. T. Raimondi, S. C. Dickinson, L. E. N. Rees, T. Go, T. A. Cogan, A. Dodson, P. P. Parnigotto, A. P. Hollander, M. A. Birchall, M. T. Conconi, P. Macchiarini, and S. Mantero. A double-chamber rotating bioreactor for the development of tissue-engineered hollow organs: From concept to clinical trial. *Biomaterials*, 30(29):5260–5269, October 2009.

[22] A. Atala. Tissue engineering of reproductive tissues and organs. *Fertility and Sterility*, 98(1):21–29, July 2012.

[23] M. Aubert, M. A. J. Chaplain, S. R. McDougall, A. Devlin, and C. A. Mitchell. A Continuum Mathematical Model of the Developing Murine Retinal Vasculature. *Bulletin of Mathematical Biology*, 73(10):2430–2451, February 2011.

[24] H. G. Augustin, G. Young Koh, G. Thurston, and K. Alitalo. Control of vascular morphogenesis and homeostasis through the angiopoietin-Tie system. *Nature Reviews Molecular Cell Biology*, 10(3):165–177, March 2009.

[25] F. Azuaje. Computational discrete models of tissue growth and regeneration. *Briefings in Bioinformatics*, 12(1):64–77, January 2011.

[26] S. B. Bailey, M. E. Eichler, A. Villadiego, and K. M. Rich. The influence of fibronectin and laminin during Schwann cell migration and peripheral nerve regeneration through silicon chambers. *Journal of Neurocytology*, 22(3):176–184, March 1993.

[27] I. Baldea, I. Teacoe, D. E. Olteanu, C. Vaida-Voievod, A. Clichici, A. Sirbu, G. A. Filip, and S. Clichici. Effects of different hypoxia degrees on endothelial cell cultures- Time course study. *Mechanisms of Ageing and Development*, 172:45–50, June 2018.

[28] D. Balding and D. McElwain. A mathematical model of tumour-induced capillary growth. *Journal of Theoretical Biology*, 114(1):53–73, May 1985.

[29] U. J. Balis, K. Behnia, B. Dwarakanath, S. N. Bhatia, S. J. Sullivan, M. L. Yarmush, and M. Toner. Oxygen Consumption Characteristics of Porcine Hepatocytes. *Metabolic Engineering*, 1(1):49–62, January 1999.

[30] P. R. Baraniak and T. C. McDevitt. Stem cell paracrine actions and tissue regeneration. *Regenerative medicine*, 5(1):121–143, January 2010.

[31] I. Barkefors, S. L. Jan, L. Jakobsson, E. Hejll, G. Carlson, H. Johansson, J. Jarvius, J. W. Park, N. L. Jeon, and J. Kreuger. Endothelial Cell

Migration in Stable Gradients of Vascular Endothelial Growth Factor A and Fibroblast Growth Factor 2 EFFECTS ON CHEMOTAXIS AND CHEMOKINESIS. *Journal of Biological Chemistry*, 283(20):13905–13912, May 2008.

[32] D. O. Bates and S. J. Harper. Regulation of vascular permeability by vascular endothelial growth factors. *Vascular Pharmacology*, 39(4):225–237, November 2002.

[33] D. O. Bates. Vascular endothelial growth factors and vascular permeability. *Cardiovascular Research*, 87(2):262–271, July 2010.

[34] E. J. Battegay. PDGF-BB modulates endothelial proliferation and angiogenesis in vitro via PDGF β-receptors. *The Journal of Cell Biology*, 125(4):917–928, May 1994.

[35] J. W. Beeckman. Mathematical description of heterogeneous materials. *Chemical Engineering Science*, 45(8):2603–2610, January 1990.

[36] A. Beenken and M. Mohammadi. The FGF family: biology, pathophysiology and therapy. *Nature Reviews Drug Discovery*, 8(3):235–253, March 2009.

[37] K. Belanger, T. M. Dinis, S. Taourirt, G. Vidal, D. L. Kaplan, and C. Egles. Recent Strategies in Tissue Engineering for Guided Peripheral Nerve Regeneration. *Macromolecular Bioscience*, 16(4):472–481, April 2016.

[38] G. J. Bennett. Neuropathic pain: New insights, new interventions. *Hospital Practice*, 33(10):95–114, October 1998.

[39] A. Berger, E. M. Dukes, and G. Oster. Clinical characteristics and economic costs of patients with painful neuropathic disorders. *The Journal of Pain*, 5(3):143–149, April 2004.

[40] D. A. Berk, F. Yuan, M. Leunig, and R. K. Jain. Fluorescence photobleaching with spatial Fourier analysis: measurement of diffusion in light-scattering media. *Biophysical Journal*, 65(6):2428–2436, December 1993.

[41] F. Berthiaume, T. J. Maguire, and M. L. Yarmush. Tissue engineering and regenerative medicine: History, progress, and challenges. *Annual Review of Chemical and Biomolecular Engineering*, 2(1):403–430, 2011.

[42] T. J. Best, S. E. Mackinnon, R. Midha, D. A. Hunter, and P. J. Evans. Revascularization of peripheral nerve autografts and allografts. *Plastic and Reconstructive Surgery*, 104(1):152–160, July 1999.

[43] B. S. Betts-Obregon, S. Vellanki, J. Buikema, A. T. Tsin, and K. Wright. Effect of Glucose on Retinal Endothelial Cell Viability and VEGF Secretion. *HSOA Journal of Cell Biology & Cell Metabolism*, 3(1), 2016.

[44] K. S. Bhangra, F. Busuttil, J. B. Phillips, and A. A. Rahim. Using Stem Cells to Grow Artificial Tissue for Peripheral Nerve Repair. *Stem Cells International*, 2016, 2016.

[45] D. Bhatnagar, J. S. Bushman, N. S. Murthy, A. Merolli, H. M. Kaplan, and J. Kohn. Fibrin glue as a stabilization strategy in peripheral nerve repair when using porous nerve guidance conduits. *Journal of Materials Science: Materials in Medicine*, 28(5), May 2017.

[46] F. Billy, B. Ribba, O. Saut, H. Morre-Trouilhet, T. Colin, D. Bresch, J.-P. Boissel, E. Grenier, and J.-P. Flandrois. A pharmacologically based multiscale mathematical model of angiogenesis and its use in investigating the efficacy of a new cancer treatment strategy. *Journal of Theoretical Biology*, 260(4):545–562, October 2009.

[47] R. Blanco and H. Gerhardt. VEGF and Notch in Tip and Stalk Cell Selection. *Cold Spring Harbor Perspectives in Medicine*, 3(1):a006569, January 2013.

[48] C. P. Blobel. 3D trumps 2D when studying endothelial cells. *Blood*, 115(25):5128–5130, June 2010.

[49] J.-M. Boutry, J.-J. Hauw, A. Gansmüller, N. Di-Bert, M. Pouchelet, and A. B.-V. Evercooren. Establishment and characterization of a mouse Schwann cell line which produces myelin in vivo. *Journal of Neuroscience Research*, 32(1):15–26, May 1992.

[50] T. B. Boving and P. Grathwohl. Tracer diffusion coefficients in sedimentary rocks: correlation to porosity and hydraulic conductivity. *Journal of Contaminant Hydrology*, 53(1-2):85–100, December 2001.

[51] J. G. Boyd and T. Gordon. Neurotrophic factors and their receptors in axonal regeneration and functional recovery after peripheral nerve injury. *Molecular Neurobiology*, 27(3):277–323, June 2003.

[52] A. J. Bretland, J. Lawry, and R. M. Sharrard. A study of death by anoikis in cultured epithelial cells. *Cell Proliferation*, 34(4):199–210, August 2001.

[53] C. J. W. Breward, H. M. Byrne, and C. E. Lewis. The role of cell-cell interactions in a two-phase model for avascular tumour growth. *Journal of Mathematical Biology*, 45(2):125–152, August 2002.

[54] R. A. Brown, M. Wiseman, C.-B. Chuo, U. Cheema, and S. N. Nazhat. Ultrarapid Engineering of Biomimetic Materials and Tissues: Fabrication of Nano- and Microstructures by Plastic Compression. *Advanced Functional Materials*, 15(11):1762–1770, November 2005.

[55] R. P. Bunge. The role of the Schwann cell in trophic support and regeneration. *Journal of Neurology*, 242:S19–S21, December 1994.

[56] I. Burova, C. Peticone, D. De Silva Thompson, J. C. Knowles, I. Wall, and R. J. Shipley. A parameterised mathematical model to elucidate

osteoblast cell growth in a phosphate-glass microcarrier culture. *Journal of Tissue Engineering*, 10:204173141983026, January 2019.

[57] P. H. Burri, R. Hlushchuk, and V. Djonov. Intussusceptive angiogenesis: Its emergence, its characteristics, and its significance. *Developmental Dynamics*, 231(3):474–488, November 2004.

[58] H. Byrne and L. Preziosi. Modelling solid tumour growth using the theory of mixtures. *Mathematical Medicine and Biology: A Journal of the IMA*, 20(4):341–366, December 2003.

[59] H. M. Byrne, J. R. King, D. L. S. McElwain, and L. Preziosi. A two-phase model of solid tumour growth. *Applied Mathematics Letters*, 16(4):567–573, May 2003.

[60] F. Cao, A. H. Sadrzadeh Rafie, O. J. Abilez, H. Wang, B. Pruitt, C. Zarins, and J. C. Wu. In vivo imaging and evaluation of different biomatrices for improvement of stem cell survival. *Journal of Tissue Engineering and Regenerative Medicine*, 1(6):465–468, November 2007.

[61] P. Carmeliet and R. K. Jain. Molecular mechanisms and clinical applications of angiogenesis. *Nature*, 473(7347):298–307, May 2011.

[62] P. Carmeliet, Y. Dor, J.-M. Herbert, D. Fukumura, K. Brusselmans, M. Dewerchin, M. Neeman, F. Bono, R. Abramovitch, P. Maxwell, C. J. Koch, P. Ratcliffe, L. Moons, R. K. Jain, D. Collen, and E. Keshet. Role of HIF-1α in hypoxia-mediated apoptosis, cell proliferation and tumour angiogenesis. *Nature*, 394(6692):485–490, July 1998.

[63] P. Carmeliet. Mechanisms of angiogenesis and arteriogenesis. *Nature Medicine*, 6(3):389–395, April 2000.

[64] A. Carreau, B. E. Hafny-Rahbi, A. Matejuk, C. Grillon, and C. Kieda. Why is the partial oxygen pressure of human tissues a crucial parameter?

Small molecules and hypoxia. *Journal of Cellular and Molecular Medicine*, 15(6):1239–1253, June 2011.

[65] A. Cattin, J. J. Burden, L. Van Emmenis, F. E. Mackenzie, J. J. A. Hoving, N. G. Calavia, Y. Guo, M. McLaughlin, L. H. Rosenberg, V. Quereda, D. Jamecna, I. Napoli, S. Parrinello, T. Enver, C. Ruhrberg, and A. C. Lloyd. Macrophage-Induced Blood Vessels Guide Schwann Cell-Mediated Regeneration of Peripheral Nerves. *Cell*, 162(5):1127–1139, August 2015.

[66] L. J. Chamberlain, I. V. Yannas, A. Arrizabalaga, H. P. Hsu, T. V. Norregaard, and M. Spector. Early peripheral nerve healing in collagen and silicone tube implants: Myofibroblasts and the cellular response. *Biomaterials*, 19(15):1393–1403, August 1998.

[67] N. S. Chandel, E. Maltepe, E. Goldwasser, C. E. Mathieu, M. C. Simon, and P. T. Schumacker. Mitochondrial reactive oxygen species trigger hypoxia-induced transcription. *Proceedings of the National Academy of Sciences*, 95(20):11715–11720, September 1998.

[68] C.-J. Chang and S.-h. Hsu. The effect of high outflow permeability in asymmetric poly(DL-lactic acid-*co*-glycolic acid) conduits for peripheral nerve regeneration. *Biomaterials*, 27(7):1035–1042, March 2006.

[69] J.-Y. Chang, T.-Y. Ho, H.-C. Lee, Y.-L. Lai, M.-C. Lu, C.-H. Yao, and Y.-S. Chen. Highly Permeable Genipin-Cross-linked Gelatin Conduits Enhance Peripheral Nerve Regeneration. *Artificial Organs*, 33(12):1075–1085, December 2009.

[70] M. A. J. Chaplain and A. M. Stuart. A model mechanism for the chemotactic response of endotheliai cells to tumour angiogenesis factor. *IMA Journal of Mathematics Applied in Medicine & Biology*, 10:149–168, 1993.

[71] U. Cheema, Z. Rong, O. Kirresh, A. J. MacRobert, P. Vadgama, and R. A. Brown. Oxygen diffusion through collagen scaffolds at defined densities: implications for cell survival in tissue models. *Journal of Tissue Engineering and Regenerative Medicine*, 6(1):77–84, February 2011.

[72] R. R. Chen, E. A. Silva, W. W. Yuen, A. A. Brock, C. Fischbach, A. S. Lin, R. E. Guldberg, and D. J. Mooney. Integrated approach to designing growth factor delivery systems. *The FASEB Journal*, 21(14):3896–3903, December 2007.

[73] T. T. Chen, A. Luque, S. Lee, S. M. Anderson, T. Segura, and M. L. Iruela-Arispe. Anchorage of VEGF to the extracellular matrix conveys differential signaling responses to endothelial cells. *The Journal of Cell Biology*, 188(4):595–609, February 2010.

[74] G. Chen, X. Shi, C. Sun, M. Li, Q. Zhou, C. Zhang, J. Huang, Y. Qiu, X. Wen, Y. Zhang, Y. Zhang, S. Yang, L. Lu, J. Zhang, Q. Yuan, J. Lu, G. Xu, Y. Xue, Z. Jin, C. Jiang, M. Ying, and X. Liu. VEGF-Mediated Proliferation of Human Adipose Tissue-Derived Stem Cells. *PLoS ONE*, 8(10), October 2013.

[75] J. A. Chiarotto and R. P. Hill. A quantitative analysis of the reduction in oxygen levels required to induce up-regulation of vascular endothelial growth factor (VEGF) mRNA in cervical cancer cell lines. *British Journal of Cancer*, 80(10):1518–1524, July 1999.

[76] C. H. Cho, J. Park, D. Nagrath, A. W. Tilles, F. Berthiaume, M. Toner, and M. L. Yarmush. Oxygen uptake rates and liver-specific functions of hepatocyte and 3T3 fibroblast co-cultures. *Biotechnology and Bioengineering*, 97(1):188–199, May 2007.

[77] H. Chou, L. Wu, L. Zeng, and A. Chang. Evaluation of solute diffusion tortuosity factor models for variously saturated soils. *Water Resources Research*, 48(10), October 2012.

[78] D. C. Chow, L. A. Wenning, W. M. Miller, and E. T. Papoutsakis. Modeling pO_2 distributions in the bone marrow hematopoietic compartment. II. Modified Kroghian models. *Biophysical Journal*, 81(2):685–696, August 2001.

[79] C. A. Chung, C. W. Yang, and C. W. Chen. Analysis of cell growth and diffusion in a scaffold for cartilage tissue engineering. *Biotechnology and Bioengineering*, 94(6):1138–1146, August 2006.

[80] C. A. Chung, C. W. Chen, C. P. Chen, and C. S. Tseng. Enhancement of cell growth in tissue-engineering constructs under direct perfusion: Modeling and simulation. *Biotechnology and Bioengineering*, 97(6):1603–1616, August 2007.

[81] P. Ciaramitaro, M. Mondelli, F. Logullo, S. Grimaldi, B. Battiston, A. Sard, C. Scarinzi, G. Migliaretti, G. Faccani, and D. Cocito. Traumatic peripheral nerve injuries: epidemiological findings, neuropathic pain and quality of life in 158 patients. *Journal of the Peripheral Nervous System*, 15(2):120–127, June 2010.

[82] S. Coakley, R. Smallwood, and M. Holcombe. Using X-Machines as a Formal Basis for Describing Agents in Agent-Based Modelling. *Proceedings of the SpringSim 2006 Conference*, 2006.

[83] F. Colazzo, P. Sarathchandra, R. T. Smolenski, A. H. Chester, Y.-T. Tseng, J. T. Czernuszka, M. H. Yacoub, and P. M. Taylor. Extracellular matrix production by adipose-derived stem cells: Implications for heart valve tissue engineering. *Biomaterials*, 32(1):119–127, January 2011.

[84] F. Coletti, S. Macchietto, and N. Elvassore. Mathematical Modeling of Three-Dimensional Cell Cultures in Perfusion Bioreactors. *Industrial & Engineering Chemistry Research*, 45(24):8158–8169, November 2006.

[85] M. J. Cooke, K. Vulic, and M. S. Shoichet. Design of biomaterials to

enhance stem cell survival when transplanted into the damaged central nervous system. *Soft Matter*, 6(20):4988–4998, October 2010.

[86] R. H. Coy, O. R. Evans, J. B. Phillips, and R. J. Shipley. An integrated theoretical-experimental approach to accelerate translational tissue engineering. *Journal of Tissue Engineering and Regenerative Medicine*, 12(1):e53–e59, October 2016.

[87] T. I. Croll, S. Gentz, K. Mueller, M. Davidson, A. J. O'Connor, G. W. Stevens, and J. J. Cooper-White. Modelling oxygen diffusion and cell growth in a porous, vascularising scaffold for soft tissue engineering applications. *Chemical Engineering Science*, 60(17):4924–4934, September 2005.

[88] J. A. Currie. Gaseous diffusion in porous media. Part 2. - Dry granular materials. *British Journal of Applied Physics*, 11(8):318–323, 1960.

[89] J. H. Cushman, L. S. Bennethum, and B. X. Hu. A primer on upscaling tools for porous media. *Advances in Water Resources*, 25(8-12):1043–1067, 2002.

[90] Y. Dai and A. C. Foley. Tissue engineering approaches to heart repair. *Critical Reviews in Biomedical Engineering*, 42(3):213–227, 2014.

[91] W. Daly, L. Yao, D. Zeugolis, A. Windebank, and A. Pandit. A biomaterials approach to peripheral nerve regeneration: bridging the peripheral nerve gap and enhancing functional recovery. *Journal of The Royal Society Interface*, 9(67):202–221, February 2012.

[92] P. Danielsson, L. Dahlin, and B. Povlsen. Tubulization Increases Axonal Outgrowth of Rat Sciatic Nerve after Crush Injury. *Experimental Neurology*, 139(2):238–243, June 1996.

[93] J. T. Daub and R. M. H. Merks. A Cell-Based Model of Extracellular-

Matrix-Guided Endothelial Cell Migration During Angiogenesis. *Bulletin of Mathematical Biology*, 75(8):1377–99, August 2013.

[94] L. G. de Pillis, A. E. Radunskaya, and C. L. Wiseman. A validated mathematical model of cell-mediated immune response to tumor growth. *Cancer Research*, 65(17):7950–7958, September 2005.

[95] F. De Smet, I. Segura, K. De Bock, P. J. Hohensinner, and P. Carmeliet. Mechanisms of Vessel Branching: Filopodia on Endothelial Tip Cells Lead the Way. *Arteriosclerosis, Thrombosis, and Vascular Biology*, 29(5):639–649, May 2009.

[96] J. M. P. Q. Delgado. A Simple Experimental Technique to Measure Tortuosity in Packed Beds. *The Canadian Journal of Chemical Engineering*, 84(6):651–655, May 2006.

[97] M. Dellinger, R. Hunter, M. Bernas, N. Gale, G. Yancopoulos, R. Erickson, and M. Witte. Defective remodeling and maturation of the lymphatic vasculature in Angiopoietin-2 deficient mice. *Developmental Biology*, 319(2):309–320, July 2008.

[98] R. Deumens, A. Bozkurt, M. F. Meek, M. A. E. Marcus, E. A. J. Joosten, J. Weis, and G. A. Brook. Repairing injured peripheral nerves: Bridging the gap. *Progress in Neurobiology*, 92(3):245–276, November 2010.

[99] P. G. di Summa, D. F. Kalbermatten, E. Pralong, W. Raffoul, P. J. Kingham, and G. Terenghi. Long-term in vivo regeneration of peripheral nerves through bioengineered nerve grafts. *Neuroscience*, 181:278–291, May 2011.

[100] P. G. di Summa, D. F. Kalbermatten, W. Raffoul, G. Terenghi, and P. J. Kingham. Extracellular Matrix Molecules Enhance the Neurotrophic Effect of Schwann Cell-Like Differentiated Adipose-Derived Stem Cells and Increase Cell Survival Under Stress Conditions. *Tissue Engineering Part A*, 19(3):368–379, February 2013.

[101] T. B. Ducker and G. J. Hayes. Experimental Improvements in the Use of Silastic Cuff for Peripheral Nerve Repair. *Journal of Neurosurgery*, 28(6):582–587, June 1968.

[102] J. R. Duffy, F. E. Warburg, S. F. T. Koelle, M. U. Werner, and P. R. Nielsen. Pain-related psychological distress, self-rated health and significance of neuropathic pain in Danish soldiers injured in Afghanistan. *Acta Anaesthesiologica Scandinavica*, 59(10):1367–1376, November 2015.

[103] X. Dun and D. B. Parkinson. Visualizing Peripheral Nerve Regeneration by Whole Mount Staining. *PLoS ONE*, 10(3):e0119168, March 2015.

[104] H. F. Dvorak. Vascular Permeability Factor/Vascular Endothelial Growth Factor: A Critical Cytokine in Tumor Angiogenesis and a Potential Target for Diagnosis and Therapy. *Journal of Clinical Oncology*, 20(21):4368–4380, November 2002.

[105] S. L. Ennis, M. P. Galea, D. N. O'Neal, and M. J. Dodson. Peripheral neuropathy in the hands of people with diabetes mellitus. *Diabetes Research and Clinical Practice*, 119:23–31, September 2016.

[106] N. Epstein. On tortuosity and the tortuosity factor in flow and diffusion through porous media. *Chemical Engineering Science*, 44(3):777–779, January 1989.

[107] M. Ezra, J. Bushman, D. Shreiber, M. Schachner, and J. Kohn. Porous and Nonporous Nerve Conduits: The Effects of a Hydrogel Luminal Filler With and Without a Neurite-Promoting Moiety. *Tissue Engineering. Part A*, 22(9-10):818–826, May 2016.

[108] E. Fagiani and G. Christofori. Angiopoietins in angiogenesis. *Cancer Letters*, 328(1):18–26, January 2013.

[109] Q. Fang, S. Sakadžić, L. Ruvinskaya, A. Devor, A. M. Dale, and D. A.

Boas. Oxygen Advection and Diffusion in a Three Dimensional Vascular Anatomical Network. *Optics Express*, 16(22):17530–17541, October 2008.

[110] H. Fansa and G. Keilhoff. Comparison of different biogenic matrices seeded with cultured Schwann cells for bridging peripheral nerve defects. *Neurological Research*, 26(2):167–173, March 2004.

[111] H. Fansa, W. Schneider, and G. Keilhoff. Revascularization of Tissue-Engineered Nerve Grafts and Invasion of Macrophages. *Tissue Engineering*, 7(5):519–524, October 2001.

[112] S. J. Farber, G. M. Hoben, D. A. Hunter, Y. Yan, P. J. Johnson, S. E. Mackinnon, and M. D. Wood. Vascularization is delayed in long nerve constructs compared with nerve grafts. *Muscle & Nerve*, 54(2):319–321, August 2016.

[113] A. Faroni, S. A. Mobasseri, P. J. Kingham, and A. J. Reid. Peripheral nerve regeneration: Experimental strategies and future perspectives. *Advanced Drug Delivery Reviews*, 82-83:160–167, March 2015.

[114] I. Fatt. Pore Structure of Sintered Glass from Diffusion and Resistance Measurements. *The Journal of Physical Chemistry*, 63(5):751–752, May 1959.

[115] B. Feng, Z. Jinkang, W. Zhen, L. Jianxi, C. Jiang, L. Jian, M. Guolin, and D. Xin. The effect of pore size on tissue ingrowth and neovascularization in porous bioceramics of controlled architecturein vivo. *Biomedical Materials*, 6(1):015007, jan 2011.

[116] N. Ferrara and T. Davis-Smyth. The Biology of Vascular Endothelial Growth Factor. *Endocrine Reviews*, 18(1):4–25, February 1997.

[117] U. Fiedler, Y. Reiss, M. Scharpfenecker, V. Grunow, S. Koidl, G. Thurston, N. W. Gale, M. Witzenrath, S. Rosseau, N. Suttorp,

A. Sobke, M. Herrmann, K. T. Preissner, P. Vajkoczy, and H. G. Augustin. Angiopoietin-2 sensitizes endothelial cells to TNF-α and has a crucial role in the induction of inflammation. *Nature Medicine*, 12(2):235–239, February 2006.

[118] I. Filippi, I. Saltarella, C. Aldinucci, F. Carraro, R. Ria, A. Vacca, and A. Naldini. Different Adaptive Responses to Hypoxia in Normal and Multiple Myeloma Endothelial Cells. *Cellular Physiology and Biochemistry*, 46(1):203–212, 2018.

[119] J. M. Fishman, A. Tyraskis, P. Maghsoudlou, L. Urbani, G. Totonelli, M. A. Birchall, and P. De Coppi. Skeletal muscle tissue engineering: Which cell to use? *Tissue Engineering Part B: Reviews*, 19(6):503–515, December 2013.

[120] J. Folkman. Angiogenesis in cancer, vascular, rheumatoid and other disease. *Nature Medicine*, 1(1):27–30, January 1995.

[121] X. Fontana, M. Hristova, C. D. Costa, S. Patodia, L. Thei, M. Makwana, B. Spencer-Dene, M. Latouche, R. Mirsky, K. R. Jessen, R. Klein, G. Raivich, and A. Behrens. c-Jun in Schwann cells promotes axonal regeneration and motoneuron survival via paracrine signaling. *The Journal of Cell Biology*, 198(1):127–141, July 2012.

[122] L. Fredriksson, H. Li, and U. Eriksson. The PDGF family: four gene products form five dimeric isoforms. *Cytokine & Growth Factor Reviews*, 15(4):197–204, August 2004.

[123] S. M. Frisch and R. A. Screaton. Anoikis mechanisms. *Current Opinion in Cell Biology*, 13(5):555–562, 2001.

[124] S. P. Frostick, Q. Yin, and G. J. Kemp. Schwann cells, neurotrophic factors, and peripheral nerve regeneration. *Microsurgery*, 18(7):397–405, January 1998.

[125] C. J. Galban and B. R. Locke. Analysis of cell growth kinetics and substrate diffusion in a polymer scaffold. *Biotechnology and Bioengineering*, 65(2):121–132, October 1999.

[126] V. Galvão, J. G. V. Miranda, and R. Ribeiro-dos-Santos. Development of a two-dimensional agent-based model for chronic chagasic cardiomyopathy after stem cell transplantation. *Bioinformatics*, 24(18):2051–2056, September 2008.

[127] J. R. García and A. J. García. Biomaterial mediated strategies targeting vascularization for bone repair. *Drug Delivery and Translational Research*, 6(2):77–95, April 2016.

[128] L. B. Gardner, Q. Li, M. S. Park, W. M. Flanagan, G. L. Semenza, and C. V. Dang. Hypoxia Inhibits G_1/S Transition through Regulation of p27 Expression. *Journal of Biological Chemistry*, 276(11):7919–7926, March 2001.

[129] A. A. Garrouch, L. Ali, and F. Qasem. Using Diffusion and Electrical Measurements to Assess Tortuosity of Porous Media. *Industrial & Engineering Chemistry Research*, 40(20):4363–4369, October 2001.

[130] J. Gavard, V. Patel, and J. S. Gutkind. Angiopoietin-1 Prevents VEGF-Induced Endothelial Permeability by Sequestering Src through mDia. *Developmental Cell*, 14(1):25–36, January 2008.

[131] S. Gebb and T. Stevens. On lung endothelial cell heterogeneity. *Microvascular Research*, 68(1):1–12, July 2004.

[132] M. Georgiou, S. C. J. Bunting, H. A. Davies, A. J. Loughlin, J. P. Golding, and J. B. Phillips. Engineered neural tissue for peripheral nerve repair. *Biomaterials*, 34(30):7335–7343, October 2013.

[133] M. Georgiou, J. P. Golding, A. J. Loughlin, P. J. Kingham, and J. B. Phillips. Engineered neural tissue with aligned, differentiated adipose-

derived stem cells promotes peripheral nerve regeneration across a critical sized defect in rat sciatic nerve. *Biomaterials*, 37:242–251, January 2015.

[134] H. Gerhardt, M. Golding, M. Fruttiger, C. Ruhrberg, A. Lundkvist, A. Abramsson, M. Jeltsch, C. Mitchell, K. Alitalo, D. Shima, and C. Betsholtz. VEGF guides angiogenic sprouting utilizing endothelial tip cell filopodia. *The Journal of Cell Biology*, 161(6):1163–1177, June 2003.

[135] S. Geuna, S. Raimondo, F. Fregnan, K. Haastert-Talini, and C. Grothe. *In vitro* models for peripheral nerve regeneration. *European Journal of Neuroscience*, 43(3):287–296, February 2016.

[136] B. Ghanbarian, A. G. Hunt, R. P. Ewing, and M. Sahimi. Tortuosity in Porous Media: A Critical Review. *Soil Science Society of America Journal*, 77(5):1461, September 2013.

[137] P. E. Gill, W. Murray, and M. A. Saunders. SNOPT: An SQP Algorithm for Large-Scale Constrained Optimization. *SIAM Review*, 47(1):99–131, January 2005.

[138] F. Gonzalez-Perez, E. Udina, and X. Navarro. Chapter Ten - Extracellular Matrix Components in Peripheral Nerve Regeneration. In S. Geuna, I. Perroteau, P. Tos, and B. Battiston, editors, *Tissue Engineering of the Peripheral Nerve: Stem Cells and Regeneration Promoting Factors*, volume 108 of *International Review of Neurobiology*, pages 257 – 275. Academic Press, 2013.

[139] A. Grützkau, S. Krüger-Krasagakes, H. Baumeister, C. Schwarz, H. Kögel, P. Welker, U. Lippert, B. M. Henz, and A. Möller. Synthesis, Storage, and Release of Vascular Endothelial Growth Factor/Vascular Permeability Factor (VEGF/VPF) by Human Mast Cells: Implications for the Biological Significance of $VEGF_{206}$. *Molecular Biology of the Cell*, 9(4):875–884, April 1998.

[140] X. Gu, F. Ding, and D. F. Williams. Neural tissue engineering options for peripheral nerve regeneration. *Biomaterials*, 35(24):6143–6156, August 2014.

[141] V. Guénard, N. Kleitman, T. K. Morrissey, R. P. Bunge, and P. Aebischer. Syngeneic Schwann Cells Derived from Adult Nerves Seeded in Semipermeable Guidance Channels Enhance Peripheral Nerve Regeneration. *Journal of Neuroscience*, 12(9):3310–3320, September 1992.

[142] P. Han and D. M. Bartels. Temperature Dependence of Oxygen Diffusion in H_2O and D_2O. *The Journal of Physical Chemistry*, 100(13):5597–5602, January 1996.

[143] M. Hangai, T. Murata, N. Miyawaki, C. Spee, J. I. Lim, S. He, D. R. Hinton, and S. J. Ryan. Angiopoietin-1 Upregulation by Vascular Endothelial Growth Factor in Human Retinal Pigment Epithelial Cells. *Investigative Ophthalmology & Visual Science*, 42(7):1617–1625, June 2001.

[144] J. C. Haselgrove, I. M. Shapiro, and S. F. Silverton. Computer modeling of the oxygen supply and demand of cells of the avian growth cartilage. *American Journal of Physiology - Cell Physiology*, 265(2):C497–C506, August 1993.

[145] P. Hay, A. Veitch, M. Smith, R. Cousins, and J. Gaylor. Oxygen Transfer in a Diffusion-Limited Hollow Fiber Bioartificial Liver. *Artificial Organs*, 24(4):278–288, April 2000.

[146] J. A. Haythornthwaite and L. M. Benrud-Larson. Psychological aspects of neuropathic pain. *The Clinical Journal of Pain*, 16(2 Suppl):S101–105, June 2000.

[147] D. v. Heimburg, K. Hemmrich, S. Zachariah, H. Staiger, and N. Pallua. Oxygen consumption in undifferentiated versus differentiated adipogenic mesenchymal precursor cells. *Respiratory Physiology & Neurobiology*, 146(2-3):107–116, April 2005.

[148] W. Heine, K. Conant, J. W. Griffin, and A. Höke. Transplanted neural stem cells promote axonal regeneration through chronically denervated peripheral nerves. *Experimental Neurology*, 189(2):231–240, October 2004.

[149] C.-H. Heldin. Targeting the PDGF signaling pathway in tumor treatment. *Cell Communication and Signaling*, 11(1):97, December 2013.

[150] M. Hellström, L.-K. Phng, and H. Gerhardt. VEGF and Notch Signaling: The Yin and Yang of Angiogenic Sprouting. *Cell Adhesion & Migration*, 1(3):133–136, 2007.

[151] M. Hellström, L.-K. Phng, J. J. Hofmann, E. Wallgard, L. Coultas, P. Lindblom, J. Alva, A.-K. Nilsson, L. Karlsson, N. Gaiano, K. Yoon, J. Rossant, M. L. Iruela-Arispe, M. Kalén, H. Gerhardt, and C. Betsholtz. Dll4 signalling through Notch1 regulates formation of tip cells during angiogenesis. *Nature*, 445(7129):776–780, February 2007.

[152] C. E. Hill, A. Hurtado, B. Blits, B. A. Bahr, P. M. Wood, M. B. Bunge, and M. Oudega. Early necrosis and apoptosis of Schwann cells transplanted into the injured rat spinal cord. *European Journal of Neuroscience*, 26(6):1433–1445, September 2007.

[153] M. I. Hobson, R. Brown, C. J. Green, and G. Terenghi. Interrelationships between angiogenesis and nerve regeneration: a histochemical study. *British Journal of Plastic Surgery*, 50(2):125–131, February 1997.

[154] D. I. Holmes and I. Zachary. The vascular endothelial growth factor (VEGF) family: angiogenic factors in health and disease. *Genome Biology*, 6(2):209, 2005.

[155] B. Holmquist, M. Kanje, J. M. Kerns, and N. Danielsen. A mathematical model for regeneration rate and initial delay following surgical repair of peripheral nerves. *Journal of Neuroscience Methods*, 48(1-2):27–33, June 1993.

[156] M. S. Hossain, D. J. Bergstrom, and X. B. Chen. A mathematical model and computational framework for three-dimensional chondrocyte cell growth in a porous tissue scaffold placed inside a bi-directional flow perfusion bioreactor. *Biotechnology and Bioengineering*, 112(12):2601–2610, December 2015.

[157] K. A. Houck, D. W. Leung, A. M. Rowland, J. Winer, and N. Ferrara. Dual regulation of vascular endothelial growth factor bioavailability by genetic and proteolytic mechanisms. *Journal of Biological Chemistry*, 267(36):26031–26037, December 1992.

[158] R. Hsu and T. W. Secomb. A Green's function method for analysis of oxygen delivery to tissue by microvascular networks. *Mathematical Biosciences*, 96(1):61–78, September 1989.

[159] S. Hsu, R. Thakar, D. Liepmann, and S. Li. Effects of shear stress on endothelial cell haptotaxis on micropatterned surfaces. *Biochemical and Biophysical Research Communications*, 337(1):401–409, November 2005.

[160] J. Hu, Q.-T. Zhu, X.-L. Liu, Y.-b. Xu, and J.-K. Zhu. Repair of extended peripheral nerve lesions in rhesus monkeys using acellular allogenic nerve grafts implanted with autologous mesenchymal stem cells. *Experimental Neurology*, 204(2):658–666, April 2007.

[161] M. E. Hubbi and G. L. Semenza. Regulation of cell proliferation by hypoxia-inducible factors. *American Journal of Physiology - Cell Physiology*, 309(12):C775–C782, December 2015.

[162] D. E. Ingber. Fibronectin controls capillary endothelial cell growth by modulating cell shape. *Proceedings of the National Academy of Sciences of the United States of America*, 87(9):3579–3583, May 1990.

[163] H. Itosaka, S. Kuroda, H. Shichinohe, H. Yasuda, S. Yano, S. Kamei, R. Kawamura, K. Hida, and Y. Iwasaki. Fibrin matrix provides a suitable scaffold for bone marrow stromal cells transplanted into injured

spinal cord: A novel material for CNS tissue engineering. *Neuropathology*, 29(3):248–257, June 2009.

[164] N. Iversen and B. B. Jørgensen. Diffusion coefficients of sulfate and methane in marine sediments: Influence of porosity. *Geochimica et Cosmochimica Acta*, 57(3):571–578, February 1993.

[165] E. Jabbarzadeh and C. F. Abrams. Strategies to Enhance Capillary Formation Inside Biomaterials: A Computational Study. *Tissue Engineering*, 13(8):2073–2086, August 2007.

[166] H. V. Jain and T. L. Jackson. A Hybrid Model of the Role of VEGF Binding in Endothelial Cell Migration and Capillary Formation. *Frontiers in Oncology*, 3, May 2013.

[167] L. Jakobsson, C. A. Franco, K. Bentley, R. T. Collins, B. Ponsioen, I. M. Aspalter, I. Rosewell, M. Busse, G. Thurston, A. Medvinsky, S. Schulte-Merker, and H. Gerhardt. Endothelial cells dynamically compete for the tip cell position during angiogenic sprouting. *Nature Cell Biology*, 12(10):943–953, October 2010.

[168] M. Jeansson, A. Gawlik, G. Anderson, C. Li, D. Kerjaschki, M. Henkelman, and S. E. Quaggin. Angiopoietin-1 is essential in mouse vasculature during development and in response to injury. *The Journal of Clinical Investigation*, 121(6):2278–2289, June 2011.

[169] C.-B. Jenq and R. E. Coggeshall. Nerve regeneration through holey silicone tubes. *Brain Research*, 361(1-2):233–241, December 1985.

[170] C.-B. Jenq and R. E. Coggeshall. Permeable tubes increase the length of the gap that regenerating axons can span. *Brain Research*, 408(1-2):239–242, April 1987.

[171] C.-B. Jenq, L. L. Jenq, and R. E. Coggeshall. Nerve regenera-

tion changes with filters of different pore size. *Experimental Neurology*, 97(3):662–671, September 1987.

[172] K. R. Jessen and R. Mirsky. The repair Schwann cell and its function in regenerating nerves. *The Journal of Physiology*, 594(13):3521–3531, July 2016.

[173] R. Jeyaraj, N. G, G. Kirby, J. Rajadas, A. Mosahebi, A. M. Seifalian, and A. Tan. Vascularisation in regenerative therapeutics and surgery. *Materials Science and Engineering: C*, 54:225–238, September 2015.

[174] J. W. Ji, F. Mac Gabhann, and A. S. Popel. Skeletal muscle VEGF gradients in peripheral arterial disease: simulations of rest and exercise. *American Journal of Physiology - Heart and Circulatory Physiology*, 293(6):H3740–H3749, December 2007.

[175] H. Jia, Y. Wang, X.-J. Tong, G.-B. Liu, Q. Li, L.-X. Zhang, and X.-H. Sun. Sciatic nerve repair by acellular nerve xenografts implanted with BMSCs in rats xenograft combined with BMSCs. *Synapse*, 66(3):256–269, March 2011.

[176] B. H. Jiang, G. L. Semenza, C. Bauer, and H. H. Marti. Hypoxia-inducible factor 1 levels vary exponentially over a physiologically relevant range of O_2 tension. *American Journal of Physiology - Cell Physiology*, 271(4):C1172–C1180, October 1996.

[177] A. Jones, H. Byrne, J. Gibson, and J. Dold. A mathematical model of the stress induced during avascular tumour growth. *Journal of Mathematical Biology*, 40(6):473–499, June 2000.

[178] S. N. Jorgensen and J. R. Sanders. Mathematical models of wound healing and closure: a comprehensive review. *Medical & Biological Engineering & Computing*, 54(9):1297–1316, September 2016.

[179] W. Jurecka, H. P. Ammerer, and H. Lassmann. Regeneration of a transected peripheral nerve. An autoradiographic and electron microscopic study. *Acta Neuropathologica*, 32(4):299–312, October 1975.

[180] N. Kakudo, N. Morimoto, T. Ogawa, S. Taketani, and K. Kusumoto. Hypoxia Enhances Proliferation of Human Adipose-Derived Stem Cells via HIF-1α Activation. *PLoS ONE*, 10(10):e0139890, October 2015.

[181] P. K. Kallio and M. Vastamäki. An analysis of the results of late reconstruction of 132 median nerves. *The Journal of Hand Surgery: British & European Volume*, 18(1):97–105, February 1993.

[182] M. R. Kano, Y. Morishita, C. Iwata, S. Iwasaka, T. Watabe, Y. Ouchi, K. Miyazono, and K. Miyazawa. VEGF-A and FGF-2 synergistically promote neoangiogenesis through enhancement of endogenous PDGF-B-PDGFRβ signaling. *Journal of Cell Science*, 118(16):3759–3768, August 2005.

[183] H. M. Kaplan, P. Mishra, and J. Kohn. The overwhelming use of rat models in nerve regeneration research may compromise designs of nerve guidance conduits for humans. *Journal of Materials Science: Materials in Medicine*, 26(8), August 2015.

[184] J. B. Kearney. The VEGF receptor flt-1 (VEGFR-1) is a positive modulator of vascular sprout formation and branching morphogenesis. *Blood*, 103(12):4527–4535, February 2004.

[185] S. Kehoe, X. Zhang, and D. Boyd. FDA approved guidance conduits and wraps for peripheral nerve injury: A review of materials and efficacy. *Injury*, 43(5):553–572, May 2012.

[186] J. M. Kelm, C. Diaz Sanchez-Bustamante, E. Ehler, S. P. Hoerstrup, V. Djonov, L. Ittner, and M. Fussenegger. VEGF profiling and angiogenesis in human microtissues. *Journal of Biotechnology*, 118(2):213–229, August 2005.

[187] D. Kim, S. Connolly, S. Zhao, R. Beuerman, R. Voorhies, and D. Kline. Comparison of Macropore, Semipermeable, and Nonpermeable Collagen Conduits in Nerve Repair. *Journal of Reconstructive Microsurgery*, 9(6):415–420, November 1993.

[188] P. J. Kingham, D. F. Kalbermatten, D. Mahay, S. J. Armstrong, M. Wiberg, and G. Terenghi. Adipose-derived stem cells differentiate into a Schwann cell phenotype and promote neurite outgrowth in vitro. *Experimental Neurology*, 207(2):267–274, October 2007.

[189] J. Kleinheinz, S. Jung, K. Wermker, C. Fischer, and U. Joos. Release kinetics of $VEGF_{165}$ from a collagen matrix and structural matrix changes in a circulation model. *Head & Face Medicine*, 6:17, July 2010.

[190] P. G. Klemens. Thermal conductivity of composites. *International Journal of Thermophysics*, 11(5):6, September 1990.

[191] A. Köhn-Luque, W. de Back, Y. Yamaguchi, K. Yoshimura, M. A. Herrero, and T. Miura. Dynamics of VEGF matrix-retention in vascular network patterning. *Physical Biology*, 10(6):066007, December 2013.

[192] L. E. Kokai, Y.-C. Lin, N. M. Oyster, and K. G. Marra. Diffusion of soluble factors through degradable polymer nerve guides: Controlling manufacturing parameters. *Acta Biomaterialia*, 5(7):2540–2550, September 2009.

[193] E. Kon, A. Roffi, G. Filardo, G. Tesei, and M. Marcacci. Scaffold-Based Cartilage Treatments: With or Without Cells? A Systematic Review of Preclinical and Clinical Evidence. *Arthroscopy: The Journal of Arthroscopic & Related Surgery*, 31(4):767–775, April 2015.

[194] J. A. Kouyoumdjian. Peripheral nerve injuries: A retrospective survey of 456 cases. *Muscle & Nerve*, 34(6):785–788, December 2006.

[195] F. Kreuzer. Oxygen supply to tissues: The Krogh model and its assumptions. *Experientia*, 38(12):1415–1426, December 1982.

[196] B. L. Krock, N. Skuli, and M. C. Simon. Hypoxia-Induced Angiogenesis: Good and Evil. *Genes & Cancer*, 2(12):1117–1133, December 2011.

[197] A. Krogh. The number and distribution of capillaries in muscles with calculations of the oxygen pressure head necessary for supplying the tissue. *The Journal of Physiology*, 52(6):409–415, May 1919.

[198] H. Kumar and D.-K. Choi. Hypoxia Inducible Factor Pathway and Physiological Adaptation: A Cell Survival Pathway?, 2015.

[199] C. Kut, F. Mac Gabhann, and A. S. Popel. Where is VEGF in the body? A meta-analysis of VEGF distribution in cancer. *British Journal of Cancer*, 97(7):978–985, October 2007.

[200] K. Kuwabara, S. Ogawa, M. Matsumoto, S. Koga, M. Clauss, D. J. Pinsky, P. Lyn, J. Leavy, L. Witte, and J. Joseph-Silverstein. Hypoxia-mediated induction of acidic/basic fibroblast growth factor and platelet-derived growth factor in mononuclear phagocytes stimulates growth of hypoxic endothelial cells. *Proceedings of the National Academy of Sciences of the United States of America*, 92(10):4606–4610, May 1995.

[201] A. Lafosse, C. Dufeys, C. Beauloye, S. Horman, and D. Dufrane. Impact of Hyperglycemia and Low Oxygen Tension on Adipose-Derived Stem Cells Compared with Dermal Fibroblasts and Keratinocytes: Importance for Wound Healing in Type 2 Diabetes. *PLoS ONE*, 11(12):e0168058, December 2016.

[202] T. D. Lagerlund and P. A. Low. Mathematical modeling of time-dependent oxygen transport in rat peripheral nerve. *Computers in Biology and Medicine*, 23(1):29–47, January 1993.

[203] E. S. Lai, N. F. Huang, J. P. Cooke, and G. G. Fuller. Aligned Nanofibrillar Collagen Regulates Endothelial Organization and Migration. *Regenerative Medicine*, 7(5):649–661, September 2012.

[204] L. Lamalice, F. Le Boeuf, and J. Huot. Endothelial Cell Migration During Angiogenesis. *Circulation Research*, 100(6):782–794, March 2007.

[205] K. A. Landman and A. Q. Cai. Cell Proliferation and Oxygen Diffusion in a Vascularising Scaffold. *Bulletin of Mathematical Biology*, 69(7):2405–2428, October 2007.

[206] R. Langer and J. P. Vacanti. Tissue engineering. *Science*, 260(5110):920–926, May 1993.

[207] R. Lanza, R. Langer, and J. P. Vacanti. *Principles of Tissue Engineering*. Academic Press, 2013.

[208] M. W. Laschke, Y. Harder, M. Amon, I. Martin, J. Farhadi, A. Ring, N. Torio-Padron, R. Schramm, M. Rücker, D. Junker, J. M. Häufel, C. Carvalho, M. Heberer, G. Germann, B. Vollmar, and M. D. Menger. Angiogenesis in Tissue Engineering: Breathing Life into Constructed Tissue Substitutes. *Tissue Engineering*, 12(8):2093–2104, August 2006.

[209] M. Laschke, A. Elitzsch, B. Vollmar, P. Vajkoczy, and M. Menger. Combined inhibition of vascular endothelial growth factor (VEGF), fibroblast growth factor and platelet-derived growth factor, but not inhibition of VEGF alone, effectively suppresses angiogenesis and vessel maturation in endometriotic lesions. *Human Reproduction*, 21(1):262–268, January 2006.

[210] S. K. Lee and S. W. Wolfe. Peripheral nerve injury and repair. *The Journal of the American Academy of Orthopaedic Surgeons*, 8(4):243–252, August 2000.

[211] J. T. Leith and S. Michelson. Secretion rates and levels of vascular endothelial growth factor in clone A or HCT-8 human colon tumour cells as a function of oxygen concentration. *Cell Proliferation*, 28(8):415–430, August 1995.

[212] G. Lemon, J. R. King, H. M. Byrne, O. E. Jensen, and K. M. Shakesheff. Mathematical modelling of engineered tissue growth using a multiphase porous flow mixture theory. *Journal of Mathematical Biology*, 52(5):571–594, May 2006.

[213] G. Lemon, S. L. Waters, F. R. Rose, and J. R. King. Mathematical modelling of human mesenchymal stem cell proliferation and differentiation inside artificial porous scaffolds. *Journal of Theoretical Biology*, 249(3):543–553, December 2007.

[214] G. Lemon, D. Howard, M. J. Tomlinson, L. D. Buttery, F. R. A. J. Rose, S. L. Waters, and J. R. King. Mathematical modelling of tissue-engineered angiogenesis. *Mathematical Biosciences*, 221(2):101–120, October 2009.

[215] A. Lenard, E. Ellertsdottir, L. Herwig, A. Krudewig, L. Sauteur, H.-G. Belting, and M. Affolter. In Vivo Analysis Reveals a Highly Stereotypic Morphogenetic Pathway of Vascular Anastomosis. *Developmental Cell*, 25(5):492–506, June 2013.

[216] H. A. Levine, S. Pamuk, B. D. Sleeman, and M. Nilsen-Hamilton. Mathematical Modeling of Capillary Formation and Development in Tumor Angiogenesis: Penetration into the Stroma. *Bulletin of Mathematical Biology*, 63(5):801–863, September 2001.

[217] M. C. Lewis, B. D. MacArthur, J. Malda, G. Pettet, and C. P. Please. Heterogeneous proliferation within engineered cartilaginous tissue: the role of oxygen tension. *Biotechnology and Bioengineering*, 91(5):607–615, September 2005.

[218] S.-T. Li, S. J. Archibald, C. Krarup, and R. D. Madison. Peripheral nerve repair with collagen conduits. *Clinical Materials*, 9(3):195–200, 1992.

[219] S. Li, S. Bhatia, Y.-L. Hu, Y.-T. Shiu, Y.-S. Li, S. Usami, and S. Chien. Effects of morphological patterning on endothelial cell migration. *Biorheology*, 38(2):101–108, 2001.

[220] S. Liekens, E. De Clercq, and J. Neyts. Angiogenesis: regulators and clinical applications. *Biochemical Pharmacology*, 61(3):253–270, February 2001.

[221] P. Lindahl, B. R. Johansson, P. Levéen, and C. Betsholtz. Pericyte Loss and Microaneurysm Formation in PDGF-B-Deficient Mice. *Science*, 277(5323):242–245, July 1997.

[222] P. Lindblom, H. Gerhardt, S. Liebner, A. Abramsson, M. Enge, M. Hellström, G. Bäckström, S. Fredriksson, U. Landegren, H. C. Nyström, G. Bergström, E. Dejana, A. Östman, P. Lindahl, and C. Betsholtz. Endothelial PDGF-B retention is required for proper investment of pericytes in the microvessel wall. *Genes & Development*, 17(15):1835–1840, August 2003.

[223] G. Liu, A. A. Qutub, P. Vempati, F. Mac Gabhann, and A. S. Popel. Module-based multiscale simulation of angiogenesis in skeletal muscle. *Theoretical Biology & Medical Modelling*, 8:6, April 2011.

[224] L. Liu, J. Wang, S. Duan, L. Chen, H. Xiang, Y. Dong, and W. Wang. Systematic evaluation of sericin protein as a substitute for fetal bovine serum in cell culture. *Scientific Reports*, 6(1):1–10, August 2016.

[225] A. V. Ljubimov. Growth Factor Synergy in Angiogenesis. In J. Penn, editor, *Retinal and Choroidal Angiogenesis*, pages 289–310. Springer Netherlands, Dordrecht, 2008.

[226] I. B. Lobov, P. C. Brooks, and R. A. Lang. Angiopoietin-2 displays VEGF-dependent modulation of capillary structure and endothelial cell survival *in vivo*. *Proceedings of the National Academy of Sciences of the United States of America*, 99(17):11205–11210, August 2002.

[227] G. Lundborg and H. A. Hansson. Nerve regeneration through preformed pseudosynovial tubes: a preliminary report of a new experimental model for studying the regeneration and reorganization capacity of peripheral nerve tissue. *The Journal of Hand Surgery*, 5(1):35–38, 1980.

[228] G. Lundborg. Nerve injury and repair–a challenge to the plastic brain. *Journal of the Peripheral Nervous System*, 8(4):209–226, December 2003.

[229] F. Mac Gabhann and A. S. Popel. Dimerization of VEGF receptors and implications for signal transduction: a computational study. *Biophysical Chemistry*, 128(2-3):125–139, July 2007.

[230] F. Mac Gabhann, M. T. Yang, and A. S. Popel. Monte Carlo simulations of VEGF binding to cell surface receptors in vitro. *Biochimica et Biophysica Acta (BBA) - Molecular Cell Research*, 1746(2):95–107, December 2005.

[231] F. Mac Gabhann, J. W. Ji, and A. S. Popel. Multi-scale Computational Models of Pro-angiogenic Treatments in Peripheral Arterial Disease. *Annals of Biomedical Engineering; New York*, 35(6):982–994, June 2007.

[232] F. Mac Gabhann, J. W. Ji, and A. S. Popel. VEGF gradients, receptor activation, and sprout guidance in resting and exercising skeletal muscle. *Journal of Applied Physiology*, 102(2):722–734, February 2007.

[233] F. Mackenzie and C. Ruhrberg. Diverse roles for VEGF-A in the nervous system. *Development*, 139(8):1371–1380, April 2012.

[234] S. Madduri and B. Gander. Schwann cell delivery of neurotrophic factors for peripheral nerve regeneration. *Journal of the Peripheral Nervous System*, 15(2):93–103, June 2010.

[235] S. Madduri and B. Gander. Growth factor delivery systems and repair strategies for damaged peripheral nerves. *Journal of Controlled Release*, 161(2):274–282, July 2012.

[236] S. A. Maggelakis and A. E. Savakis. A mathematical model of growth factor induced capillary growth in the retina. *Mathematical and Computer Modelling*, 24(7):33–41, October 1996.

[237] A. N. Makanya, R. Hlushchuk, and V. G. Djonov. Intussusceptive angiogenesis and its role in vascular morphogenesis, patterning, and remodeling. *Angiogenesis*, 12(2):113–123, June 2009.

[238] J. Malda, J. Rouwkema, D. E. Martens, E. P. le Comte, F. K. Kooy, J. Tramper, C. A. van Blitterswijk, and J. Riesle. Oxygen Gradients in Tissue-Engineered PEGT/PBT Cartilaginous Constructs: Measurement and Modeling. *Biotechnology and Bioengineering*, 86(1):9–18, April 2004.

[239] J. Malda, P. van den Brink, P. Meeuwse, M. Grojec, D. Martens, J. Tramper, J. Riesle, and C. van Blitterswijk. Effect of Oxygen Tension on Adult Articular Chondrocytes in Microcarrier Bioreactor Culture. *Tissue Engineering*, 10(7-8):987–994, July 2004.

[240] S. B. Mamer, S. Chen, J. C. Weddell, A. Palasz, A. Wittenkeller, M. Kumar, and P. I. Imoukhuede. Discovery of High-Affinity PDGF-VEGFR Interactions: Redefining RTK Dynamics. *Scientific Reports*, 1(7):16439, November 2017.

[241] C. Mantovani, D. Mahay, M. Kingham, G. Terenghi, S. G. Shawcross, and M. Wiberg. Bone marrow- and adipose-derived stem cells show expression of myelin mRNAs and proteins. *Regenerative Medicine*, 5(3):403–410, May 2010.

[242] N. V. Mantzaris, S. Webb, and H. G. Othmer. Mathematical modeling of tumor-induced angiogenesis. *Journal of Mathematical Biology*, 49(2):111–187, February 2004.

[243] C. Marchesi, M. Pluderi, F. Colleoni, M. Belicchi, M. Meregalli, A. Farini, D. Parolini, L. Draghi, M. E. Fruguglietti, M. Gavina, L. Porretti, A. Cattaneo, M. Battistelli, A. Prelle, M. Moggio, S. Borsa, L. Bello, D. Spagnoli, S. M. Gaini, M. C. Tanzi, N. Bresolin, N. Grimoldi, and Y. Torrente. Skin-Derived Stem Cells Transplanted into Resorbable Guides Provide Functional Nerve Regeneration After Sciatic Nerve Resection. *Glia*, 55(4):425–438, March 2007.

[244] R. E. Marcus. The effect of low oxygen concentration on growth, glycolysis, and sulfate incorporation by articular chondrocytes in monolayer culture. *Arthritis & Rheumatism*, 16(5):646–656, September 1973.

[245] J. C. Maxwell. *A treatise on electricity and magnetism*. Clarendon Press, London, 1837.

[246] M. Mazzone, D. Dettori, R. L. de Oliveira, S. Loges, T. Schmidt, B. Jonckx, Y.-M. Tian, A. A. Lanahan, P. Pollard, C. R. de Almodovar, F. De Smet, S. Vinckier, J. Aragonés, K. Debackere, A. Luttun, S. Wyns, B. Jordan, A. Pisacane, B. Gallez, M. G. Lampugnani, E. Dejana, M. Simons, P. Ratcliffe, P. Maxwell, and P. Carmeliet. Heterozygous Deficiency of *PHD2* Restores Tumor Oxygenation and Inhibits Metastasis via Endothelial Normalization. *Cell*, 136(5):839–851, March 2009.

[247] R. M. R. McAllister, S. E. A. Gilbert, J. S. Calder, and P. J. Smith. The epidemiology and management of upper limb peripheral nerve injuries in modern practice. *Journal of Hand Surgery*, 21(1):4–13, February 1996.

[248] A. I. McClatchey and A. S. Yap. Contact inhibition (of proliferation) redux. *Current Opinion in Cell Biology*, 24(5):685–694, October 2012.

[249] S. R. McDougall, A. R. A. Anderson, M. A. J. Chaplain, and J. A. Sherratt. Mathematical Modelling of Flow Through Vascular Networks: Implications for Tumour-induced Angiogenesis and Chemotherapy Strategies. *Bulletin of Mathematical Biology*, 64(4):673–702, July 2002.

[250] S. R. McDougall, A. R. Anderson, and M. A. Chaplain. Mathematical modelling of dynamic adaptive tumour-induced angiogenesis: Clinical implications and therapeutic targeting strategies. *Journal of Theoretical Biology*, 241(3):564–589, August 2006.

[251] S. R. McDougall, M. G. Watson, A. H. Devlin, C. A. Mitchell, and M. A. J. Chaplain. A hybrid discrete-continuum mathematical model of pattern prediction in the developing retinal vasculature. *Bulletin of Mathematical Biology*, 74(10):2272–2314, October 2012.

[252] M. F. Meek and W. F. A. Den Dunnen. Porosity of the wall of a Neurolac® nerve conduit hampers nerve regeneration. *Microsurgery*, 29(6):473–478, January 2009.

[253] N. Mehio, S. Dai, and D.-e. Jiang. Quantum Mechanical Basis for Kinetic Diameters of Small Gaseous Molecules. *The Journal of Physical Chemistry A*, 118(6):1150–1154, February 2014.

[254] R. S. Mellick and J. B. Cavanagh. Changes in Blood Vessel Permeability During Degeneration and Regeneration in Peripheral Nerves. *Brain*, 91(1):141–160, March 1968.

[255] S. J. Mentzer and M. A. Konerding. Intussusceptive Angiogenesis: Expansion and Remodeling of Microvascular Networks. *Angiogenesis*, 17(3):499–509, July 2014.

[256] R. M. H. Merks, S. V. Brodsky, M. S. Goligorksy, S. A. Newman, and J. A. Glazier. Cell elongation is key to in silico replication of in vitro vasculogenesis and subsequent remodeling. *Developmental Biology*, 289(1):44–54, January 2006.

[257] R. M. H. Merks, E. D. Perryn, A. Shirinifard, and J. A. Glazier. Contact-Inhibited Chemotaxis in De Novo and Sprouting Blood-Vessel Growth. *PLoS Computational Biology*, 4(9):e1000163, September 2008.

[258] J. Metzcar, Y. Wang, R. Heiland, and P. Macklin. A Review of Cell-Based Computational Modeling in Cancer Biology. *JCO Clinical Cancer Informatics*, (3):1–13, February 2019.

[259] G. J. Mick, X. Wang, and K. McCormick. White Adipocyte Vascular Endothelial Growth Factor: Regulation by Insulin. *Endocrinology*, 143(3):948–953, March 2002.

[260] F. Milde, M. Bergdorf, and P. Koumoutsakos. A Hybrid Model for Three-Dimensional Simulations of Sprouting Angiogenesis. *Biophysical Journal*, 95(7):3146–3160, October 2008.

[261] R. J. Millington and J. P. Quirk. Permeability of porous solids. *Transactions of the Faraday Society*, 57:1200–1207, 1961.

[262] A. Minchenko, T. Bauer, S. Salceda, and J. Caro. Hypoxic stimulation of vascular endothelial growth factor expression in vitro and in vivo. *Laboratory Investigation*, 71(3):374–379, September 1994.

[263] S. Missios, K. Bekelis, and R. J. Spinner. Traumatic peripheral nerve injuries in children: epidemiology and socioeconomics. *Journal of Neurosurgery: Pediatrics*, 14(6):688–694, October 2014.

[264] A. Mosahebi, B. Woodward, M. Wiberg, R. Martin, and G. Terenghi. Retroviral labeling of Schwann cells: In vitro characterization and in vivo transplantation to improve peripheral nerve regeneration. *Glia*, 34(1):8–17, March 2001.

[265] A. Muheremu and Q. Ao. Past, present, and future of nerve conduits in the treatment of peripheral nerve injury. *BioMed Research International*, 2015, 2015.

[266] D. Mukhopadhyay, L. Tsiokas, X. M. Zhou, D. Foster, J. S. Brugge, and V. P. Sukhatme. Hypoxic induction of human vascular endothelial growth factor expression through c-Src activation. *Nature*, 375(6532):577–581, June 1995.

[267] M. N. Nakatsu and C. C. Hughes. Chapter 4 An Optimized Three-Dimensional In Vitro Model for the Analysis of Angiogenesis. In *Methods in Enzymology*, volume 443, pages 65–82. Elsevier, 2008.

[268] M. N. Nakatsu, R. C. A. Sainson, S. Pérez-del-Pulgar, J. N. Aoto, M. Aitkenhead, K. L. Taylor, P. M. Carpenter, and C. C. W. Hughes. $VEGF_{121}$ and $VEGF_{165}$ Regulate Blood Vessel Diameter Through Vascular Endothelial Growth Factor Receptor 2 in an *in vitro* Angiogenesis Model. *Laboratory Investigation*, 83(12):1873–1885, December 2003.

[269] I. Napoli, L. Noon, S. Ribeiro, A. Kerai, S. Parrinello, L. Rosenberg, M. Collins, M. Harrisingh, I. White, A. Woodhoo, and A. Lloyd. A Central Role for the ERK-Signaling Pathway in Controlling Schwann Cell Plasticity and Peripheral Nerve Regeneration In Vivo. *Neuron*, 73(4):729–742, February 2012.

[270] A. R. Nectow, K. G. Marra, and D. L. Kaplan. Biomaterials for the Development of Peripheral Nerve Guidance Conduits. *Tissue Engineering Part B: Reviews*, 18(1):40–50, February 2012.

[271] J. E. Nesmith, J. C. Chappell, J. G. Cluceru, and V. L. Bautch. Blood vessel anastomosis is spatially regulated by Flt1 during angiogenesis. *Development*, 144(5):889–896, March 2017.

[272] P. G. Newrick, A. J. Wilson, J. Jakubowski, A. J. Boulton, and J. D. Ward. Sural nerve oxygen tension in diabetes. *British Medical Journal (Clinical Research Edition)*, 293(6554):1053–1054, October 1986.

[273] Q. T. Nguyen, J. R. Sanes, and J. W. Lichtman. Pre-existing pathways

promote precise projection patterns. *Nature Neuroscience*, 5(9):861–867, September 2002.

[274] B. Nicholson and S. Verma. Comorbidities in Chronic Neuropathic Pain. *Pain Medicine*, 5(Suppl 1):S9–S27, March 2004.

[275] J. Noble, C. A. Munro, V. S. Prasad, and R. Midha. Analysis of upper and lower extremity peripheral nerve injuries in a population of patients with multiple injuries. *The Journal of Trauma*, 45(1):116–122, July 1998.

[276] K.-A. Norton and A. S. Popel. Effects of endothelial cell proliferation and migration rates in a computational model of sprouting angiogenesis. *Scientific Reports*, 6:36992, November 2016.

[277] E. C. Novosel, C. Kleinhans, and P. J. Kluger. Vascularization is the key challenge in tissue engineering. *Advanced Drug Delivery Reviews*, 63(4–5):300–311, April 2011.

[278] H. Nukada. Post-traumatic endoneurial neovascularization and nerve regeneration: a morphometric study. *Brain Research*, 449(1–2):89–96, May 1988.

[279] S. S. Nunes, K. A. Greer, C. M. Stiening, H. Y. Chen, K. R. Kidd, M. A. Schwartz, C. J. Sullivan, H. Rekapally, and J. B. Hoying. Implanted Microvessels Progress through Distinct Neovascularization Phenotypes. *Microvascular research*, 79(1):10–20, January 2010.

[280] D. A. Núñez. *Experimental estimate of the diffusivity of Vascular Endothelial Growth Factor*. Thesis, Massachusetts Institute of Technology, 2006.

[281] B. Obradovic, J. H. Meldon, L. E. Freed, and G. Vunjak-Novakovic. Glycosaminoglycan deposition in engineered cartilage: Experiments and mathematical model. *AIChE Journal*, 46(9):1860–1871, September 2000.

[282] D. Odedra, L. L. Chiu, M. Shoichet, and M. Radisic. Endothelial cells guided by immobilized gradients of vascular endothelial growth factor

on porous collagen scaffolds. *Acta Biomaterialia*, 7(8):3027–3035, August 2011.

[283] S. H. Oh and J. H. Lee. Fabrication and characterization of hydrophilized porous PLGA nerve guide conduits by a modified immersion precipitation method. *Journal of Biomedical Materials Research Part A*, 80(3):530–538, March 2007.

[284] S. H. Oh, J. H. Kim, K. S. Song, B. H. Jeon, J. H. Yoon, T. B. Seo, U. Namgung, I. W. Lee, and J. H. Lee. Peripheral nerve regeneration within an asymmetrically porous PLGA/Pluronic F127 nerve guide conduit. *Biomaterials*, 29(11):1601–1609, April 2008.

[285] S. Okinaga and A. Nagano. Can vascularization improve the surgical outcome of the intercostal nerve transfer for traumatic brachial plexus palsy? A clinical comparison of vascularized and non-vascularized methods. *Microsurgery*, 19(4):176–180, 1999.

[286] C. O'Leary, J. L. Gilbert, S. O'Dea, F. J. O'Brien, and S.-A. Cryan. Respiratory Tissue Engineering: Current Status and Opportunities for the Future. *Tissue Engineering Part B: Reviews*, 21(4):323–344, August 2015.

[287] L. Olsen, J. A. Sherratt, P. K. Maini, and F. Arnold. A mathematical model for the capillary endothelial cell-extracellular matrix interactions in wound-healing angiogenesis. *IMA Journal of Mathematics Applied in Medicine and Biology*, 14:261–281, December 1997.

[288] H. Orbay, A. C. Uysal, H. Hyakusoku, and H. Mizuno. Differentiated and undifferentiated adipose-derived stem cells improve function in rats with peripheral nerve gaps. *Journal of Plastic, Reconstructive & Aesthetic Surgery*, 65(5):657–664, May 2012.

[289] M. E. Orme and M. A. J. Chaplain. A mathematical model of the first steps of tumour-related angiogenesis: Capillary sprout formation and

secondary branching. *IMA Journal of Mathematics Applied in Medicine & Biology*, 13(2):73–98, June 1996.

[290] M. E. Orme and M. A. J. Chaplain. Two-dimensional models of tumour angjogenesis and anti-angiogenesis strategies. *IMA Journal of Mathematics Applied in Medicine & Biology*, 14(3):189–205, September 1997.

[291] C. O'Rourke, A. G. E. Day, C. Murray-Dunning, L. Thanabalasundaram, J. Cowan, L. Stevanato, N. Grace, G. Cameron, R. A. L. Drake, J. Sinden, and J. B. Phillips. An allogeneic 'off the shelf' therapeutic strategy for peripheral nerve tissue engineering using clinical grade human neural stem cells. *Scientific Reports*, 8(1):2951, February 2018.

[292] M. A. Ostrowski, N. F. Huang, T. W. Walker, T. Verwijlen, C. Poplawski, A. S. Khoo, J. P. Cooke, G. G. Fuller, and A. R. Dunn. Microvascular Endothelial Cells Migrate Upstream and Align Against the Shear Stress Field Created by Impinging Flow. *Biophysical Journal*, 106(2):366–374, January 2014.

[293] M. R. Owen, T. Alarcón, P. K. Maini, and H. M. Byrne. Angiogenesis and vascular remodelling in normal and cancerous tissues. *Journal of Mathematical Biology*, 58(4-5):689–721, April 2009.

[294] M. R. Owen, I. J. Stamper, M. Muthana, G. W. Richardson, J. Dobson, C. E. Lewis, and H. M. Byrne. Mathematical Modeling Predicts Synergistic Antitumor Effects of Combining a Macrophage-Based, Hypoxia-Targeted Gene Therapy with Chemotherapy. *Cancer Research*, 71(8):2826–2837, April 2011.

[295] H.-C. Pan, C.-J. Chen, F.-C. Cheng, S.-P. Ho, M.-J. Liu, S.-M. Hwang, M.-H. Chang, and Y.-C. Wang. Combination of G-CSF Administration and Human Amniotic Fluid Mesenchymal Stem Cell Transplantation Promotes Peripheral Nerve Regeneration. *Neurochemical Research; New York*, 34(3):518–527, March 2009.

[296] J.-A. Park, K.-S. Choi, S.-Y. Kim, and K.-W. Kim. Coordinated interaction of the vascular and nervous systems: from molecule- to cell-based approaches. *Biochemical and Biophysical Research Communications*, 311(2):247–253, November 2003.

[297] J. Parker, N. Mitrousis, and M. S. Shoichet. Hydrogel for simultaneous tunable growth factor delivery and enhanced viability of encapsulated cells in vitro. *Biomacromolecules*, 17(2):476–484, January 2016.

[298] A. Parr, I. Kulbatski, T. Zahir, X. Wang, C. Yue, A. Keating, and C. Tator. Transplanted adult spinal cord-derived neural stem/progenitor cells promote early functional recovery after rat spinal cord injury. *Neuroscience*, 155(3):760–770, August 2008.

[299] S. Parrinello, I. Napoli, S. Ribeiro, P. W. Digby, M. Fedorova, D. B. Parkinson, R. D. S. Doddrell, M. Nakayama, R. H. Adams, and A. C. Lloyd. EphB Signaling Directs Peripheral Nerve Regeneration through Sox2-Dependent Schwann Cell Sorting. *Cell*, 143(1):145–155, October 2010.

[300] V. Patel, G. Joseph, A. Patel, S. Patel, D. Bustin, D. Mawson, L. M. Tuesta, R. Puentes, M. Ghosh, and D. D. Pearse. Suspension Matrices for Improved Schwann-Cell Survival after Implantation into the Injured Rat Spinal Cord. *Journal of Neurotrauma*, 27(5):789–801, May 2010.

[301] N. P. Patel, K. A. Lyon, and J. H. Huang. An update- tissue engineered nerve grafts for the repair of peripheral nerve injuries. *Neural Regeneration Research*, 13(5):764–774, May 2018.

[302] D. D. Pearse, A. R. Sanchez, F. C. Pereira, C. M. Andrade, R. Puzis, Y. Pressman, K. Golden, B. M. Kitay, B. Blits, P. M. Wood, and M. B. Bunge. Transplantation of Schwann cells and/or olfactory ensheathing glia into the contused spinal cord: Survival, migration, axon association, and functional recovery. *Glia*, 55(9):976–1000, July 2007.

[303] J. C. Pelton, C. E. Wright, M. Leitges, and V. L. Bautch. Multiple endothelial cells constitute the tip of developing blood vessels and polarize to promote lumen formation. *Development*, 141(21):4121–4126, November 2014.

[304] G. Penkert, W. Bini, and M. Samii. Revascularization of nerve grafts: an experimental study. *Journal of Reconstructive Microsurgery*, 4(4):319–325, July 1988.

[305] M. S. Pepper, N. Ferrara, L. Orci, and R. Montesano. Potent synergism between vascular endothelial growth factor and basic fibroblast growth factor in the induction of angiogenesis in vitro. *Biochemical and Biophysical Research Communications*, 189(2):824–831, December 1992.

[306] H. Perfahl, H. M. Byrne, T. Chen, V. Estrella, T. Alarcón, A. Lapin, R. A. Gatenby, R. J. Gillies, M. C. Lloyd, P. K. Maini, M. Reuss, and M. R. Owen. Multiscale Modelling of Vascular Tumour Growth in 3D: The Roles of Domain Size and Boundary Conditions. *PLoS ONE*, 6(4), April 2011.

[307] H. Perfahl, B. D. Hughes, T. Alarcón, P. K. Maini, M. C. Lloyd, M. Reuss, and H. M. Byrne. 3D hybrid modelling of vascular network formation. *Journal of Theoretical Biology*, 414:254–268, February 2017.

[308] G. Pettet, H. Byrne, D. McElwain, and J. Norbury. A model of wound-healing angiogenesis in soft tissue. *Mathematical Biosciences*, 136(1):35–63, August 1996.

[309] W. Philipp, L. Speicher, and C. Humpel. Expression of Vascular Endothelial Growth Factor and Its Receptors in Inflamed and Vascularized Human Corneas. *Investigative Ophthalmology & Visual Science*, 41(9):2514–2522, August 2000.

[310] J. B. Phillips and R. Brown. Micro-structured Materials and Mechan-

ical Cues in 3D Collagen Gels. In J. W. Haycock, editor, *3D Cell Culture*, volume 695, pages 183–196. Humana Press, Totowa, NJ, 2011.

[311] J. B. Phillips and B. R. Micro-structured materials and mechanical cues in 3d collagen gels. *Methods in Molecular Biology*, 695:183–96, 2011.

[312] L.-K. Phng and H. Gerhardt. Angiogenesis: A Team Effort Coordinated by Notch. *Developmental Cell*, 16(2):196–208, February 2009.

[313] L.-K. Phng, F. Stanchi, and H. Gerhardt. Filopodia are dispensable for endothelial tip cell guidance. *Development*, 140(19):4031–4040, October 2013.

[314] C. Picioreanu, M. C. M. van Loosdrecht, and J. J. Heijnen. A New Combined Differential-Discrete Cellular Automaton Approach for Biofilm Modeling: Application for Growth in Gel Beads. *Biotechnology and Bioengineering*, 57(6):718–731, March 1998.

[315] E. A. Pierce, E. D. Foley, and L. E. Smith. Regulation of vascular endothelial growth factor by oxygen in a model of retinopathy of prematurity. *Archives of Ophthalmology*, 114(10):1219–1228, October 1996.

[316] L. Pisani. Simple Expression for the Tortuosity of Porous Media. *Transport in Porous Media*, 88(2):193–203, February 2011.

[317] R. J. Podhajsky and R. R. Myers. The vascular response to nerve transection: neovascularization in the silicone nerve regeneration chamber. *Brain Research*, 662(1-2):88–94, October 1994.

[318] R. J. Podhajsky and R. R. Myers. A diffusion-reaction model of nerve regeneration. *Journal of Neuroscience Methods*, 60(1-2):79–88, August 1995.

[319] J. V. Pohlmeyer, S. L. Waters, and L. J. Cummings. Mathematical Model of Growth Factor Driven Haptotaxis and Proliferation in a Tissue Engineering Scaffold. *Bulletin of Mathematical Biology*, 75(3):393–427, March 2013.

[320] A. S. Popel. Theory of oxygen transport to tissue. *Critical Reviews in Biomedical Engineering*, 17(3):257–321, 1989.

[321] Prockop D J. "Stemness" Does Not Explain the Repair of Many Tissues by Mesenchymal Stem/Multipotent Stromal Cells (MSCs). *Clinical Pharmacology & Therapeutics*, 82(3):241–243, September 2007.

[322] B. Prpa, P. M. Huddleston, K. An, and M. B. Wood. Revascularization of nerve grafts: a qualitative and quantitative study of the soft-tissue bed contributions to blood flow in canine nerve grafts. *The Journal of Hand Surgery*, 27(6):1041–1047, November 2002.

[323] M. Quintard and S. Whitaker. Convection, dispersion, and interfacial transport of contaminants: Homogeneous porous media. *Advances in Water Resources*, 17(4):221–239, January 1994.

[324] M. Quintard and S. Whitaker. Coupled, nonlinear mass transfer and heterogeneous reaction in porous media. In K. Vafai, editor, *Handbook of Porous Media*, chapter 1, pages 3–37. Taylor & Francis Group, LLC, Boca Raton, FL, USA, 2005.

[325] A. A. Qutub and A. S. Popel. Elongation, proliferation & migration differentiate endothelial cell phenotypes and determine capillary sprouting. *BMC Systems Biology*, 3(1):13, January 2009.

[326] M. Raica and A. M. Cimpean. Platelet-Derived Growth Factor (PDGF)/PDGF Receptors (PDGFR) Axis as Target for Antitumor and Antiangiogenic Therapy. *Pharmaceuticals*, 3(3):572–599, March 2010.

[327] S. Ramakrishnan, V. Anand, and S. Roy. Vascular Endothelial growth factor signaling in hypoxia and Inflammation. *Journal of Neuroimmune Pharmacology*, 9(2):142–160, March 2014.

[328] R. Rangarajan and M. H. Zaman. Modeling cell migration in 3D. *Cell Adhesion & Migration*, 2(2):106–109, April 2008.

[329] S. Razaq, R. Yasmeen, A. W. Butt, N. Akhtar, and S. N. Mansoor. The pattern of peripheral nerve injuries among Pakistani soldiers in the war against terror. *Journal of the College of Physicians and Surgeons–Pakistan: JCPSP*, 25(5):363–366, May 2015.

[330] M. Redza-Dutordoir and D. A. Averill-Bates. Activation of apoptosis signalling pathways by reactive oxygen species. *Biochimica et Biophysica Acta (BBA) - Molecular Cell Research*, 1863(12):2977–2992, December 2016.

[331] D. Ribatti and E. Crivellato. "Sprouting angiogenesis", a reappraisal. *Developmental Biology*, 372(2):157–165, December 2012.

[332] H. Rieger and M. Welter. Integrative models of vascular remodeling during tumor growth. *Wiley Interdisciplinary Reviews: Systems Biology and Medicine*, 7(3):113–129, May 2015.

[333] A. M. Robertson, C. Huxley, R. H. M. King, and P. K. Thomas. Development of early postnatal peripheral nerve abnormalities in Trembler-J and PMP22 transgenic mice. *Journal of Anatomy*, 195(3):331–339, October 1999.

[334] H. E. Rosberg, K. S. Carlsson, S. Högård, B. Lindgren, G. Lundborg, and L. B. Dahlin. Injury to the human median and ulnar nerves in the forearm–analysis of costs for treatment and rehabilitation of 69 patients in southern Sweden. *Journal of Hand Surgery: British & European Volume*, 30(1):35–39, February 2005.

[335] C. Ruhrberg, H. Gerhardt, M. Golding, R. Watson, S. Ioannidou, H. Fujisawa, C. Betsholtz, and D. T. Shima. Spatially restricted patterning cues provided by heparin-binding VEGF-A control blood vessel branching morphogenesis. *Genes & Development*, 16(20):2684–2698, October 2002.

[336] G. E. Rutkowski and C. A. Heath. Development of a Bioartificial

Nerve Graft. I. Design Based on a Reaction-Diffusion Model. *Biotechnology Progress*, 18(2):362–372, March 2002.

[337] G. E. Rutkowski and C. A. Heath. Development of a Bioartificial Nerve Graft. II. Nerve Regeneration in Vitro. *Biotechnology Progress*, 18(2):373–379, March 2002.

[338] R. Sacco, P. Causin, P. Zunino, and M. T. Raimondi. A multiphysics/multiscale 2D numerical simulation of scaffold-based cartilage regeneration under interstitial perfusion in a bioreactor. *Biomechanics and Modeling in Mechanobiology*, 10(4):577–589, July 2011.

[339] R. C. A. Sainson, J. Aoto, M. N. Nakatsu, M. T. Holderfield, E. M. Conn, E. S. H. Koller, and C. C. W. Hughes. Cell-autonomous notch signaling regulates endothelial cell branching and proliferation during vascular tubulogenesis. *The FASEB Journal*, 19(8):1027–1029, June 2005.

[340] K. Sanen, W. Martens, M. Georgiou, M. Ameloot, I. Lambrichts, and J. Phillips. Engineered neural tissue with Schwann cell differentiated human dental pulp stem cells: potential for peripheral nerve repair? *Journal of Tissue Engineering and Regenerative Medicine*, 11(12):3362–3372, December 2017.

[341] J. A. Sanz-Herrera, J. M. Garcia-Aznar, and M. Doblaré. A mathematical approach to bone tissue engineering. *Philosophical Transactions of the Royal Society A: Mathematical, Physical and Engineering Sciences*, 367(1895):2055–2078, May 2009.

[342] M. D. Sarker, X. B. Chen, and D. J. Schreyer. Experimental approaches to vascularisation within tissue engineering constructs. *Journal of Biomaterials Science: Polymer Edition*, 26(12):683–734, August 2015.

[343] M. Sarker, S. Naghieh, A. D. McInnes, D. J. Schreyer, and X. Chen. Strategic Design and Fabrication of Nerve Guidance Conduits for Pe-

ripheral Nerve Regeneration. *Biotechnology Journal*, 13(7):1700635, July 2018.

[344] M. Scianna, L. Preziosi, and K. Wolf. A Cellular Potts model simulating cell migration on and in matrix environments. *Mathematical Biosciences and Engineering*, 10(1):235–261, February 2013.

[345] T. Secomb, R. Hsu, N. Beamer, and B. Coull. Theoretical Simulation of Oxygen Transport to Brain by Networks of Microvessels: Effects of Oxygen Supply and Demand on Tissue Hypoxia. *Microcirculation*, 7(4):237–247, August 2000.

[346] T. W. Secomb, R. Hsu, E. Y. H. Park, and M. W. Dewhirst. Green's Function Methods for Analysis of Oxygen Delivery to Tissue by Microvascular Networks. *Annals of Biomedical Engineering*, 32(11):1519–1529, November 2004.

[347] T. W. Secomb, J. P. Alberding, R. Hsu, M. W. Dewhirst, and A. R. Pries. Angiogenesis: An Adaptive Dynamic Biological Patterning Problem. *PLoS Computational Biology*, 9(3):e1002983, March 2013.

[348] D. G. Seifu, A. Purnama, K. Mequanint, and D. Mantovani. Small-diameter vascular tissue engineering. *Nature Reviews Cardiology*, 10(7):410–421, May 2013.

[349] M. Shakeel, P. C. Matthews, R. S. Graham, and S. L. Waters. A continuum model of cell proliferation and nutrient transport in a perfusion bioreactor. *Mathematical Medicine and Biology: A Journal of the IMA*, 30(1):21–44, March 2013.

[350] A. Shamloo and S. C. Heilshorn. Matrix density mediates polarization and lumen formation of endothelial sprouts in VEGF gradients. *Lab on a Chip*, 10(22):3061–3068, October 2010.

[351] A. Shamloo, N. Ma, M.-m. Poo, L. L. Sohn, and S. C. Heilshorn. Endothelial cell polarization and chemotaxis in a microfluidic device. *Lab on a Chip*, 8(8):1292–1299, July 2008.

[352] H.-C. Shih, T.-A. Lee, H.-M. Wu, P.-L. Ko, W.-H. Liao, and Y.-C. Tung. Microfluidic Collective Cell Migration Assay for Study of Endothelial Cell Proliferation and Migration under Combinations of Oxygen Gradients, Tensions, and Drug Treatments. *Scientific Reports*, 9(1):1–10, June 2019.

[353] K. Shintani, T. Uemura, K. Takamatsu, T. Yokoi, E. Onode, M. Okada, and H. Nakamura. Protective effect of biodegradable nerve conduit against peripheral nerve adhesion after neurolysis. *Journal of Neurosurgery*, 129(3):815–824, September 2018.

[354] R. J. Shipley and S. L. Waters. Fluid and mass transport modelling to drive the design of cell-packed hollow fibre bioreactors for tissue engineering applications. *Mathematical Medicine and Biology*, 29(4):329–359, December 2012.

[355] Y. Shirosaki, T. Okayama, K. Tsuru, S. Hayakawa, and A. Osaka. Synthesis and cytocompatibility of porous chitosan-silicate hybrids for tissue engineering scaffold application. *Chemical Engineering Journal*, 137(1):122–128, March 2008.

[356] M. M. Sholley, G. P. Ferguson, H. R. Seibel, J. L. Montour, and J. D. Wilson. Mechanisms of neovascularization. Vascular sprouting can occur without proliferation of endothelial cells. *Laboratory Investigation*, 51(6):624–634, December 1984.

[357] D. Shweiki, A. Itin, D. Soffer, and E. Keshet. Vascular endothelial growth factor induced by hypoxia may mediate hypoxia-initiated angiogenesis. *Nature*, 359(6398):843–845, October 1992.

[358] M. Siemionow and E. Sonmez. Nerve allograft transplantation: A review. *Journal of Reconstructive Microsurgery*, 23(8):511–520, November 2007.

[359] J. T. Smith, J. T. Elkin, and W. M. Reichert. Directed cell migration on fibronectin gradients: Effect of gradient slope. *Experimental Cell Research*, 312(13):2424–2432, August 2006.

[360] M. Sondell, G. Lundborg, and M. Kanje. Vascular endothelial growth factor stimulates Schwann cell invasion and neovascularization of acellular nerve grafts. *Brain Research*, 846(2):219–228, November 1999.

[361] J. R. Sparrow and J. A. Kiernan. Endoneurial vascular permeability in degenerating and regenerating peripheral nerves. *Acta Neuropathologica*, 53(3):181–188, September 1981.

[362] A. Stempien-Otero, A. Karsan, C. J. Cornejo, H. Xiang, T. Eunson, R. S. Morrison, M. Kay, R. Winn, and J. Harlan. Mechanisms of Hypoxia-induced Endothelial Cell Death: ROLE OF p53 IN APOPTOSIS. *Journal of Biological Chemistry*, 274(12):8039–8045, March 1999.

[363] A. Stéphanou, S. McDougall, A. Anderson, and M. Chaplain. Mathematical modelling of flow in 2D and 3D vascular networks: Applications to anti-angiogenic and chemotherapeutic drug strategies. *Mathematical and Computer Modelling*, 41(10):1137–1156, May 2005.

[364] M. G. P. Stoker and H. Rubin. Density Dependent Inhibition of Cell Growth in Culture. *Nature*, 215(5097):171–172, July 1967.

[365] C. L. Stokes and D. A. Lauffenburger. Analysis of the roles of microvessel endothelial cell random motility and chemotaxis in angiogenesis. *Journal of Theoretical Biology*, 152(3):377–403, October 1991.

[366] C. L. Stokes, D. A. Lauffenburger, and S. K. Williams. Migration of

individual microvessel endothelial cells: stochastic model and parameter measurement. *Journal of Cell Science*, 99(2):419–430, June 1991.

[367] I. Streeter and U. Cheema. Oxygen consumption rate of cells in 3D culture: The use of experiment and simulation to measure kinetic parameters and optimise culture conditions. *Analyst*, 136(19):4013–4019, September 2011.

[368] B. M. Strem, K. C. Hicok, M. Zhu, I. Wulur, Z. Alfonso, R. E. Schreiber, J. K. Fraser, and M. H. Hedrick. Multipotential differentiation of adipose tissue-derived stem cells. *The Keio Journal of Medicine*, 54(3):132–141, September 2005.

[369] S. Sun, M. Wheeler, M. Obeyesekere, and C. W. J. Patrick. A deterministic model of growth factor-induced angiogenesis. *Bulletin of Mathematical Biology*, 67(2):313–337, March 2005.

[370] T. Sun, P. McMinn, S. Coakley, M. Holcombe, R. Smallwood, and S. MacNeil. An integrated systems biology approach to understanding the rules of keratinocyte colony formation. *Journal of the Royal Society Interface*, 4(17):1077–1092, December 2007.

[371] T. Sun, S. Adra, R. Smallwood, M. Holcombe, and S. MacNeil. Exploring Hypotheses of the Actions of TGF-β1 in Epidermal Wound Healing Using a 3D Computational Multiscale Model of the Human Epidermis. *PLoS ONE*, 4(12):e8515, December 2009.

[372] C. Suri, P. F. Jones, S. Patan, S. Bartunkova, P. C. Maisonpierre, S. Davis, T. N. Sato, and G. D. Yancopoulos. Requisite Role of Angiopoietin-1, a Ligand for the TIE2 Receptor, during Embryonic Angiogenesis. *Cell*, 87(7):1171–1180, December 1996.

[373] R.-J. Swijnenburg, S. Schrepfer, F. Cao, J. I. Pearl, X. Xie, A. J. Connolly, R. C. Robbins, and J. C. Wu. In vivo imaging of embryonic stem

cells reveals patterns of survival and immune rejection following transplantation. *Stem Cells and Development*, 17(6):1023–1029, December 2008.

[374] S. Takano, Y. Yoshii, S. Kondo, H. Suzuki, T. Maruno, S. Shirai, and T. Nose. Concentration of Vascular Endothelial Growth Factor in the Serum and Tumor Tissue of Brain Tumor Patients. *Cancer Research*, 59(9):2185–2190, May 1996.

[375] K. Tang, E. C. Breen, H. Wagner, T. D. Brutsaert, M. Gassmann, and P. D. Wagner. HIF and VEGF relationships in response to hypoxia and sciatic nerve stimulation in rat gastrocnemius. *Respiratory Physiology & Neurobiology*, 144(1):71–80, November 2004.

[376] J. Tao, Y. Hu, S. Wang, J. Zhang, X. Liu, Z. Gou, H. Cheng, Q. Liu, Q. Zhang, S. You, and M. Gou. A 3D-engineered porous conduit for peripheral nerve repair. *Scientific Reports*, 7(1):46038, December 2017.

[377] I. M. Tarlov and J. A. Epstein. Nerve Grafts: the Importance of an Adequate Blood Supply. *Journal of Neurosurgery*, 2(1):49–71, January 1945.

[378] C. A. Taylor, D. Braza, J. B. Rice, and T. Dillingham. The incidence of peripheral nerve injury in extremity trauma. *American Journal of Physical Medicine & Rehabilitation*, 87(5):381–385, May 2008.

[379] M. M. Tomadakis and S. V. Sotirchos. Transport properties of random arrays of freely overlapping cylinders with various orientation distributions. *The Journal of Chemical Physics*, 98(1):616–626, January 1993.

[380] P. Tomlins, P. Grant, S. Mikhalovsky, S. James, and L. Mikhalovska. Measurement of Pore Size and Porosity of Tissue Scaffolds. *Journal of ASTM International*, 1(1):1–8, 2004.

[381] S. Tong and F. Yuan. Numerical Simulations of Angiogenesis in the Cornea. *Microvascular Research*, 61(1):14–27, January 2001.

[382] F. R. Troeh, J. D. Jabro, and D. Kirkham. Gaseous diffusion equations for porous materials. *Geoderma*, 27(3):239–253, April 1982.

[383] D. S. Tsai and W. Strieder. Effective Conductivities of Random Fiber Beds. *Chemical Engineering Communications*, 40(1–6):207–218, 1986.

[384] A. Tufro-McReddie, V. F. Norwood, K. W. Aylor, S. J. Botkin, R. M. Carey, and R. A. Gomez. Oxygen regulates vascular endothelial growth factor-mediated vasculogenesis and tubulogenesis. *Developmental Biology*, 183(2):139–149, March 1997.

[385] C. Urbich, E. Dernbach, A. Reissner, M. Vasa, A. M. Zeiher, and S. Dimmeler. Shear Stress-Induced Endothelial Cell Migration Involves Integrin Signaling Via the Fibronectin Receptor Subunits α_5 and β_1. *Arteriosclerosis, Thrombosis, and Vascular Biology*, 22(1):69–75, January 2002.

[386] A. D. van der Meer, K. Vermeul, A. A. Poot, J. Feijen, and I. Vermes. A microfluidic wound-healing assay for quantifying endothelial cell migration. *American Journal of Physiology-Heart and Circulatory Physiology*, 298(2):H719–H725, November 2009.

[387] V. W. van Hinsbergh and P. Koolwijk. Endothelial sprouting and angiogenesis: matrix metalloproteinases in the lead. *Cardiovascular Research*, 78(2):203–212, February 2008.

[388] P. Van Pham, N. B. Vu, and N. K. Phan. Hypoxia promotes adipose-derived stem cell proliferation via VEGF. *Biomedical Research and Therapy*, 3(1):476–482, February 2016.

[389] N. Varongchayakul, D. Huttner, M. W. Grinstaff, and A. Meller. Sensing Native Protein Solution Structures Using a Solid-state Nanopore: Unraveling the States of VEGF. *Scientific Reports*, 8(1):1017, January 2018.

[390] M. Vastamäki, P. K. Kallio, and K. A. Solonen. The results of

secondary microsurgical repair of ulnar nerve injury. *Journal of Hand Surgery: British & European Volume*, 18(3):323–326, June 1993.

[391] P. Vempati, A. S. Popel, and F. Mac Gabhann. Formation of VEGF isoform-specific spatial distributions governing angiogenesis: computational analysis. *BMC Systems Biology*, 5:59, May 2011.

[392] P. Vempati, A. S. Popel, and F. Mac Gabhann. Extracellular regulation of VEGF: isoforms, proteolysis, and vascular patterning. *Cytokine & Growth Factor Reviews*, 25(1):1–19, February 2014.

[393] D. Vestweber. VE-Cadherin: The Major Endothelial Adhesion Molecule Controlling Cellular Junctions and Blood Vessel Formation. *Arteriosclerosis, Thrombosis, and Vascular Biology*, 28(2):223–232, February 2008.

[394] C. L. A. M. Vleggeert-Lankamp, J. Wolfs, A. P. Pêgo, R. van den Berg, H. Feirabend, and E. Lakke. Effect of nerve graft porosity on the refractory period of regenerating nerve fibers: Laboratory investigation. *Journal of Neurosurgery*, 109(2):294–305, August 2008.

[395] D. von Tell, A. Armulik, and C. Betsholtz. Pericytes and vascular stability. *Experimental Cell Research*, 312(5):623–629, March 2006.

[396] B. A. Wagner, S. Venkataraman, and G. R. Buettner. The Rate of Oxygen Utilization by Cells. *Free Radical Biology & Medicine*, 51(3):700–712, August 2011.

[397] D. Walker, J. Southgate, G. Hill, M. Holcombe, D. Hose, S. Wood, S. Mac Neil, and R. Smallwood. The epitheliome: agent-based modelling of the social behaviour of cells. *Biosystems*, 76(1-3):89–100, August 2004.

[398] A. Waller. Experiments on the Section of the Glossopharyngeal and Hypoglossal Nerves of the Frog, and Observations of the Alterations

Produced Thereby in the Structure of Their Primitive Fibres. *Philosophical Transactions of the Royal Society of London*, 5:423–429, 1850.

[399] J. Walpole, J. C. Chappell, J. G. Cluceru, F. Mac Gabhann, V. L. Bautch, and S. M. Peirce. Agent-based model of angiogenesis simulates capillary sprout initiation in multicellular networks. *Integrative Biology*, 7(9):987–997, September 2015.

[400] S. Walsh and R. Midha. Practical considerations concerning the use of stem cells for peripheral nerve repair. *Neurosurgical Focus*, 26(2):E2, February 2009.

[401] S. K. Walsh, R. Kumar, J. K. Grochmal, S. W. P. Kemp, J. Forden, and R. Midha. Fate of stem cell transplants in peripheral nerves. *Stem Cell Research*, 8(2):226–238, March 2012.

[402] D. Wang, H.-J. S. Huang, A. Kazlauskas, and W. K. Cavenee. Induction of Vascular Endothelial Growth Factor Expression in Endothelial Cells by Platelet-derived Growth Factor through the Activation of Phosphatidylinositol 3-Kinase. *Cancer Research*, 59(7):1464–1472, April 1999.

[403] L. Wang, M. T. Sanford, Z. Xin, G. Lin, and T. F. Lue. Role of Schwann cells in the regeneration of penile and peripheral nerves. *Asian Journal of Andrology*, 17(5):776–782, September 2015.

[404] M. L. Wang, M. Rivlin, J. G. Graham, and P. K. Beredjiklian. Peripheral nerve injury, scarring, and recovery. *Connective Tissue Research*, 60(1):3–9, January 2019.

[405] J. P. Ward and J. R. King. Mathematical modelling of avascular-tumour growth. *Mathematical Medicine and Biology: A Journal of the IMA*, 14(1):39–69, March 1997.

[406] M. G. Watson, S. R. McDougall, M. A. J. Chaplain, A. H. Devlin, and C. A. Mitchell. Dynamics of angiogenesis during murine retinal

development: a coupled in vivo and in silico study. *Journal of The Royal Society Interface*, 9(74):2351–2364, September 2012.

[407] G. Weddell. Axonal regeneration in cutaneous nerve plexuses. *Journal of Anatomy*, 77(Pt 1):49–62.3, October 1942.

[408] A. Weerasuriya. Patterns of change in endoneurial capillary permeability and vascular space during nerve regeneration. *Brain Research*, 510(1):135–139, February 1990.

[409] H. L. Weissberg. Effective Diffusion Coefficient in Porous Media. *Journal of Applied Physics*, 34(9):2636–2639, 1963.

[410] A. D. Widgerow, A. A. Salibian, S. Lalezari, and G. R. D. Evans. Neuromodulatory nerve regeneration: Adipose tissue-derived stem cells and neurotrophic mediation in peripheral nerve regeneration. *Journal of Neuroscience Research*, 91(12):1517–1524, December 2013.

[411] M. Witkowska-Zimny and K. Walenko. Stem cells from adipose tissue. *Cellular and Molecular Biology Letters*, 16(2):236–257, June 2011.

[412] M. B. Wood. Peroneal nerve repair: Surgical results. *Clinical Orthopaedics and Related Research*, 267:206–210, June 1991.

[413] P. Wu, Y. Fu, and K. Cai. Regulation of the migration of endothelial cells by a gradient density of vascular endothelial growth factor. *Colloids and Surfaces B: Biointerfaces*, 123:181–190, November 2014.

[414] W.-D. Xu, J.-G. Xu, and Y.-D. Gu. Comparative clinic study on vascularized and nonvascularized full-length phrenic nerve transfer. *Microsurgery*, 25(1):16–20, 2005.

[415] Y. Xu, L. Liu, Y. Li, C. Zhou, F. Xiong, Z. Liu, R. Gu, X. Hou, and C. Zhang. Myelin-forming ability of Schwann cell-like cells induced from rat adipose-derived stem cells in vitro. *Brain Research*, 1239:49–55, November 2008.

[416] S. Yi, L. Xu, and X. Gu. Scaffolds for peripheral nerve repair and reconstruction. *Experimental Neurology*, 319, September 2018.

[417] D. Yuen, J. Jenssen, and G. Rodriguez. A semipermeable, kink resistant type I collagen-based nerve guide for PNS repair. *Transactions of the Society for Biomaterials*, (228), 2003.

[418] D. F. Zawicki, R. K. Jain, G. W. Schmid-Schoenbein, and S. Chien. Dynamics of neovascularization in normal tissue. *Microvascular Research*, 21(1):27–47, January 1981.

[419] Q.-X. Zhang, C. J. Magovern, C. A. Mack, K. T. Budenbender, W. Ko, and T. K. Rosengart. Vascular endothelial growth factor is the major angiogenic factor in omentum: Mechanism of the omentum-mediated angiogenesis. *Journal of Surgical Research*, 67(2):147–154, 1997.

[420] D. Zhang, X. Wu, J. Chen, and K. Lin. The development of collagen based composite scaffolds for bone regeneration. *Bioactive Materials*, 3(1):129–138, March 2018.

[421] S. Zhou, Z. Cui, and J. P. G. Urban. Nutrient gradients in engineered cartilage: Metabolic kinetics measurement and mass transfer modeling. *Biotechnology and Bioengineering*, 101(2):408–421, October 2008.

[422] L.-N. Zhou, J.-W. Zhang, X.-L. Liu, and L.-H. Zhou. Co-Graft of Bone Marrow Stromal Cells and Schwann Cells into Acellular Nerve Scaffold for Sciatic Nerve Regeneration in Rats. *Journal of Oral and Maxillofacial Surgery*, 73(8):1651–1660, August 2015.

[423] D. W. Zochodne. *Neurobiology of Peripheral Nerve Regeneration*. Cambridge University Press, Cambridge, October 2008.

[424] P. A. Zuk. The adipose-derived stem cell: Looking back and looking ahead. *Molecular Biology of the Cell*, 21(11):1783–1787, June 2010.